THE INSTABILITY OF SOME TIME PERIODICALLY FORCED FLOWS

A THESIS SUBMITTED TO THE UNIVERSITY OF LONDON
FOR THE DEGREE OF DOCTOR OF PHILOSOPHY
AND TO IMPERIAL COLLEGE
FOR THE DIPLOMA OF IMPERIAL COLLEGE
BY

Gursharan Sagoo

Imperial College of Science, Technology and Medicine,
Department of Mathematics,
Huxley Building,
180 Queen's Gate, London SW7 2BZ

August 2003

Abstract

In this thesis the instability of two viscous incompressible flows is discussed by using numerical and analytical methods. The first problem concerns the steady streaming flow, that is contained within a hollow stationary cylinder and induced by the transverse oscillation of a solid inner cylinder. The small gap limit is taken so that a series solution in odd powers of the angular variable is possible. From the studies by Hall & Papageorgiou [37] and Watson *et al.* [97], it is known that the leading order equation has solutions that are steady, quasi-periodic and chaotic (period doubling). Since all the higher order equations are driven by the solution at leading order; the series solution for the steady streaming flow is investigated with an interest to determine any chaotic structures.

The second problem concerns the flow in a horizontal circular pipe, that is subject to torsional oscillations about a vertical axis that passes symmetrically through the pipe. The onset of a new axisymmetric roll-type instability, as observed experimentally by Bolton & Maurer [10] for the corresponding rectangular tank problem (of small width), is sought in the high-frequency ($\bar{\Phi} \gg 1$) and small-amplitude limit ($\alpha \ll 1$). A perturbation of the WKBJ type is imposed upon the basic state, so that the slow angular variation of the disturbance is accounted for in the linear stability equations. Accordingly, a dispersion relation for the dimensionless frequency parameter $\bar{\Phi}$ is derived. In order to identify the most dangerous disturbance, it is necessary to minimise the eigenvalue $B = \alpha \bar{\Phi}^{-1/4}$. The theory of Soward & Jones [82] is used to show that an acceptable solution of the governing eigenvalue problem, cannot be obtained for real values of the latitudinal variable θ; instead, the correct minimum is found in the complex θ-plane.

Acknowledgements

I would like to thank Professor Philip Hall for his excellent supervision and guidance over my undergraduate and postgraduate years at Imperial College. I would also like to thank Professor Demetrios Papageorgiou and the rest of the Mathematics Department at New Jersey Institute of Technology for their kind hospitality during the Spring semester 2000.

A special thanks goes out to my brothers Pardeep and Kuldev for their laughter and encouragement. On the same note I would also like to thank Sinéad, Kheng, Ioannis, Shahid, Nick, Kirsty, Mark, Sadi, Dave, Sharon, George, Gihan and the rest of my friends in the Department for their encouragement and helpful advice.

Finally, I would like to acknowledge the financial assistance of the Engineering and Physical Sciences Research Council.

Dedication

This thesis is dedicated to my dearly loved mother Kulbinder
and to the memory of my grandfather Santa Singh Sagoo.

Contents

Abstract 2

Acknowledgements 3

List of abbreviations 12

1 Introduction 13

1.1 Thermal convection 15

1.2 Centrifugal instability 17

1.2.1 Taylor vortices 17

1.2.2 Görtler vortices 19

1.2.3 Stokes layers 23

1.3 Nonlinearity 24

1.4 The transversely oscillating cylinder 26

Overview 28

2 The steady streaming flow between cylinders 31

2.1 Introduction 32

2.2 Formulation 43

2.2.1 Steady streaming at small values of Re_s 46

2.2.2 Steady streaming at $O(1)$ values of Re_s 48

2.2.3 Transformation to the small gap width limit 51

2.3 Asymptotic solutions 54

2.3.1 Asymptotic solutions for small R_s 56
2.3.2 The steady state asymptotic solutions for large R_s 58
2.4 Numerical Work 69
2.4.1 Numerical Results 72
2.4.2 Stability Analysis 82
2.4.3 Steady state comparisons 90
2.4.4 Fourier series decomposition 117
2.5 A generalisation of the boundary conditions 122
2.5.1 Steady asymptotic solutions 125
2.5.2 Numerical Results 127
2.6 Upwind differencing 141
2.6.1 The cylinder problem (original boundary condition) 141
2.6.2 The modified problem 157
2.7 Conclusion 166

3 The flow in a torsionally oscillating pipe 175
3.1 Introduction 176
3.2 Formulation 185
3.2.1 Basic flow 187
3.2.2 Asymptotic expansions for $\Phi \gg 1$ 191
3.2.3 Stability Analysis 193
3.2.4 Discussion of theory 194
3.2.5 Simplifications of symmetry 199
3.3 Numerical Results 200
3.3.1 Fourier series analysis 205
3.3.2 Search for the saddle point 212
3.4 Conclusion 217

Bibliography 220

List of Figures

1.1 The formation of Görtler vortices on a concave wall. 21

2.1 The free jets emerging from a collision of the outer layers for $Re_s \gg 1$. 35
2.2 Streamlines and velocity profiles of the steady Bickley jet. 37
2.3 Boundary layers in the two-cylinder problem, $Re_s \gg 1$ and $\alpha = O(1)$ . . 39
2.4 The configuration of the cylinders in the complex ζ-plane. 45
2.5 The Stokes layers on the inner and outer cylinders. 48
2.6 A schematic diagram of the different flow regimes of $\Psi^{(0)}$ 55
2.7 A comparison of Yuan's solution for $f^{(0,1)}$ with the Fourier series representation (6 terms) 63
2.8 The first and second derivatives of $f^{(0,1)}$. 64
2.9 The divergence of $f^{(0,1)}_{\eta\eta\eta}$ near $\eta = 0,\ 1$. 64
2.10 The time period of the symmetric solution of $\Psi^{(0)}$ 73
2.11 The symmetric solution of $\Psi^{(0)}$ (steady state) 74
2.12 The periodic symmetric solution of $\Psi^{(0)}$ at $R_s = 1600$ 74
2.13 The symmetric time periodic solution of $\Psi^{(0)}$ at $R_s = 300$, 3D view . . . 75
2.14 The symmetric time periodic solution of $\Psi^{(0)}$ at $R_s = 300$, 2D view. . . 75
2.15 The asymmetric steady state of $\Psi^{(0)}$ 76
2.16 The Poincaré cross sections and return maps of $\Psi^{(0)}$ at $R_s = 79,\ 81$ . . 76
2.17 The Poincaré cross section and return map of $\Psi^{(0)}$ at $R_s = 85$ 77
2.18 The Poincaré cross section of $\Psi^{(0)}$ at $R_s = 86$ 78
2.19 The Poincaré cross section and return map of $\Psi^{(0)}$ at $R_s = 90$ 79

2.20 A diagram of the critical values R_n 80
2.21 Neutral points for growth rates $\gamma_n(R_n)$ 86
2.22 The continuation curves of the growth rates γ_n. 87
2.23 The eigenfunction of $\Psi^{(6)}$ at various values of R_s 87
2.24 The different branches of the growth rate $\gamma_n(R_s)$ for fixed n 88
2.25 A 3D plot of Ψ at $R_s = 35$. 95
2.26 A contour plot of Ψ at $R_s = 35$. 95
2.27 The agreement of DNS for Ψ with: 1) the series solution, and 2) the asymptotic solution for small R_s 97
2.28 The θ-profiles of Ψ at $R_s = 15$, 30, 40 50. 98
2.29 The wavy/discontinuous θ-profiles of Ψ at $R_s = 44$, 47. 98
2.30 The numerical solution for Ψ at $R_s = 50$, 55, 60, 65 with $\Delta\theta = 2\pi/128$. 100
2.31 Part I. The numerical solution for Ψ at $R_s = 50$, 55, 60 with $\Delta\theta = 2\pi/256$.101
2.32 Part II. The numerical solution for Ψ at $R_s = 60$, 65 with $\Delta\theta = 2\pi/256$. 102
2.33 The numerical solution for Ψ at $R_s = 47$ with $\Delta\theta = 2\pi/128$, $2\pi/256$, $2\pi/384$. 103
2.34 The FFT of Ψ at $R_s = 47$ with $\Delta\theta = 2\pi/128$, $2\pi/256$, $2\pi/384$. 104
2.35 The numerical solutions for Ψ at $R_s = 47$ and $R_s = 48$. 105
2.36 The numerical solution for Ψ at $R_s = 50$, with $\Delta\theta = 2\pi/384$. 107
2.37 The numerical solution for Ψ at $R_s = 55$, with $\Delta\theta = 2\pi/384$. 108
2.38 The filtered solutions for Ψ at $R_s = 50$ and $R_s = 55$. 109
2.39 The magnitude of each term $\Psi^{(n)}$ versus Reynolds number 111
2.40 The magnitude of each term $\Psi^{(n)}$ versus Reynolds number 112
2.41 Energy spectra of the Fourier modes at $R_s = 300$ 120
2.42 Energy spectra of the Fourier modes at $R_s = 1600$ 121
2.43 The numerical solution for $\bar{\Psi}$ at $R_s = 40$. 128
2.44 The DNS for $\bar{\Psi}$ at $R_s = 10$, 20, 30, 40, 50. 128
2.45 Exponential BC: The agreement of $\bar{\Psi}$ with: 1) the series solution, and 2) the asymptotic solution for small R_s 130

2.46 The DNS for $\bar{\Psi}$ at $R_s = 50,\ 60,\ 70,\ 80$ with $\Delta\xi = 2\pi/128$. 132
2.47 The DNS for $\bar{\Psi}$ at $R_s = 50,\ 60,\ 70,\ 80$ with $\Delta\xi = 2\pi/256$. 133
2.48 The DNS for $\bar{\Psi}$ at $R_s = 50,\ 60,\ 70,\ 80$ with $\Delta\xi = 2\pi/512$. 134
2.49 The FFT of $\bar{\Psi}$ at $R_s = 60$ with $\Delta\xi = 2\pi/128,\ 2\pi/256,\ 2\pi/512$. 135
2.50 The magnitude of each term $\bar{\Psi}^{(n)}$ versus Reynolds number 138
2.51 The numerical solution for Ψ_{sym} at $R_s = 50,\ 60,\ 100,\ 130$. 143
2.52 A snapshot contour diagram of Ψ at $R_s = 160$ (unsteady regime). 145
2.53 The numerical solution for Ψ at $R_s = 130,\ 140,\ 160,\ 200$ and 300. 146
2.54 The steady θ-profiles of Ψ_{sym} at $R_s = 200,\ 300$. 147
2.55 The Poincaré cross section of Ψ at $R_s = 140,\ 160,\ 180$. 149
2.56 The Poincaré cross section of Ψ at $R_s = 200,\ 220$. 150
2.57 The Poincaré cross section of Ψ at $R_s = 260,\ 300$. 151
2.58 The Poincaré cross section of Ψ at $R_s = 120,\ 125$ with $\Delta\theta = \pi/256$. . . 153
2.59 The Poincaré cross section of Ψ at $R_s = 130,\ 135,\ 140$ with $\Delta\theta = \pi/256$. 154
2.60 The Poincaré cross section of $\Psi^{(0)}$ from $R_s = 120$ to 200. 156
2.61 The numerical solution for $\bar{\Psi}$ at $R_s = 50,\ 70,\ 110,\ 160$. 158
2.62 The numerical solution for $\bar{\Psi}$ at $R_s = 180,\ 200,\ 300,\ 400$. 159
2.63 The Poincaré cross section of $\bar{\Psi}$ at $R_s = 170,\ 180,\ 200,\ 220$ with $\Delta\theta = 2\pi/256$. 162
2.64 The Poincaré cross section of $\bar{\Psi}$ at $R_s = 240,\ 260$ with $\Delta\theta = 2\pi/256$. . . 163
2.65 The Poincaré cross section of $\bar{\Psi}$ at $R_s = 170,\ 180,\ 200,\ 220$ with $\Delta\theta = 2\pi/512$. 164
2.66 The Poincaré cross section of $\bar{\Psi}$ at $R_s = 240,\ 260$ with $\Delta\theta = 2\pi/512$. . . 165

3.1 The unstable interface between two rolls in the circular pipe problem. . 177
3.2 Cylindrical and spherical Taylor-Couette flow 179
3.3 The rotating circular pipe with body coordinates (r^*, θ, z^*). 186
3.4 The Stokes and anti-Stokes lines in complex θ-plane 197
3.5 The evolution of the stability surface in (k, B, ζ)-space. 202
3.6 The neutral stability surface and contour lines near the discontinuity. . . 203

3.7 The magnitude of $\mathrm{Re}\{\tilde{u}\}$ with $k = 1$ and $\mu = 0$. 204
3.8 The magnitude of $\mathrm{Re}\{\tilde{w}\}$ with $k = 1$ and $\mu = 0$. 204
3.9 The neutral stability curves in the k-B plane produced by time marching. 205
3.10 The difference between the results computed by time marching and the eigen mode analysis. 207
3.11 The upper and lower neutral stability curves of the Hele-Shaw cell instability at $k = 0.46$. 209
3.12 The growth rate μ_{HS} at $\zeta = 0.12$ and $0.38 < k < 0.41$. 209
3.13 The upper and lower neutral stability curves for $0.10 \leqslant \zeta \leqslant 0.12$. 210
3.14 The error associated with computing the upper stability curve 211
3.15 The lower neutral stability curves for $k = 0.20,\ 0.32,\ 0.40$ 213
3.16 The lower neutral stability surface of the S mode. 213
3.17 The lower neutral stability surface of the S mode. 214
3.18 The neutral stability curves of the S mode at $\zeta = 0.0,\ -0.016,\ -0.032$. 215
3.19 The energy spectrum of the S mode at the saddle point, calculated with $(N, I) = (6, 100)$ 216
3.20 The energy spectrum of the S mode at the saddle point, calculated with $(N, I) = (8, 100)$ 216

List of Tables

1.1 The range of μ and the corresponding azimuthal wave number of least stable mode in cylindrical Taylor-Couette flow. 19

2.1 The route to chaos dependence on Δ; Hall & Papageorgiou [37] 42
2.2 A summary of the numerical solutions for $\Psi^{(0)}$ 55
2.3 The size of the timestep required to calculate $\Psi^{(0)}$. 72
2.4 The neutral stability points R_n for each term $\Psi^{(n)}$. 85
2.5 Estimates for convergence angle using Δ_e 92
2.6 The agreement of the series solution (2.34) with the DNS of the governing equations (2.33). 96
2.7 The approximate values of R_s at which $\|\Psi^{(n)}\| \approx \|\Psi^{(n+1)}\|$ 113
2.8 The agreement of $\Psi^{(n)}$ with the small-R_s asymptotic solution (2.43) . . 116
2.9 Exponential BC: the agreement of the series solution with the DNS of governing equations (2.102). 129
2.10 The agreement of $\bar{\Psi}^{(n)}$ with small-R_s asymptotic solution 139
2.11 Exponential BC: the agreement of the series solution with the steady asymptotic solution for large R_s. 140
2.12 The agreement of the series solution (2.34) with the DNS of the governing equations (2.33) (using UWD). 144
2.13 The time period of $\Psi^{(0)}$ and Ψ versus Reynolds number. 152
2.14 Exponential BC: the agreement of the series solution with the DNS of governing equations (2.102) (using UWD). 160

2.15 The time period of $\bar{\Psi}$ versus Reynolds number. 161

List of abbreviations

BC	Boundary condition
DFT	Discrete fourier transform
DNS	Direct numerical solution
FD	Finite difference
FFT	Fast fourier transform
LHS	Left-hand side
MAC	Marker and cell (staggered grid finite differences)
MAPP	Mike's Arbitrary Precision Package (C library)
ODE	Ordinary differential equation
PDE	Partial differential equation
PS	Pseudospectral
RHS	Right-hand side
UWD	Upwind differencing
VSF	Vorticity-stream function

The copyright of this thesis rests with the author and no quotation from it or information derived from it may be published without the prior consent of the author.

Chapter 1

Introduction

Fluid mechanics is a vast and interesting field of study, the mathematical understanding of which, is beneficial to many areas such as aeronautics, geophysics, industry and blood flow analysis to name but a few. Over the years, our understanding of these and indeed other intricate dynamical systems, has been developed by the comprehensive analysis of numerous simplified systems. In these simplified prototype problems, one is often interested in the laminar structures of the flow and their possible destabilisation to secondary states or transition to turbulence.

In 1883 Osborne Reynolds [64] recorded, his now renowned, experimental observations for incompressible flow in a long pipe of circular cross section. Visualisation of the fluid motion was achieved by the introduction of a dye streak, the evolution of which, was then monitored downstream. For a particular fluid of fixed viscosity, Reynolds observed that a stable laminar flow always existed for small enough fluid velocities. In this case the dye streak continued throughout the pipe in a smooth straight line. Reynolds also reported that the laminar flow (at significantly small velocities) was sensitive to the initial conditions at the pipe inlet. Small variations of the fiuid velocity at the inlet, would interfere with the straight line propagation of the dye, causing it to sway within the tube.

In his analysis, Reynolds introduced the similarity parameter R_e, defined as

$$R_e = \frac{UL}{\nu}\,, \tag{1.1}$$

where U is a typical fiow velocity, ν is the kinematic viscosity and L is a length scale

associated with the radius of the pipe. By expressing the fluid velocity and pressure using these scales, the Navier-Stokes equations can then be written in non-dimensional form. In this manner, the overall effect of the scales $\{U,\ L,\ \nu\}$ then enter the governing equations via the Reynolds number. Therefore a flow with different values of $\{U,\ L,\ \nu\}$, but same Reynolds number, has the same non-dimensional Navier-Stokes solution. For large values of R_e, Reynolds observed the appearance of turbulent spots that caused the dye in the remaining part of the pipe to diffuse strongly. Further increases in R_e resulted in the turbulent behaviour being initiated closer to the inlet. Reynolds then continued his experimental study of the pipe flow problem by giving the critical Reynolds number for pipes with different wall roughness (for further details regarding these experiments see Drazin & Reid [19]).

Most of the stability work around this time was focused on linear and typically inviscid theory. This was largely due to the incorrect perception, that the main effect of viscosity is to dissipate the energy being transferred to the perturbations, thus viscosity was initially perceived as a purely stabilising feature of the flow. Of course under this pretence, the highest derivatives in the equations of motion disappear, thus motivating further analytical progress.

The now popular *normal mode analysis*, was first introduced to fluid stability problems by Stokes, Lord Kelvin and Lord Rayleigh. The latter authors sought to extend the use of the normal mode analysis, since it had already been applied successfully to many other dynamical systems. The idea behind this analysis, rests on the assumption that any perturbation can be resolved into a sum of modes varying in time like e^{st}, where t denotes time. The equations of motion are then linearised about the basic state, thus giving rise to an eigenvalue problem for s (which is complex in general). In practice the level of difficulty associated with these equations prevents any analytical progress and it is often necessary to calculate s numerically. If the real part of s is found to be strictly less than zero, the flow is said to be *asymptotically stable* to that mode, and if s equals zero the flow is said to be *neutrally stable*. Hence an *asymptotically growing* disturbance is associated with $\mathrm{Re}\{s\} > 0$; note, this does not necessarily

mean that the ensuing motion is turbulent, in many cases the latter condition also indicates a bifurcation to a secondary laminar state.

However, when the method of normal modes is applied to the pipe flow problem (investigated by Reynolds), it is surprisingly found that the flow is linearly stable at all values of R_e. This result is clearly inconsistent with the turbulent flow observed experimentally by Reynolds, implying that the resolution of this discrepancy would require a full nonlinear description of the flow.

The mechanism by which a realised instability is initiated varies greatly from one problem to another. Subsequently, many canonical problems have been investigated over the years to enhance our understanding of the respective transition phase for each flow. Because this thesis considers two specific problems, some of the more relevant background is provided in addition to some general review.

1.1 Thermal convection

One of the first and indeed simplest instability mechanisms to be observed, was the overturning instability associated with a horizontal fluid layer resting on a heated plate. In the vicinity of the plate, the fluid is less dense than the remaining part resting above it. Therefore once the destabilising effects of buoyancy dominate over the stabilising ones of viscosity and thermal conductivity, the instability is initiated and is assisted by the action of body forces, which in this case is gravity. This instability was first reported in 1881 by Thomson [95] who described the instability qualitatively, but the first set of experimental data was documented by Bénard [4] in 1900. Bénard's experimental study later inspired Rayleigh to investigate the problem theoretically.

In 1916 Rayleigh [62] formulated the associated stability problem using linear theory and subsequently he introduced an important dimensionless parameter called the Rayleigh number. The Rayleigh number represents the temperature gradient across the fluid layer. Moreover, in terms of stability characteristics, the Rayleigh number is the ratio of buoyancy effects to the stabilising influences of thermal diffusion and viscous dissipation.

However it was later shown by Block [9] and Pearson [59], that the instability in the regime investigated by Bénard, i.e. the case of thin free-surface fluid layers, is in fact driven by the variation of the surface tension (with temperature) and not the mechanism associated with the exchange of light fluid and heavy fluid. The failure of Rayleigh's description, for the case of thin layers, was due to the inadequacy of his mathematical model. In Rayleigh's analysis, the fluid is confined between two horizontal rigid plates. However in the experiments conducted by Bénard, the upper surface of the fluid layer was unbounded and open to the air. Since the upper surface is free, surface tension forces have an affect on the flow and in the case of thin fluid layers, these forces are more dominant than the effects of buoyancy. The importance of this subtle difference was explained by Pearson [59], who incorporated the appropriate surface tension effects by formulating the stability problem using the Marangoni number (named after the 19^{th} century Italian investigator). Despite this important amendment by Pearson, some fifty eight years after Bénard's investigation, the name 'Rayleigh-Bénard' convection has remained firmly attached to this type of instability. This is probably due to the fact that Rayleigh's work is still applicable to regimes where the fluid layer is thick. In these cases, the variation of the surface tension is outweighed by the dominating effects of buoyancy, and the instability proceeds via the mechanism initially assumed for this problem.

Many variations of the classical Rayleigh-Bénard problem have been investigated since the amendment by Pearson e.g. Yih & Lin [102] have investigated the modulated heating of the upper and lower plates. In the latter study, the Rayleigh number is supplemented by the Prandtl number (ratio of kinematic viscosity to thermal diffusivity) in the nonlinear flow description. A thorough discussion of the latter investigation, and indeed other modified versions of Rayleigh-Bénard problem, can be found in the review article by Davis [16] and the references therein.

1.2 Centrifugal instability

It is known that a flow moving along a curved path will experience a centrifugal body forced (subject to an orientation about a local radius of curvature) and under certain conditions e.g. large angular velocities, this force can provide the appropriate means for instability. This centrifugal force, which acts normal to the streamlines, is essentially balanced by the pressure gradients along the normals; therefore a temporal imbalance of these forces can have a destabilising effect on the fluid motion. The extent and precise description of this destabilisation has been heavily investigated in many configurations, some of which are described below.

1.2.1 Taylor vortices

As the name suggests, Taylor (1921, [91]) was the first to observe the appearance of these toroidal vortices in, certain regimes of, his experimental analysis concerning the flow between two coaxial cylinders. In this experiment the inner and outer cylinders are allowed to rotate independently with respective angular velocities Ω_1 and Ω_2. The vortices develop in the streamwise sense and align themselves periodically in the axial direction. In this configuration, any two neighbouring vortices are rotating in opposite directions, as shown in figure 3.2 on page 179. In the subsequent viscous analysis, the Taylor number T was introduced to represent the ratio of the centrifugal effects to the viscosity of the flow. At small values of the Taylor number, the viscous forces are dominant and accordingly it is anticipated that the flow is stable. In contrast, the centrifugal forces are destabilising and therefore instability is expected at large values of T. By letting L represent a convenient length scale, the Taylor number can be defined as

$$T = \frac{4\Omega^2 L^4}{\nu^2}, \tag{1.2}$$

where Ω is the angular velocity of the swirling flow.

However, some important related studies were carried out prior to Taylor's experiment, namely those by Couette [14], Mallock [50] and Rayleigh [63]. In 1890 Couette

[14] sought to measure the viscosity of a fluid contained between two coaxial cylinders (with $\Omega_1 = 0$ and $\Omega_2 > 0$) by measuring the torque exerted by the flow on the stationary inner cylinder. He observed that below some critical value Ω_{2c} the torque increased linearly with Ω_2, and above this critical value the magnitude of the exerted torque is found to increase more rapidly. The onset of this rapid increase was clearly marked in the experiment, by the transition of the laminar circumferential flow to an unstable state.

Later Mallock [50] investigated the configuration in which the outer cylinder is at rest ($\Omega_2 = 0$) and the inner one is made to rotate. Despite this minor change in the experimental setup, the results were fundamentally different to the findings of Couette. Mallock found that the flow in this regime was unstable for every non-zero value of Ω_1.

The inviscid problem was later investigated theoretically in 1916 by Rayleigh [63]. By using a elegant argument based on the conservation of angular momentum, Rayleigh proved that $\Phi > 0$ is a necessary and sufficient condition for stability to axisymmetric disturbances; here the Rayleigh discriminant Φ is given by

$$\Phi = \frac{1}{r^3}\frac{\mathrm{d}}{\mathrm{d}r}\left(\Omega r^2\right)^2, \tag{1.3}$$

and r denotes the radial coordinate. Although Rayleigh derived this result for inviscid flow, Synge (1933, [88]) has shown this condition is also applicable to viscous flows in the special case where $\mu = \Omega_2/\Omega_1 > 0$ (note, Yih [101] has also presented a much simpler proof of this condition).

Intrigued by the findings of Mallock, Taylor [91] conducted an experimental investigation of the flow between two counter rotating cylinders. For separation gaps of small width, Taylor observed that the rotational Couette flow, for large enough Taylor numbers, would give way to a secondary flow in which the toroidal vortices would appear as before. He also noted that upon further increasing the swirl (with $\mu < -1$), the axisymmetric vortices become wavy and a non-axisymmetric instability is present. In the followup paper two years later, Taylor [92] supplemented his experimental findings with a theoretical result that predicted the onset of vortices extremely well (in the

$-0.73 < \mu < 0,$	$m = 0$
$-0.76 < \mu < -0.73,$	$m = 1$
$-0.796 < \mu < -0.76,$	$m = 2$
$-0.88 < \mu < -0.796,$	$m = 3$
$-1.08 < \mu < -0.88,$	$m = 4$
$\ldots\ldots < \mu < -1.08,$	$m = 5$

Table 1.1: The range of μ investigated by DiPrima *et al.* [49], and the corresponding azimuthal wave number of least stable mode.

small gap limit).

Later, DiPrima [17] investigated the stability of Couette flow to three-dimensional disturbances. Again, a linear eigenvalue problem is derived and for the specific cases $\mu = 0,\ 0.5$ (in the small gap limit), it is found that the three-dimensional disturbances are slightly more stable than the corresponding axisymmetric ones. DiPrima [49] went on to extend this work with his colleagues Kruger and Gross, by considering the case of counter rotating cylinders ($\mu < 0$). In this study the least stable mode, for $\mu < -0.73$, is found to be non-axisymmetric and the associated azimuthal wave number is found to increase rapidly as μ is decreased from this value, see table 1.1. Moreover, this result also agrees well with experimental observations of Snyder (1968, [80]). An extensive discussion of the Taylor vortex system can be found in the review article by Stuart [86].

1.2.2 Görtler vortices

In 1940 Görtler [24] theoretically explored the destabilisation of a boundary layer on a concave surface. Görtler formulated this problem under the *parallel flow* assumption, which neglects the growth of the boundary layer. Moreover, under this assumption the basic state is assumed to be independent of the streamwise coordinate and the small normal velocity component is neglected too. Consequently, the governing set of partial differential equations reduce to a set of linear ordinary differential equations, and as a

result the stability analysis is greatly simplified.

The critical parameter in this case is the Görtler number, which can be thought of as spatially varying equivalent of the Taylor number. The Görtler number, G, is defined as

$$G = \frac{U_\infty \delta_M}{\nu}\left(\frac{\delta_M}{r_0}\right), \qquad \text{with} \qquad \delta_M = \int_0^\infty \frac{u}{U_\infty}(1 - \frac{u}{U_\infty})\,\mathrm{d}y. \tag{1.4}$$

Here r_0 is the radius of curvature of the flow, U_∞ is a typical velocity scale associated with the external flow and y is the coordinate variable normal to the curved surface. The momentum thickness δ_M is defined as: the thickness of a fluid layer with a uniform velocity U_∞ and a streamwise momentum flux equal to the defect of boundary layer momentum flux (compared with flux in the absence of the boundary layer). The length scale represented by δ_M is related to the drag force, $D = \rho U_\infty^2 \delta_M$, which acts on the surface of the curved plate, see Young §2.10 [103]. By using δ_M as a characteristic length (as opposed to using the boundary layer thickness), Görtler [24] showed that the neutral stability curve is not dependent on the shape of the unperturbed velocity profile. This result was later found to be in agreement with the work of Hämmerlin [38].

By employing the parallel flow assumption, Görtler calculated the critical value of G as

$$G_c \approx 0.58. \tag{1.5}$$

Subsequently, Görtler's analysis demonstrated the existence of an instability that takes the form of vortices whose axes are parallel to the main flow, as shown in figure 1.1. Although Taylor and Görtler vortices both arise through essentially the same centrifugal mechanism, Görtler vortices are significantly different because they develop in a basic state which is spatially growing, whereas Taylor vortices are confined by the bounding geometry of the cylinder walls.

A complete understanding of the Görtler problem is particularly relevant to aerodynamics, where the theory can be used to discuss the flow past the curved regions found on the wings of aircraft, jet inlets and the surfaces of turbine blades.

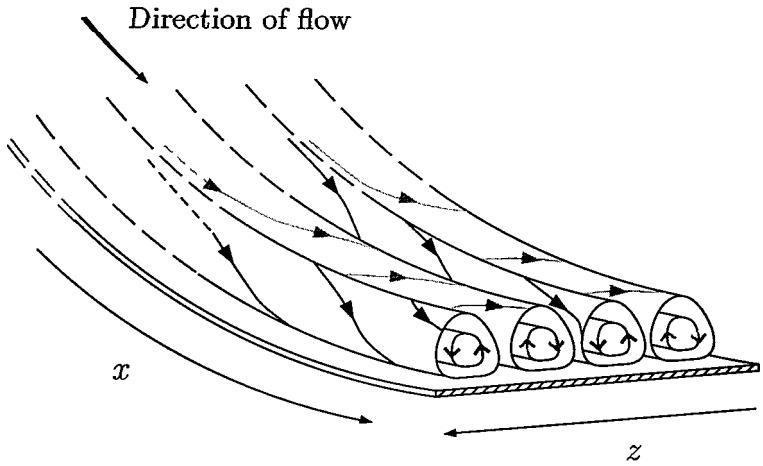


Fig. 1.1: The formation of Görtler vortices on a concave wall. Here the downstream and spanwise coordinates are denoted by x and z respectively.

The boundary layer transition was later studied experimentally by Liepmann [45]. Liepmann showed that the critical Reynolds number for concave walls (see (1.8)) is lower than the corresponding value for a flat plate, thus implying that concavity has a destabilising effect on the flow. It is of interest to note that the critical value of G obtained experimentally by Liepmann is

$$G_c \approx 7.3. \tag{1.6}$$

Of course the above value is profoundly different to the one calculated by Görtler (1.5). Indeed all of the subsequent studies that were based on the assumption of parallel flow, were all found to agree poorly with the data collected from the experimental investigations.

It was later shown by Hämmerlin [38], that the critical value of G_c calculated by Görtler (1.5) occurs with zero wavenumber. The physical interpretation of the latter result, indicates that Görtler's analysis predicts vortices of infinite spanwise wavelength, which is not the case observed in the experiments. In view of this shortcoming, Hämmerlin [39] reconsidered the Görtler problem and reintroduced some of the terms associated with effects of curvature (that had previously been neglected in favour of simplification). The analysis of Smith [79], additionally included some of the terms

associated with the boundary layer growth. In both of these studies it was discovered that the wavenumber associated with the least stable disturbance is nonzero. Hämmerlin obtained the value

$$G_c \approx 0.3, \tag{1.7}$$

for the critical Görtler number, and a very similar value was also obtained by Smith. Despite the relative success of the above work, many 'improved' yet truncated versions of the stability equations have since been studied and are known to produce inconsistent results at $O(1)$ values of the spanwise wavenumber. A detailed comparison of these calculations can be found in the review article by Herbert [41].

These discrepancies were finally resolved by Hall [28] [30], who obtained a consistent set of non-separable partial differential equations for the non-parallel linear stability problem in the limit of high Reynolds numbers and small surface-curvature. In the latter study, the Görtler number is expressed in terms of the Reynolds number R_e and the local radius of curvature a. Accordingly, the Görtler number is defined as

$$G = \frac{2L}{a} R_e^{\frac{1}{2}}. \tag{1.8}$$

Hall [30] has shown that the full partial differential system must necessarily be retained for $O(1)$ wavenumbers to describe the spatial growth of the boundary layer. Hall has also argued that a local stability analysis, i.e. assuming perturbations in the form of normal modes, is formerly justified when the boundary layer thickness is large compared to the spanwise wavelength of the Görtler vortices. When the boundary layer thickness is of the order of the spanwise wavelength or smaller, which is always the case in some upstream region near the leading edge of the plate, the set of full non-separable equations has to be integrated by resorting to a downstream marching technique. Since the spatial stability problem is parabolic, the streamwise evolution of a disturbance is entirely dependent on the form and streamwise location of the imposed initial perturbation. Because the vortex growth is dependent on the history of the flow, the concept of a distinct neutral curve at any given location has no meaning for the Görtler problem. Instead, the stability is discussed in terms of a dimensionless energy

function (of the disturbance) and its turning points. Further details are given in the original papers [28] [30] and the review articles by Hall [34] and Saric [70].

1.2.3 Stokes layers

The centrifugal instability of a Stokes layer on a torsionally oscillating cylinder has been investigated theoretically and experimentally by Seminara & Hall [76] [77]. In the configuration under investigation, the cylinder is immersed in an unbounded incompressible fluid, and for high frequency oscillations the flow is confined to a thin boundary layer. At leading order the boundary layer is found to be of Stokes type. Moreover, the importance of the centripetal forces becomes increasingly small as the ratio of the Stokes layer thickness to the radius of the cylinder tends to zero i.e. as $\sqrt{(\nu/\omega)}/a \to 0$, where ω is the frequency and a is the radius of the cylinder. Therefore, centripetal forces have a negligible effect on the basic flow at leading order. However, by imposing a disturbance that is rotationally symmetric and axially periodic, it is shown that the basic state is susceptible to an instability of the Taylor vortex type.

The linear stability equations derived in [76] have coefficients that are periodic in time and thus a Floquet analysis is used to reduce these equations, into an infinite set of coupled ordinary differential equations. This infinite set of equations is then truncated and solved numerically. An analytic series solution is also obtained for the same system, and the results from both methods of integration are found to be consistent. The critical Taylor and axial wavenumber are calculated to be (numerical result quoted)

$$T_c^{(1)} = 164.42, \qquad a_c^{(1)} = 0.85852, \tag{1.9}$$

respectively. An experimental investigation was also undertaken to physically observe the instability using ink dye. The critical values obtained by Seminara & Hall from this experiment are

$$T_c^{(1)} = 150.0, \qquad a_c^{(1)} = 0.88. \tag{1.10}$$

As mentioned by the authors themselves, the above values are perhaps subject to some experimental error because the visualisation method was rather crude, but sufficient

for the purpose of observing the instability qualitatively. In the same experiment Seminara & Hall also report a secondary instability at $T_c^{(2)} \simeq 185$. At this value of Taylor number, the neighbouring vortices appear to interact and form bigger vortices with an axial wavenumber $a_c^{(2)} \simeq 0.17$. The linear instability analysis of [76] could not explain this secondary instability.

However, Seminara & Hall [77] did investigate the development of the flow for $T \gtrsim T_c^{(1)} = 164.42$ using a weakly nonlinear theory. A multiple scales analysis was used to derive an amplitude equation (see section 1.3) for the disturbance, and subsequently the authors were able to show that a stable axially-periodic flow bifurcates from the basic circumferential state. Accordingly, the authors concluded that second bifurcation at $T_c^{(2)} \simeq 185$ must be associated with an instability of the secondary state evaluated for $T \gtrsim T_c^{(1)}$. Later on, Hall [27] considered the stability of this secondary state to subharmonic perturbations (axisymmetric modes with twice the axial wavelength of the basic flow) by using linear theory. The theoretical value obtained from this calculation is

$$T_c^{(2)} = 183.8, \tag{1.11}$$

which agrees extremely well with the experimental value $T \simeq 185$ obtained in [76]. Moreover, Park, Barenghi and Donnelly [58] have also confirmed, from their experimental investigation, the presence of a subharmonic mode near this critical Taylor number (which they estimate as $T_c^{(2)} = 181.7$). In the latter investigation it is also found that further equilibrium states do not exist above the second critical Taylor number $T_c^{(2)}$.

1.3 Nonlinearity

To understand the evolution of a flow near the onset of transition (or beyond), one is usually required to adopt a nonlinear analysis. This is because the nonlinear terms are no longer negligible and must be incorporated in any flow description near the critical value of some dimensionless control parameter e.g. Taylor number. For many flows,

where a linear neutral stability curve can be constructed, the amplitude $A(t)$ of the imposed disturbance is found to obey an equation of Stuart-Landau type. Here t is time and the Stuart-Landau equation is

$$\frac{\mathrm{d}(|A|^2)}{\mathrm{d}t} = \sigma |A|^2 - \gamma |A|^4 + \ldots, \tag{1.12}$$

and σ is the growth rate (in time) predicted by linear theory, and γ is a constant that is usually determined by the solvability condition of the leading order nonlinear stability equation. Moreover, the Landau constant γ is a measure of the nonlinearity and with γ set equal to zero, equation (1.12) reduces to the same equation that is derived from linear theory. If equation (1.12) is truncated at $O(|A|^6)$, it is then possible to integrate the equation directly to give the following analytic solution:

$$|A|^2 = \frac{\sigma A_0^2}{(\sigma - \gamma A_0^2)\exp[-\sigma t] + \gamma A_0^2}, \tag{1.13}$$

where A_0 is the initial nonzero amplitude of the disturbance. From (1.13) it is evident that the fate of an initial disturbance is dependent on the signs of σ and γ. For the case $\gamma > 0$ with $T > T_c$ i.e. the Taylor number exceeding its critical value (thus $\sigma > 0$); it is easily shown from (1.13) that A converges to a finite value over time, namely

$$A \to (\sigma/\gamma)^{\frac{1}{2}} \qquad \text{as} \quad t \to +\infty. \tag{1.14}$$

This is called *supercritical stability* because the secondary flow with $T > T_c$ has a finite amplitude, and resulting flow will therefore a settle into a new laminar state. This new laminar state is stable provided that the second least stable growth rate in time remains negative (this usually occurs for $0 < T - T_c \ll 1$, see Drazin & Reid [19]). Conversely for $T < T_c$, a *subcritical instability* is said to exist if the flow is stable to all disturbances with arbitrarily small amplitudes, but unstable to a particular disturbance with sufficiently large, yet finite, amplitude.

In contrast, the nonlinear effects which govern the growth of Görtler vortices cannot be described by the concept of a disturbance amplitude $A(t)$, as used in a Stuart-Watson type analysis. In the Stuart-Watson method, energy is passed down from the fundamental to higher harmonics and the mean flow (here the 'fundamental' is

understood as appropriate term in the spanwise Fourier expansion of the disturbance), see Stuart [85] and Hall [29]. A consistent flow description of the aforementioned problem was first put forward by Hall [29][32][33], who proposed a 'mean-field' theory in which the higher order harmonics have no role. In the latter studies, Hall examines the streamwise evolution of Görtler vortices and his earlier linear analysis [28][30] is used to determine the streamwise starting point of growth/decay i.e. the streamwise location ($x = x^*$) where the flow is determined to be neutrally stable. From Hall's analysis it is found that the mean-flow correction and fundamental component of the vortex satisfy a pair of simultaneous partial differential equations. Generally these equations must be solved numerically, although an asymptotic description is also possible for small wavelength vortices at large distances from $x = x^*$, see Hall & Lakin [33]. Further developments were also made by Hall [32] for $O(1)$ wavenumbers. In this case it was discovered that the streamwise velocity profile is highly inflexional and therefore likely to break down via a Rayleigh type instability. Subsequently, the breakdown of the longitudinal vortices in a curved boundary layer has been investigated by Hall & Horseman [35]. In the latter study, the temporal instability of an inviscid travelling wave disturbance is investigated and the results are found to agree qualitatively with the experimental observations of Swearingen & Blackwelder [87]. A summary of the linear and nonlinear development of Görtler vortices in growing boundary layers can be found in Hall [34].

1.4 The transversely oscillating cylinder

In his experimental investigation of this problem, Honji [44] observed the appearance of axially periodic vortices of the Taylor-Görtler type, close to the surface of a transversely oscillating circular cylinder. He also noted that this instability is only in effect for sufficiently large oscillation amplitudes. Outside the Stokes layer which exists at the cylinder wall, there is a steady flow which persists and is referred to as the steady streaming component of the flow. This steady flow is generated by the associated Reynolds stresses of the fluctuating flow within the Stokes layer. In Honji's experi-

ments, it is observed that the steady streaming flow causes the indicator dye to diffuse away from the Stokes layer i.e. away from where it is first introduced. At larger amplitudes of oscillation the vortices disappear, and the resulting flow is separated and turbulent. Prior to the publication of [44], Taylor-Görtler vortices had primarily been associated with the torsional action of the cylinder. Despite this difference in cylinder motion, Honji believed that essentially the same Stokes layer instability is present in both problems.

Hall [31] addressed the stability of this flow by using both linear and weakly nonlinear theory. To describe the flow in [31], the following nondimensional parameters are defined:

$$\beta = \frac{\omega a^2}{\nu}, \qquad \lambda = \frac{U_0}{\omega a}, \qquad R_s = \frac{U_0^2}{\omega \nu} = \lambda^2 \beta. \tag{1.15}$$

Here, a is the radius of the cylinder, U_0 is a typical velocity and ω is the oscillation frequency. The parameter λ represents the ratio of the amplitude of oscillation to the cylinder radius and is considered to be small. The steady streaming Reynolds number for the flow is denoted by R_s and the nondimensional frequency is represented by β. Particular attention is given to the large frequency limit where $\beta \to \infty$ and $R_s = O(\beta^{\frac{1}{2}})$. In this case, the linear stability equations only depend on the radial variable and time. Moreover, the periodicity of the coefficients in the governing equations, permits the use of Floquet theory to reduce the system into an infinite set of coupled ordinary differential equations. The numerical solution of this system then determines the coefficients in the expansion for critical steady streaming Reynolds number, R_{sc}, in the limit $\beta \to \infty$. The latter calculation by Hall gives

$$R_{sc} = 4.24\beta^{\frac{1}{2}} + 1.95\beta^{\frac{1}{4}} + \ldots \tag{1.16}$$

This expansion agrees extremely well with the experimental data collected by Honji. Although expansion (1.16) is formerly valid for $\beta \to \infty$ i.e. $\lambda = O(\beta^{-\frac{1}{4}})$, the approximation is also found to agree equally well for $\lambda \sim 1$. To compare this result to the corresponding value for the torsionally oscillating cylinder, it is convenient to write

$$R_s = \frac{T\beta^{\frac{1}{2}}}{2}, \tag{1.17}$$

where T is the Taylor number. Hence the critical Taylor number for this problem is $T_c = 8.48$, and the corresponding value for the torsionally oscillating cylinder is $T_c^{(1)} = 164.42$, see §1.2.3. It is apparent that the transverse oscillation of the cylinder is by far the most unstable configuration, however there are no simple physical arguments that explain why this result should be expected.

From Hall's weakly nonlinear analysis, it is shown that the outer steady streaming boundary layer is driven simultaneously by the basic oscillatory flow and the instability. This in turn implies that the instability has an $O(1)$ influence on the steady streaming flow. Moreover, Hall's nonlinear analysis indicates that the vortex instability is in fact subcritical in nature. This result is rather unexpected since it is not inline with the supercritical behaviour observed in other Taylor-Görtler systems e.g. torsionally oscillating/rotating cylinders (except for the case of counter rotating cylinders see DiPrima & Sjbrand [18]). It is interesting to note, that near the predicted value of the critical Taylor number, Honji observes what appears to be a steady state with vortex cells. Hall suggests that this steady state could arise after a large amplitude subcritical disturbance is stabilised by higher-order nonlinear effects. It is clear that the definitive nature of the bifurcation can only be understood by solving the full stability equations with a Fourier analysis in the axial direction. However, the numerical undertaking of such a problem is not simple because the governing set of partial differential equations are coupled and nonlinear.

Overview

In chapter 2, the steady streaming flow between two cylinders (induced by the high frequency transverse oscillations of the inner cylinder) is discussed in the small gap limit. For asymptotically small (and large) values of the steady streaming Reynolds number, R_s, it is possible to derive the asymptotic forms of the governing stream function Ψ. These asymptotic solutions are then compared to the numerical solutions for Ψ.

The numerical solutions for the governing equations of motion are sought via two

methods. In the first method the governing PDE is solved directly and this solution is referred to as the DNS. In the second method, Ψ is expanded in a θ-power series i.e.

$$\Psi = \sum_{n=0}^{\infty} \theta^{2n+1} \Psi^{(n)},$$

and in this manner the governing PDE is reduced to an infinite set of coupled ODEs (note, here θ denotes the angular variable). The results obtained via these two different methods are analysed and it is found that both approaches produce identical results for $R_s \ll 1$. However as R_s is increased to $R_s \approx 50$ it is found that a shock like discontinuity manifests in the DNS. The plane of this shock lies in the radial direction and is confined to the θ-range $5^\circ \lessapprox \theta \lessapprox 40^\circ$.

For $R_s > R_1 \approx 6.6$ it is found that the term $\Psi^{(1)}$ becomes unbounded in the time marching procedure that is used to calculate the series solution. Moreover, it is found that the terms: $\Psi^{(2)}$, $\Psi^{(3)}$ and $\Psi^{(4)}$ become unbounded at $R_2 \approx 4.2$, $R_3 \approx 3.0$ and $R_4 \approx 2.4$ respectively. Accordingly, a linear stability analysis is formulated and consequently it is shown that $R_n \sim \frac{1}{2n+1}$ as $n \to \infty$. In view of this result, the terms in the series solution are sought without time marching. In fact, since the DNS for Ψ is steady for $R_s < 50$, each term in the series solution is calculated directly by solving the appropriate boundary value problem. By calculating the terms $\Psi^{(n)}$ in this manner, it is found that the series solution converges over a progressively smaller θ-range as R_s is increased from $R_s = 0$ to $R_s = 50$. However, for $R_s > 2800$ it is found that the series solution converges to the asymptotic solution of the PDE, in contrast presence of the shock discontinuity still persists in the DNS. Moreover, by modifying the boundary conditions of the physical problem, it is found that the qualitative features of DNS and series solution remain unchanged.

In chapter 3, the onset of a new roll-type instability is sought for a torsionally oscillating circular pipe. Moreover, the onset of this instability is sought in the high-frequency ($\Phi \gg 1$) and small-amplitude limit ($\alpha \ll 1$). By considering disturbances that are symmetric about the horizontal diameter of the pipe, it is found that the governing stability equations at $\theta = 0$, reduce to those which govern the onset of

the roll-type instability in a Hele-Shaw cell, see Hall [36]. Note, here θ denotes the latitudinal variable measured from the horizontal diameter of the pipe.

By imposing a perturbation of the WKBJ type upon the base flow, a dispersion relation for the dimensionless frequency parameter Φ is derived. In order to identify the most dangerous disturbance, it is necessary to minimise the eigenvalue $B = \alpha\Phi^{1/4}$. Note $B = B(\theta, k)$, where k denotes the wavenumber of the imposed disturbance. The theory of Soward & Jones [82] is used to show that the minimised value of B corresponding to the Hele-Shaw cell, does not correspond to physically acceptable solutions for the circular pipe problem. Accordingly, it is necessary to minimise B over the entire $\{\theta, k\}$-domain, where θ and k are now principally allowed to be complex variables. By considering the symmetry of the problem, it is shown that the minimisation of B can be achieved by considering $\mathrm{Re}\{\theta\} = 0$ and $k \in \mathbb{R}$. Proceeding in this manner, the stability equations are time marched over the $\{\theta, k\}$-domain with the intention of finding the saddle point $\{\theta_0, k_0\}$ at which B is minimised; this saddle point is defined by the conditions:

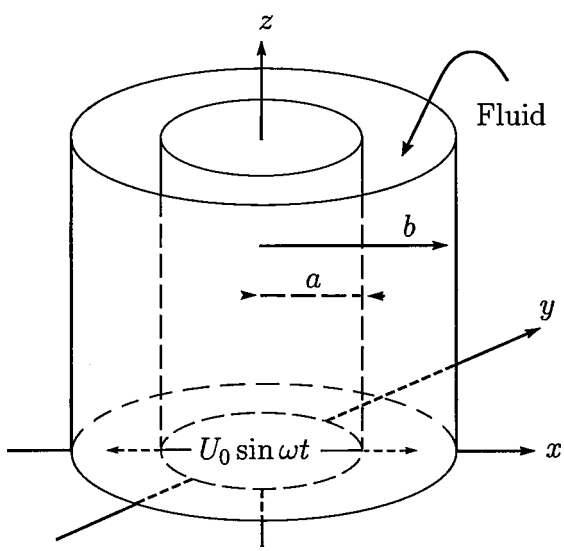
$$\frac{\mathrm{d}B}{\mathrm{d}\theta} = 0 \quad \text{with} \quad \frac{\mathrm{d}B}{\mathrm{d}k} = 0.$$

By time marching the stability equations it is found that there is a discontinuity in the neutral stability surface. Accordingly, the numerical approach is reformulated and the perturbations in the stability equations are expanded in a Fourier series in time. The resulting system leads to an eigenvalue problem for the growth rate in time. By using the Fourier series approach, the presence of the discontinuity in the neutral stability surface (computed via time marching) is explained. Thereafter, the required values of $\{\theta_0, k_0\}$ are identified.

Chapter 2

The steady streaming flow induced by an oscillating cylinder

The viscous flow under consideration, is incompressible and bounded by two infinitely long cylinders which are aligned in the direction of the z-axis. The outer cylinder is stationary and the inner cylinder oscillates transversely along the x-axis with velocity $U_0 \sin \omega t$. The steady streaming component of the flow is considered for oscillations of high frequency and small amplitude, and the small gap-width limit is taken (i.e. the



limit where the ratio of the radii tends to unity). At leading order the slip velocity on the inner cylinder is proportional to θ (cylindrical polar angle in the x-y plane) and

independent of time. Since the flow in the vicinity of $\theta = 0$ is one of stagnation type, a solution represented by a series expansion in θ is sought. In this manner, the local structure near $\theta = 0$ is incorporated into the full description of the flow field.

From the recent studies by Hall & Papageorgiou [37] and Watson *et al.* [97], it is known that the leading order equation from the series expansion supports steady, periodic and chaotic period-doubling solutions. This leading order equation appears in the study by Hall & Papageorgiou [37], as the governing equation for the steady streaming flow between two parallel walls, driven by the time-periodic action of the upper wall in the high Reynolds number and small-amplitude limit. In the latter investigation many interesting flow structures are discovered. Moreover, these structures are particularly important because they are relevant to flows of stagnation type. Hence for the present study, the solutions of the driven system of equations are explored with intention to relate the flow structures found in [37] [97], both laminar and chaotic, to the present steady streaming flow under consideration.

2.1 Introduction

The flow that is induced by an oscillating circular cylinder immersed in an incompressible viscous fluid, has been studied analytically and numerically by many authors, notably by Stuart [83][84], Riley [65][66][67], Duck & Smith [20] and Haddon & Riley [25]. Our concern is with the bounded version of this problem. Here, a stationary outer cylinder of radius b, contains the fluid and the transversely oscillating inner cylinder, of radius a and velocity $U_0 \sin \omega t^*$. The following dimensionless parameters have been used in previous studies and are defined here to aid further discussion:

$$\begin{gathered} \epsilon = U_0/\omega a, \qquad M^2 = \omega a^2/\nu, \\ Re = U_0 a/\nu = \epsilon M^2, \qquad Re_s = U_0^2/\omega\nu = \epsilon^2 M^2 \qquad \alpha = b/a. \end{gathered} \tag{2.1}$$

Here ν is the kinematic viscosity, Re is the usual Reynolds number and ϵ is the frequency parameter. Since the present study considers oscillations of small amplitude

and high frequency, ϵ is small and is used as a perturbation parameter. It is helpful to review the analysis of Stuart [84] to discuss some of the key features concerning steady streaming flow; consequently, this will demonstrate the importance of the parameters M and Re_s.

In 1966 Stuart considered the flow that develops around a single cylinder which oscillates transversely in an infinite fluid medium, henceforth this will be referred to as the one-cylinder problem. From this study is it known that when a cylinder of radius a ($\gg (\nu/\omega)^{\frac{1}{2}}$) oscillates with velocity $U_0 \sin \omega t$, a time independent flow is generated along with the main fluctuating part. If ϵ is used as a perturbation parameter to expand the associated stream function in a regular series, it is seen from the Navier-Stokes equations that the steady component arises from nonlinear interactions of the leading approximation. From equation (2.4) (the Navier-Stokes) it can be seen that the nonlinear terms enter at $O(\epsilon)$; accordingly, the induced steady streaming flow enters at $O(\epsilon)$ in the expansion of the stream function.

Following Stuart's analysis, in order to facilitate the outer leading order inviscid solution, it is necessary to introduce a Stokes shear-wave boundary layer at the cylinder wall. Within this $O(\nu/\omega)^{\frac{1}{2}}$ layer, the effects of viscosity are reintroduced so that the flow adjusts appropriately to meet the cylinder surface with zero velocity. To use the matching principle described above, it is important that the boundary layer does not separate from the cylinder wall. By examining the boundary layer on a cylinder which accelerates from rest, Stuart has shown that separation can only occur if the cylinder traverses a distance $O(3a/10)$ i.e $U_0/\omega \sim 3a/10$. However, since the present problem considers oscillations of high frequency and small amplitude, the condition $\epsilon = U_0/\omega a \ll 1$ ensures that the boundary layer remains attached to the cylinder surface. Moreover, the parameter M is identified as the ratio of the distance length scale a, to the viscous one of length $(\nu/\omega)^{\frac{1}{2}}$. In the present discussion, the length scale of the cylinder is significantly greater than the shear-wave layer thickness, so the assumption, M large (exact gauge to be specified later), will be implicit hereafter.

At $O(\epsilon)$ in the matching procedure, it is required that the tangential steady stream-

ing velocity component is zero at the edge of the Stokes layer. However, it is found that the inner solution, i.e. the solution for the Stokes layer, cannot simultaneously obey the boundary conditions at the wall together with the ones imposed at infinity i.e. at the edge of the Stokes layer. The streaming flow, which persists outside the Stokes shear-wave layer, is produced by the action of the large *Reynolds stresses* that arise from the nonlinear effects of the fluctuating flow acting on the steady component. These Reynolds stresses constitute part of the stress components that act on fluid element in the mean flow, and arise because there is a mean transport of momentum due to the velocity fluctuations, see Stuart ([84], §9). As a result of this, the matching procedure is modified and the zero velocity criteria at infinity (for the steady component) is relaxed to finite velocity, a full discussion concerning the validity of this procedure can be found in Riley [65]. At the edge of the shear-wave layer this streaming velocity is $O(\epsilon U_0)$, and a Reynolds number specifically for this streaming flow is formed by writing $Re_s = a\epsilon U_0/\nu = U_0^2/\omega\nu$. The parameter Re_s governs the steady flow which persists outside the shear-wave layer and is referred to as the steady streaming Reynolds number.

In the limit $Re_s \to \infty$, a steady streaming boundary layer of thickness $O(aRe_s^{-\frac{1}{2}})$ forms at the cylinder surface. Since this streaming layer is larger than the $O(\nu/\omega)^{\frac{1}{2}}$ Stokes shear-wave layer, it is referred to as the *outer* layer. Consequently it is within this outer streaming layer, that the tangential streaming velocity decays to zero. For intermediate values of R_s, the flow adjustment takes place over a wider region. Additionally, Stuart [84] has also demonstrated that the steady flow in the outer layer is not significantly affected by the potential flow in the core region, hence substantiating the validity of the governing equations derived for the outer layer. For $Re_s \gg 1$, Stuart sought a solution for the steady flow in the outer layer via a formal series expansion. Moreover, Stuart's expansion was centred at the upper stagnation point on the oscillating cylinder, denoted by the point S in figure 2.1. In the analysis, a 'small' perturbation parameter was introduced for the expansion of the governing stream function. Eventually the small parameter was set equal to unity and the resulting series

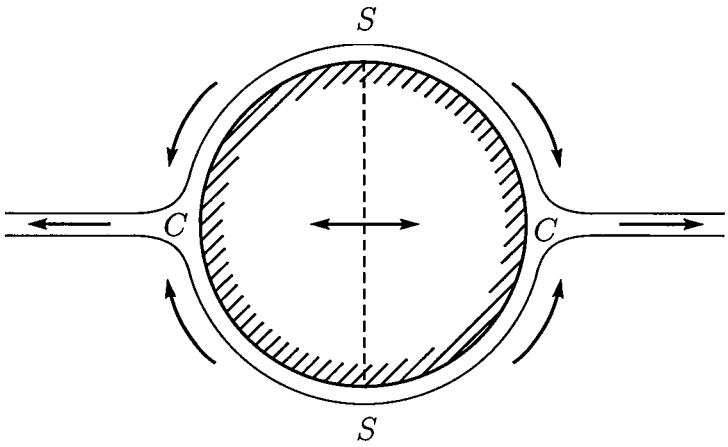


Fig. 2.1: The free jets emerging from a collision of the outer boundary layers for $Re_s \gg 1$. Here, S and C denote stagnation and collision points respectively.

solution was found to converge. By using this approach, Stuart was able to evaluate the first few terms of his series analytically, and consequently the method of Fettis [22], which had been used for ODEs, was successfully extended to PDEs.

However, the latter series solution was of limited use because more terms were required in order to obtain a converged solution at the axis of oscillation. Despite this restriction, Stuart believed there would be an inevitable collision of the outer boundary layers at the axis of oscillation, and that a free jet would ensue from the point of impact, as shown in figure 2.1.

A few years later, Riley [65] also pursued the one-cylinder problem and his *inner-outer* expansion method proved to be more effective. In this procedure, ϵ is used as a perturbation parameter and the series expansions for the inner Stokes layer and outer streaming layer are matched in the large R_s limit. In this way, Riley analytically obtained the first few terms of his series and by using the first term alone, he was able to confirm Stuart's postulate regarding the collision of the outer boundary layers. Moreover, the inner-outer expansion procedure was also useful in ratifying the *a priori* assumption, initially made by Schlichting [72], that the streaming velocity is finite at the edge of the shear-wave layer. This implicit assumption, was shown to be a necessary condition for matching to proceed correctly.

The expansion obtained by Riley was consistent with the one calculated previously by Stuart, and unfortunately its convergence was also limited to small angles away from the upper stagnation point. Riley [66] went on to extend his analysis to the separate cases: $Re_s = O(1)$, $M = O(1)$ and $Re = O(1)$ (the case $M \ll 1$ is also considered briefly but this case is physically less important). For the case $Re = O(1)$, Riley showed that the Reynolds number does not play an important part in determining the leading order fluctuating flow within the inner and outer layers. This is because the condition $Re = O(1)$ simply implies the boundary layer approximation for the inner layer, viz $M \gg 1$. More importantly, for the case $Re_s = O(1)$ i.e without assuming an outer layer, it is shown that the streaming flow outside the shear-wave layer is determined by the full steady Navier-Stokes equations. Subsequently, this paper formed the theoretical basis for the many numerical investigations that were to follow.

Davidson & Riley [15] generalised the analysis used for the one-cylinder problem by studying the flow induced by a periodically oscillated elliptical cylinder; note, the class of oscillations considered in this study are not necessarily harmonic. The latter authors also conducted an experimental investigation for the special case of the harmonically oscillated circular cylinder. The main aim of this experiment was to examine the propagation of free jet, which radiates outward and along the axis of oscillation, see figure 2.1. The authors expected that the jet profile would in essence resemble the Bickley jet solution (see below). The experimental results in this study, confirmed that this expectation was indeed correct.

Bickley [8] obtained the exact analytic solution for a flow entering a stationary fluid through a small smooth hole in a vertical separating wall, as shown in figure 2.2. Such solutions are very rare and therefore a connection with the cylinder problem was desirable for further analytical progress. In the experiments by Davidson & Riley, the free jet was formed within one diameter of the cylinder surface and its profile agreed qualitatively with the Bickley jet solution. By numerically integrating the boundary layer equations, Davidson & Riley obtained estimates for the momentum flux of the free

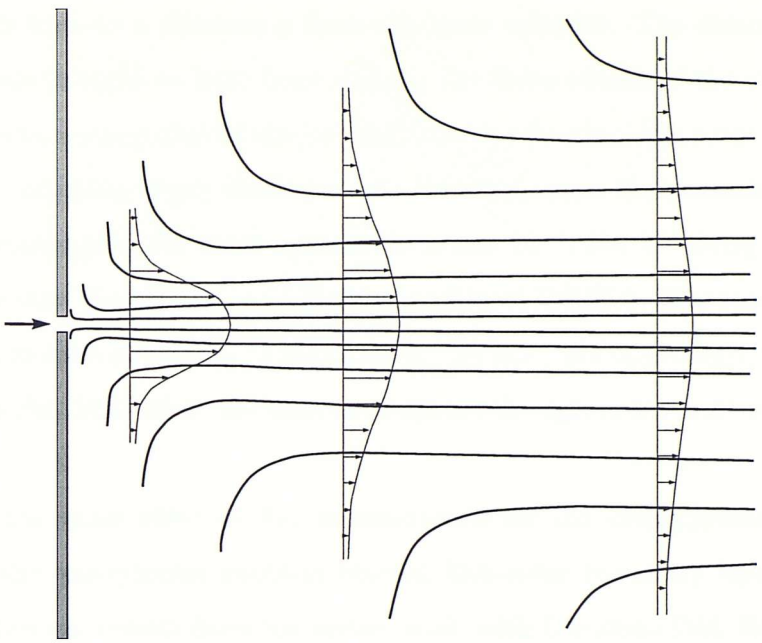


Fig. 2.2: Streamlines and velocity profiles of the steady Bickley jet.

jet. These estimates were found to be in good agreement with the measurements made in the experiment, thus substantiating the flow model used to describe the propagation of the free jet.

For the one-cylinder problem, Bertelsen [7] sought to compare the analytic solutions for the steady streaming flow (evaluated by Riley and Stuart), to the data collected in his experimental investigation. In Bertelsen's experiment, the fluid and the oscillating cylinder are both contained within a large cylinder that is stationary. From this experiment it is observed that the steady streaming layer, on the inner cylinder, is formed at $Re_s \approx 100$. The velocity measurements made within this steady layer, are found to be in good agreement with the solutions obtained from the analysis of the unbounded one-cylinder problem. However, at distances exceeding $2aRe_s^{-\frac{1}{2}}$ from the inner cylinder, and at angles greater than 16.3° from the upper stagnation point, the flow is no longer described by the theory of the one-cylinder problem. Moreover, Bertelsen observed that the free jet becomes unstable for $Re_s > 100$. This instability is initiated at the surface of the outer bounding cylinder, and at $Re_s = 400$ the in-

stability trails back to a distance a from the inner cylinder. The discrepancies with the theory were thought to have been due to: the finite effects of the outer cylinder, curvature effects, propagation of the jet into the outer flow and the outer flow vorticity effects on the boundary layer development. However, since the governing parameter for steady streaming on the outer cylinder is of size 10^{-4}, the bounding effects of the outer cylinder were thought to be negligible, see Stuart [84] §5.2. The remaining effects were thought to have an $O(Re_s^{-\frac{1}{2}})$ influence on the flow; yet opposingly, it is observed that changing Re_s from 90 to 400 does not improve the agreement between theory and experiment.

To see if the finite effect of Re_s is responsible for the disagreements, Riley [67] re-examined the one-cylinder problem beyond first-order boundary layer theory. By using the numerical results from his earlier work with Davidson [15], Riley produced an $O(Re_s^{-\frac{1}{2}})$ correction to the slip velocity on the inner cylinder. This correction is obtained by assuming a flow model based on the Bickley jet profile and then calculating the outer flow to a higher order accuracy. However, this analysis failed to reconcile the differences seen in the experiments, therefore suggesting that the finite effect of Re_s only contributes marginally to the disagreement.

Finally, Duck & Smith [20] were able to show that the bounding effects of the outer cylinder were indeed responsible for the discrepancies. By following the inner-outer expansion procedure of Riley, Duck & Smith extended the original analysis by calculating the terms in the inner and outer expansions for the boundary layers on *both* cylinders. In this way, the steady streaming slip-velocity (at the edge of the Stokes layer) was calculated on each cylinder, and the core-region velocity distribution was computed numerically by solving the steady Navier-Stokes equations with $Re_s = O(1)$. The velocity field that was determined by the latter calculation, was found to agree extremely well with the experimental measurements made by Bertelsen within the streaming boundary layers. Hence, the work by Duck & Smith demonstrated that the presence of the outer cylinder cannot be ignored in the theoretical analysis, and that second-order boundary layer theory is unnecessary for this problem.

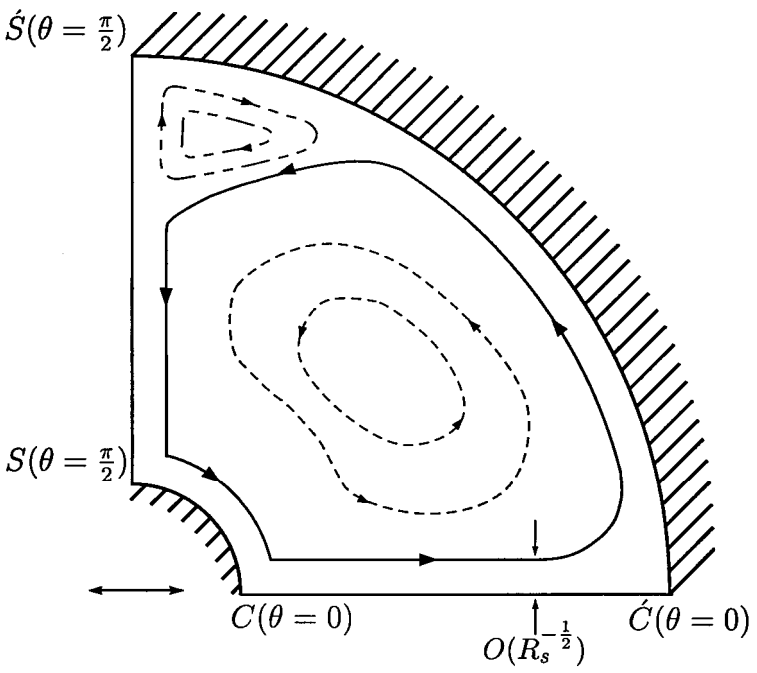


Fig. 2.3: Schematic of boundary layer development in the two-cylinder problem, $Re_s \gg 1$ and $\alpha = O(1)$

Figure 2.3 shows the basic flow pattern for large but finite Re_s. Observe, that a steady streaming layer is also formed on the outer cylinder. Moreover close to the pole $\acute{S}$, this streaming layer detaches and thus results in a free shear-layer. This free shear-layer eventually rejoins the streaming layer on the inner cylinder by reattaching at the pole S. The separation on the outer cylinder occurs sooner as the value of Re_s is increased; accordingly, the pocket of slow eddying flow increases in the same manner.

Haddon & Riley [25] were also conducting a numerical investigation into the two-cylinder problem around the same time as Duck & Smith. However, in the approach used by Haddon & Riley, the steady equations of motion were solved by using a vorticity-stream function (VSF) update method. Moreover, the numerical code used in this investigation was an unsteady Navier-Stokes solver. Therefore the required steady solutions were obtained by allowing the time marched solutions to settle into steady states. The results from this method did not reproduce the level of agreement, with Bertelsen's experiments, that had been achieved by Duck & Smith. Despite this fact,

the results were an improvement on all the theoretical investigations prior to the work by Duck & Smith. The numerical method used by Haddon & Riley was not memory efficient and this became restrictive at larger values of the steady streaming Reynolds number. At large values of Re_s i.e. $Re_s \approx 400$, the steady streaming layer becomes very thin. Consequently, this indicates that the numerical solver requires more mesh points in order to give a better resolution within the thinner streaming layer. In view of this idea, Haddon & Riley believe that the restriction of mesh points in their calculations, is the reason why their results are not as accurate as those obtained by Duck & Smith.

A flow model for $Re_s \gg 1$ with $\alpha \gg 1$ has been proposed by Duck & Smith and the problem is still open to further theoretical developments. However it is likely that further investigations will be numerical. Recently, Panagopoulos *et al.* [56] have studied the one-cylinder problem with accompanying torsional oscillations. In the latter study, the corresponding inner shear-wave solutions are derived and the outer flow is computed numerically. It is shown that as the amplitude of torsional oscillation increases relative to the transverse amplitude, the emerging free jets are displaced from the x-axis to higher angles of elevation towards the upper stagnation point. The streamlines of these jets are straight and radiate symmetrically from the centre of the inner cylinder.

The problem investigated in this chapter, concerns the steady streaming flow between two cylinders, which is induced by the transverse motion of the inner vibrating cylinder. The flow is considered in small gap limit and the possibility of chaotic period-doubling solutions is investigated. The premise for anticipating such solutions is inferred from the recent study by Hall & Papageorgiou [37], henceforth referred to as H. & P.

The latter authors consider the motion of a viscous incompressible fluid between two infinitely long parallel walls; in this configuration, the flow is driven by the harmonic oscillations of the upper wall. The flow is characterised by a Reynolds number R and amplitude of oscillation Δ with $0 < \Delta < 1$. For small Reynolds numbers the flow is unique, stable and symmetric. On increasing the Reynolds number, the flow

loses stability to a symmetry-breaking perturbation and a secondary stable state is attained. This secondary state remains stable for a range of Reynolds numbers; upon increasing the Reynolds number further, an inherent instability is initiated. The form of this instability is determined by the size of amplitude parameter Δ; a summary of the various routes to chaos is given in table 2.1.

For small values of Δ, the flow develops on two distinct time scales. The fast variation of the flow occurs on the short $O(1)$ time scale and the modulation of the flow varies on the longer $O(R)$ scale. For particularly small values of $\Delta(< 0.45)$ the period-doubling, which occurs on the modulational time scale, is hard to observe. This is because the large amplitude variation on the faster $O(1)$ time scale, obscures the periodic signal associated with the modulation. In this case, the underlying flow structure is determined by converting to the longer $O(R)$ time scale and then taking limit $\Delta \to 0$ with $\Delta^2 R = \frac{3}{2} Re_s = O(1)$. In this limit, the governing steady streaming equations are

$$\Psi_{\eta\eta t} = \frac{1}{Re_s}\Psi_{\eta\eta\eta\eta} + \Psi_{\eta\eta\eta}\Psi - \Psi_{\eta\eta}\Psi_{\eta}, \tag{2.2a}$$

$$\Psi(\eta = \mp 1) = 0, \quad \Psi_{\eta}(\eta = \mp 1) = -1. \tag{2.2b-e}$$

Here Ψ is the stream function for the steady streaming flow. Since the time modulation of Ψ is considered on a long $O(R)$ scale, the term $\Psi_{\eta\eta t}$ is incorporated into the governing unsteady equation for Ψ. Had an $O(1)$ time scale been considered instead of the $O(R)$ scale, the equation for Ψ would have been steady. Note, for general steady streaming problems, the slip conditions at each wall are given by the outer limit of the appropriate boundary layer expansions of Ψ near each wall. Accordingly, in the context of steady streaming problems, equation (2.2) is understood to be the governing equation for Ψ in the core $|\eta| < 1$. However, since the *steady* forcing at each wall, $\eta = \mp 1$, is induced by the Reynolds stresses (as will be explained in detail later on), the equation for Ψ (in the core) is regarded as a steady streaming problem. This 'steady streaming' terminology can be a little confusing since the governing equations for Ψ are in fact unsteady. However, one must keep in mind that the steady streaming terminology actually refers to the *steady* forcing induced by the Reynolds stresses at each wall.

$0.65 < \Delta < 1$	Period-doubling - Feigenbaum route to chaos.
$0.45 < \Delta < 0.65$	A period-4π solution is obtained after a long chaotic transient phase. The duration of the transient phase increases with Re_s.
$0 < \Delta < 0.45$	Quasi-periodic solution attained with period-doubling occurring on the longer modulational time scale.

Table 2.1: The route to chaos dependence on Δ.

By solving the above equations numerically, H. & P. have shown that the solutions for $Re_s < 17.23$ are steady, stable and η-symmetric. Upon increasing Re_s further, a symmetry-breaking bifurcation occurs and a stable secondary steady flow is attained. At slightly higher values of the streaming Reynolds number ($Re_s \approx 53$) the flow becomes periodic in time. After this onset of unsteadiness, the time period of the flow doubles at specific values of Re_s. Moreover, the interval between each successive bifurcation decreases, and via this period-doubling cascade the flow rapidly becomes chaotic. This chaotic flow structure for asymptotically small Δ, is found to conform with the structures calculated for small but finite Δ. Therefore, H. & P. conclude that for small values of Δ, the steady streaming flow will eventually turn chaotic for large enough Reynolds numbers.

In essence, equation (2.2a) is a scaled version of the Navier-Stokes equations, with missing derivatives in the second space variable. Since this equation is known to support chaotic solutions, its relationship with the two-cylinder problem will now be established. The governing equations for the steady streaming flow in the two-cylinder problem (in the notation of Duck & Smith [20]) are

$$\epsilon^{-2}\frac{\partial(\nabla^2\Psi_{10}^{(s)})}{\partial t} + \frac{1}{\rho}\frac{\partial(\nabla^2\psi_{10}^{(s)},\psi_{10}^{(s)})}{\partial(\rho,\phi)} = \frac{1}{Re_s}\nabla^2\nabla^2\psi_{10}^{(s)}, \tag{2.3a}$$

$$\psi_{10}^{(s)} = 0, \quad \frac{\partial\psi_{10}^{(s)}}{\partial\rho} = \frac{3\alpha^4\sin 2\phi}{2\left(\alpha^2-1\right)^2}, \quad \frac{3\sin 2\phi}{2\alpha\left(\alpha^2-1\right)^2}, \quad \rho = 1,\ \alpha. \tag{2.3b}$$

Here $\psi_{10}^{(s)}$ is the associated stream function, ρ is the radial distance measured from the

centre of the inner cylinder and ϕ is the angular coordinate. Although equations (2.3) are formally derived later, it is helpful to discuss them here to see how they relate to the steady streaming equations studied by H. & P. Observe, that equation (2.2a) would be similar to (2.3a) if the derivatives in the latter equation are dominant w.r.t ρ with $\rho \sim 1$; these conditions are equivalent to taking the small gap approximation. Under the aforementioned limit, equation (2.3a) only differs from (2.2a) by some derivatives in ϕ. Note also that it is necessary to convert to a long $O(\epsilon^{-2})$ time scale, in order to preserve the time dependence in the equation for $\psi_{10}^{(s)}$. Moreover, it will be seen later that the boundary layer solutions for $\psi_{10}^{(s)}$ (the outer limit of which, give the slip conditions (2.3b)) are unchanged by the shifting to an $O(\epsilon^{-2})$ time scale.

Next, if we seek a power series solution to equation (2.3a) in ϕ, then the leading order approximation is a scaled steady version of (2.2a). As a result, all the higher order equations, resulting from the series substitution, are forced by the solution at leading order. This leading order solution is given by Ψ, which is determined from the set of equations (2.2). This means that the equation studied by H. & P. is linked to (2.3), by the fact that it determines the leading order contribution to the solution of streaming flow. Hence, the motivation for studying the two-cylinder problem in the small gap limit is now clear.

In the next section the problem is formulated and in section 2.3 some asymptotic solutions to the governing equations are presented. Thereafter, the findings of the numerical investigations are discussed and subsequently a linear stability analysis formulated. In addition, a simple extension is made to the present problem by altering boundary conditions on both cylinders, and finally some conclusions are drawn.

2.2 Formulation

It is convenient to use cylindrical polar coordinates (r, ϑ) to describe the configuration of the two cylinders in the complex z-plane (where $z = r\,e^{i\vartheta}$). Accordingly, the inner cylinder of radius a and transverse velocity $-U_0 \sin \omega t$, is located at $z = a\,e^{i\vartheta} + U_0 \omega^{-1} \cos \omega t$. Similarly, the outer cylinder of radius b, which is stationary,

is located at $z = b\,e^{i\vartheta}$.

Since the flow is incompressible, we may introduce a stream function $\tilde{\psi}$ and then express the Navier-Stokes equations in vorticity form. By scaling distance and time using a and ω^{-1} respectively, the Navier-Stokes equations can be written as

$$\nabla^2\tilde{\psi}_t + \frac{\epsilon}{r}\frac{\partial(\nabla^2\tilde{\psi},\tilde{\psi})}{\partial(r,\vartheta)} = \frac{1}{M^2}\nabla^2\nabla^2\tilde{\psi}, \tag{2.4}$$

with no-slip boundary conditions

$$\tilde{\psi} = \tilde{\psi}_r = 0, \quad \text{at} \quad z = e^{i\vartheta} + \epsilon\,\cos\omega t,\ \alpha\, e^{i\vartheta}, \tag{2.5}$$

and

$$\nabla^2 = \nabla^2_{(r,\vartheta)} = \frac{\partial^2}{\partial r^2} + \frac{1}{r}\frac{\partial}{\partial r} + \frac{1}{r^2}\frac{\partial^2}{\partial\vartheta^2}.$$

The parameters: ϵ, M and α are as defined in (2.1). The high-frequency small amplitude assumption ensures that ϵ is small. We shall therefore use this parameter to expand the stream function in a series later on.

Next, a conformal map is used to transform the dynamics in the z-plane, to a static configuration in the ζ-plan. Both the inner and outer cylinders are mapped onto concentric circles that are stationary. In this case the oscillation enters the governing equations via the inhomogeneous boundary conditions. The aforementioned transformation was first obtained by Segel [74], who used this map (and many others like it) to obtain a system of equations for which a solution by series is possible. If we use (ρ,ϕ) to denote polar coordinates in the complex ζ-plane, the required transformation is given by

$$\zeta = \frac{z - \epsilon\cos\omega t^* - \gamma}{1 + \gamma\epsilon\cos\omega t^* - z\gamma} = \rho e^{i\phi}, \tag{2.6}$$

with

$$\gamma = \frac{2\epsilon\cos\omega t^*}{\alpha^2 - 1 - \epsilon^2\cos^2\omega t^* + \left((\alpha^2 - 1 - \epsilon^2\cos^2\omega t^*)^2 - 4\epsilon^2\cos^2\omega t^*\right)^{\frac{1}{2}}}. \tag{2.7}$$

The inner cylinder is then mapped onto $\rho = 1$, and the outer one is mapped onto

$$\rho = \frac{\alpha}{1 + \epsilon\gamma} = \alpha + O(\epsilon^2). \tag{2.8}$$

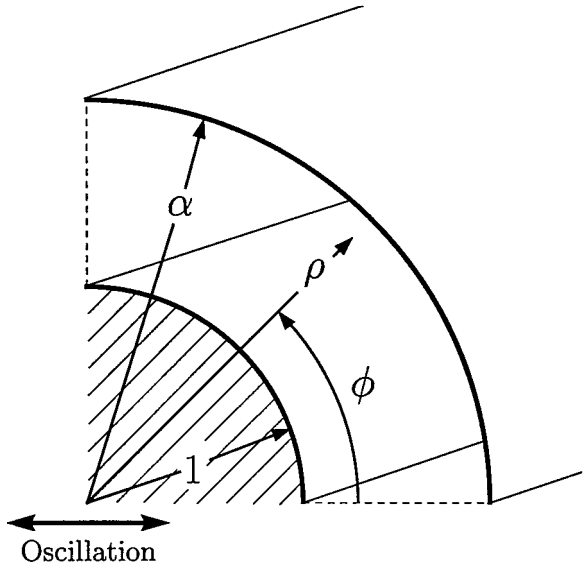


Fig. 2.4: The configuration of the cylinders in the complex ζ-plane.

The invariance of the Laplace stream function equation under such a conformal map, is well known and can be verified by using the Cauchy-Riemann equations together with the chain-rule. More precisely, the Laplacian of the stream function in the z-plane, is related to that in the ζ-plane in the following way:

$$\nabla^2_{(r,\vartheta)}\tilde{\psi} = \nabla^2_{(\rho,\phi)}\psi \left|\frac{\mathrm{d}\zeta}{\mathrm{d}z}\right|^2 \quad \text{with} \quad \tilde{\psi}[r(\rho,\phi),\vartheta(\rho,\phi)] = \psi(\rho,\phi). \tag{2.9}$$

In addition, the Jacobian chain-rule is required for mapping the nonlinear terms in the Navier-Stokes equations. The required relationship is

$$\frac{\partial(\tilde{\psi}_1,\tilde{\psi}_2)}{\partial(r,\vartheta)} = \frac{\partial(\psi_1,\psi_2)}{\partial(\rho,\phi)}\frac{\partial(\rho,\phi)}{\partial(r,\vartheta)}. \tag{2.10}$$

The Jacobian $J = J(\rho,\phi,t)$ for the above transformation is given by

$$\begin{aligned} J = \left|\frac{dz}{d\zeta}\right|^2 = \frac{\partial(r,\vartheta)}{\partial(\rho,\phi)} &= \left(1-\gamma^2\right)^2\left(1+2\rho\gamma\cos\phi+\rho^2\gamma^2\right)^{-2} \\ &= 1-\frac{4\rho\epsilon\cos t\cos\phi}{\alpha^2-1}+O\left(\epsilon^2\right). \end{aligned} \tag{2.11}$$

Hence, after the conformal map (2.6) is applied to the Navier-Stokes equations (2.4-2.5), the transformed equations of motion are:

$$J\frac{\partial}{\partial t}\left(\frac{\nabla^2\psi}{J}\right)+\frac{\epsilon}{\rho}\frac{\partial(\nabla^2\psi/J,\psi)}{\partial(\rho,\phi)} = \frac{1}{M^2}\nabla^2\left(\frac{\nabla^2\psi}{J}\right), \tag{2.12}$$

with the boundary conditions

$$\left.\begin{aligned}\frac{\partial\psi}{\partial\phi} &= -\cos\phi\sin t + \frac{\epsilon\sin 2t\cos 2\phi}{\alpha^2-1} + O\left(\epsilon^2\right)\\ \frac{\partial\psi}{\partial\rho} &= -\sin\phi\sin t + \frac{\epsilon\sin 2t\sin 2\phi}{\alpha^2-1} + O\left(\epsilon^2\right)\end{aligned}\right\} \quad \text{on} \quad \rho = 1 \tag{2.13a,b}$$

and

$$\frac{\partial\psi}{\partial\phi} = \frac{\partial\psi}{\partial\rho} = 0 \quad \text{on} \quad \rho = \alpha + O\left(\epsilon^2\right). \tag{2.14a,b}$$

Hence, to leading order both cylinders are stationary. Note, the unsteady correction term for the outer cylinder, see (2.8), occurs at $O(\epsilon^2)$ and is negligible because $\epsilon \ll 1$. Moreover, it is seen from (2.13a,b), that in compensation for simpler geometry, the vibration has now been incorporated into boundary conditions which are no longer homogeneous.

2.2.1 Steady streaming at small values of Re_s

Most of the results established here, are directly applicable to the case $Re_s = O(1)$ which is considered in section 2.2.2. The underlying assumption for $Re_s = \epsilon^2 M^2 \ll 1$, is $0 < \epsilon \ll M^{-1} \ll 1$. Here the small parameter ϵ is the ratio of the oscillation amplitude to the inner cylinder radius a, and the large parameter M represents the ratio of a to the viscous length scale $(\nu/\omega)^{\frac{1}{2}}$.

We start by expanding the stream function in a regular ϵ series. Thereafter the limit $\epsilon \to 0$ is taken with M held fixed and large. The $O(\epsilon)$ term in the stream function expansion is separated into steady and unsteady components, the steady term being associated with the steady streaming flow. Hence we write

$$\psi\left(\mathbf{x}, t, M, \epsilon\right) = \psi_0\left(\mathbf{x}, t, M\right) + \epsilon\left\{\psi_1^{(u)}\left(\mathbf{x}, t, M\right) + \psi_1^{(s)}\left(\mathbf{x}, M\right)\right\} + O(\epsilon^2). \tag{2.15}$$

Here the superscripts (s) and (u) respectively denote the steady and unsteady components of ψ_1. Moreover, $\mathbf{x}$ is used to denote the coordinate variables (ρ, ϕ).

Next, the stream function expansion (2.15) is substituted into the Navier-Stokes equations (2.12). By collecting terms at each order of ϵ, we obtain the following

equations for ψ_i:

$$\frac{\partial}{\partial t}\left(\nabla^2\psi_0\right) = \frac{1}{M^2}\nabla^2\nabla^2\psi_0, \tag{2.16}$$

$$\frac{\partial}{\partial t}\left(\nabla^2\psi_1^{(u)}\right) - \frac{1}{M^2}\nabla^2\nabla^2\psi_1^{(u)} = -\left\{\frac{1}{\rho}\frac{\partial(\nabla^2\psi_0,\psi_0)}{\partial(\rho,\phi)} - \frac{4\rho\nabla^2\psi_0\sin t\cos\phi}{\alpha^2-1} - \frac{1}{M^2}\nabla^2\left(\frac{4\rho\cos t\cos\phi\nabla^2\psi_0}{\alpha^2-1}\right)\right\}^{(u)}, \tag{2.17}$$

$$\frac{1}{M^2}\nabla^2\nabla^2\psi_1^{(s)} = \left\{\frac{1}{\rho}\frac{\partial(\nabla^2\psi_0,\psi_0)}{\partial(\rho,\phi)} - \frac{4\rho\nabla^2\psi_0\sin t\cos\phi}{\alpha^2-1} - \frac{1}{M^2}\nabla^2\left(\frac{4\rho\cos t\cos\phi\nabla^2\psi_0}{\alpha^2-1}\right)\right\}^{(s)}, \tag{2.18}$$

with boundary conditions

$$\left.\begin{array}{ll} \dfrac{\partial\psi_0}{\partial\phi} = -\cos\phi\sin t, & \dfrac{\partial\psi_0}{\partial\rho} = -\sin\phi\sin t \\ \dfrac{\partial\psi_1}{\partial\phi} = \dfrac{\cos 2\phi\sin 2t}{\alpha^2-1}, & \dfrac{\partial\psi_1}{\partial\rho} = \dfrac{\sin 2\phi\sin 2t}{\alpha^2-1} \end{array}\right\} \quad \text{on} \quad \rho = 1 \tag{2.19a-d}$$

and

$$\frac{\partial\psi_i}{\partial\phi} = \frac{\partial\psi_i}{\partial\rho} = 0 \quad \text{on} \quad \rho = \alpha. \tag{2.20}$$

In the matching procedure that follows, equations (2.16)-(2.18) are solved in the *core region*, $1 < \rho < \alpha$, with inviscid boundary conditions i.e. with conditions that ensure zero normal velocity at $\rho = 1,\ \alpha$. These core region solutions are then matched with the *inner* solutions that are valid within the Stokes layers at $\rho = 1,\ \alpha$. By standard boundary layer arguments it can be shown from (2.16) that these Stokes layers are of thickness $O(M^{-1})$. Duck & Smith [20] have carried out the above matching procedure and from their calculations the following core region solutions are obtained:

$$\psi_0(\mathrm{x},t,M) = \frac{\sin t\sin\phi}{\alpha^2-1}\left(\rho - \frac{\alpha^2}{\rho}\right) + O\left(M^{-1}\right), \tag{2.21}$$

$$\psi_1^{(u)}(\mathrm{x},t,M) = \frac{-\sin 2t\sin 2\phi}{2\left(\alpha^2-1\right)^2\left(1+\alpha^2\right)}\left(\rho^2 - \frac{\alpha^4}{\rho^2}\right) + O\left(M^{-1}\right), \tag{2.22}$$

$$\psi_1^{(s)}(\mathrm{x},M) = \frac{3\sin 2\phi}{4\alpha\rho^2\left(\alpha^2-1\right)^4}\left\{\left(1+\alpha^4\right)\rho^6 - \left(1+\alpha^2\right)\left(2-\alpha^2+2\alpha^4\right)\rho^4 + \left(1+2\alpha^2+2\alpha^6+\alpha^8\right)\rho^2 - \alpha^2\left(1+\alpha^6\right)\right\} + O\left(M^{-1}\right). \tag{2.23}$$

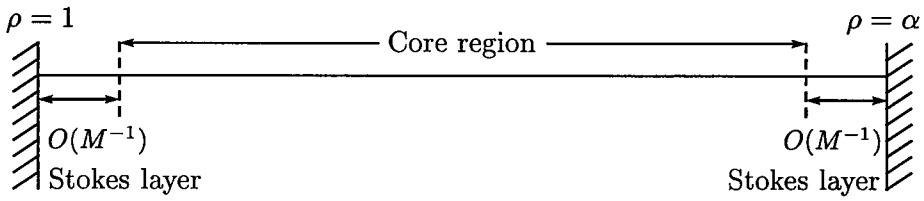


Fig. 2.5: The Stokes layers on the inner and outer cylinders. Note, for $Re_s \ll 1$ there are no steady streaming layers.

The dependence of the above solutions on t and ϕ, can easily be inferred from the boundary conditions (2.19)-(2.20). In fact, the core region solutions for ψ_0 and $\psi_1^{(u)}$ are easily calculated from (2.16)-(2.17) directly and without the need of matching. This is because the boundary layer solutions associated with $\{\psi_0,\ \psi_1^{(u)}\}$ decay to zero at the edge of the Stokes layers and do not impose any conditions on the core solutions. However, the steady component $\psi_1^{(s)}$ is different in that its boundary layer solution does not decay to zero at the edge of the Stokes layer. Hence, a slip velocity is produced by this boundary layer solution and the core solution of $\psi_1^{(s)}$ is matched to this condition.

The boundary layer solutions for: ψ_0, $\psi_1^{(u)}$, $\psi_1^{(s)}$ and scalings used to obtain them can be referenced in Duck & Smith [20], henceforth referred to as D. & S. The matching procedure used by the latter authors is analogous to the method used by Riley [66]. In Riley's paper, the formulation of these expansions are discussed in greater detail (but only within the context of the unbounded one-cylinder problem).

2.2.2 Steady streaming at $O(1)$ values of Re_s

As before, the stream function ψ is expanded in a regular ϵ power series. The $O(\epsilon)$ term in the expansion is once again separated into two parts: ψ_1^u and ψ_1^s, and these components will now vary on two different time scales. Note, the superscript 's' is now understood to mean 'streaming' and not 'steady'. As before ψ_1^u will vary on the short $O(1)$ time scale, and now ψ_1^s will capture the steady streaming evolution of the flow by varying on a long time scale.

To obtain the appropriate time scale for ψ_1^s, we first simplify the Navier-Stokes equations (2.12) and then consider the required scalings. By expanding the Jacobian

terms in (2.12) and noting that $J \simeq 1 + O(\epsilon)$, we have

$$\nabla^2\psi_t + \frac{\epsilon}{\rho}\left\{\frac{1}{J}\frac{\partial(\nabla^2\psi,\psi)}{\partial(\rho,\phi)} - \frac{\nabla^2\psi}{J^2}\frac{\partial(J,\psi)}{\partial(\rho,\phi)}\right\} = \frac{1}{M^2}\nabla^2\nabla^2\psi - \frac{4\epsilon\cos t}{\alpha^2-1}\nabla^2\left(\rho\cos\phi\nabla^2\psi\right) + \nabla^2\psi\frac{J_t}{J} + \ldots$$

Therefore in order to introduce the time variation of ψ_1^s, into the leading order steady streaming equation, it is required that

$$\epsilon\frac{\partial}{\partial t}\left(\nabla^2\psi_1^s\right) \sim \frac{\epsilon}{M^2}\nabla^2\nabla^2\psi_1^s \quad \text{with} \quad Re_s = \epsilon^2M^2 \sim O(1).$$

This implies that an $O(\epsilon^{-2})$ time scale is appropriate for ψ_1^s and therefore we write

$$\psi\left(\mathbf{x},t,M,\epsilon\right) = \psi_0\left(\mathbf{x},t,M\right) + \epsilon\left\{\psi_1^u\left(\mathbf{x},t,M\right) + \psi_1^s\left(\mathbf{x},T,M\right)\right\} + O(\epsilon^2), \tag{2.24}$$

with $T = \epsilon^2 t$. By substituting the above stream function expansion into (2.12), it is found that the equations for ψ_0 and ψ_1^u are exactly those derived for the small Re_s limit, namely (2.16) and (2.17). Hence the corresponding solutions for ψ_0 and ψ_1^u are the same as ones obtained in the previous section, see (2.21)-(2.22). However this is not the case for ψ_1^s. It is useful to note that within the core region, the entire RHS of equation (2.18) is zero; this occurs because ψ_0 is proportional to $\sin t$ within the core. Therefore, upon considering the $O(\epsilon^3)$ inertial terms in (2.12), it is found that the steady streaming equation for $1 < \rho < \alpha$ is given by

$$\frac{\partial}{\partial T}\left(\nabla^2\psi_{10}^s\right) + \frac{1}{\rho}\frac{\partial(\nabla^2\psi_{10}^s,\psi_{10}^s)}{\partial(\rho,\phi)} = \frac{1}{Re_s}\nabla^2\nabla^2\psi_{10}^s, \tag{2.25}$$

with

$$\psi_1^s = \psi_{10}^s + M^{-1}\psi_{11}^s + O\left(M^{-2}\right) \quad \text{and} \quad M \sim \epsilon^{-1}.$$

Hence the full Navier-Stokes equations govern the steady streaming flow in the core.

Next, we obtain the boundary conditions for (2.25). These boundary conditions are determined by the outer limit of the Stokes layer solutions at $\rho = 1,\ \alpha$. Let us now demonstrate that the Stokes layer solutions for $Re_s \ll 1$, remain unchanged for $Re_s = O(1)$. When expanding the stream function ψ_0^s in the boundary layers, the

appropriate scalings are:

$$\xi = M\,(\rho - 1)\,2^{-\frac{1}{2}}, \qquad \Psi_{10}^{(s)} = M\psi_1^s\,2^{-\frac{1}{2}} \quad \text{for} \quad \rho \sim 1 \quad \text{and} \tag{2.26}$$

$$\tilde{\xi} = M\,(\alpha - \rho)\,2^{-\frac{1}{2}}, \qquad \tilde{\Psi}_{10}^{(s)} = M\psi_1^s\,2^{-\frac{1}{2}} \quad \text{for} \quad \rho \sim \alpha. \tag{2.27}$$

Note, the RHS of equation (2.18) is no longer zero in the boundary layers. Moreover, the leading order terms on the RHS of (2.18) are of order ϵM i.e. of the same size as the viscous term on the LHS. However, the inertial and time derivative terms in (2.25) are of size $\epsilon^3 M$, and so they do not enter the governing Stokes layer equations. This means that the Stokes layer equations for $Re_s = O(1)$, are exactly the same as the ones obtained for $Re_s \ll 1$.

The solutions in the Stokes layers are obtained by solving the appropriate forms of equations (2.16)-(2.18) near $\rho = 1,\ \alpha$. The resulting Stokes layer solutions for ψ_0 and ψ_1^u are then matched to the solutions calculated for the core region. However, since the core solution for ψ_1^s is determined by (2.25), the outer limit of the corresponding Stokes layers solutions at $\rho = 1,\ \alpha$, will specify the required boundary conditions for (2.25). The Stokes layer solutions for ψ_1^s have been calculated by D. & S. [20] and are given by

$$\begin{aligned}\Psi_{10}^{(s)} = \Big\{&6\alpha^4\xi - \alpha^2(13\alpha^2+8) + \alpha^4 e^{-2\xi} + 4\alpha^2(3\alpha^2+2)e^{-\xi}\cos\xi \\ &+ 8\alpha^2(\alpha^2+1)e^{-\xi}\sin\xi + 4\alpha^4\xi e^{-\xi}\sin\xi\Big\}\frac{\sin 2\phi}{4(\alpha^2-1)^2},\end{aligned} \tag{2.28a}$$

$$\begin{aligned}\tilde{\Psi}_{10}^{(s)} = \Big\{&-6\tilde{\xi} + (13+8\alpha^2) - e^{-2\tilde{\xi}} - 4(2\alpha^2+3)e^{-\tilde{\xi}}\cos\tilde{\xi} \\ &- 8(\alpha^2+1)e^{-\tilde{\xi}}\sin\tilde{\xi} - 4\tilde{\xi}e^{-\tilde{\xi}}\sin\tilde{\xi}\Big\}\frac{\sin 2\phi}{4\alpha(\alpha^2-1)^2}.\end{aligned} \tag{2.28b}$$

The outer limit of the above Stokes layer solutions give the following slip velocity conditions:

$$\frac{\partial\psi_{10}^s}{\partial\rho} = \frac{3\alpha^4\sin 2\phi}{2\,(\alpha^2-1)^2} \quad \text{on} \quad \rho = 1 \quad \text{and} \tag{2.29a}$$

$$\frac{\partial\psi_{10}^s}{\partial\rho} = \frac{3\sin 2\phi}{2\alpha\,(\alpha^2-1)^2} \quad \text{on} \quad \rho = \alpha. \tag{2.29b}$$

As one might have expected, equations (2.25) and (2.29) without the time derivative, are identical to the equations derived by D. & S. [20] for the steady streaming flow

between two cylinders. Moreover, if the slip condition on the outer cylinder is ignored, equations (2.25) and (2.29a) are the same as the corresponding ones derived by Riley [65] for the one-cylinder problem. Henceforth the terms "steady streaming Reynolds number" and "Reynolds number" will be used interchangeably unless otherwise stated.

In the next section, the steady streaming equations, (2.25) and (2.29), are considered in the small gap limit. Thereafter, a solution to the resulting equation is sought in the form of a powers series in ϕ.

2.2.3 Transformation to the small gap width limit

To investigate the small gap limit it is convenient to write $\alpha = 1+h$ and then consider the limit $h \to 0$ (note, ϵ is less than h since $(1+\epsilon) < \alpha = b/a$). It is also convenient to make the following change of coordinate variables:

$$\theta = 2\phi, \qquad \text{therefore} \qquad 0 \le \phi \le \frac{\pi}{2} \quad \mapsto \quad 0 \le \theta \le \pi, \tag{2.30a}$$

$$\eta = \frac{2(\rho-1)}{h} - 1, \qquad \text{and} \qquad 1 \le \rho \le \alpha \quad \mapsto \quad -1 \le \eta \le 1. \tag{2.30b}$$

Accordingly, the boundary conditions (2.29) can be written as

$$\frac{\partial \psi_{10}^s}{\partial \eta} = \frac{3\,(h+1)^4 \sin\theta}{4h\,(h+2)^2} \qquad \text{at} \quad \eta = -1 \quad \text{and}$$

$$\frac{\partial \psi_{10}^s}{\partial \eta} = \frac{3\sin\theta}{4h\,(h+1)\,(h+2)^2} \qquad \text{at} \quad \eta = +1.$$

The boundary conditions above suggest that $\psi_{10}^s \sim h^{-1}$ as $h \to 0$. Hence, ψ_{10}^s is scaled accordingly by writing

$$\psi_{10}^s = -\frac{3}{16h}\Psi + f_o + hf_1 + O(h^2).$$

Under this scaling, the governing equation in the core is

$$\frac{h^2}{4}\frac{\partial}{\partial T}\left(\Psi_{\eta\eta}\right) - \frac{3}{16}\left\{\Psi_{\eta\eta\eta}\Psi_\theta - \Psi_{\eta\eta\theta}\Psi_\eta\right\} = \frac{1}{Re_s}\Psi_{\eta\eta\eta\eta}. \tag{2.31}$$

From the above equation it is clear that T must vary on an $O(h^2)$ scale. This latter scaling, together with a minor redefinition of the Reynolds number, will define the

steady streaming problem in its canonical form. The scalings required for T and Re_s are

$$\tau = \frac{3}{4}h^{-2}T, \qquad R_s = \frac{3}{16}Re_s. \tag{2.32}$$

Thus in the small gap width limit $h \to 0$, the governing equation for the steady streaming flow is

$$\Psi_{\eta\eta\tau} = \frac{1}{R_s}\Psi_{\eta\eta\eta\eta} + \Psi_{\eta\eta\eta}\Psi_\theta - \Psi_{\eta\eta\theta}\Psi_\eta \tag{2.33a}$$

with boundary conditions

$$\Psi(\theta = 0) = 0, \quad \Psi(\eta = \mp 1) = 0, \quad \Psi_\eta(\eta = \mp 1) = -\sin\theta. \tag{2.33b-f}$$

By considering the physical symmetry of the flow in each quadrant, we note that (2.33) must be solved in the range $0 < \theta < \pi$. In the new angular coordinate variable, $\theta = 0$ corresponds to the axis of oscillation and $\theta = \pi$ represents the line passing through the poles of the cylinders i.e. the line $\theta = \pi$ passes through the points S and $\acute{S}$ in figure 2.3. It is important to mention that by taking the small gap limit, we have lost the second order curvature terms i.e. the terms involving ∂_θ^2. By neglecting these second order curvature terms, it is impossible to impose periodic boundary conditions in the θ-direction. However, by virtue of the fact that periodicity cannot be enforced in the θ-direction, it is possible to seek a solution to Ψ in the form of a power series in θ. Since the flow is symmetric about the axis of oscillation ($\theta = 0$), a series solution is sought in odd powers of θ to coincide with the geometry. Hence Ψ is expanded as

$$\Psi = \sum_{n=0}^{\infty} \Psi^{(n)}(\eta, \tau)\, \theta^{2n+1}. \tag{2.34}$$

The above expansion is then substituted into the equations of motion (2.33) to give

$$\sum_{n=0}^{\infty}\theta^{2n+1}\Psi^{(n)}_{\eta\eta\tau} = \frac{1}{R_s}\sum_{n=0}^{\infty}\theta^{2n+1}\Psi^{(n)}_{\eta\eta\eta\eta} + \sum_{i=0}^{\infty}(2i+1)\theta^{2i}\Psi^{(i)}\sum_{j=0}^{\infty}\theta^{2j+1}\Psi^{(j)}_{\eta\eta\eta} - \sum_{k=0}^{\infty}\theta^{2k+1}\Psi^{(k)}_{\eta}\sum_{l=0}^{\infty}(2l+1)\theta^{2l}\Psi^{(l)}_{\eta\eta}, \tag{2.35}$$

$$\Psi(\eta=\mp1) = \sum_{n=0}^{\infty}\theta^{2n+1}\Psi^{(n)}(\eta=\mp1) = 0, \tag{2.36a,b}$$

$$\Psi_{\eta}(\eta=\mp1) = \sum_{n=0}^{\infty}\theta^{2n+1}\Psi^{(n)}_{\eta}(\eta=\mp1) = -\sin\theta. \tag{2.36c,d}$$

Upon collecting the coefficients of θ^{2n+1}, it is found that $\Psi^{(n)}$ is governed by the equations:

$$\Psi^{(n)}_{\eta\eta\tau} = \frac{1}{R_s}\Psi^{(n)}_{\eta\eta\eta\eta} + \sum_{i=0}^{n}(2i+1)\left[\Psi^{(i)}\Psi^{(n-i)}_{\eta\eta\eta} - \Psi^{(n-i)}_{\eta}\Psi^{(i)}_{\eta\eta}\right], \tag{2.37a}$$

$$\Psi^{(n)}(\eta=\mp1) = 0, \quad \Psi^{(n)}_{\eta}(\eta=\mp1) = \frac{(-1)^{n+1}}{(2n+1)!}. \tag{2.37b-e}$$

Hence the governing equation for Ψ is reduced to an infinite set of coupled ODEs. These coupled equations must be solved numerically to in order to obtain each $\Psi^{(n)}$. Fortunately, by computing $\Psi^{(0)}$ first, the terms in (2.37) can be evaluated in a recursive manner.

In the procedure used to solve (2.37), $\Psi^{(0)}$ is computed numerically by time marching. This calculation is straightforward because the equation at $n = 0$ is uncoupled from the higher order terms $\Psi^{(n\geq1)}$. From equations (2.37) it is seen that $\Psi^{(0)}$ satisfies

$$\Psi^{(0)}_{\eta\eta\tau} = \frac{1}{R_s}\Psi^{(0)}_{\eta\eta\eta\eta} + \Psi^{(0)}\Psi^{(0)}_{\eta\eta\eta} - \Psi^{(0)}_{\eta}\Psi^{(0)}_{\eta\eta}, \tag{2.38a}$$

$$\Psi^{(0)}(\eta=\mp1) = 0, \quad \Psi^{(0)}_{\eta}(\eta=\mp1) = -1. \tag{2.38b-e}$$

By starting the numerical calculation with an initial condition of zero-flow, the numerical solution for $\Psi^{(0)}$ is determined by time marching as $\tau \to \infty$. At the next order, $n = 1$, $\Psi^{(1)}$ is easily determined because $\Psi^{(0)}$ is already known at this stage. Once again an initial condition of zero flow is imposed for $\Psi^{(1)}$ and the numerical solution is found by time marching as $\tau \to \infty$. It is clear from (2.37a) that the solution at any

order, say $n = k$, is only dependent on the lower order terms, $\Psi^{(0)}, \ldots, \Psi^{(k-1)}$. Moreover, since these lower order terms are already known at this stage of the calculation, the equation at the current order, $n = k$, is linear in $\Psi^{(k)}$. Therefore, it is possible to repeat this recursive procedure indefinitely to obtain a truncated solution at any desired order.

In the following section, some asymptotic solutions are calculated for the cases of small and large R_s. In section 2.4, these asymptotic forms are compared with numerical solutions acquired from solving the series equations (2.37). Moreover the asymptotic solutions are also compared to the solutions obtained by solving the equation of motion (2.33) directly.

2.3 Asymptotic solutions

We note here that the governing equation for $\Psi^{(0)}$ in (2.37), is identical to the equation that has been studied by H. & P [37], namely equation (2.2). In their study, H. & P. consider the induced flow between two flat walls driven by the periodic action of the upper wall. The mechanical system investigated by H. & P., closely resembles (near $\theta = 0$) the physical motion of the two cylinders in the present study. Therefore, a solution represented by θ-series (to the cylinder problem), is certainly intuitive with respect to the dynamics of the system. Before embarking on any further analysis, it is helpful to summarise the findings of H. & P. to serve as a guide.

In the discussion that follows, the terminology "steady solution" is used to identify a numerical solution, of a typically *unsteady* governing equation, that converges to a steady state for $\tau > \tau_c$, where τ_c is some finite (and usually small) value of time. Moreover, the phrase "steady solutions" will also be used throughout this chapter to describe steady state numerical solutions, that are obtained via time marching as $\tau \to \infty$.

From their numerical work, H. & P. find that the numerical solution for $\Psi^{(0)}$ is steady and symmetric for small values of R_s. Upon increasing R_s, this solution encoun-

$0 < R_s < 17.3$	The solutions for $\Psi^{(0)}$ are steady and symmetric in η.
$17.3 < R_s < 53.8$	The symmetric solution is lost and a new steady secondary state is acquired.
$53.8 < R_s < 74.0$	$\Psi^{(0)}$ becomes unsteady and periodic in time. At $R_s \approx 54$ the period of $\Psi^{(0)}$ is 3.11.
$74.0 < R_s < 78.6$	The period-doubling cascade to chaos begins and the flow reaches a fully chaotic state for $R_s \gtrsim 82.14$.

Table 2.2: A summary of the numerical solutions for $\Psi^{(0)}$.

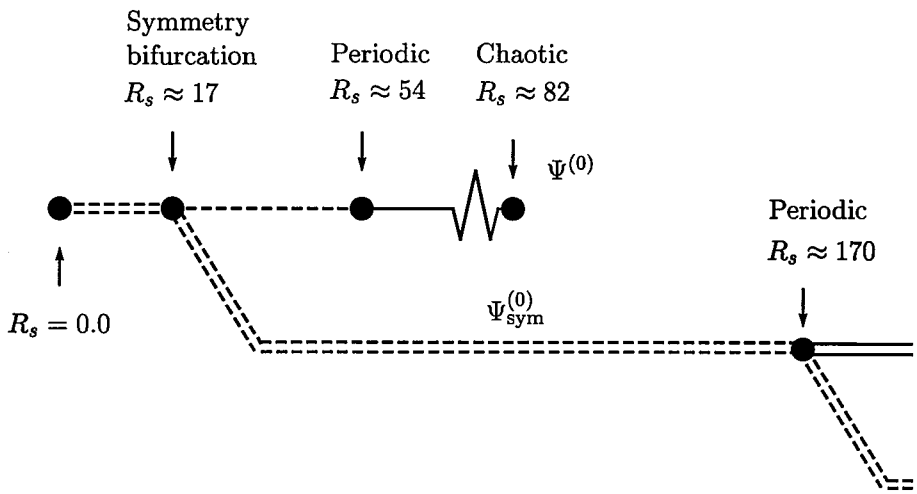


Fig. 2.6: A schematic diagram showing the different flow regimes of $\Psi^{(0)}$ at various Reynolds numbers. A dashed line represents a steady solution, a solid line indicates an unsteady solution and a double line indicates a symmetric solution. Here $\Psi^{(0)}_{\text{sym}}$ is used to label the symmetric regime. In this hierarchy diagram, the regimes of $\Psi^{(0)}$ are arranged so that the most preferred state is towards the top of the schematic.

ters a symmetry-breaking bifurcation from which a stable secondary state is attained, see table 2.2 and figure 2.6. This secondary state then becomes periodic in time after a Hopf bifurcation at $R_s \approx 53.8$. When R_s is increased further, the solution enters a period-doubling cascade and eventually becomes chaotic at $R_s \approx 82.1$.

However, if the boundary conditions are changed to force the symmetric solution, the resulting solution for $\Psi^{(0)}$ is steady up to $R_s \approx 170$. The latter classification, regarding the steady regime, has been established by Watson, Banks, Zaturska and Drazin [97], henceforth WBZD. In their study, WBZD have investigated equation (2.2) in the context of channel flow driven by accelerating walls. From their results it is known that after a Hopf bifurcation, $\Psi^{(0)}_{\text{sym}}$ enters a periodic regime for $R_s > 170$ (here the subscript 'sym' denotes the symmetric solution). This periodic regime is temporally unstable since the chaotic solution is the preferred mode.

2.3.1 Asymptotic solutions for small R_s

In the small Reynolds number limit, each term $\Psi^{(n)}$ (from (2.34)) is expanded in the following manner:

$$\Psi^{(n)} = \psi_0^n + R_s\psi_1^n + R_s^2\psi_2^n + \dots \tag{2.39}$$

Here it is assumed that τ is $O(1)$ i.e. it is assumed that τ does not scale with the Reynolds number. Consequently, the time derivative term in (2.37a) is not present in the equation for ψ_0^n; accordingly, there is no time dependence in the higher order equations. Hence, the resulting solutions for $\Psi^{(n)}$ are steady and the first few terms

are given by

$$\Psi^{(0)} = -\frac{1}{2}\eta\left(\eta^2-1\right) + \frac{R_s}{280}\eta\left(\eta^2-1\right)^2\left(2+\eta^2\right) + \frac{R_s^2}{3880800}\eta\left(\eta^2-1\right)^2\left(201-50\eta^2-301\eta^4+42\eta^6\right)+\ldots,$$

$$\Psi^{(1)} = \frac{1}{12}\eta\left(\eta^2-1\right) - \frac{R_s}{420}\eta\left(\eta^2-1\right)^2\left(2+\eta^2\right) + \frac{R_s^2}{4656900}\eta\left(\eta^2-1\right)^2\left(-4209-1394\eta^2+5579\eta^4+672\eta^6\right)+\ldots,$$

$$\Psi^{(2)} = -\frac{1}{240}\eta\left(\eta^2-1\right) + \frac{R_s}{2100}\eta\left(\eta^2-1\right)^2\left(2+\eta^2\right) + \frac{R_s^2}{332640000}\eta\left(\eta^2-1\right)^2\left(-1374-53\eta^2+1799\eta^4+267\eta^6\right)+\ldots \quad (2.40\text{a-c})$$

The general expression for the term $\Psi^{(n)}$ is

$$\Psi^{(n)} = \frac{(-1)^{n+1}}{2(2n+1)!}\eta\left(\eta^2-1\right) + R_s\frac{(-1)^n\,(2)^{2n-3}}{35\,(2n+1)!}\eta\left(\eta^2-1\right)^2\left(2+\eta^2\right) + O(R_s^2). \quad (2.41)$$

When directly solving the series equations (2.37), it is difficult to obtain a general expression for the $O(R_s^2)$ correction to $\Psi^{(n)}$ i.e. the $O(R_s^2)$ term in (2.41). This difficulty arises because the governing equation for ψ_2^n, see (2.39), contains products of combinatorial summations. For general n, these expressions are difficult to simplify, and therefore a general expression for the $O(R_s^2)$ correction is not accessible via this direct approach. The $O(R_s^2)$ corrections in (2.40a-c) have been calculated by evaluating the product of the combinatorial summations for the specific cases $n = 0,\ 1,\ 2$. However, if an asymptotic solution for small R_s is sought directly from the equation of motion (2.33), the following solution is obtained:

$$\Psi(\eta,\theta) = -\frac{1}{2}\left(\eta^3-\eta\right)\sin\theta + \frac{R_s}{560}\eta\left(\eta^2-1\right)^2\left(2+\eta^2\right)\sin 2\theta + \frac{R_s^2}{62092800}\eta\left(\eta^2-1\right)^2\left[\left(-591-2294\eta^2+161\eta^4+1428\eta^6\right)\sin\theta + 3\left(423+166\eta^2-553\eta^4-84\eta^6\right)\sin 3\theta\right]+\ldots \quad (2.42)$$

As expected the above solution is unique and steady for $R_s \ll 1$. Note, that representation (2.42) is readily decomposable into a θ-power series. Therefore, by expanding the above solution for small θ and collecting coefficients at each order of R_s, it is possible to write down the general solution for $\Psi^{(n)}$. The expansion obtained in this manner is

$$\Psi^{(n)} = \frac{(-1)^{n+1}}{2(2n+1)!}\eta\left(\eta^2-1\right) + R_s\frac{(-1)^n\,(2)^{2n-3}}{35\,(2n+1)!}\eta\left(\eta^2-1\right)^2\left(2+\eta^2\right) + R_s^2\frac{(-1)^n\eta\left(\eta^2-1\right)^2}{62092800\;(2n+1)!}\big[\left(-591-2294\eta^2+161\eta^4+1428\eta^6\right) + 3^{2n+2}\left(423+166\eta^2-553\eta^4-84\eta^6\right)\big] + O(R_s^3). \quad (2.43)$$

Hence by solving equation (2.33) for $R_s \ll 1$, it is possible to calculate the $O(R_s^2)$ correction to $\Psi^{(n)}$ indirectly.

The asymptotic forms calculated above will serve as a check on our numerical work. As previously mentioned, the above steady solutions for $\Psi^{(n)}$ will be found numerically by time marching as $\tau \to \infty$. Moreover, we now expect that the numerical solutions of (2.37) are steady and η-symmetric for small values of R_s.

2.3.2 The steady state asymptotic solutions for large R_s

Without the time derivative, equation (2.33a) reduces to the familiar Berman's equation; within this context, $\Psi^{(0)}$ is interpreted as the Berman similarity solution, see Berman [6]. Due to its frequent appearance in channel flow problems, Berman's equation has been studied by many authors. In particular, the steady solutions of Berman's equation have been studied analytically and numerically by Proudman [61], Robinson [69], Sellars [75], Terrill [93][94], Yuan [104] and Zaturska, Drazin & Banks [105].

Since $\Psi^{(0)}$ satisfies Berman's equation, it is interesting to note how the accompanying boundary conditions (2.37b-e) correspond to other channel flow configurations. If the derivative boundary conditions (2.37d, e) are negated and then interchanged with (2.37a, b), the resulting equation for $\Psi^{(0)}$ determines the flow in a channel with porous walls. In this case, injection/suction through the walls is represented by neg-

ative/positive Reynolds numbers respectively. However, if the boundary conditions (2.37b-e) remain unchanged and the Reynolds number is negative, the resulting equation models the flow in a channel with accelerating walls, see WBZD [97].

From the earlier discussion in section 2.3, it is anticipated that there are two steady state structures for $O(1)$ values of R_s, namely the symmetric and asymmetric regimes (see figure 2.6). In view of this result, the symmetric and asymmetric regimes are considered separately in the analysis that follows.

Symmetric Solutions

As with the small R_s limit, the initial approach will be to solve the series equations (2.37) directly. Thereafter, it is seen that this calculation yields an intuitive result, which is consistent with the alternative approach of solving the equation of motion (2.33). Since we are concerned with symmetric solutions, it is sufficient to impose boundary conditions on one wall, and then enforce the necessary symmetry condition at $\eta = 0$. In this way, the resulting solution automatically satisfies the appropriate conditions on the remaining wall. Next, for each term $\Psi^{(n)}$, the outer expansion is written in the form

$$\Psi^{(n)}(\eta, R_s) = f^{(n,0)} + f^{(n,1)} R_s^{-1} + \dots \quad \text{as} \quad R_s \to \infty. \tag{2.44}$$

At $O(1)$, the classical Berman's equation for $\Psi^{(0)}$ yields

$$f^{(0,0)} f^{(0,0)}_{\eta\eta\eta} - f^{(0,0)}_{\eta} f^{(0,0)}_{\eta\eta} = 0, \tag{2.45a}$$

$$f^{(0,0)} = f^{(0,0)}_{\eta\eta} = 0, \quad \eta = 0 \quad \text{and} \quad f^{(0,0)} = 0, \; f^{(0,0)}_{\eta} = -1, \quad \eta = 1 \tag{2.45b}$$

$$\Longrightarrow \; f^{(0,0)} = \frac{(-1)^{k+1}}{k\pi} \sin k\pi\eta \quad \text{with} \quad k \neq 0 \in \mathbb{Z}. \tag{2.46}$$

For convenience and without loss of generality, the integer eigenvalue k is set equal to unity. In this case, $f^{(n,0)}$ satisfies

$$\frac{\sin\pi\eta}{\pi}F_\eta - (2n+1)\cos\pi\eta\, F = \sum_{j=1,n>1}^{j=n-1} f_\eta^{(n-j,0)} f_{\eta\eta}^{(n,0)} - f^{(j,0)} f_{\eta\eta\eta}^{(n-j,0)}, \tag{2.47a}$$

$$f^{(n,0)} = f_{\eta\eta}^{(n,0)} = 0 \quad \text{at} \quad \eta = 0 \quad \text{and} \tag{2.47b}$$

$$f^{(n,0)} = 0, \quad f_\eta^{(n,0)} = \frac{(-1)^{n+1}}{(2n+1)!} \quad \text{at} \quad \eta = 1 \tag{2.47c}$$

$$\text{with} \quad F = f_{\eta\eta}^{(n,0)} + \pi^2 f^{(n,0)}.$$

By using the expansion

$$(\sin\pi\eta)^{2n+1} = \sum_{j=0}^{j=n} \sin\{(2j+1)\pi\eta\}\ (-1)^j \binom{2n+1}{n-j}, \tag{2.48}$$

the homogeneous solution to (2.47) can be represented as

$$f_h^{(n,0)} = \left[\sum_{j=1}^{j=n} \frac{\sin(2j+1)\pi\eta}{1-(2j+1)^2}(-1)^j\binom{2n+1}{n-j} - \frac{\pi\eta}{2}\cos\pi\eta\binom{2n+1}{n}\right] c_{n,1} + c_{n,2}\cos\pi\eta + c_{n,3}\sin\pi\eta, \tag{2.49}$$

where the terms $c_{n,i}$ denote arbitrary constants. From (2.47a) it is clear that the equation for $f^{(1,0)}$ is homogeneous; consequently, $c_{1,1}$ and $c_{1,2}$ must be zero in order to satisfy the symmetry conditions. This in turn implies that the equation for $f^{(2,0)}$ is homogeneous, and by using the principle of induction on $f^{(n,0)}$, it can be shown that every subsequent equation is homogeneous. Subsequently this implies that the constants $c_{n,1}$ and $c_{n,2}$ are all zero. Hence by using the remaining constants $c_{n,3}$ to obey the boundary conditions, it is seen that the leading order approximation to $\Psi^{(n)}$ is given by

$$f^{(n,0)} = \frac{(-1)^n}{(2n+1)!\pi}\sin\pi\eta. \tag{2.50}$$

This expression for $f^{(n,0)}$ is now substituted back into the series expansion (2.34), which gives the following simple expression for the governing stream function $\Psi(\eta,\theta)$:

$$\begin{aligned}\Psi(\eta,\theta) = \sum_{n=0}^{\infty}\Psi^{(n)}\theta^{2n+1} &= \frac{\sin\pi\eta}{\pi}\sum_{n=0}^{\infty}\frac{(-1)^n}{(2n+1)!}\theta^{2n+1} + O(R_s^{-1}) \\ &= \pi^{-1}\sin\theta\sin\pi\eta + O(R_s^{-1}).\end{aligned} \tag{2.51}$$

The above result is consistent with the alternative approach of solving the equation of motion (2.33) directly, and then decomposing the solution into a θ-power series to obtain an approximation for $\Psi^{(n)}$.

Proceeding to $O(R_s^{-1})$, it is found that $f^{(n,1)}$ (for $n > 1$) satisfies the equation

$$-\frac{\pi^3(-1)^n \sin\pi\eta}{(2n+1)!} = \sum_{j=1,n>1}^{j=n-1} \frac{(-1)^j}{(2j)!}\left\{\pi^{-1}\sin\pi\eta\, F_\eta^{n-j} - \cos\pi\eta \frac{(2(n-j)+1)}{2j+1} F^{n-j}\right\}$$
$$+ (2n+1)\left\{\frac{(-1)^n}{(2n+1)!}\frac{\sin\pi\eta}{\pi} F_\eta^0 - \cos\pi\eta\, F^n\right\}$$
$$+\left\{-\frac{(-1)^n}{(2n+1)!}\cos\pi\eta\, F^0 + \frac{\sin\pi\eta}{\pi} F_\eta^n\right\} \quad (2.52a)$$

$$f^{(n,1)} = f_{\eta\eta}^{(n,1)} = 0,\ \eta = 0 \quad \text{and} \quad f^{(n,1)} = f_\eta^{(n,1)} = 0,\ \eta = 1 \quad (2.52b)$$
$$\text{with} \quad F^i = f_{\eta\eta}^{(i,1)} + \pi^2 f^{(i,1)}.$$

The homogeneous form of (2.52a) is

$$\pi^{-1}(\sin\pi\eta)^{2n+2}\frac{\mathrm{d}}{\mathrm{d}\eta}\left[F^n(\sin\pi\eta)^{-2n-1}\right] = 0. \quad (2.53)$$

By expanding $(\sin\pi\eta)^{2n+1}$ in a Fourier series, see (2.48), it is found that the solution to (2.53) is similar to (2.49) and is given by

$$f_h^{(n>1,1)} = \left[\sum_{j=1}^{j=n} \frac{\sin(2j+1)\pi\eta}{1-(2j+1)^2}(-1)^j\binom{2n+1}{n-j}\right.$$
$$\left. - \frac{\pi\eta}{2}\cos\pi\eta\binom{2n+1}{n}\right] d_{n,1} + d_{n,1}\cos\pi\eta + d_{n,2}\sin\pi\eta, \quad (2.54)$$

where $d_{n,i}$ are arbitrary constants. As before, it is expected that the solution for $f^{(0,1)}$ will simplify the inhomogeneous terms in (2.52a). Hence, by proceeding with this view the next objective is solve the following equation for $f^{(0,1)}$:

$$\pi^{-1}\sin\pi\eta\, F_\eta^0 - \cos\pi\eta\, F^0 = -\pi^3\sin\pi\eta. \quad (2.55)$$

A general solution to the above equation can be obtained as follows:

$$\frac{\mathrm{d}}{\mathrm{d}\eta}\left[F^0(\sin\pi\eta)^{-1}\right] = -\pi^4(\sin\pi\eta)^{-1},$$
$$\Longrightarrow\ F^0 = f_{\eta\eta}^{(0,1)} + \pi^2 f^{(0,1)} = -\pi^3\sin\pi\eta\,\ln(\tan\tfrac{1}{2}\pi\eta) + \lambda\sin\pi\eta.$$

Yuan [104] has represented the analytic solution to this equation in the form

$$f^{(0,1)} = \tfrac{1}{2}\pi(\pi\eta\cos\pi\eta - \sin\pi\eta)\ln(\tan\tfrac{1}{2}\pi\eta) - \tfrac{1}{2}\pi\sin\pi\eta - \tfrac{1}{2}\pi\cos\pi\eta \int_0^{x=\pi\eta} \frac{x}{\sin x}\mathrm{d}x. \quad (2.56)$$

In Yuan's study, solution (2.56) represents the $O(R_s^{-1})$ correction to the flow in a channel with large injection through porous walls. Although the above solution satisfies the required boundary conditions at $\eta = 0,\ 1$, Terrill [94] has indicated that the third derivative is undefined at the origin. This divergence is essentially brought about by the neglect of the highest derivative in the equation of motion (2.33a). In view of this, it is necessary to introduce an $O(R_s^{-\frac{1}{2}})$ boundary layer near $\eta = 0$. The solution within this layer is then matched with solution (2.56), which is now interpreted as an outer solution. Accordingly an inner solution is sought in the form $f^{(0,1)} = R_s^{-\frac{1}{2}} g$, with

$$\xi = R_s^{\frac{1}{2}}\eta \quad (2.57a)$$

and

$$g(\xi, R_s) = g_0 + R_s^{-1}g_1 + R_s^{-2}\ln R_s\, g_2 + R_s^{-2}g_3 + \ldots \quad (2.57b)$$

Here, the appropriate scaling for the inner variable ξ has been chosen by expanding the full outer solution (2.44) close to $\eta = 0$, and then noting the scale upon which η must vary so that the $O(1)$ and $O(R_s^{-1})$ terms are comparable. The complete procedure regarding the derivation of this scaling is given in Terrill [94].

Continuing with the present boundary layer analysis, one finds that the required inner solution $g(x, R_s)$ must satisfy the conditions

$$g(0) = g(0)_{\eta\eta} = 0,$$
$$\lim_{\eta\to 0} f^{(0,1)}(\eta, R_s) = \lim_{\xi\to\infty} R_s^{-\frac{1}{2}} g(\xi, R_s) \quad \text{as} \quad R_s \to \infty.$$

By solving the resulting boundary layer equations at successive orders, it is found that the $g(x, R_s)$ is given by

$$g = \xi - \frac{\pi^3}{R_s}\left(\frac{\xi^3}{6} + \xi\right) + \ldots \quad (2.58)$$

As one might have anticipated from (2.56), the nontrivial form of $f^{(0,1)}$ does not simplify the higher order equations for $f^{(n,1)}$. However, despite the added level of

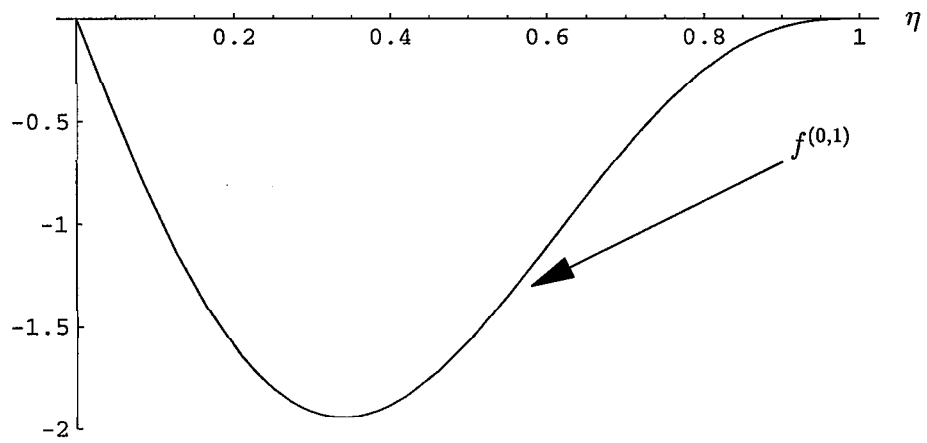


Fig. 2.7: A comparison of Yuan's solution for $f^{(0,1)}$ with the Fourier series representation (6 terms). Both solutions are indistinguishable on the scale of this plot.

difficulty, it is possible to infer something about the Fourier series of $f^{(n,1)}$, namely that all the terms are proportional to $\sin 2m\pi\eta$, with the exception of one term which is proportional to $\sin \pi\eta$. This implies that $f^{(n,1)}$ is composed of a homogeneous solution which has period 2 in η-space, and an inhomogeneous term which has period 1. To prove this latter claim, we start by noting that equation (2.56) is not a unique representation of $f^{(0,1)}$. Returning to (2.55), we observe that it is possible to seek a solution in the form of a Fourier series. Accordingly, $f^{(0,1)}$ is expressed in the form

$$f^{(0,1)} = \sum_{m=1}^{\infty} a_m^0 \sin m\pi\eta.$$

Substituting the latter series into (2.55) gives the equation

$$-2\pi \sin \pi\eta = \sum_{m=1}^{\infty} a_m^0 (m-1)(1-m^2) S_{m+1} - \sum_{m=1}^{\infty} a_m^0 (m+1)(1-m^2) S_{m-1}, \quad (2.59)$$

$$\text{with} \quad S_{m+1} = \sin(m+1)\pi\eta.$$

For $m \geqslant 2$, the above system yields the difference equation

$$a_{m+2}^0 (1-(m+2)^2)(m+3) - a_m^0 (1-m^2)(m-1) = 0, \quad (2.60a)$$

$$\text{with} \quad a_1^0 = \text{ arbitrary} \quad \text{and} \quad a_2^0 = -2\pi, \; a_3^0 = 0; \quad (2.60b)$$

$$\Longrightarrow \quad a_m^0 \sim \frac{\text{constant}}{(m^2-1)^2}. \quad (2.61)$$

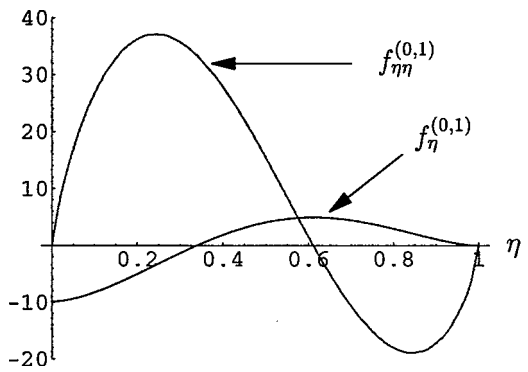


Fig. 2.8: The first and second derivatives of $f^{(0,1)}$ using 20 terms in the Fourier series (2.62), $R_s \gg 1$

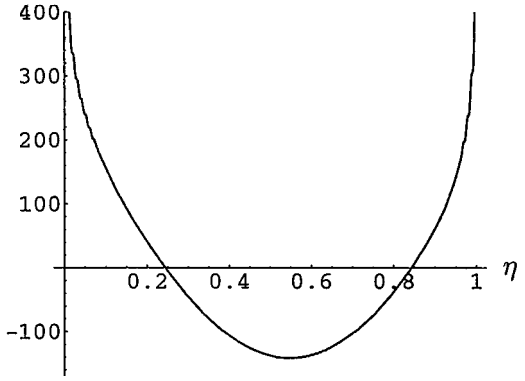


Fig. 2.9: The divergence of $f_{\eta\eta\eta}^{(0,1)}$ near $\eta =$ 0, 1. Here 100 terms are used in Fourier series.

Hence an alternative representation for $f^{(0,1)}$ is

$$f^{(0,1)} = -2\pi \sum_{k=1}^{\infty} \frac{\sin 2k\pi\eta}{(4k^2-1)^2} + a_1^0 \sin \pi\eta, \tag{2.62}$$

$$\text{and} \quad a_1^0 = -4\pi \sum_{k=1}^{\infty} \frac{k}{(4k^2-1)^2} = -\frac{\pi}{2} \sum_{k=1}^{\infty} \left\{ \frac{1}{(2k-1)^2} - \frac{1}{(2k+1)^2} \right\} = -\frac{\pi}{2}. \tag{2.63}$$

By using the comparison test, it is easy to verify that the above series (2.62) and its first two derivatives are absolutely convergent for all values of η. However, on taking the third derivative, the terms a_m vary like $1/m$; consequently, it is expected that this derivative diverges (as does the third derivative of Yuan's representation). Due to the rapid convergence of series (2.62), only a small number of terms are required (approximately 4) for a numerical comparison with Yuan's representation (2.56). However, when comparing derivatives, the series representation does not converge as fast and therefore more terms are required, see figures 2.8 and 2.9.

Next, it is shown that all the terms in Fourier series of $f^{(n,1)}$ are of the form S_{2m}, apart from one which is of the form S_1 (recall that $S_k = \sin k\pi\eta$). By proceeding in the same way as before, $f^{(n,1)}$ is expanded in the form

$$f^{(n,1)} = \sum_{m=1}^{\infty} a_m^n \sin m\pi\eta.$$

After some rearranging, equation (2.52a) can be rewritten as

$$\sum_{k=1}^{\infty} a_k^n (k^2-1)\Big[S_{k+1}(2n+1-k)+S_{k-1}(2n+1+k)\Big] = -2\pi \sin \pi\eta$$
$$+\frac{(-1)^n}{(2n+1)!}\sum_{k=1}^{\infty} a_k^0 (k^2-1)\Big[S_{k+1}((2n+1)k-1)-S_{k-1}((2n+1)k+1)\Big]$$
$$+\sum_{j=1,n>1}^{n-1}\frac{(-1)^j}{(2j)!}\sum_{k=1}^{\infty} a_k^{n-j}(k^2-1)\Big[(S_{k+1}-S_{k-1})k-\frac{(2(n-j)+1)}{2j+1}(S_{k+1}+S_{k-1})\Big] \tag{2.64}$$

Although equation (2.64) appears intimidating, it is easy to observe that a_1^n is arbitrary because of the (k^2-1) factor in all summations. The coefficient a_1^n corresponds to the homogeneous solution which is proportional to S_1 in all the functions $f^{(n,1)}$. Since this proof relies on the principle of induction, let us start by fixing a value for n, say $n=N$. To help with the proof all the terms corresponding to $f^{(N,1)}$ have been placed on the LHS of (2.64), and all the lower order inhomogeneous terms are on the RHS.

Next, observe that for any given value of k, all the sine terms appearing in the summations of (2.64) are all of the same form i.e. if $k=2m$ then all the summation terms in (2.64) are of the form S_{2m+1}, and if $k=2m+1$ then all the terms are of the form S_{2m}. It is now *assumed* that $a_{2m+1}^n = 0$ for $n<N$ i.e. that all the lower order terms (on the RHS) have a Fourier series consisting purely of the modes S_{2m} (with the exception of S_1).

It is now shown that all the sine terms appearing on the RHS are of the form S_{2m+1}. Since it is assumed that $a_{2m+1}^n = 0$ for $n<N$, it is clear that $a_{2m+1}^0 = a_{2m+1}^{n-j} = 0$ in the summations on the RHS. This means that the summations on the RHS only contribute sine terms of the form S_{2m+1}.

Now, because the terms on the RHS are of the form S_{2m+1}, it follows that this must also be the case on the LHS of (2.64). Hence, in order to suppress the instigation of S_{2m} terms on the LHS, it is necessary to take $a_{2m+1}^N = 0$. Therefore it follows immediately that $f^{(N,1)}$ is comprised purely of S_{2m} terms (this is the induction step). It is now shown that the result is true for $f^{(0,1)}$. In the Fourier expansion of $f^{(0,1)}$

(2.62), it is clearly seen that $a_1^0 \neq 0$, $a_{2m}^0 \neq 0$ and $a_{2m+1}^0 = 0$ (for $m > 0$) i.e that $f^{(0,1)}$ is purely comprised of sine terms of the form S_{2m} and S_1. Therefore, since this rule holds for $f^{(0,1)}$, by the principle of induction it holds for all terms $f^{(n,1)}$.

The difficulty in evaluating $f^{(n,1)}$ is echoed, and probably better understood, in the governing equation of motion (2.33). Here, the equivalent procedure would be to determine Υ in the expansion

$$\Psi(\eta, \theta, R_s) = \pi^{-1} \sin\theta \sin\pi\eta + R_s^{-1}\Upsilon(\eta, \theta) + \ldots$$

The governing equation for $\Upsilon(\eta, \theta)$ is then given by

$$\pi^{-1} \sin\pi\eta \cos\theta \, F_\eta - \sin\theta \cos\pi\eta \, F_\theta = -\pi^3 \sin\theta \sin\pi\eta, \tag{2.65a}$$

$$\Upsilon = \Upsilon_{\eta\eta} = 0 \quad \text{at} \quad \eta = 0 \quad \text{and} \quad \Upsilon = \Upsilon_\eta = 0 \quad \text{at} \quad \eta = 1, \tag{2.65b}$$

$$\text{with} \quad F = \Upsilon_{\eta\eta} + \pi^2 \Upsilon.$$

By using quasi-linear PDE theory the general solution for F can be expressed in the form

$$F = \pi^3 i \left[\int \frac{A}{\sqrt{A^2 - \sin^2\theta}} \, \mathrm{d}\theta \right] + H(\sin\theta \sin\pi\eta). \tag{2.66}$$

Here $A = \sin\theta \sin\pi\eta$, H is an arbitrary function and $i = \sqrt{-1}$. The value A is held fixed for the integration and thereafter it is replaced with its functional representation in terms of θ and η. The arbitrary function H is determined from the boundary conditions once a representation for the general solution of $\Upsilon(\eta, \theta)$ is obtained. However, in order to evaluate the general solution for Υ, it is necessary to find a particular solution that corresponds to the elliptic integral in (2.66). The evaluation of the aforementioned particular integral is nontrivial and for this reason it is impossible to proceed analytically.

Asymmetric Solutions

The existence of a steady asymmetric state is readily anticipated from the studies of WBZD [97] and H. & P. [37], see figure 2.6. To avoid the tedious approach of solving

the series equation (2.37), the asymptotic solution presented in this section is derived directly from the equation of motion (2.33). It is a simple matter verify the consistency of both approaches i.e. eliminate the possibility of eigen/complimentary solutions in the series equation approach.

By proceeding in a similar way to WBZD, the outer solution is expanded in inverse powers of $R_s^{\frac{1}{2}}$ and a logarithmic dependence is included at $O(R_s \ln R_s)$. Accordingly, the core region expansion is written in the form

$$\Psi(\eta,\theta,R_s) = \sin\theta \left\{ \chi^{(0)}(\eta) + R_s^{-\frac{1}{2}}\chi^{(1)}(\eta) + R_s^{-1}\ln R_s\, \chi^{(2)}(\eta) \right\} + R_s^{-1}\chi^{(3)}(\eta,\theta) + \ldots \tag{2.67}$$

Here Ψ obeys the inviscid boundary conditions

$$\Psi(\eta = \mp 1) = 0. \tag{2.68}$$

To satisfy the remaining conditions at $\eta = \mp 1$, it is necessary to reintroduce the effects of viscosity within a boundary layer of thickness $R_s^{-\frac{1}{2}}$ at each wall. The required boundary layer solution at $\eta = -1$ is obtained by writing

$$\Psi(\eta,\theta) = R_s^{-\frac{1}{2}} g^-(\xi,\theta) \quad \text{with} \quad \xi = (1+\eta)R_s^{\frac{1}{2}}, \tag{2.69a}$$

$$g^-(\xi,\theta) = g_0^-(\xi)\sin\theta + R_s^{-1}g_1^- + R_s^{-2}\ln R_s\, g_2^- + R_s^{-2}g_3^- + \ldots, \tag{2.69b}$$

$$\text{and} \quad g^- = 0,\ g_\xi^- = -\sin\theta \quad \text{at} \quad \xi = 0, \tag{2.69c}$$

$$\text{with} \quad \lim_{\eta\to -1}\Psi(\eta,\theta,R_s) = \lim_{\xi\to\infty} R_s^{-\frac{1}{2}} g^-(\xi,\theta,R_s) \quad \text{as} \quad R_s \to \infty. \tag{2.69d}$$

Similarly, the required expansion at $\eta = +1$ is given by

$$\Psi(\eta,\theta) = R_s^{-\frac{1}{2}} g^+(x,\theta) \quad \text{with} \quad x = (1-\eta)R_s^{\frac{1}{2}}, \tag{2.70a}$$

$$g^+(x,\theta) = g_0^+(x)\sin\theta + R_s^{-1}g_1^+ + R_s^{-2}\ln R_s\, g_2^+ + R_s^{-2}g_3^+ + \ldots, \tag{2.70b}$$

$$\text{and} \quad g^+ = 0,\ g_x^+ = \sin\theta \quad \text{at} \quad x = 0, \tag{2.70c}$$

$$\text{with} \quad \lim_{\eta\to +1}\Psi(\eta,\theta,R_s) = \lim_{x\to\infty} R_s^{-\frac{1}{2}} g^+(x,\theta,R_s) \quad \text{as} \quad R_s \to \infty. \tag{2.70d}$$

At leading order it is found that

$$\chi^{(0)} = -2\pi^{-1}\cos\tfrac{1}{2}\pi\eta, \tag{2.71}$$

$$g_0^- = -\xi, \tag{2.72}$$

$$g_0^{+\prime\prime\prime} - g_0^+ g_0^{+\prime\prime} + g_0^{+\prime 2} = 1, \tag{2.73a}$$

$$\text{with} \quad g_0^+ = 0,\ g_0^{+\prime} = 1,\ x = 0 \quad \text{and} \quad g_0^{+\prime} \to -1 \quad \text{as} \quad x \to \infty. \tag{2.73b}$$

The above equation for $g_0^+(x)$ has been integrated numerically by WBZD and from this calculation it is known that

$$g_0^+(x) \simeq -x + \delta \quad \text{as} \quad x \to \infty, \quad \text{with} \quad \delta \simeq 1.96612. \tag{2.74}$$

By continuing with the matching procedure, one finds that the higher order terms in core region expansion (2.67) are given by

$$\chi^{(1)} = \tfrac{1}{2}\delta\sin\tfrac{1}{2}\pi\eta + \delta\pi^{-1}(\tfrac{1}{2}\pi\eta\sin\tfrac{1}{2}\pi\eta + \cos\tfrac{1}{2}\pi\eta), \tag{2.75}$$

$$\chi^{(2)} = A\sin\tfrac{1}{2}\pi\eta + B(\tfrac{1}{2}\pi\eta\sin\tfrac{1}{2}\pi\eta + \cos\tfrac{1}{2}\pi\eta), \tag{2.76}$$

with

$$g_1^+ = g_1^- = g_2^- = 0. \tag{2.77}$$

Note that $\chi^{(2)}$ is an eigensolution to the governing equations for $\chi^{(1)}$. The constants A and B are used to match the outer solution to the inner expansion. In order to satisfy the matching condition for $\chi^{(2)}$, it is found that A and B must satisfy the relation $A + \frac{1}{2}\pi B + \frac{1}{4}\pi = 0$. Since g_0^+ is only known numerically, it is necessary to determine g_2^+ in the same way. However, the correction term g_2^+ is of limited use to our investigation because we are primarily concerned with the unsteady regime, that bifurcates from the steady asymmetric state at a moderate Reynolds number $R_s \approx 54$. For this reason the matching procedure is not pursued any further.

Next, by writing the core flow solution in a θ-series, we may express $\Psi^{(n)}$ as

$$\Psi^{(n)} = \frac{(-1)^n}{R_s^{\frac{1}{2}}(2n+1)!}\Big\{ -2R_s^{\frac{1}{2}}\pi^{-1}\cos\tfrac{1}{2}\pi\eta + \tfrac{1}{2}\delta\sin\tfrac{1}{2}\pi\eta + \delta\pi^{-1}(\tfrac{1}{2}\pi\eta\sin\tfrac{1}{2}\pi\eta + \cos\tfrac{1}{2}\pi\eta) + O(R_s^{-\frac{1}{2}}\ln R_s)\Big\}. \tag{2.78}$$

It is interesting to note that two decaying solutions also exist for the unsteady problem. In the inviscid core region these solutions can be written as

$$\Psi(\eta,\theta,\tau) \sim \begin{cases} \sin\theta \sin\pi\eta\, e^{-\pi^2\tau/R_s} + O(R^{-1}), \\ \sin\theta \cos\tfrac{1}{2}\pi\eta\, e^{-\pi^2\tau/R_s} + O(R^{-\frac{1}{2}}). \end{cases}$$

The no-slip conditions at the walls are satisfied by the boundary layer solutions and in this case, these boundary layer solutions have to be computed numerically. However, since the core flow is driven to rest in both of the profiles above, it is unlikely that solutions of this type are physically relevant to the present study.

In the next section, the full unsteady series equations (2.37) are solved numerically. The solutions obtained from this calculation are then compared with the asymptotic results derived above. For sufficiently large values of R_s, it is found that the velocity profiles associated with the functions $\Psi^{(n)}$ begin to diverge i.e. grow without bound during time marching; consequently, a linear stability analysis is formulated in the section thereafter.

2.4 Numerical Work

In the numerical scheme that is used to solve (2.37), the η-range $(-1,1)$ is partitioned into I intervals of equal length $\Delta\eta = 2/I$. Next, the governing series equation (2.37a), is discretized by using a central difference scheme that is $O(\Delta\eta^2 + \Delta\tau^2)$ accurate. The terms on the RHS of (2.37a) are treated explicitly at each timestep and the standard Crank-Nicholson method is applied to the viscous term $\Psi^{(n)}_{\eta\eta\eta\eta}$. The discretized boundary conditions are then used to eliminate the fictitious values of $\Psi^{(n)}$ outside η-domain $(-1,1)$. By following this procedure, each term $\Psi^{(n)}$ is then determined by the inversion of a penta-diagonal matrix A. Additionally, it should be noted that matrix A is symmetric with constant coefficients. To compute the terms $\Psi^{(n)}$, the matrix A is inverted at each timestep by using its LU factorisation.

$$\mathsf{A}\boldsymbol{x} = \begin{pmatrix} (c_0+c_2) & c_1 & c_2 & 0 & \cdots & 0 \\ c_1 & c_0 & c_1 & c_2 & 0 & \cdots & 0 \\ c_2 & c_1 & c_0 & c_1 & c_2 & 0 & \cdots & 0 \\ 0 & c_2 & c_1 & c_0 & c_1 & c_2 & 0 & \cdots & 0 \\ 0 & 0 & c_2 & c_1 & c_0 & c_1 & c_2 & 0 & \cdots & 0 \\ \cdots & \cdots & \cdots & \cdots & \cdots & \cdots & \cdots & \cdots & \cdots & \cdots \\ 0 & \cdots & \cdots & \cdots & 0 & c_2 & c_1 & (c_0+c_2) \end{pmatrix} \begin{pmatrix} \Psi^{(n)}_{-1+\Delta\eta} \\ \Psi^{(n)}_{-1+2\Delta\eta} \\ \vdots \\ \vdots \\ \Psi^{(n)}_{+1-2\Delta\eta} \\ \Psi^{(n)}_{+1-\Delta\eta} \end{pmatrix}$$

Here $c_0 = -3/R\Delta\eta^4 - 2/\Delta\tau\Delta\eta^2$, $c_1 = 2/R\Delta\eta^4 + 1/\Delta\tau\Delta\eta^2$ and $c_2 = -1/2R\Delta\eta^4$. It is important to note that matrix A is not positive definite (this can be verified by evaluating $\boldsymbol{x}\,\mathsf{A}\,\boldsymbol{x}^{\mathrm{T}}$ with $\boldsymbol{x} = \{1, 1, \ldots, 1\}$), and neither is it diagonally dominant; therefore, a stable inversion of this matrix is not guaranteed. However, by experimenting with different sizes of: R_s, $\Delta\eta$ and $\Delta\tau$, we have found that a Cholesky factorisation of the matrix $-\mathsf{A}$ can always be obtained. Despite this fact, since we cannot prove that a Cholesky factorisation is possible for all values of $\{R_s,\ \Delta\eta,\ \Delta\tau\}$, the LU factorisation method was used instead.

For each numerical run, the flow is allowed to develop from an initial condition of zero-flow; moreover, it is found that the mesh settings $\Delta\eta = 2/800$ and $\Delta\tau = 10^{-3}$ are sufficient for these calculations. Note, that having the θ-dependence removed in the series equations, has the effect of simplifying the computational task significantly. However, in exchange for this convenience, it is necessary that the series solution (2.34) converges quickly near $\theta \approx \pi$.

In addition to the above calculation for the terms $\Psi^{(n)}$, the equation of motion (2.33) is solved directly so that a comparison of results is possible. In this direct approach, the nonlinear terms are treated explicitly and a pseudospectral (PS) method is employed to allow for the periodicity in the θ-direction. To approximate the value of Ψ_θ, the Fourier transform of $\Psi(\theta, \eta, \tau)$, denoted by $\widehat{\Psi}(k, \eta, \tau)$, is calculated and then the inverse transform of $ik\widehat{\Psi}$ is taken (see below).

$$\widehat{\Psi}(k,\eta,\tau) = \int_{-\infty}^{\infty} \Psi e^{-ik\theta}\,\mathrm{d}\theta \quad \Longrightarrow \quad \Psi_\theta(\theta,\eta,\tau) = \frac{1}{2\pi}\int_{-\infty}^{\infty} \widehat{\Psi} ike^{ik\theta}\,\mathrm{d}k.$$

By calculating Ψ_θ in this manner, the rate of convergence (of the approximation) is far superior to any finite difference (FD) scheme i.e. the error decreases faster than $O(1/I^p)$ for any integer power p (here I denotes the total number of grid points in the scheme). Moreover, since Ψ_θ is calculated in a global manner, the use of upwind differencing (UWD) is avoided.

To formulate the problem using UWD, it would be necessary to calculate Ψ_θ by choosing an "appropriate" one-sided FD formula at each station $\theta = j\Delta\theta$. A left-sided FD formula is chosen if the flow is moving to the right and the a right-sided formula is used otherwise. In this way, the upwinding scheme "improves" the numerical description of the flow by controlling the direction in which transportation errors are allowed to propagate, see [60] §19.1. As before, the Crank-Nicholson method is applied to the viscous term $\Psi_{\eta\eta\eta\eta}$, and thus the governing matrix is once again given by A. Hence, the value of Ψ at the next timestep is determined as follows:

1. The θ-derivative Ψ_θ is calculated pseudospectrally over the rectangular domain $[0 \leqslant \theta < 2\pi,\ -1 < \eta < 1]$.

2. For a fixed value of $\theta = j\Delta\theta$, the nonlinear terms are stored in the vector $\boldsymbol{x}$.

3. The value of $\Psi(\theta = j\Delta\theta)$ at the next timestep is found by evaluating $\mathrm{A}^{-1}\boldsymbol{x}$.

4. The value of j is increased and steps 2. and 3. are repeated until the entire θ-domain is passed, thus yielding a complete solution for Ψ at the next time step.

In this manner, the numerical solution is time marched until a converged result is obtained. The mesh settings used in this calculation are $\Delta\tau = 5 \times 10^{-3}$, $\Delta\eta = 2/100$ and $\Delta\theta = 2\pi/256$.

In the next section, the numerical solutions of the series equations are presented. The solutions of the equation of motion (2.33) (calculated by the PS method) are presented in the section thereafter.

R_s	$\Delta\tau$
$0 < R_s < 300$	1.0×10^{-3}
$300 < R_s < 1600$	6.0×10^{-4}
$R_s = 1650$	5.0×10^{-4}
$R_s = 1670$	1.0×10^{-5}
$R_s = 1700$	$> 1.0 \times 10^{-7}$

Table 2.3: The size of the timestep required to calculate $\Psi^{(0)}$. In these calculations, the size of $\Delta\eta$ is 1/100.

2.4.1 Numerical Results

Since the solution for $\Psi^{(0)}$ plays a pivotal role in the series solution (in that it forces the higher order terms in the expansion), this section begins with a review of the different solutions of $\Psi^{(0)}$ at various Reynolds numbers.

By forcing the symmetric solution, it is found that $\Psi^{(0)}$ is steady up to $R_s \approx 170$, see figure 2.11, after which the solution becomes periodic in time. In this symmetric regime, the time period of $\Psi^{(0)}$ increases linearly with Reynolds number, see figure 2.10. In the range $R_s = 170$ to $R_s \approx 250$, the periodic solution is in essence a modulated continuation of steady one which is proportional to $\sin \pi\eta$. In contrast, at $R_s \approx 300$, the periodic solution of $\Psi^{(0)}$ is modulated through profiles that are proportional to $\sin 2\pi\eta$ and $\sin \pi\eta$, see figures 2.13, 2.14 and c.f. equation (2.46). In the latter diagrams, τ_p is used to denote the evolution of time through one time period of the solution i.e. if T is the time period of the solution, then τ_p varies from zero to T. As R_s is further increased above $R_s = 300$, the proportionality to $\sin \pi\eta$ begins to fade out, and at $R_s = 1600$ the $\sin 2\pi\eta$ profile is dominant, see figure 2.12. Further time marching above $R_s = 1700$ requires an exceptionally small timestep, see table 2.3. Therefore, the numerical procedure is no longer efficient above the threshold value $R_s = 1700$.

The asymmetric solution of $\Psi^{(0)}$ emerges from a symmetry breaking bifurcation at $R_s = 17.3$. This asymmetric solution remains steady up until $R_s = 53.8$, see figure 2.15, after which it becomes periodic in time. Upon further increasing R_s, the solution

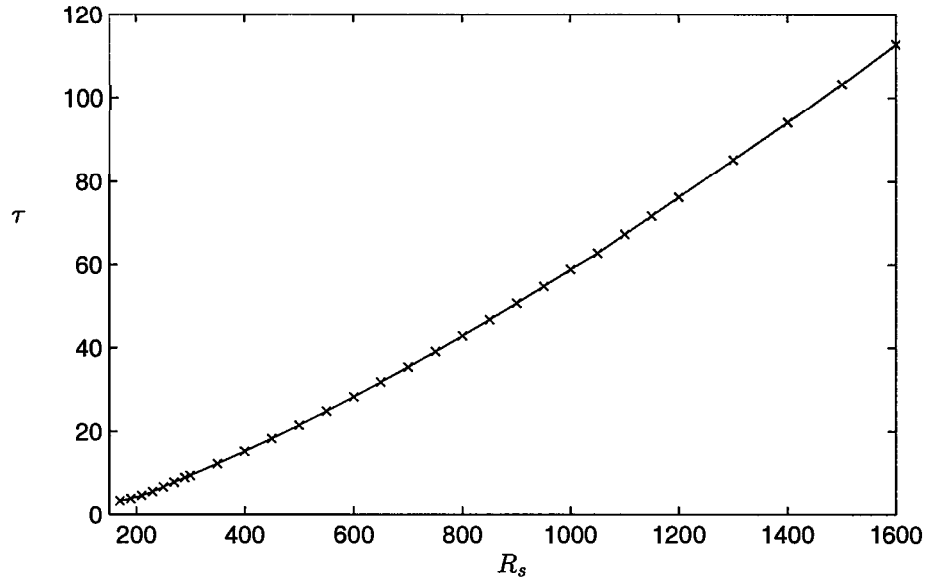


Fig. 2.10: The time period of the symmetric solution of $\Psi^{(0)}$.

begins to period-double in progressively smaller intervals of Reynolds number. This period-doubling cascade has been identified previously by H. & P. [37], and due to the appearance of self similar structures at $R_s \gtrsim 82$, see figure 2.17, it is concluded that the resulting flow is chaotic. In their study, H. & P. did not carry out an exhaustive search for laminar subwindows above $R_s = 82$. It is interesting to note that some laminar configurations do exist for $R_s > 82$ and a brief summary of these regimes is now given.

At $R_s = 86$, the presence of three distinct points in the Poincaré cross-section diagram, see figure 2.18 (a), indicates that the solution is quasi-periodic. However, a very surprising substructure is revealed when the region near $\mathcal{A}$ is enlarged, see figures 2.18 (b)-(d). In diagram (b), it is seen that the points are distributed on a straight line; moreover, one should note that this line develops on a scale that is larger than the scale associated with the numerical error, which is $O(\Delta\eta^2 + \Delta\tau^2)$. Further enlargements near $\mathcal{A}$ reveal a self-similar relation, but these self-similar structures develop on a scale that is smaller than the numerical error; therefore, one cannot justify a claim that this flow is chaotic. Since the lines/clusters shown in diagram (d) occur within the scope

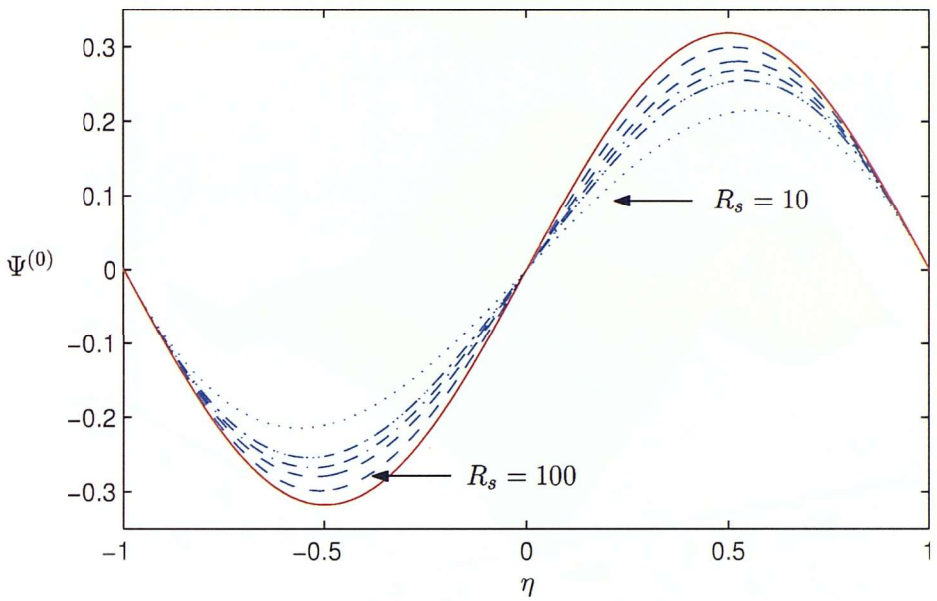


Fig. 2.11: The symmetric solution of $\Psi^{(0)}$ at $R_s = 10, 20, 30, 40, 50, 100$. The solid line indicates the large R_s asymptotic solution $\pi^{-1} \sin \pi\eta$. This symmetric solution of $\Psi^{(0)}$ becomes unsteady and periodic at $R_s \approx 170.0$.

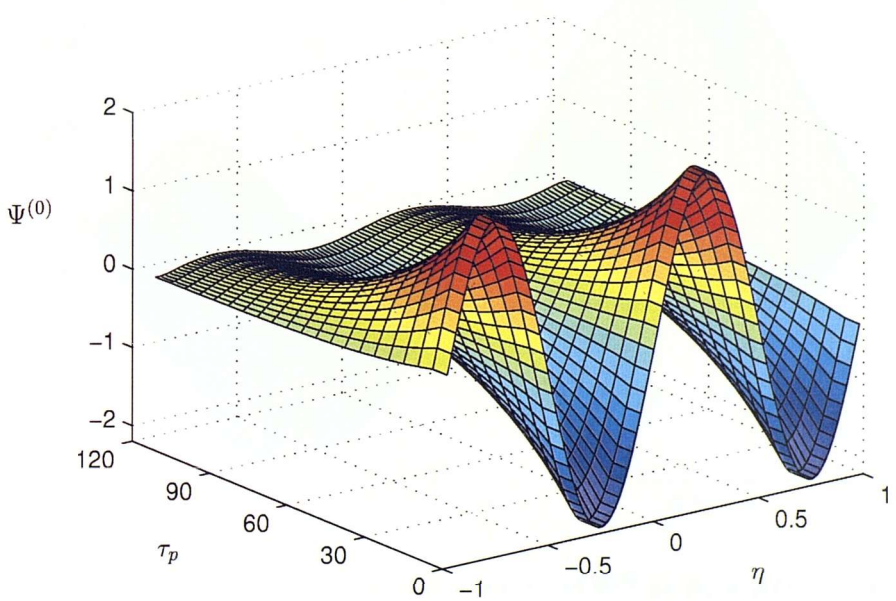


Fig. 2.12: The symmetric periodic solution of $\Psi^{(0)}$ at $R_s = 1600$. Observe the proportionality of this solution to $\sin 2\pi\eta$, and the requirement of a boundary layer at $\eta = \mp 1$ to obey the derivative boundary conditions (2.37d,e).

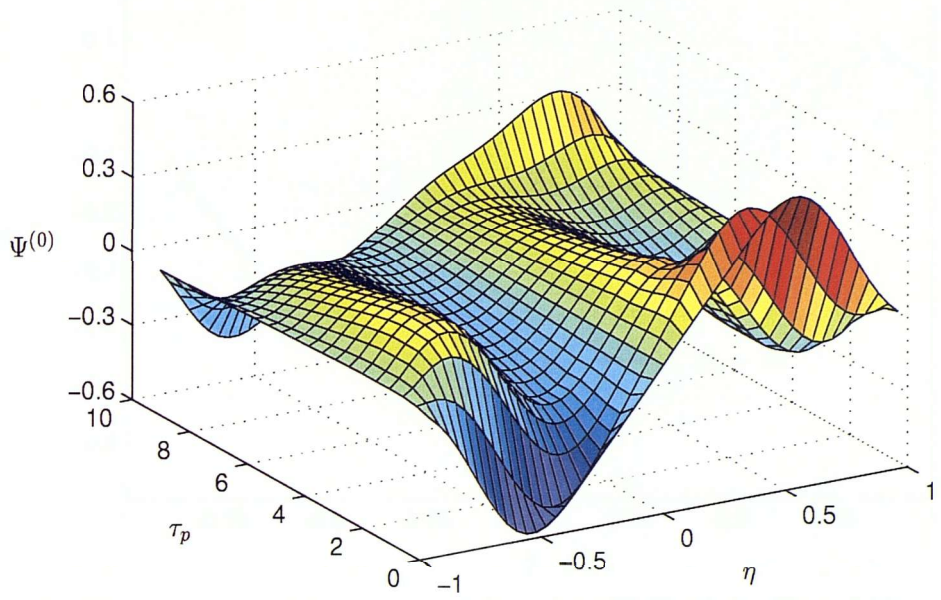


Fig. 2.13: The symmetric time periodic solution of $\Psi^{(0)}$ at $R_s = 300$, 3D view.

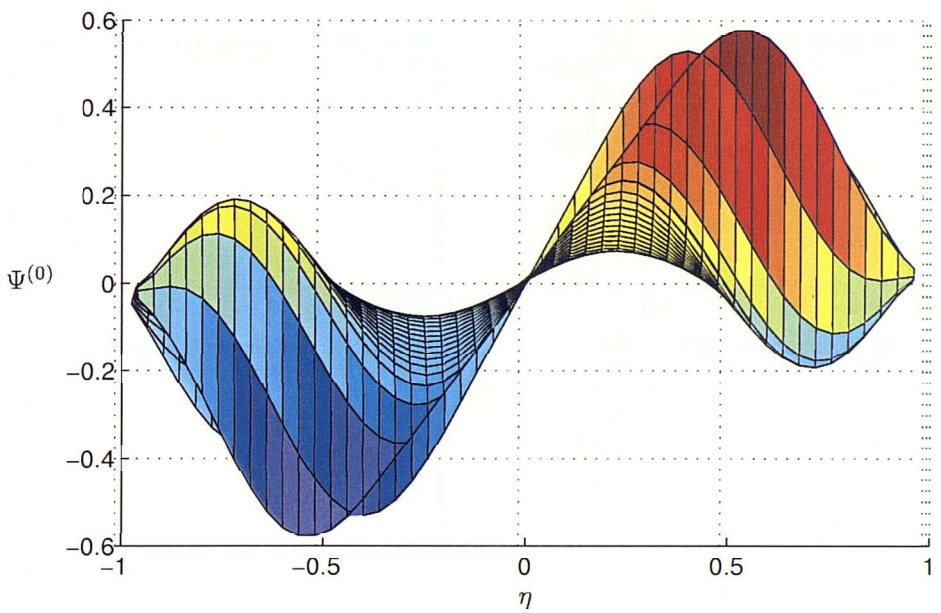


Fig. 2.14: The symmetric time periodic solution of $\Psi^{(0)}$ at $R_s = 300$, 2D view. Observe the modulation of this solution through profiles that are proportional to $\sin 2\pi\eta$ and $\sin \pi\eta$. As in figure 2.12, there are boundary layers present near $\eta = \mp 1$ (associated with the $\sin 2\pi\eta$ variation in η).

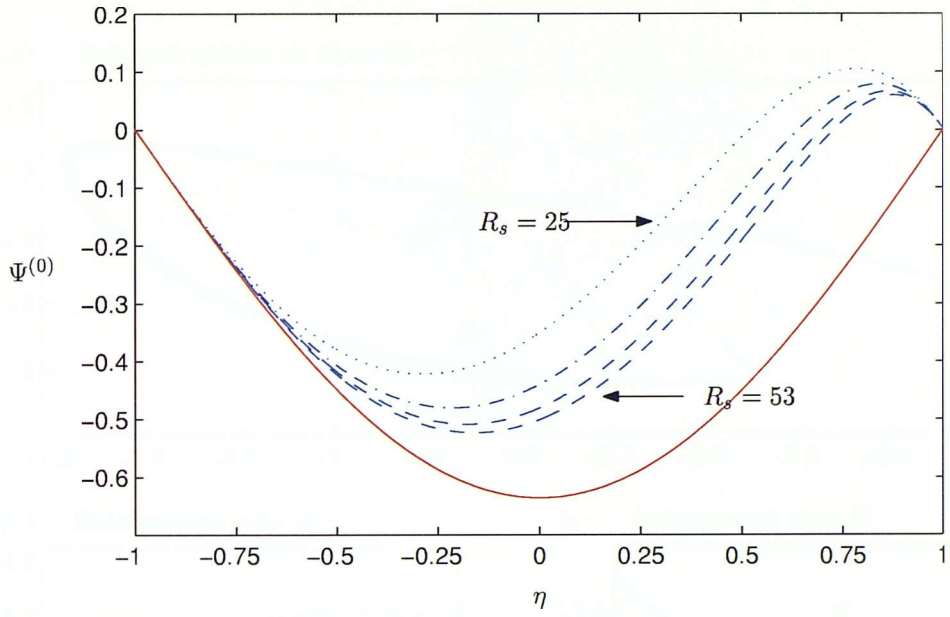


Fig. 2.15: The asymmetric steady state of $\Psi^{(0)}$ at $R_s = 25, 35, 45, 53$. The solid line indicates the leading order asymptotic solution for large R_s. This asymmetric solution becomes unsteady at $R_s \approx 54$ and chaotic at $R_s \approx 82$.

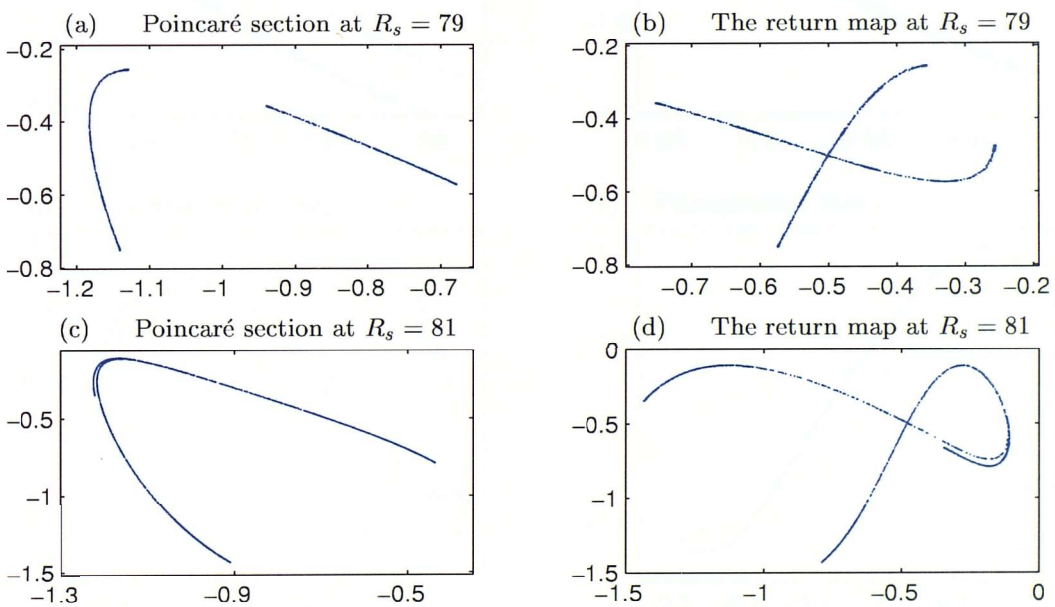


Fig. 2.16: The asymmetric regime of $\Psi^{(0)}$: (a) & (c) – The Poincaré cross sections of $\Psi^{(0)}$ at $R_s = 79,\ 81$. (b) & (d) – The associated first return maps. The coordinate variables $x_1(\tau)$, $x_2(\tau)$, $x_3(\tau)$ are given by $\Psi^{(0)}_{\eta}(\eta = 0.4)$, $\Psi^{(0)}_{\eta\eta}(\eta = 0.3)$ and $\Psi^{(0)}(\eta = -0.5)$. The Poincaré sections are taken in the plane $\dot{x}_3 = 0$.

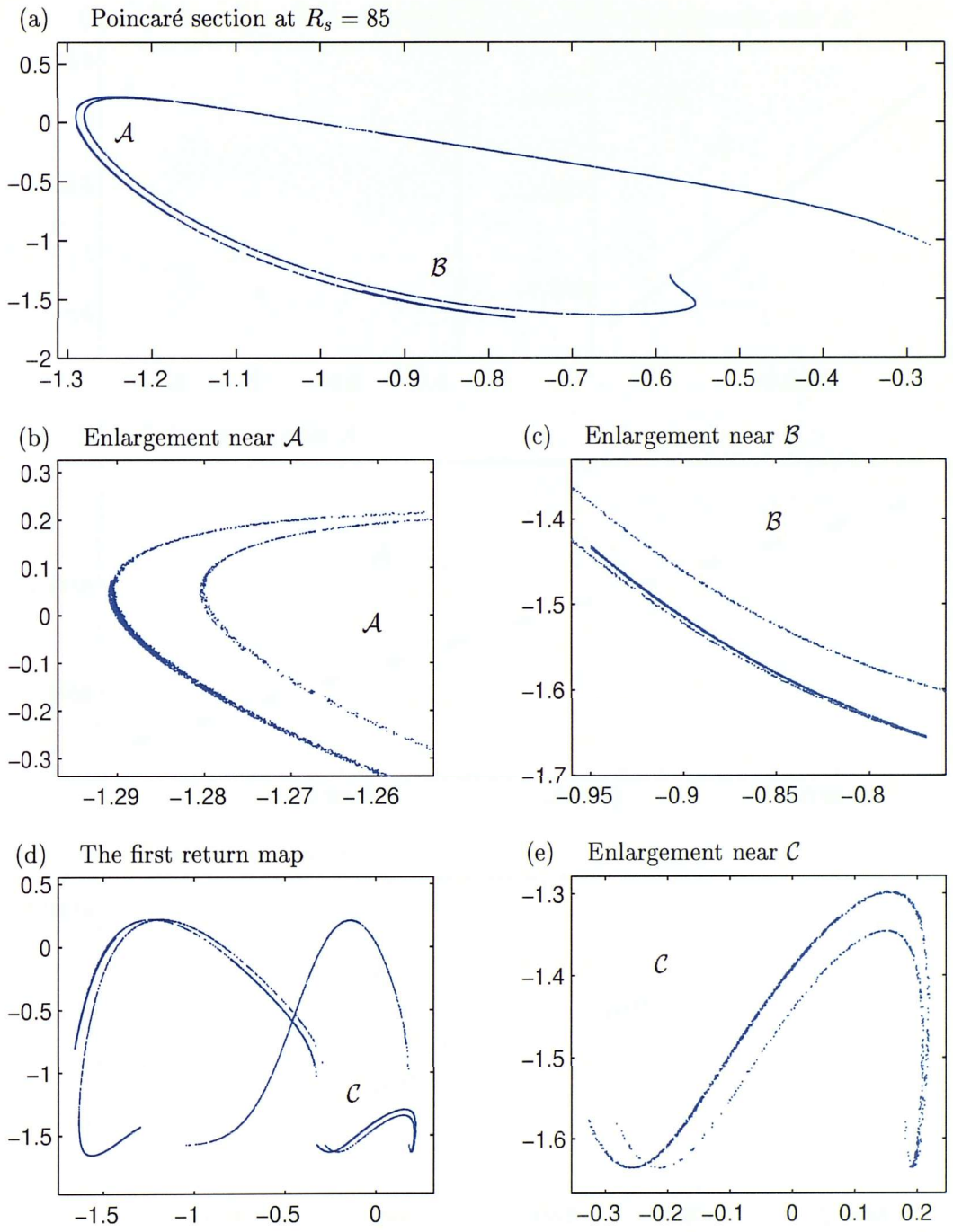


Fig. 2.17: The asymmetric regime of $\Psi^{(0)}$: (a) – The Poincaré cross section of $\Psi^{(0)}$ at $R_s = 85$. (b) & (c) – Enlargements near $\mathcal{A}$ and $\mathcal{B}$. (d) – The first return map using the $x_2(\tau)$ variable. (e) – An enlargement near $\mathcal{C}$.

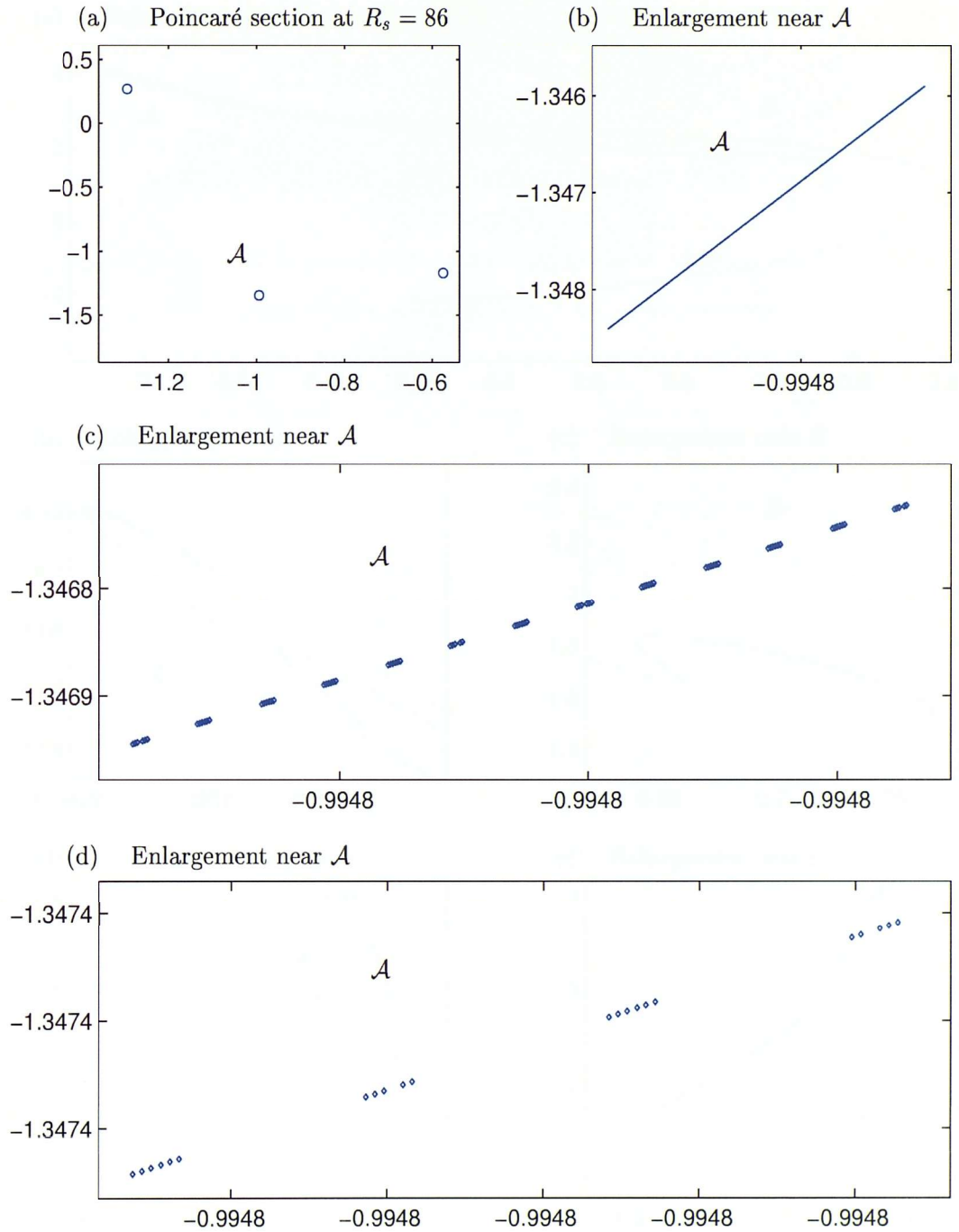


Fig. 2.18: The asymmetric regime of $\Psi^{(0)}$: (a)–(d) The successive enlargements of the Poincaré cross section at $R_s = 86$. The tick steps along the x-axis for (b), (c), and (d) are 2×10^{-4}, 3×10^{-6} and 5×10^{-7} respectively.

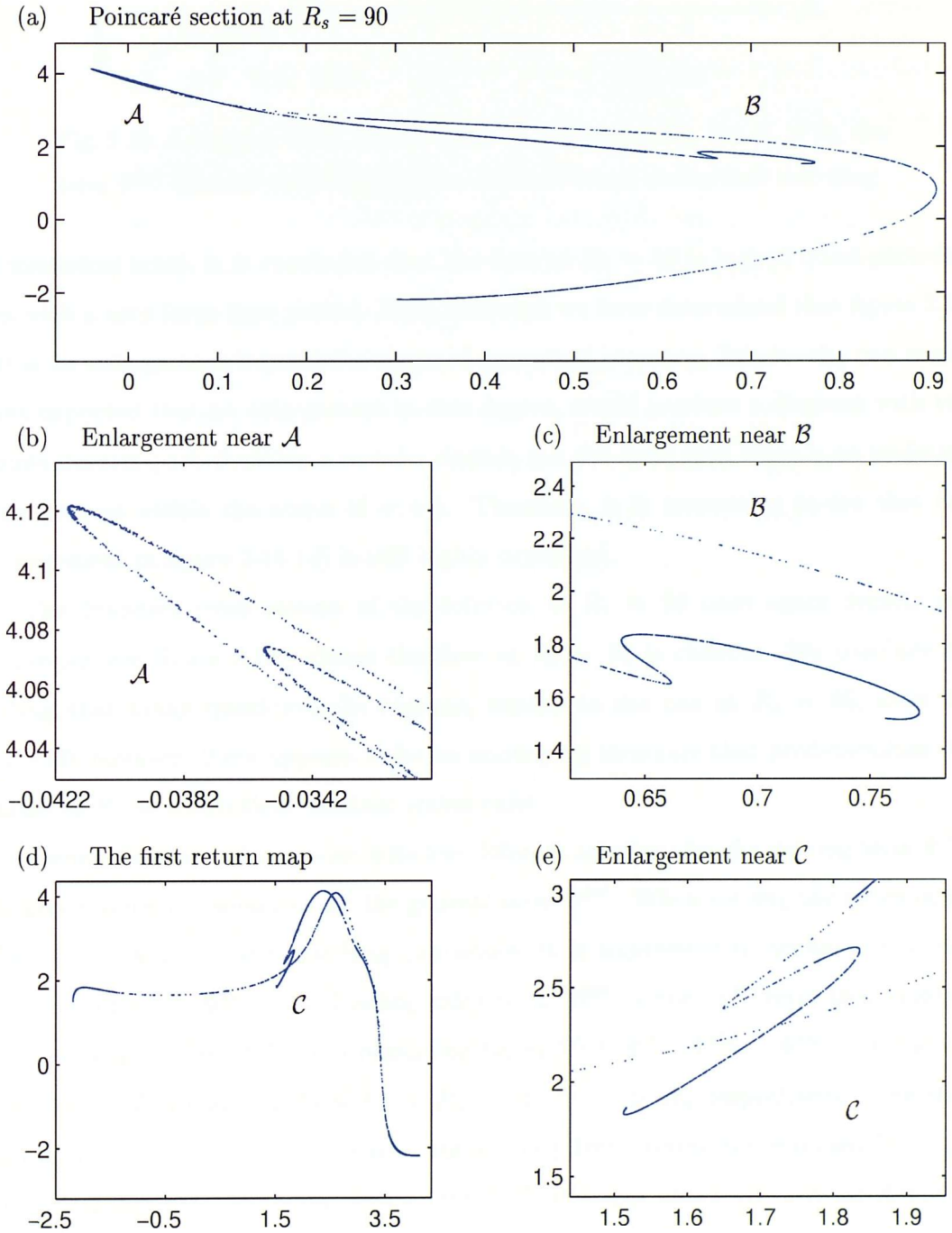


Fig. 2.19: The asymmetric regime of $\Psi^{(0)}$: (a) – The Poincaré cross section of $\Psi^{(0)}$ at $R_s = 90$. (b) & (c) – Enlargements near $\mathcal{A}$ and $\mathcal{B}$. (d) – The first return map. (e) – An enlargement of return map near $\mathcal{C}$.

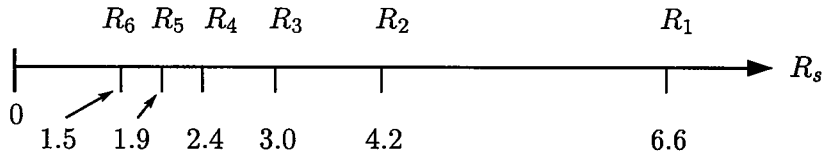


Fig. 2.20: A diagram of the critical values R_n (approximate). For $R_s > R_n$ the term $\Psi^{(n)}$ becomes unstable and grows without bound during time marching.

of numerical error, it is concluded that the flow at $R_s = 86$ is indeed quasi-periodic, but with a very large time period. Note, although we have determined that figure 2.18 (d) is an enlargement beyond the scope of numerical accuracy. Intuitively, one might have expected that an enlargement to this degree, would produce a diagram with the points densely packed within a circular domain (on the basis that there is no preferred arrangement within the scope of error). Therefore, it is interesting to see that the arrangement in figure 2.18 (d) is still highly organised.

The Poincaré cross section of the solution at $R_s = 90$ once again depicts self similarity, see figure 2.19. Hence the flow at $R_s = 90$ is chaotic. We conclude by noting that many quasi-periodic regimes, similar to the one at $R_s = 86$, exist for $R_s > 90$; however, there appears to be no underlying structure that predetermines the values of R_s at which these laminar states exist.

Having familiarised ourselves with the different solutions for the driving term $\Psi^{(0)}$, we now discuss the solutions for the general term $\Psi^{(n)}$. When solving the series equations (2.37) with a time marching procedure, it is impossible to obtain a bounded solution for every $\Psi^{(n)}$. The leading order term $\Psi^{(0)}$, is the only term that remains finite over all values of R_s, the remaining terms $\Psi^{(1)}$, $\Psi^{(2)}$, $\Psi^{(3)} \ldots \Psi^{(n)}$, become unbounded at Reynolds numbers $R_1 > R_2 > R_3 > \ldots > R_n$ respectively. Therefore as the Reynolds number is increased, successively fewer terms are obtained from this numerical method. Moreover, every term $\Psi^{(n)}$ diverges above the critical Reynolds number $R_s = R_1 \approx 7.0$, below which, the computable terms are steady and symmetric. Note, since the computable terms $\Psi^{(n)}$ are steady and symmetric, we can see that these solutions are characteristically similar to the symmetric regime of $\Psi^{(0)}$, see table

2.2. For $R_s \lesssim 0.5$, the computable terms are in good agreement with the asymptotic solutions for small R_s (2.43).

The instability described above is unaffected by refinements to the mesh size and the timestep. This implies that the instability does not arise through a lack of precision in the central difference representation. Consequently, one might expect that the instability is due to an unstable inversion of the matrix A, but one can intuitively see that this is unlikely because the same inversion method is used to compute $\Psi^{(0)}$, which is finite at all values of R_s.

To investigate the stability of the inversion process, an arbitrary precision package written by M. Ring [68] was used to compute the solutions for $\Psi^{(n)}$. The MAPP precision package used for this inversion analysis, is available in C/C++ and is capable of 50-256 significant figure precision. [Note, the variables used in MAPP are handled as strings, which are then converted to numerical values when output is desired i.e. there is no 'logical' extension of the double precision data type]. In addition, a partial pivoting scheme was introduced to ensure a stable inversion of matrix A. Moreover, to increase the accuracy of the scheme, the higher order terms were computed via an implicit scheme by writing

$$\mathcal{L}(\Psi^{(n)}) = \sum_{i=1}^{n\geqslant 2} (2i+1)\left[\Psi^{(i)}\Psi^{(n-i)}_{\eta\eta\eta} - \Psi^{(n-i)}_{\eta}\Psi^{(i)}_{\eta\eta}\right],$$

$$\text{with} \quad \mathcal{L} = \partial_{\eta\eta\tau} - \frac{1}{R_s}\partial_{\eta\eta\eta\eta} - (2n+1)\left[\Psi^{(0)}_{\eta\eta\eta} - \Psi^{(0)}_{\eta}\partial_{\eta\eta}\right] - \left[\Psi^{(0)}\partial_{\eta\eta\eta} - \Psi^{(0)}_{\eta\eta}\partial_{\eta}\right].$$

Finally, various scalings were introduced to the numerical scheme to ensure the balance, in magnitude, of any two terms involved in multiplication/division. Unfortunately, despite all the efforts described above, the instabilities did not change. Therefore, having eliminated the numerical inversion as the cause of the instability, we proceed by formulating a linear stability analysis to investigate the possible involvement of growing perturbations; this analysis follows in the next subsection. Let us briefly mention that the linear stability analysis does indeed confirm the presence of growing eigensolutions; consequently, a full discussion involving the direct numerical solution (DNS) of equation (2.33), is postponed until the stability analysis is presented. Thereafter, an

alternative method is used to compute the terms $\Psi^{(n)}$, and then a full comparison is made with the DNS of equation (2.33).

Although a detailed account of the DNS of (2.33) is deferred until §2.4.3, a qualitative summary of the results is now given. When using the PS numerical method to solve the equation of motion, it is found that a continuous solution can only be obtained for $R_s \leqslant 40$. The numerical solutions obtained for $R_s > 40$, are unacceptable because the profiles in the θ-direction are wavy/discontinuous, see figure 2.28. Moreover, these discontinuous profiles are persistent under refinements to the timestep and the mesh size (in each spatial direction). Despite the development of wavy/discontinuous profiles, the bounded solutions obtained in the regime $R_s > 40$ are still η-symmetric and steady. Accordingly, the latter regime is still regarded as a continuation of the symmetric regime associated with $R_s \leqslant 40$.

Upon increasing the Reynolds number above $R_s = 48$, the symmetric solution becomes unbounded. This divergence is caused by two growing η-profiles that are located at $\theta \approx 28°$, $152°$. By forcing the symmetric solution i.e. the rotationally η-symmetric solution, the resulting numerical solution becomes unbounded at $R_s \approx 65$. Again, this divergence is brought about by two growing η-profiles near the same angles as before.

In the next section, the stability of the terms $\Psi^{(n\geqslant 1)}$ is investigated, and consequently it is found that the terms cannot be calculated via time marching. However, since the numerical solutions of (2.33) are steady up to $R_s = 40$, the corresponding steady solutions of $\Psi^{(n\geqslant 1)}$ are computed without time marching i.e. an implicit FD scheme is used to solve the steady form of (2.37). These solutions, together with the ones found by solving (2.33), are then discussed in §2.4.3.

2.4.2 Stability Analysis

The instabilities present in the time marching suggest that for every fixed value of R_s, the formal series (2.34) must be truncated (in order to exclude the unbounded terms). Upon increasing the Reynolds number, this truncation restricts the series expansion to

progressively fewer terms, see figure 2.20. Next, a linear stability analysis is formulated to analyse the stability of each term $\Psi^{(n\geqslant 1)}$. Consequently, a critical Reynolds number R_n is obtained for each term $\Psi^{(n\geqslant 1)}$ and it is shown that $R_n \to 0$ as $n \to \infty$.

The driving term $\Psi^{(0)}$ is taken as the base flow, upon which, a disturbance with exponential time dependence is imposed. Hence the governing stream function is expanded in the form

$$\Psi(\eta, \theta, \tau) = \theta\, \Psi^{(0)} + \theta^{2n+1}\, \Phi^{(n)}(\eta)\, \exp(\gamma_n \tau). \tag{2.79}$$

Here, γ_n denotes the growth rate associated with the term $\Psi^{(n)}$. Note, since $\Psi^{(0)}$ is not affected by any growing perturbations, it is convenient to continue the use of the time marching procedure to generate this term.

By substituting the above stream function expansion into (2.33), and then taking the limit $\theta \to 0$, the leading order stability equation for $\Psi^{(n)}$ is found to be

$$\gamma_n \Phi^{(n)}_{\eta\eta} = \frac{1}{R_s}\Phi^{(n)}_{\eta\eta\eta\eta} + \Phi^{(n)}_{\eta\eta\eta}\Psi^{(0)} - \Phi^{(n)}_{\eta}\Psi^{(0)}_{\eta\eta} + (2n+1)\left(\Phi^{(n)}\Psi^{(0)}_{\eta\eta\eta} - \Phi^{(n)}_{\eta\eta}\Psi^{(0)}_{\eta}\right), \tag{2.80a}$$

$$\text{with} \quad \Phi^{(n)}(\mp 1) = \Phi^{(n)}_{\eta}(\mp 1) = 0. \tag{2.80b}$$

By evaluating (2.80a) at the boundary $\eta = -1$, it is found that the growth rate γ_n is given by

$$\gamma_n = \frac{1}{R_s}\frac{\Phi^{(n)}_{\eta\eta\eta\eta}(-1)}{\Phi^{(n)}_{\eta\eta}(-1)} + (2n+1). \tag{2.81}$$

Since $\Phi^{(n)}(\eta)$ satisfies a linear equation with homogeneous boundary conditions, the RHS of equation (2.81) can be simplified by rescaling $\Phi^{(n)}(\eta)$ so that $\Phi^{(n)}_{\eta\eta}(-1) = 1$. Hence, the critical Reynolds number R_n, at which $\Psi^{(n)}$ is neutrally stable, is found by substituting $\gamma_n(R_n) = 0$ into (2.81). This substitution gives

$$R_n = -\frac{\Phi^{(n)}_{\eta\eta\eta\eta}(-1)}{2n+1}. \tag{2.82}$$

Note, the implicit assumption that $\mathrm{Im}\{\gamma_n(R_n)\} = 0$, implies that this stability analysis excludes the description of marginal states that are time periodic, however these marginal states *are* considered in this analysis. The stability analysis considered in

this section treats both $\Phi^{(n)}$ and γ_n as complex values; however, it is found that both of these functions are real. Since the latter result is expected from the steady solutions of the equation of motion, see page 82; the analysis presented in this section, is less cumbersome if $\mathrm{Im}\{\gamma_n(R_n)\} = 0$ is assumed from the outset.

Guided by the form of R_n in (2.82), we substitute $\gamma_n = 0$ and $R_s = A_\infty/(2n+1)$ into equation (2.80) and then take limit $n \to \infty$. This gives the following stability equation for the term $\Psi^{(\infty)}$:

$$\Phi^{(\infty)}_{\eta\eta\eta\eta} + A_\infty \left(\Phi^{(\infty)} \Psi^{(0)}_{\eta\eta\eta} - \Phi^{(\infty)}_{\eta\eta} \Psi^{(0)}_{\eta} \right) = 0, \tag{2.83a}$$

$$\text{with} \quad \Phi^{(\infty)}(\mp 1) = \Phi^{(\infty)}_{\eta}(\mp 1) = 0 \quad \text{and} \quad \Psi^{(0)} = \frac{1}{2}\eta(1-\eta^2). \tag{2.83b}$$

Here $\Psi^{(0)}$ is prescribed by its small Reynolds number solution, and A_∞ is an eigenvalue for the above equation. If one can match the numerical results of (2.80) to the large n result in (2.83), then it is clear that the neutral points R_n converge to the limit point $R_s = 0$. From this result, it immediately follows that the series representation (2.34), without truncation, is unbounded at any positive Reynolds number.

As previously mentioned, γ_n and $\Phi^{(n)}$ are treated as complex valued functions in the numerical scheme that is used to solve (2.80). Accordingly, the neutral stability points are defined as the values of R_n at which $\mathrm{Re}\{\gamma_n(R_n)\} = 0$. Although equation (2.80) is a boundary value problem, it is necessary to repose the equation in initial value form, so that a shooting procedure can be used to solve it numerically. In this shooting procedure, the values of $\Phi^{(n)}$, $\Phi^{(n)}_{\eta}$ and $\Phi^{(n)}_{\eta\eta}$ are fixed at $\eta = -1$. Moreover, the parameters γ_n, R_s and $\sigma = \Phi^{(n)}_{\eta\eta\eta}(-1)$ are treated as iteration variables. The iteration variables are then continually updated by Newton's method, until $\Psi^{(n)}$ satisfies the boundary conditions at $\eta = +1$ with zero growth rate. A fourth-order Runge-Kutta scheme is used to integrate $\Psi^{(n)}$ over the η-range, and the update for iteration variables is produced by Newton's method.

In addition to the above calculation, for each fixed value of n, the growth rate is monitored as a function of Reynolds number i.e. the functions $\gamma_n(R_s)$ are determined. The trajectories that are obtained by plotting these functions are called *continuation*

n	R_n
0	17.31
1	6.610
2	4.106
3	2.980
4	2.339

n	R_n
5	1.925
6	1.422
7	1.257
10	1.021
20	0.502

n	R_n
50	2.148×10^{-1}
100	1.081×10^{-1}
400	2.716×10^{-2}
800	1.359×10^{-2}
1400	7.767×10^{-3}

Table 2.4: The neutral stability points R_n for each term $\Psi^{(n)}$.

curves. These curves are computed by using a shooting procedure that is similar to the one used previously, except this time, only γ_n and σ are used as iteration variables.

Solutions of the eigensystem

As expected, the numerical solutions of the eigensystem (2.80) are always found to be real. Moreover, from the numerical calculations it is found that the computed values of R_n, are in excellent agreement with the values of R_s at which the time marching procedure becomes unstable, see table 2.4 c.f. figure 2.20. In figure 2.21 the neutral points R_n are plotted against the term number n. From this log-log plot it can be seen that the slope of the line is -1; this result concurs with the asymptotic form $R_n \sim A_\infty/(2n+1)$, and from this graph an estimated value of 21.7628 is obtained for A_∞. By solving (2.83) the actual value of A_∞ is found to be 21.7602, which is in excellent agreement with the latter extrapolated approximation. Therefore, it is concluded that the neutral points converge to the limit point $R_s = 0$ as n becomes large. In view of this result, it is clear that if a time marching procedure is used to compute the terms $\Psi^{(n)}$, then it is necessary, in order to obtain a bounded solution, to restrict the expansion to successively fewer terms as R_s is increased. Consequently, as R_s is increased, the series solution is valid over a progressively smaller θ-range (due to the loss of terms as R_s is increased).

For each n, the growth rate is computed as a function of R_s, see figure 2.22. Once these continuation curves pass through $R_s = R_n$ they become very difficult to follow.

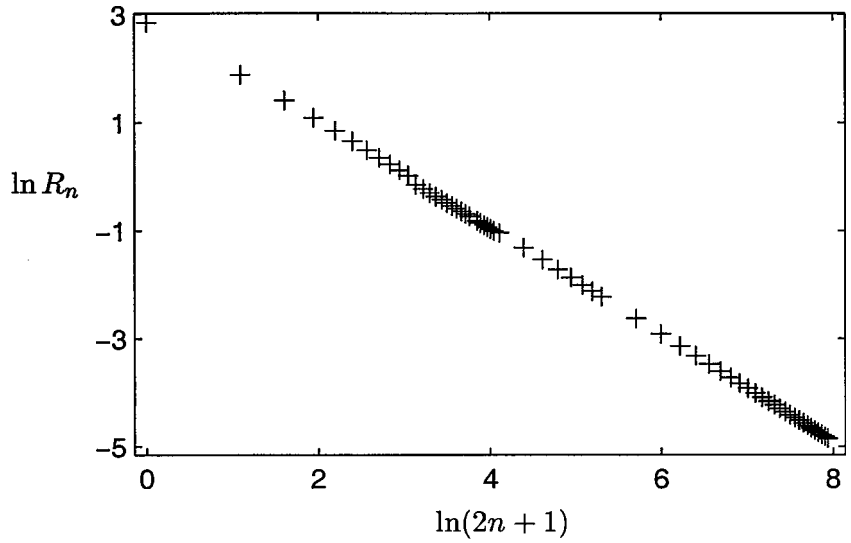


Fig. 2.21: Neutral points for growth rates $\gamma_n(R_n)$. A tail end extrapolation of this line gives $\lim_{n\to\infty} R_n(2n+1) = A_\infty = e^{3.0802}$. Note further that the line of best fit has a slope of -1.0.

For $R_s > R_n$, it is necessary to increment R_s in small amounts, in order to avoid a discontinuous jump from the 'original' continuation curve. If the increment in R_s is too large, the numerical scheme then locks onto another branch of the growth rate γ_n. In fact, a discontinuity also occurs if the initial guess for γ_n is not close enough to the next result, for this reason, the previous converged result is used as an initial guess for γ_n at the next incremented value of R_s.

It is thought that the discontinuities in figure 2.22 are due to the merging of multiple roots i.e. for a fixed value of n, there is an intersection of two different branches of γ_n (here it may help to view γ_n as an eigenvalue for the perturbation). Moreover, the numerical updates in the shooting procedure also support the latter view. At the discontinuities, the numerical update scheme projects the values of $\gamma_n(R_s)$ and σ away from the original continuation curve. Fortunately, the update procedure does not fail because the scheme always locates another root with a larger basin of convergence. In view of this, one may expect that the intersection of the multiple branches of γ_n, occurs in manner that is similar to the cases shown in figures 2.24(a), (b).

However, if the two different branches of γ_n only intersect at one point, say $R_s =$

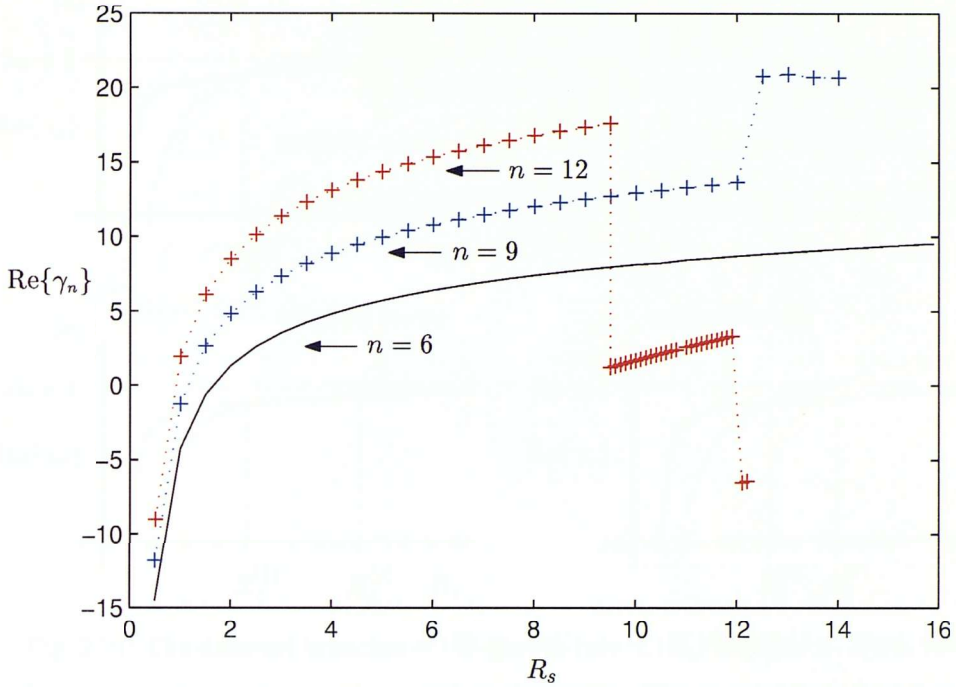


Fig. 2.22: The continuation curves of the growth rates γ_n.

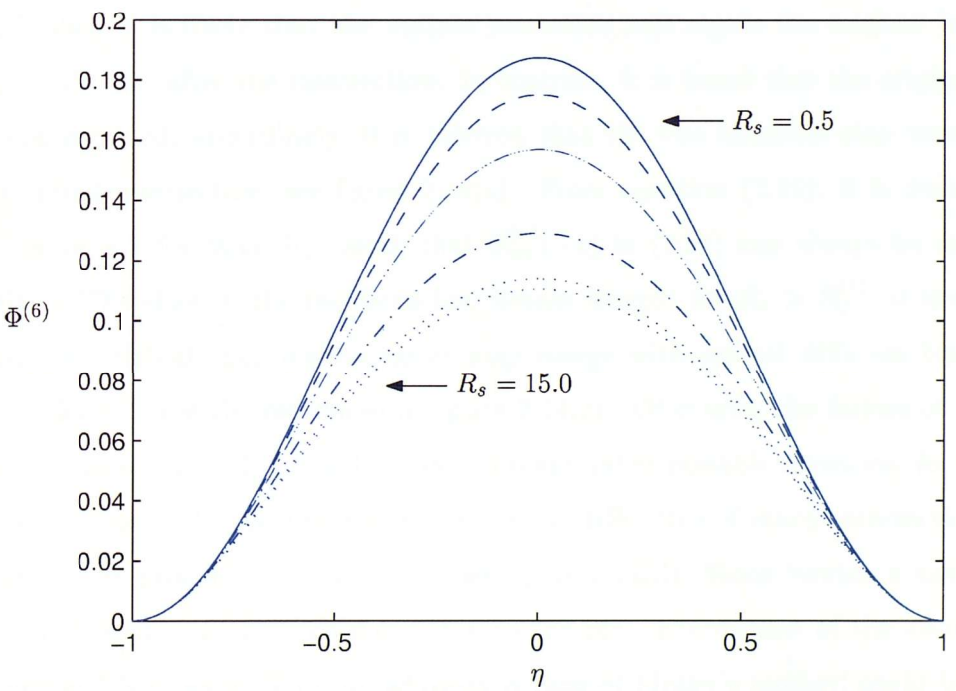


Fig. 2.23: The eigenfunction of $\Psi^{(6)}$ at $R_s = 0.5,\ 1,\ 2,\ 5,\ 10,\ 15$.

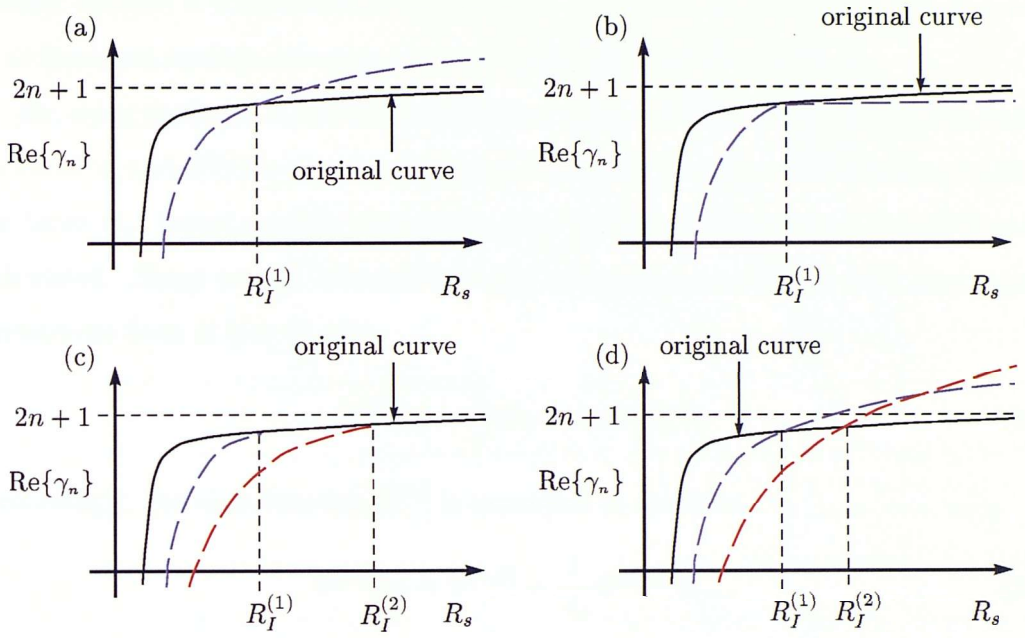


Fig. 2.24: The different branches of the growth rate $\gamma_n(R_s)$ for fixed n. Here, the solid black line indicates the original continuation curve. The remaining dashed lines (red and blue) indicate other possible solutions/branches of the growth rate γ_n.

$R_I^{(1)}$, then it is likely that the update procedure will regain the original branch for $R_s > R_I^{(1)}$ i.e. after the intersection. In contrast, it is found that the original branch is not regained; accordingly, it is inferred that the two branches stay merged after the initial intersection, see figure 2.24(c). From equation (2.81), it is deduced that $\gamma_n \to 2n+1$ for large R_s (recall that $\Phi_{\eta\eta}^{(n)}(-1)$ in (2.81) can always be rescaled to unity). Therefore, if the two branches remain merged for $R_s > R_I^{(1)}$, it is envisaged that the original continuation curve may merge with several different branches as $\gamma_n \to 2n+1$, see the red curve in figure 2.24(c). Of course, the failure of Newton's method near $R_s = R_I^{(1)}$ could be due to many other possible scenarios, for example, Newton's method may also encounter similar difficulties if many intersections occur within close proximity of each other, see figure 2.24(d). Since Newton's method does not work well near multiple roots (due to the zero determinant of the Jacobian, see Numerical Recipes §9 [60]), an adapted version of Muller's method could be used to track the original branch of the growth rate γ_n. However, this aspect is not investigated

further because it is sufficient, for the present discussion, to note that for each n, there is at least one continuation branch with $\mathrm{Re}\{\gamma_n(R_s)\} > 0$ for $R_s > R_n$.

By using the large R_s asymptotic form of $\Psi^{(0)}$, it is possible to deduce the limiting forms of γ_n and $\Phi^{(n)}$ as $n \to \infty$. From equation (2.81), one can infer that $\gamma_n \to 2n+1$ for large R_s, based on this assumption, the leading order solution for $\Phi^{(n)}$ is now calculated. Since we are interested in the symmetric solution of $\Psi^{(0)}$, the required asymptotic form is (see (2.46))

$$\Psi^{(0)}(\eta) = \frac{1}{\pi}\sin\pi\eta + O(R_s^{-1}). \tag{2.84}$$

Accordingly, the eigenfunction $\Phi^{(n)}$ is expanded in the form

$$\Phi^{(n)}(\eta) = \Phi^{(n,0)} + \frac{1}{R_s}\Phi^{(n,1)} + \ldots \tag{2.85}$$

By substituting the above expansions into (2.80), the leading order stability equation is then given by

$$\gamma_n\Phi^{(n,0)}_{\eta\eta} = \frac{1}{\pi}\sin\pi\eta\left[\Phi^{(n,0)}_{\eta\eta\eta} + \pi^2\Phi^{(n,0)}_{\eta}\right] - (2n+1)\cos\pi\eta\left[\Phi^{(n,0)}_{\eta\eta} + \pi^2\Phi^{(n,0)}\right], \tag{2.86a}$$

$$\Phi^{(n,0)}(\mp 1) = \Phi^{(n,0)}_{\eta}(\mp 1) = 0. \tag{2.86b,c}$$

By seeking a solution in terms of a Fourier series, it is found that the required solution is $\Phi^{(n,0)} = (\cos\pi\eta + 1)\lambda$, where λ is a constant. Moreover, it is interesting to note this solution also satisfies the derivative boundary conditions (2.86c) at each wall. This implies that the boundary layers at $\eta = \mp 1$ are passive at leading order. If the latter solution is normalised so that $\Phi^{(n,0)}_{\eta\eta}(-1) = 1$, the leading order approximation to the eigenfunction is then given by

$$\Phi^{(n)} = (\cos\pi\eta + 1)\pi^{-2} + \ldots \tag{2.87}$$

Perhaps the most intriguing fact about this solution is that it is independent of n. It would be desirable to compare this result with eigenfunctions that are calculated numerically. Unfortunately, as previously mentioned, the numerical difficulty associated with extending the appropriate continuation curve, prohibits such a comparison.

In order to compare (2.87) to the numerical eigenfunctions, it is necessary to extend the 'original' continuation curve, i.e. the one which passes through $R_s = R_n$, to high values of R_s, see figure 2.22. In this way, the growth rate will assume its asymptotic form $\gamma_n = 2n + 1$, which is prerequisite in the analysis above. However from our numerical work, see figure 2.22, it is found that the discontinuities inhibit the required continuation of the original branch, and therefore a comparison is not readily available.

2.4.3 Steady state comparisons

In the previous section, it was demonstrated that the presence of growing eigenfunctions inhibit the numerical computation of the terms $\Psi^{(n)}$, via time marching. The standard way to work around such difficulties (when seeking a time periodic solution) is to revert to a method which utilises the Fourier series representation. However, the Fourier series method avoids time marching, at the numerical expense of inverting a large banded matrix.

It is useful to note, that the solutions of the equation of motion (2.33) are steady and η-symmetric within the range $0 \leqslant R_s \leqslant 40$ (where $R_s = 40$ is the maximum limit of PS code being used). Therefore it follows that the leading order approximation $\Psi^{(0)}$, must also be steady and η-symmetric; moreover, it is known that the symmetric solution of $\Psi^{(0)}$ is steady up until $R_s \approx 170$. Accordingly the approach undertaken here, is to directly seek the solutions for $\Psi^{(n)}$ that are steady and η-symmetric. This approach reduces the numerical task immensely because, only the zero mode is required from the Fourier series expansion. Once again it is emphasised that for $R_s < 170$, the time marching procedure is still viable means for computing the *steady* term $\Psi^{(0)}$. For $R_s > 170$, the steady solution of $\Psi^{(0)}$ is generated by a shooting procedure. In this case, the integration over the η-domain is computed by using fourth-order Runge-Kutta with $\Delta\eta = 1/200$. The results from this calculation are found to be in agreement, with: 1) the equivalent results produced by the initial value solvers in Mathematica©, and 2) the asymptotic solution of $\Psi^{(0)}$ (2.50).

Once $\Psi^{(0)}$ has been computed, the remaining steady terms $\Psi^{(n\geqslant 1)}$ are determined

successively by directly solving each boundary value problem (2.37). In this direct approach, a finite difference scheme of order-four accuracy is employed in η-direction, and one-sided derivative formulas are used to incorporate the boundary conditions. By representing the series equations in this manner, each term $\Psi^{(n\geqslant 1)}$ is computed by the single inversion of a diagonally banded matrix. Due to the symmetry requirements, it is sufficient to consider η over the interval $[-1, 0]$; moreover, the typical mesh size used in this scheme is $\Delta\eta = 1/200$. Since there is no need for time marching, this calculation is efficient and simple to implement. It is also worth noting that the η-dependence on the full range $[-1, +1]$ has also been examined, however it is found that there are no asymmetric solutions for $\Psi^{(n\geqslant 1)}$.

To this point, we have no estimate on the number of terms required (in the series solution) to give a "good enough" approximation in the θ-direction. To obtain an estimate, we start by writing the asymptotic solution for Ψ in the limit $R_s \to 0$, this solution is given by

$$\begin{aligned}\Psi(\eta,\theta) =& \tfrac{1}{2}\eta(1-\eta^2)\sin\theta = \tfrac{1}{2}\eta(1-\eta^2)\sum_{j=0}^{\infty}\theta^{2j+1}\frac{(-1)^j}{(2j+1)!},\\ =& \sum_{j=0}^{\infty}\Psi^{(j)}\theta^{2j+1}.\end{aligned}$$

Therefore $\Psi^{(j)} = \frac{1}{2}\eta(1-\eta^2)\frac{(-1)^j}{(2j+1)!}$ as $R_s \to 0$. Hence the leading order absolute error, incurred by using $N+1$ terms in the series (as $R_s \to 0$), is given by:

$$\text{Absolute error } = \Psi(\eta,\theta) - \sum_{j=0}^{N}\Psi^{(j)}\theta^{2j+1} = \tfrac{1}{2}\eta(1-\eta^2)\Delta_e \leqslant \tfrac{1}{3\sqrt{3}}\Delta_e, \tag{2.88}$$

$$\text{with} \qquad \Delta_e = \Big(\sin\theta - \sum_{j=0}^{N}\theta^{2j+1}\frac{(-1)^j}{(2j+1)!}\Big). \tag{2.89}$$

Here, the parameter Δ_e represents the error incurred by using $N+1$ terms in the series expansion as $R_s \to 0$. Since each term $\Psi^{(j)}$ is calculated numerically, there is a margin of error associated with the numerical calculation, but this inaccuracy is not factored into the parameter Δ_e. Therefore as a crude approximation, it is assumed that all the numerical solutions for $\Psi^{(j)}$ are calculated without error. Under this assumption,

N	$\Delta_e = 10^{-3}$	$\Delta_e = 10^{-4}$
0	10.4171° or $n_\theta = 7$	4.8468°
1	37.5705° or $n_\theta = 26$	23.6762°
2	72.4172° or $n_\theta = 51$	52.0382°
3	110.705° or $n_\theta = 77$	85.5863°
4	150.710° or $n_\theta = 105$	122.079°
5	191.652° or $n_\theta = 134$	160.350°
6	233.142° or $n_\theta = 163$	199.756°

Table 2.5: The maximum angle of convergence of the series solution with $N+1$ terms and Δ_e fixed. The integer value n_θ is obtained by partitioning 360° into 256 equal intervals i.e. $n_\theta = 256\,\theta°/360°$, this value is useful for a direct comparison with table 2.6.

Δ_e serves as a measure of the error incurred by the series solution in the θ-direction, this error is henceforth referred to as the θ-error. From (2.88) it is clear, that in the limit $R_s \to 0$, the criteria for minimising the θ-error simply reduces to approximating $\sin\theta$ with enough terms in the series expansion. Table 2.5 gives some idea as to how many terms are required to maintain the θ-error within a prescribed value of Δ_e. For example, if $N = 0$ and upper bound of Δ_e is fixed to a value 10^{-4} (see table 2.5), then it is estimated that Δ_e is less than 10^{-4} for $0 \leqslant \theta \leqslant 4.8468°$.

It is also possible to derive a similar condition to (2.88) for the limit $R_s \to \infty$. For the case $R_s \to \infty$, the constant π replaces the value $3\sqrt{3}$ in (2.88). Moreover, since the absolute error is $O(\Delta_e)$ for asymptotically large/small values of R_s, it is expected that this linear proportionality is maintained at $O(1)$ values of R_s i.e. it is a valid assumption that Δ_e remains an appropriate measure of the θ-error for $R_s = O(1)$.

The results in this study indicate that a specification of $\Delta_e = 10^{-3}$, gives an approximate accuracy of 2-3 significant figures (see discussion on page 93). The latter value of Δ_e is obtained by comparing the asymptotic solutions of Ψ (2.42) (2.51), to the numerical results of the series solution (2.34), for large/small values of R_s. There-

fore, approximately 6-7 terms are required in the series solution to give a converged representation from $\theta = 0°$ to $180°$.

In summary, the concept of an error parameter, Δ_e, has been used to approximate number of terms required in the series expansion. Moreover, a prescribed value of $\Delta_e = 10^{-3}$ is found to give a 2-3 s.f. accuracy. In the following section a slightly different error measuring procedure is described. This modified procedure is preferred because the error is measured relative manner (as opposed to an absolute error measurement). However, for asymptotically small/large R_s, this modified method produces the same 2-3 s.f. accuracy as the condition $\Delta_e = 10^{-3}$.

Measuring the agreement of two solutions

The procedure described here is used to determine the extent of agreement, in all the comparisons that are subsequently discussed. Moreover, the details given here are applicable to comparisons of the type numerical-asymptotic and numerical-numerical. However, for simplicity the procedure is described in the context of comparing a numerical solution for Ψ to an asymptotic result. To compare these two solutions, it is first necessary to fix a value for R_s. Next:

1. The absolute error between the (steady) asymptotic solution and numerical solution for Ψ is computed as a surface in $[\eta, \theta]$ space.

2. Next a value for θ is chosen and then fixed (preferably this angle is chosen so that it is good estimate to the maximum extent of agreement).

3. If the maximum absolute error in the η-direction is within 1% of the asymptotic solution for Ψ, the numerical solution of Ψ is accepted as a converged result at this value of θ (and subsequently θ is increased and this step is repeated). If the error is larger than 1%, θ is reduced until the error is less than 1%.

4. This process is repeated, until a maximum angle of agreement is obtained i.e. the angle at which the maximum relative error equals 1%.

The results acquired by this procedure are accurate to 2-3 s.f. Moreover, for asymptotically small/large R_s this is procedure is equivalent to prescribing a value of $\Delta_e = 10^{-3}$.

Numerical results: symmetric (steady) series solution versus DNS

From solving the equation of motion (2.33) directly, it is known that the solution for Ψ is steady and η-symmetric for $R_s \leqslant 40$. Moreover, calculations beyond $R_s = 65$ are not possible and we shall discuss why later on in this section.

Let us now proceed by comparing the DNS of (2.33), with the steady results obtained by solving the series equations (2.37) (without time marching). At a given Reynolds number, Ψ is computed via both methods and the η-profiles of both solutions are compared at fixed values of θ (as described in the previous section). The maximum angle to which both solutions are in agreement is then recorded, see table 2.6; note, in this table the maximum angle is given in terms of the integer variable $n_\theta = 256\ \theta/2\pi$. It is useful to define n_θ because in the numerical scheme it is necessary to partition the computational θ-domain [0°, 360°] into equal intervals, in this case 256 intervals. Accordingly, since a comparison is only possible at discrete θ-intervals, it makes sense to define the maximum extent of agreement in terms of the partition number n_θ.

For $R_s \ll 1$, the series approach yields a complete solution from $\theta = 0°$ to 180°. However, at moderate values of the Reynolds number it is found that a truncation of the series is necessary. At $R_s = 20$, the 5 term approximation is found to agree with the DNS up to $n_\theta = 63$. However, at the same Reynolds number, the agreement of the 6 and 7 term approximations only extend up to $n_\theta = 57$ and $n_\theta = 55$ respectively. In this case, the agreement is found to deteriorate with the inclusion of more terms. Therefore at $R_s = 20$, the series requires truncating at $N = 5$. Despite the required truncation at $N = 5$, the trend line in table 2.6 is drawn at $N = 1$ (inclusive). This is because the results for $N = 2$ to $N = 5$ are only marginal improvements over the corresponding result at $N = 1$. Moreover, for $N = 2 \rightarrow 5$, the maximum error (as a function of θ) oscillates up to, yet within, the imposed boundary of 1%. Hence based

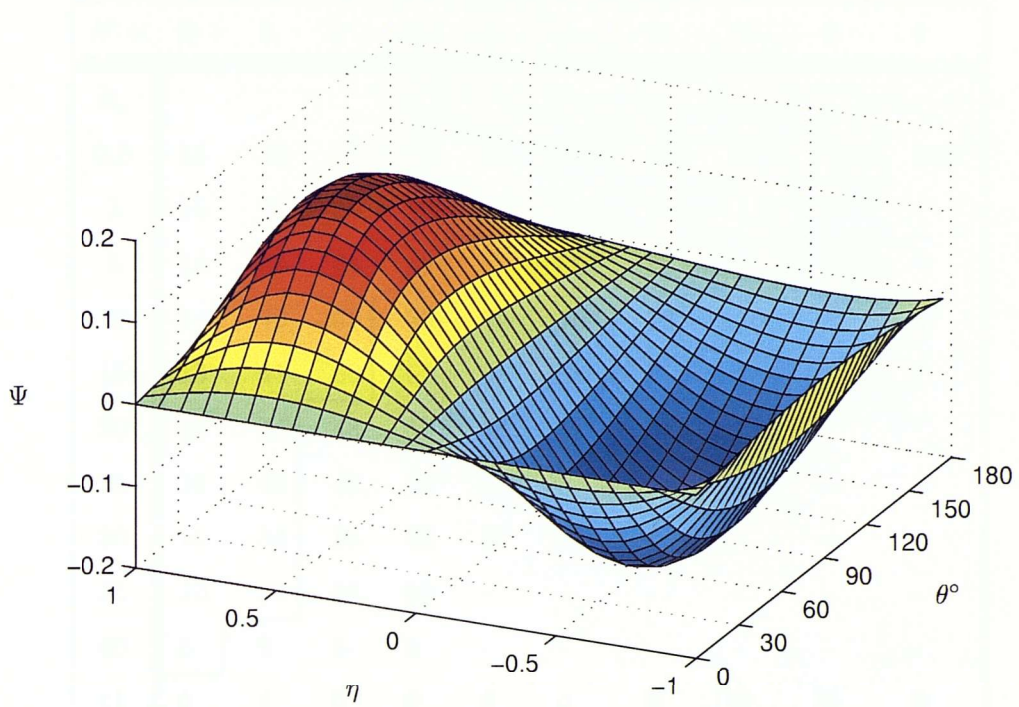


Fig. 2.25: The numerical solution for Ψ at $R_s = 35$, 3D view. This solution is calculated by the PS method with $\Delta\theta = 2\pi/128$, $\Delta\eta = 2/100$ and $\Delta\tau = 5 \times 10^{-3}$.

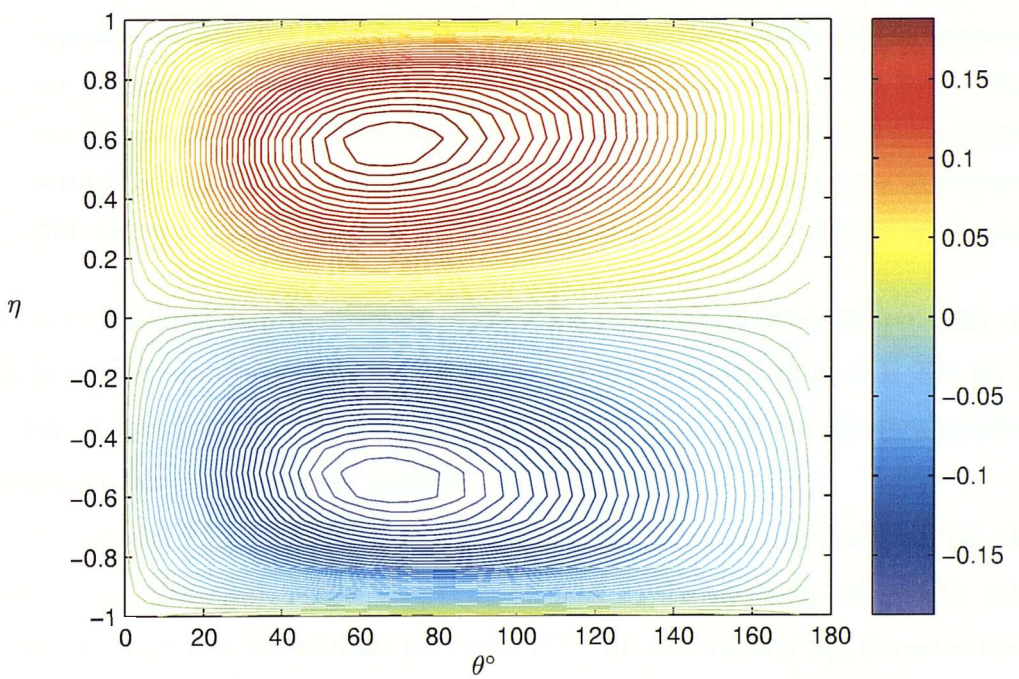


Fig. 2.26: A contour plot of Ψ at $R_s = 35$. This solution is calculated by the PS method with $\Delta\theta = 2\pi/128$, $\Delta\eta = 2/100$ and $\Delta\tau = 5 \times 10^{-3}$.

$N =$	0	1	2	3	4	5	6	7	8	9
R_s										
0.5	15	49	75	95	110	119	125	129	170	160*
2	15	46	70	89	105	117	110*	111*	114*	*
5	14	43	63	82	87	86*	92	92	90*	*
10	14	40	63	65	72	70*	73	70*	*	*
15	13	41	60	60	58*	58*	*	*	*	*
20	10	44	48	52	63	57*	55*	*	*	*
25	10	45	46	45*	45*	-	-	-	-	-
30	10	34	35	36	37	-	-	-	-	-
35	10	32	33	33	-	-	-	-	-	-
40	5	5	5	5	-	-	-	-	-	-
41	0	0	0	0	0	0	0	0	0	0

Table 2.6: The maximum partition number (in θ-direction) to which the series solution is in agreement with the DNS of equation (2.33) (maximum error of 1% along each η-profile, see page 93). In this table the maximum angle to which the two solutions are in agreement, is given in terms of the partition number $n_\theta = 256\ \theta/2\pi$. The number of terms used in the series solution is denoted by $N+1$. A dash (-) indicates no further improvement and an asterisk ($*$) denotes a deterioration in the agreement. The staggered line drawn across the table indicates the general trend of the agreement.

on these facts, the improved result at $N = 5$ is regarded as fortunate outcome due to the prescribed accuracy goal, and so the trend line is drawn at $N = 1$. For $R_s \geqslant 41$, no matter how the series solution is truncated, it is impossible to obtain a satisfactory agreement with the DNS, see table 2.6.

To test the PS numerical method (which is used to compute the direct solution of (2.33)), the numerical results were compared to: i) the small-R_s asymptotic solution (2.42), and ii) the series solution, see figure 2.27. At each value of R_s, the series solution is truncated to give the best agreement with the DNS, see table 2.6. In figure 2.27, we observe that the series solution gradually fails to represent the flow in the main core

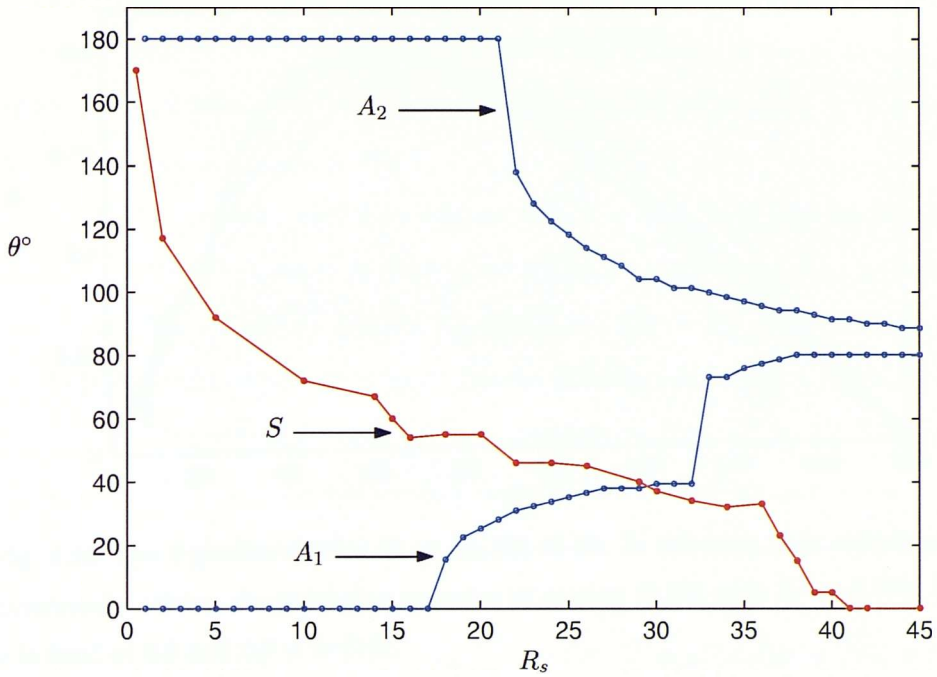


Fig. 2.27: The agreement of the DNS for Ψ with: 1) the series solution, and 2) the asymptotic solution for small R_s (2.42). The line S represents the extent to which the series solution matches with the DNS for Ψ. The vertical θ-range between the lines A_1 and A_2, shows the interval over which the DNS is in agreement with the asymptotic solution (2.42).

region as the Reynolds number is increased. Moreover we note that the asymptotic solution (2.42) approximates the numerical solution extremely well up to $R_s = 17$, after which, the solution fails to represent the flow close to $\theta = 0°$ and $\theta = 180°$. In view of this result, we may regard the series solution (2.34) as valid representation near $\theta = 0°$ i.e. the series solution adopts the role of an inner boundary layer solution (in the θ-direction). Accordingly, the small-R_s asymptotic solution for Ψ (2.42) is interpreted as the corresponding outer solution. For $R_s \gtrapprox 30$, the agreement of the asymptotic representation (curve A_1) fails to overlap with the inner solution (curve S); further examination of the DNS for Ψ, reveals why this is so.

In figure 2.28, the value of η is fixed at 0.6 and the θ-profile of the DNS for Ψ is plotted for $R_s = 15, 30, 40, 50$. From this figure it is clear that the profiles begin

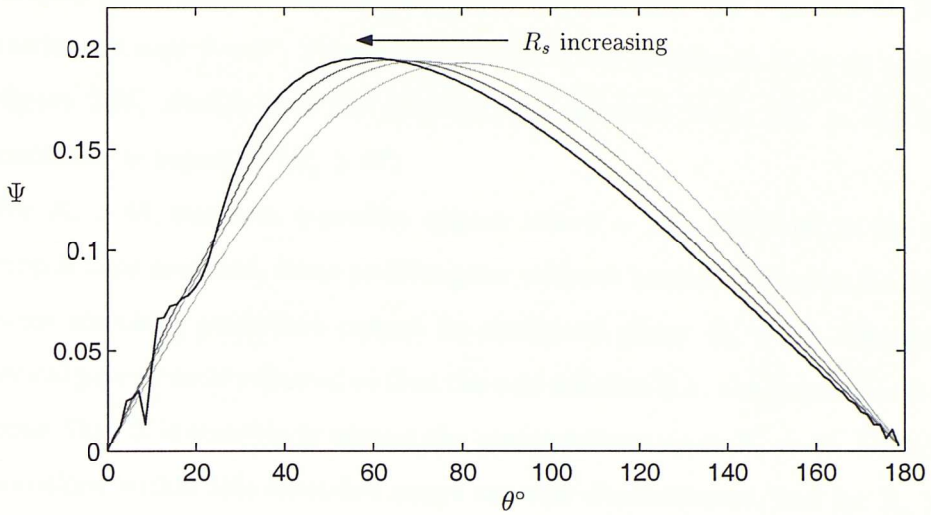


Fig. 2.28: The θ-profiles of Ψ at $R_s = 15$, 30, 40 50. In this case, Ψ is calculated by numerically solving the governing equation of motion (2.33) with $\Delta\tau = 0.001$. Here η is fixed at 0.6 and $\Delta\theta = 2\pi/128$.

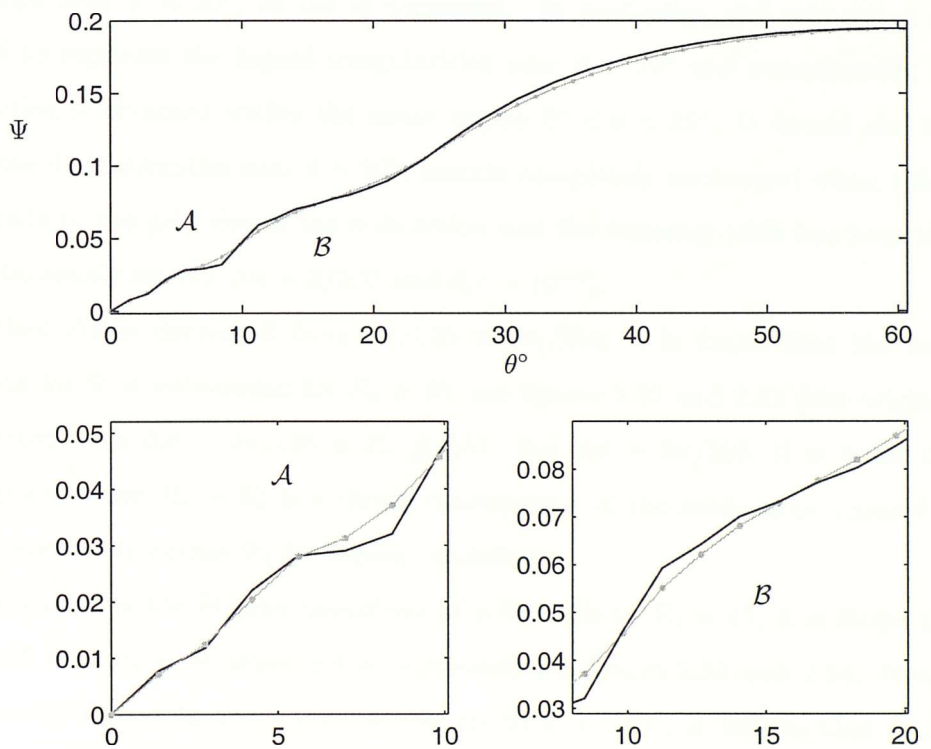


Fig. 2.29: The wavy/discontinuous θ-profiles of Ψ at $R_s = 44$, 47. Here η is fixed at 0.6 and $\Delta\theta = 2\pi/128$. The dotted line represents the solution at $R_s = 44$.

to steepen as R_s is increased. In addition, we note that the θ-profile at $R_s = 50$ is discontinuous near $\theta \approx 9°$. Further inspection of the profiles at $R_s = 44$ and $R_s = 47$, see figure 2.29, reveals that the solution first becomes wavy ($R_s = 44$) before the discontinuity is apparent ($R_s \geqslant 47$).

For $R_s > 48$, two even η-profiles appear near $\theta = 28°$, $152°$ and as the numerical solution is time marched, these profiles grow without bound. Owing to this instability, the time marching procedure cannot be continued above $R_s = 48$. However, if the numerical procedure is adjusted so that the odd solution (i.e. the η-symmetric solution) is forced, then it is possible to extend the computations up to $R_s \approx 60$. Unfortunately, the solutions within this extended range are also discontinuous, and for $R_s > 60$ it is once again impossible to obtain a bounded solution via time marching. In figures 2.30, 2.31 and 2.32, the numerical solutions acquired with $\Delta\theta = 2\pi/128$ and $\Delta\theta = 2\pi/256$ are plotted for $R_s = 50 \rightarrow 65$. From these diagrams, it is seen that a clearer structure develops near $\theta \approx 20°$, as $\Delta\theta$ is decreased. In particular, the refinement of $\Delta\theta$ is found to suppress the jagged irregularities near $\theta = 20°$ and consequently, a better resolution is obtained within the *inner* region $0° < \theta < 25°$. It should also be noted that the discontinuities near $\theta = 20°$, remain completely unchanged when refinements are made to the grid size in the η-direction and the timestep (this has been tested by simultaneously setting $\Delta\eta = 2/200$ and $\Delta\tau = 10^{-4}$).

When $\Delta\theta$ is decreased from $2\pi/128$ to $2\pi/256$, it is found that the numerical solution for Ψ is unbounded for $R_s \geqslant 60$, see figures 2.31 and 2.32 (the original value associated with $\Delta\theta = 2\pi/128$ is $R_s \gtrapprox 65$). For $\Delta\theta = 2\pi/256$, it is found that the divergence above $R_s = 60$ is a direct consequence of the steep slope (near $\theta = 25°$) which eventually causes Ψ_θ to become undefined.

By analysing the Fourier transform of a θ-profile at $R_s = 47$, it is found that the decay of $\widehat{\Psi}$ is stronger when $\Delta\theta$ is decreased, see figures 2.33 and 2.34. Note, since Ψ is a real valued function that is odd about $\theta = 180°$, it follows that its Fourier transform, $\widehat{\Psi}(k, \eta, \tau)$, is purely imaginary and odd about $k = 0$. Hence under the present circumstances it is sufficient to plot $\mathrm{Im}\{\widehat{\Psi}\}$ for positive wavenumbers. From

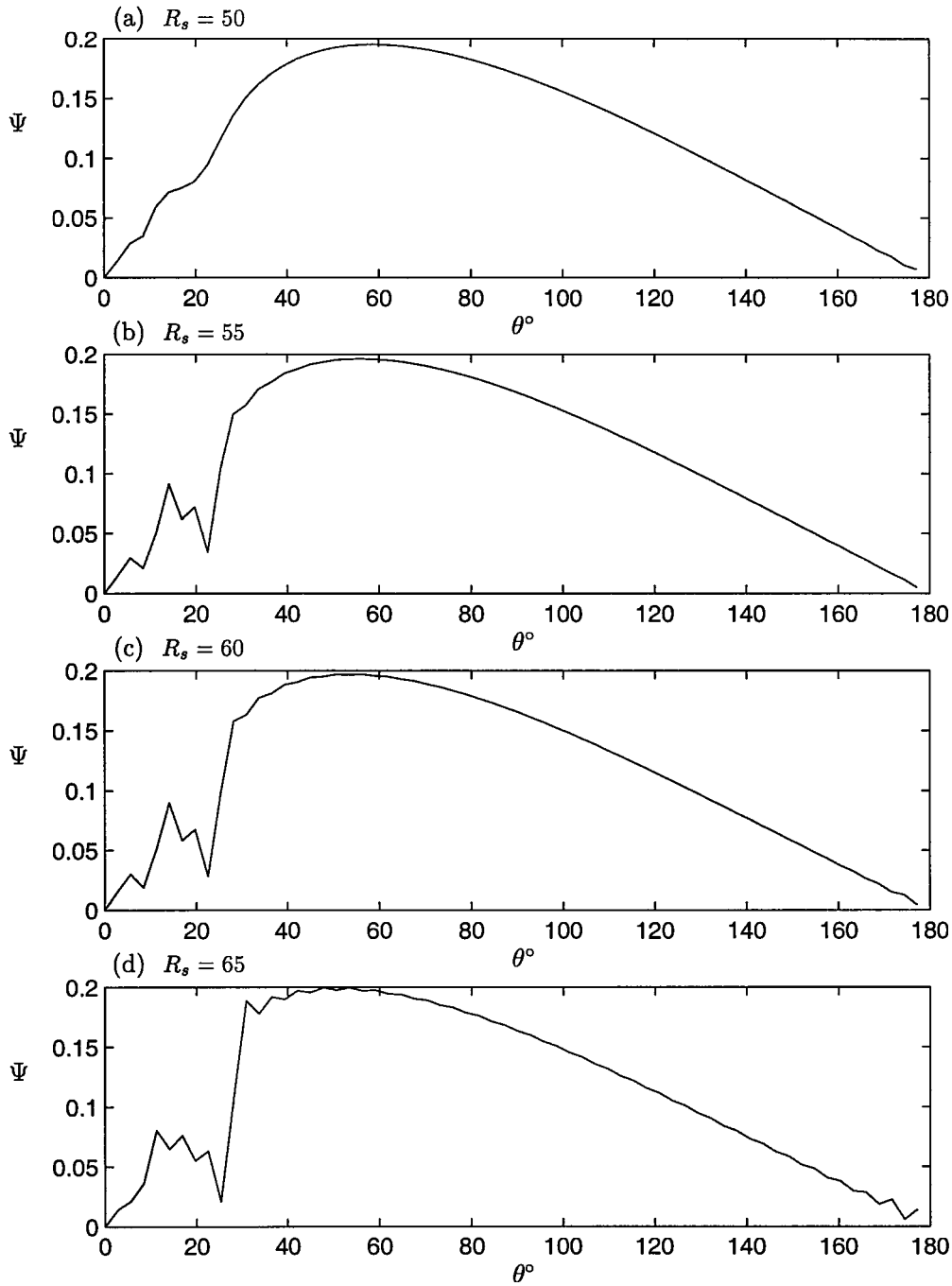
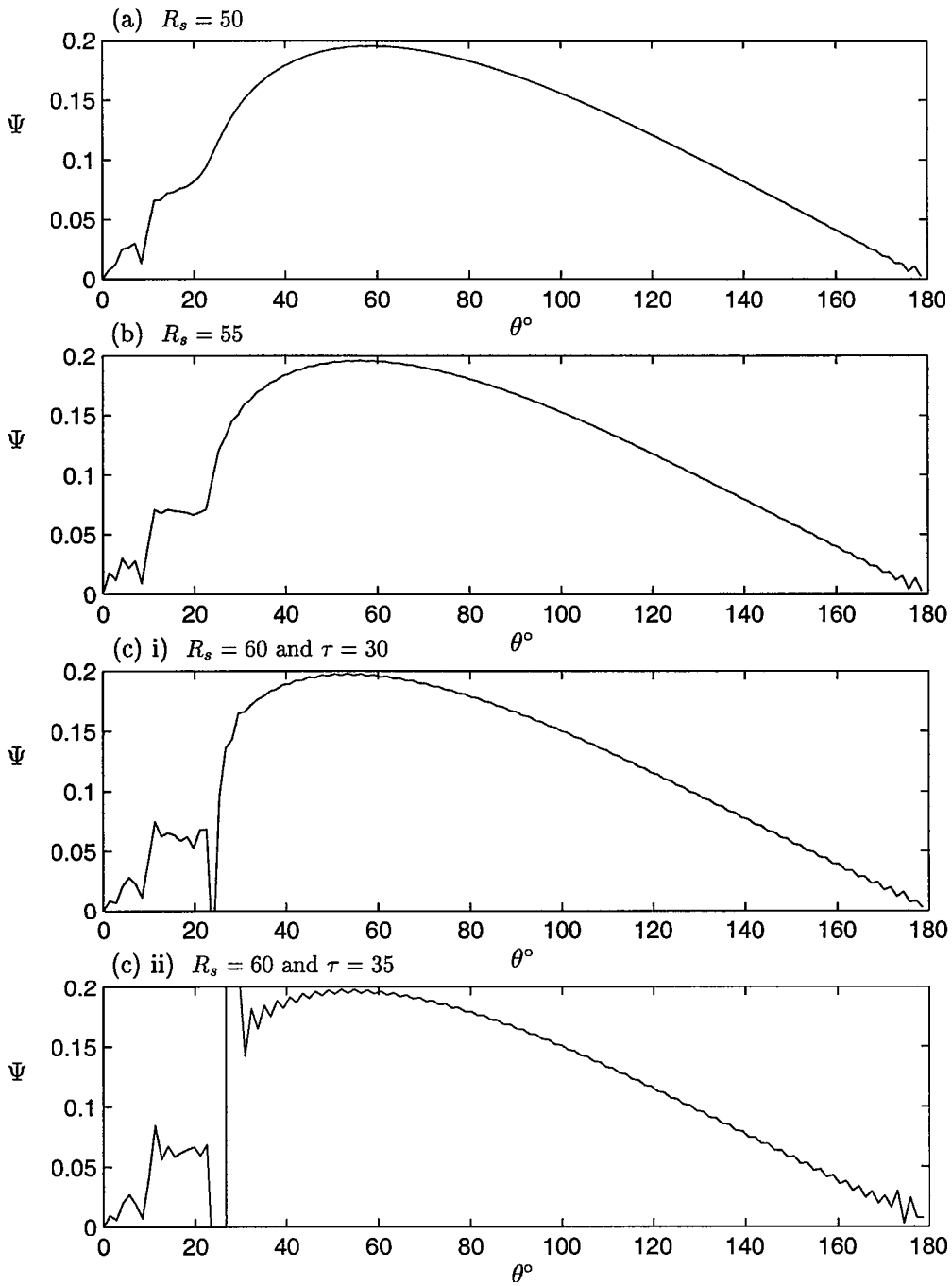
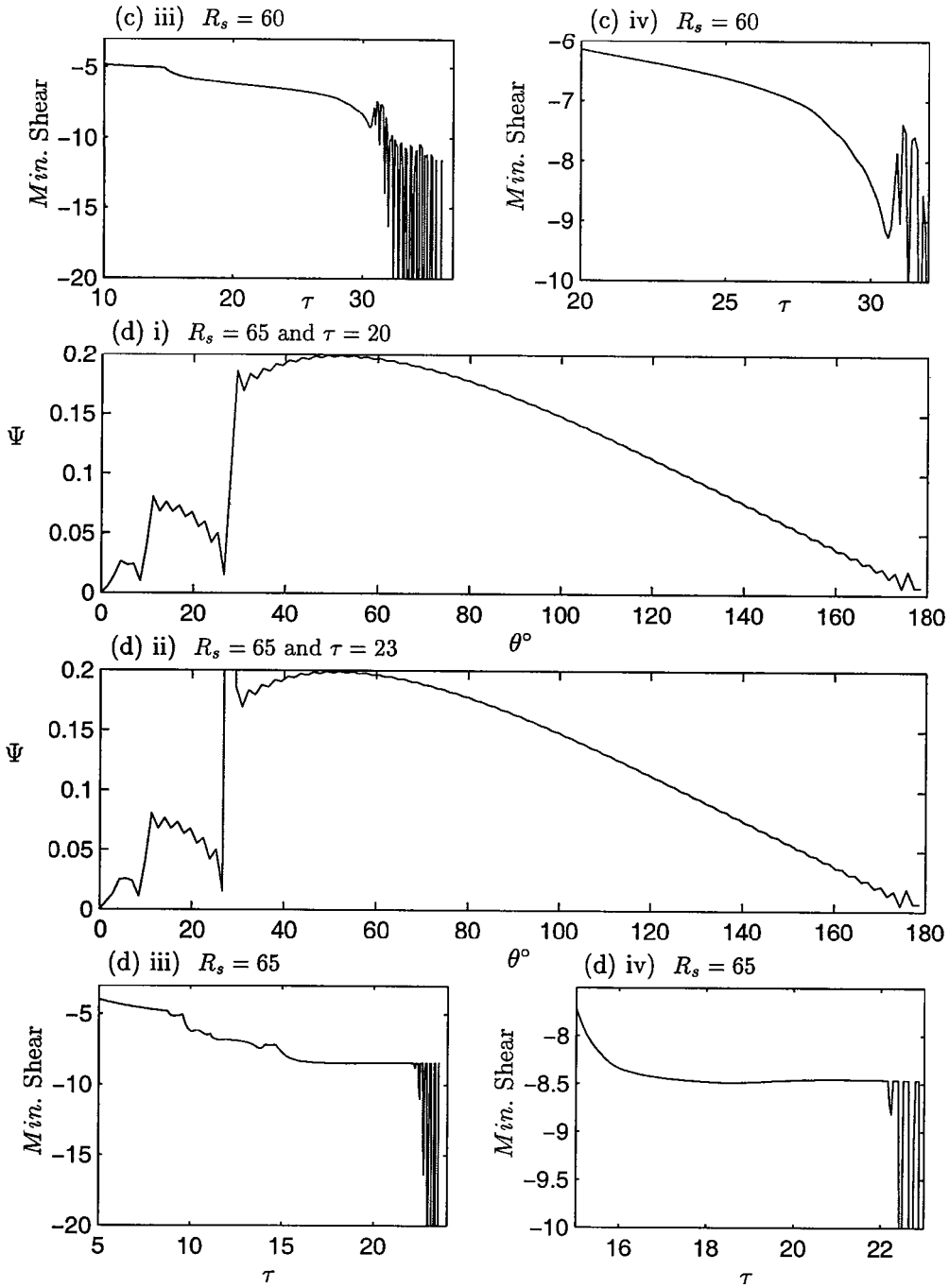


Fig. 2.30: The diagrams (a)–(d) show the numerical solutions for Ψ at $R_s = 50$, 55, 60, 65 respectively. Here η is fixed at 0.6, $\Delta\tau = 0.001$ and $\Delta\theta = 2\pi/128$.



Part I. Fig. 2.31: The diagrams (a)–(c) show the numerical solutions for Ψ at $R_s = 50$, 55 and $R_s = 60$ respectively. Here η is fixed at 0.6, $\Delta\tau = 0.001$ and $\Delta\theta = 2\pi/256$. The θ-profiles shown in (c) i) and (c) ii) are taken at $\tau = 30$ and $\tau = 35$ respectively.



Part II. Fig. 2.32: Diagrams (c) iii)–iv) and (d) iii)–iv) show the time evolution of the minimum value of shear stress along the wall $\eta = -1$. The θ-profiles shown in (d) i) and (d) ii) are taken at $\tau = 20$ and $\tau = 23$ respectively.

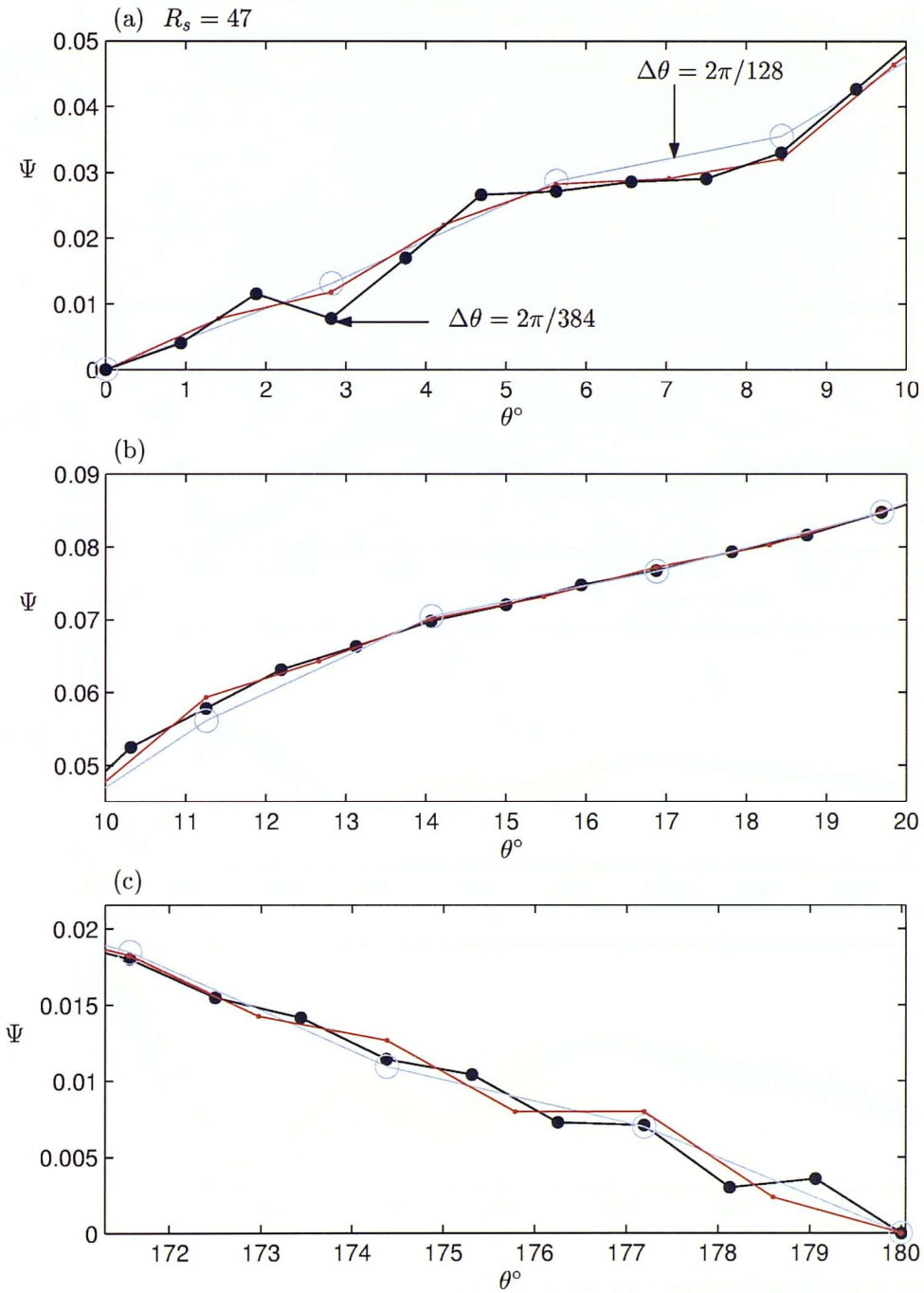


Fig. 2.33: The numerical solution for Ψ at $R_s = 47$ with $\Delta\theta = 2\pi/128$, $2\pi/256$, $2\pi/384$. Here η is fixed at 0.6 and $\Delta\tau$ is set equal to 0.001 in the computations.

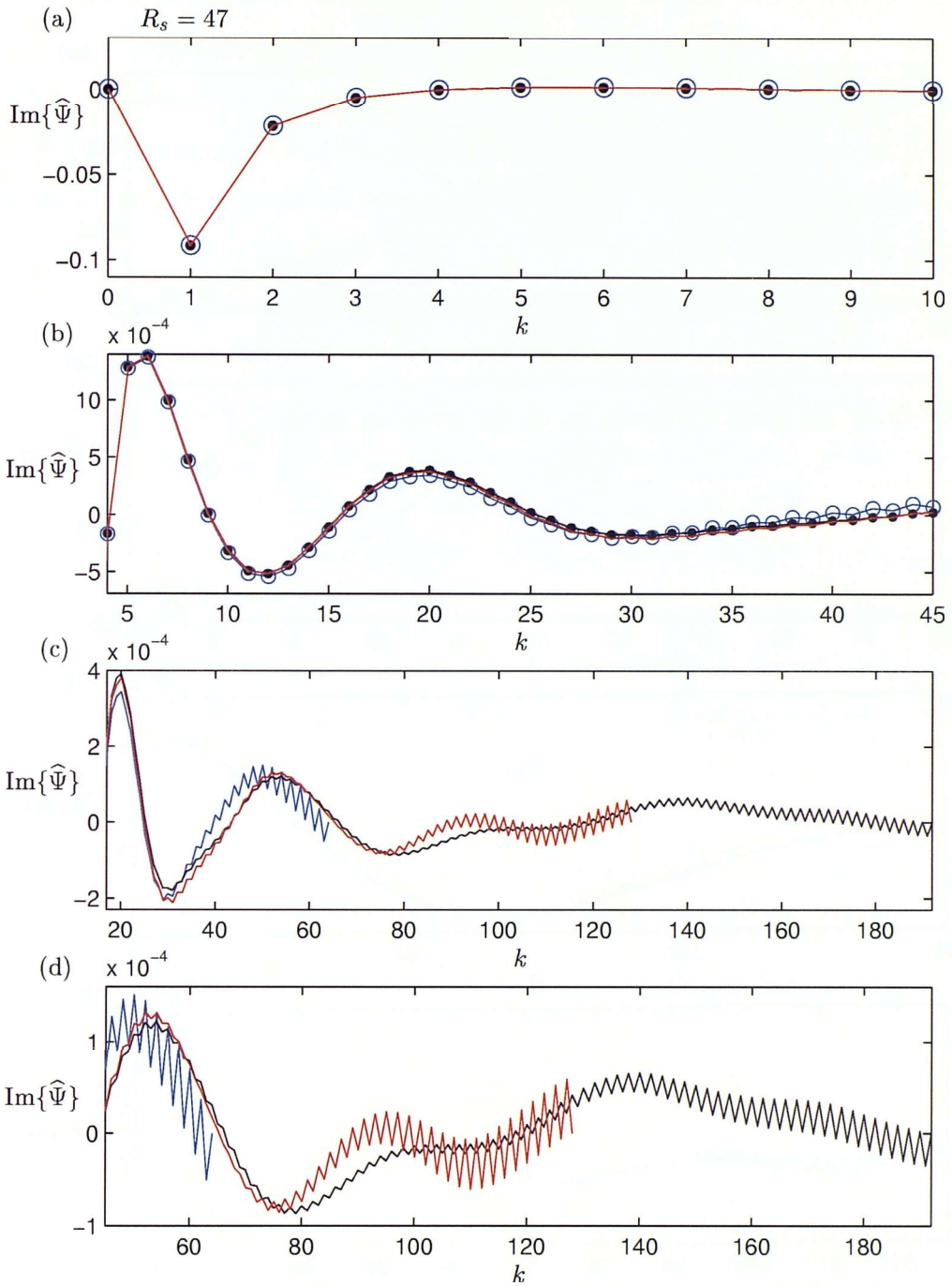


Fig. 2.34: For $R_s = 47$, the above diagrams show the FFT of the θ-profile at $\eta = 0.6$ for different numerical calculations. The different settings used in these calculations are: $\Delta\theta = 2\pi/128$ (blue curve), $\Delta\theta = 2\pi/256$ (red curve) and $\Delta\theta = 2\pi/384$ (black curve).

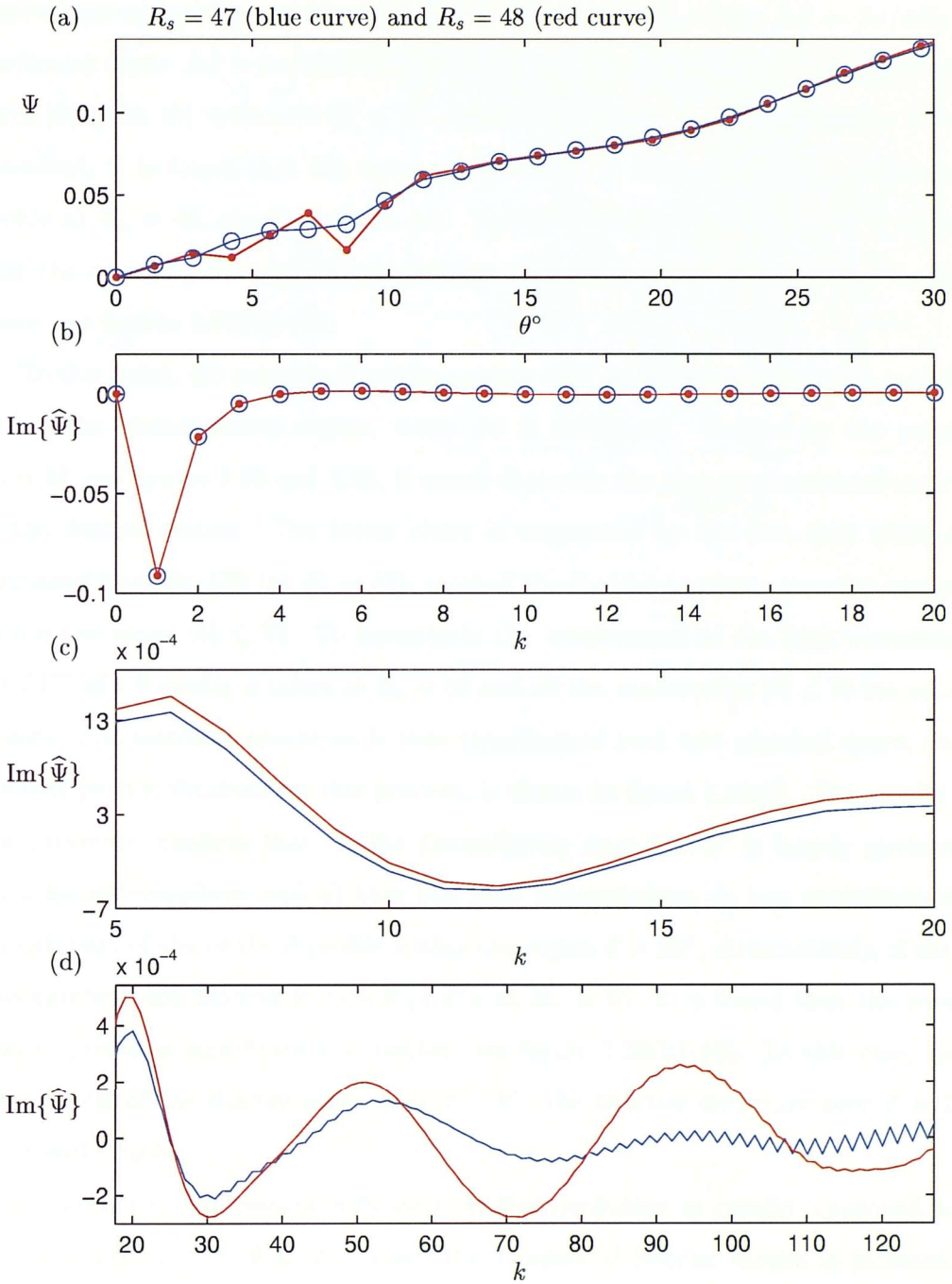


Fig. 2.35: Diagram (a) shows the numerical solution for Ψ at $R_s = 47$ (blue curve) and $R_s = 48$ (red curve). Here $\eta = 0.6$ and $\Delta\theta = 2\pi/256$ ($\Delta\tau$ is set equal to 0.001 in the computations). Diagrams (b)–(d) show the FFT of each θ-profile shown in (a).

figure 2.34, it is seen that the converged portion of each spectrum at $R_s = 47$, is given approximately by the empirical relation $-N_\theta \leqslant k \leqslant N_\theta$ where $\Delta\theta = 2\pi/4N_\theta$. For particular cases: $\Delta\theta = 2\pi/128$, $\Delta\theta = 2\pi/256$ and $\Delta\theta = 2\pi/384$ this empirical relation gives $|k| \leqslant 32$, $|k| \leqslant 64$ and $|k| \leqslant 96$ respectively. If the Reynolds number is further increased, it is found that the wavy profile at $R_s = 47$ evolves into a discontinuous profile at $R_s = 48$, see figure 2.35 (a). The FFT of the θ-profile at $R_s = 48$, shows that the emerging discontinuity is clearly marked by a weaker decay of $\widehat{\Psi}$ in Fourier space, see figures 2.35(b)–(d).

To this point, the numerical results suggest that an improved resolution is obtained within the discontinuous region, when $\Delta\theta$ is decreased. Guided by the results at $R_s = 47$, see figures 2.33 and 2.34, it seems that only the high wavenumbers contribute to the discontinuities. The latter claim is supported by the fact that when $\Delta\theta$ is decreased from $2\pi/128$ (at $R_s = 47$), most of the Fourier spectrum remains unchanged within the range $|k| \leqslant 32$. To investigate the involvement of the high wavenumbers, the FFT of a θ-profile is taken at $R_s = 50$ and all the modes with $|k| \leqslant 25$ are set equal to zero. The resulting spectrum is then transformed back into physical space, and the *residual* profile obtained by this process, is shown in figure 2.38(a). The results from this procedure confirm that: i) the discontinuity near $\theta = 9°$ is largely governed by the high wavenumbers and ii) that the high wavenumbers do not contribute to the smooth part of the of the θ-profile within the region $\theta > 25°$. Alternatively, if the high wavenumbers are filtered from a θ-profile at $R_s = 55$, it is found that the resulting filtered profile is significantly smoother, see figure 2.38(b)–(d). In this case, despite the removal of the discontinuity near $\theta = 9°$, the two-tier structure near $\theta = 25°$ is still clearly visible.

In summary, our results indicate that the resolution is greatly improved within the inner region $0° \leqslant \theta \leqslant 25°$, when the number of Fourier modes is increased (i.e when $\Delta\theta$ is decreased). The effects of the latter result are evident at $R_s = 50$, see figure 2.36 and c.f. figures 2.30(a), 2.31(a). At $R_s = 50$, when $\Delta\theta$ is decreased from $2\pi/128$ to $2\pi/384$, a single discontinuity is revealed is near $\theta = 9°$. In addition to this

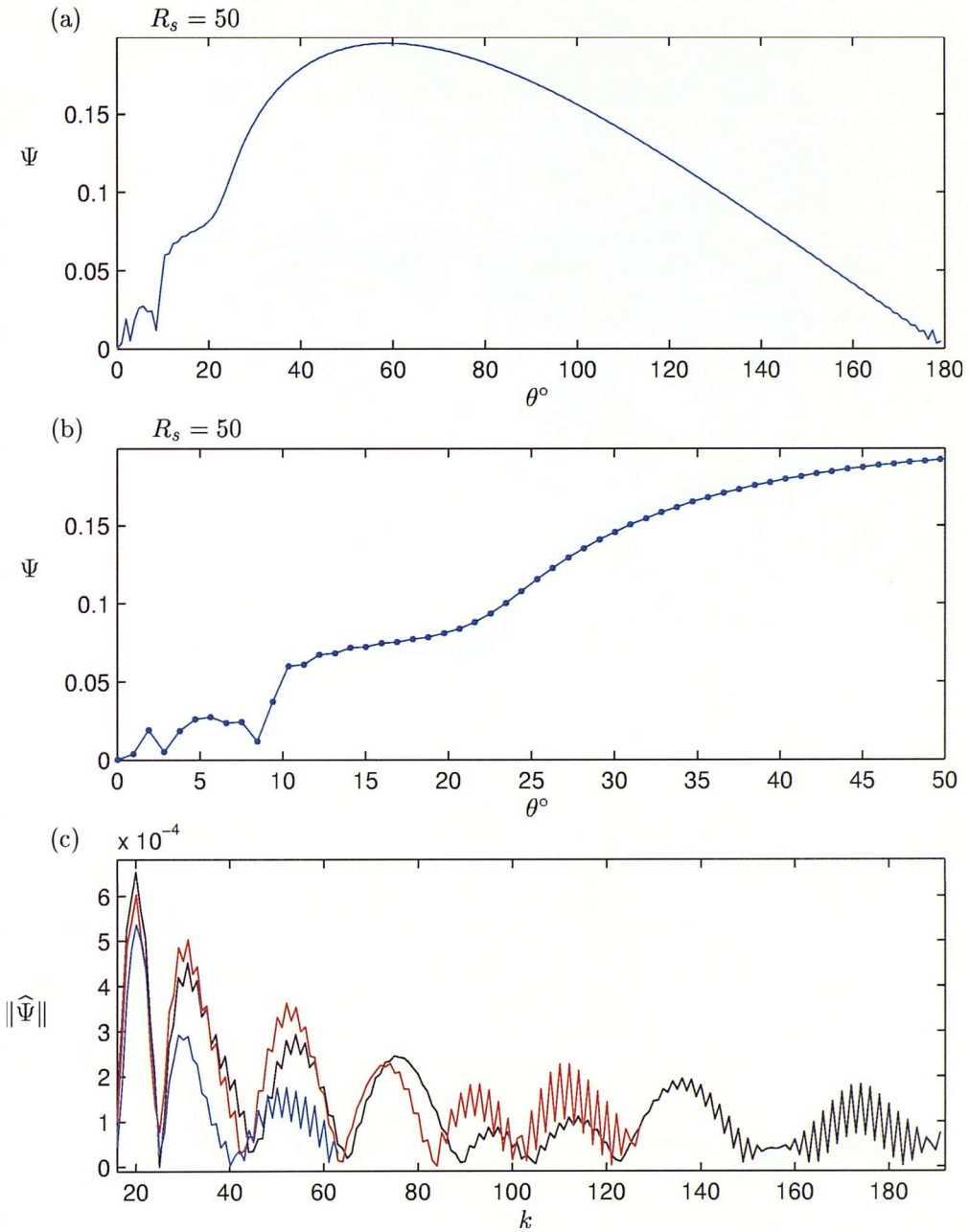


Fig. 2.36: (a)–(b): The numerical solution for Ψ at $R_s = 50$ with $\Delta\theta = 2\pi/384$. Here $\Delta\eta = 0.6$ and $\Delta\tau = 2 \times 10^{-4}$. Diagram (c) shows the FFT of the θ-profile at $\eta = 0.6$, computed with: $\Delta\theta = 2\pi/384$ (black curve), $\Delta\theta = 2\pi/256$ (red curve) and $\Delta\theta = 2\pi/128$ (blue curve).

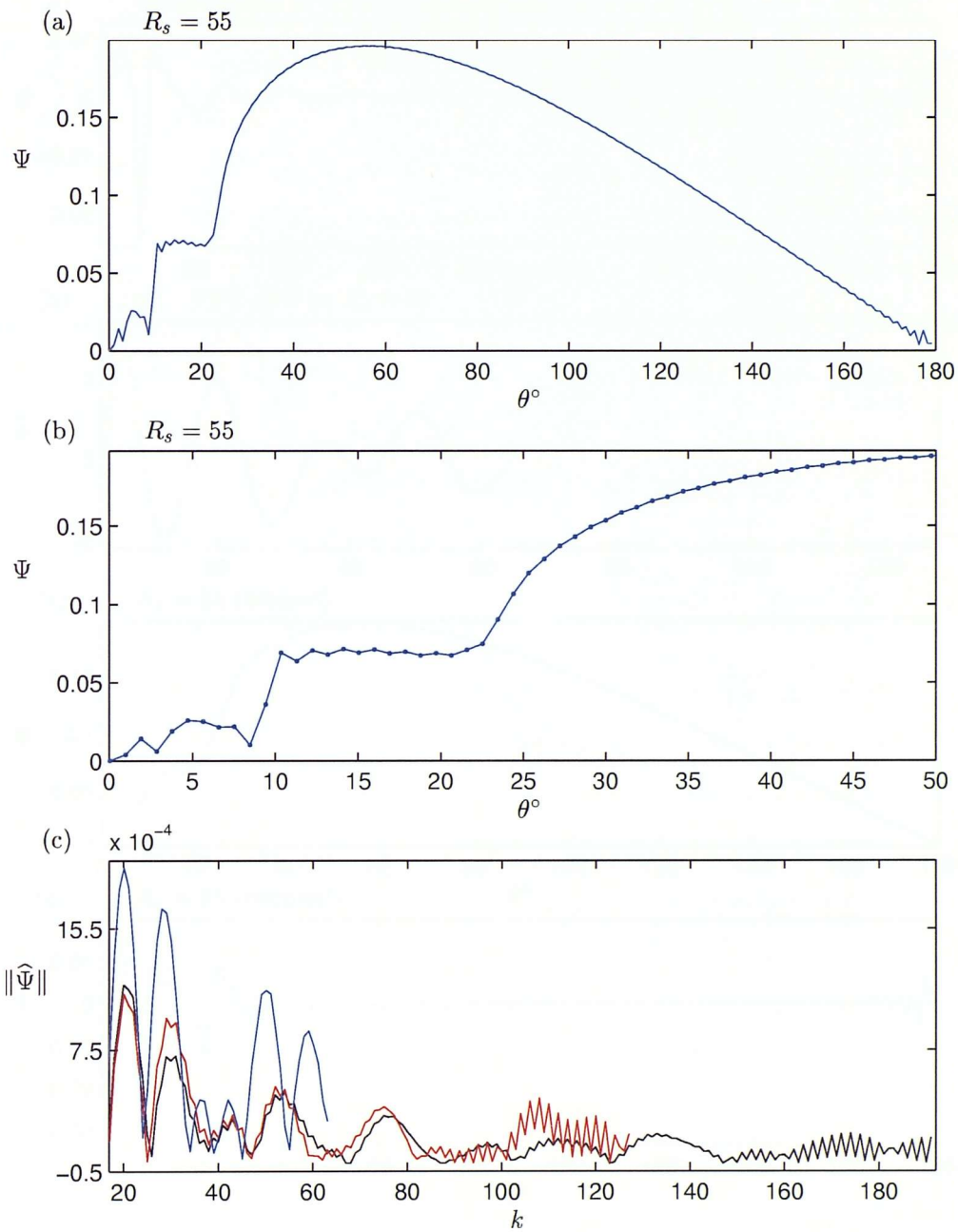


Fig. 2.37: (a)–(b): The numerical solution for Ψ at $R_s = 55$ with $\Delta\theta = 2\pi/384$. Here $\Delta\eta = 0.6$ and $\Delta\tau = 2 \times 10^{-4}$. Diagram (c) shows the FFT of the θ-profile at $\eta = 0.6$, computed with: $\Delta\theta = 2\pi/384$ (black curve), $\Delta\theta = 2\pi/256$ (red curve) and $\Delta\theta = 2\pi/128$ (blue curve).

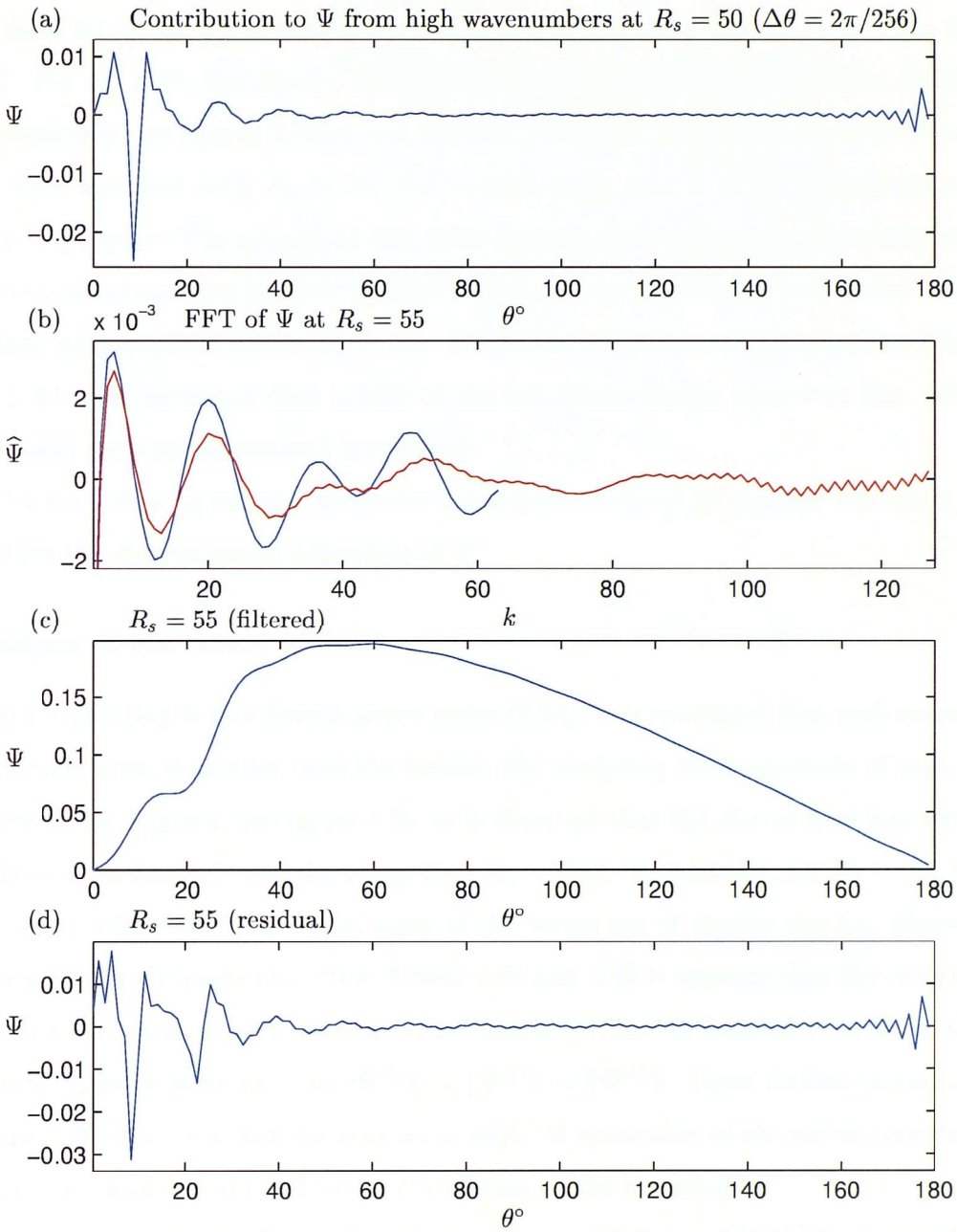


Fig. 2.38: Diagram (a) shows the contribution to Ψ from the Fourier modes with wavenumber $|k| > 25$, here $R_s = 50$ and $\eta = 0.6$. Diagram (b) shows the FFT of Ψ at $R_s = 55$ with $\Delta\theta = 2\pi/128$ and $\Delta\theta = 2\pi/256$. Diagram (c) shows the filtered solution at $R_s = 55$; here, all the Fourier modes with $|k| > 25$ are truncated, and this truncated contribution is then plotted in diagram (d).

discontinuity, it also appears that Ψ_θ is no longer continuous at $\theta \approx 25°$. By increasing R_s from 50 to 55, the θ-profile becomes increasingly steep near $\theta \approx 25°$, see figure 2.37. For $R_s > 55$, the abrupt change near $\theta = 25°$ is clearly marked by a *shock* like discontinuity, see figures 2.31(c) and 2.32(d). Moreover, when the numerical solutions are time marched with $R_s > 55$, the vertical slope near $\theta \approx 28°$ is brought about by a large spike. The growth of this spike (during time marching), eventually causes the numerical solution to grow without bound and for this reason, a bounded solution cannot be computed above $R_s = 55$. Hence, in order to evaluate the flow field for $R_s > 40$, it is envisaged that a DNS of the full Navier-Stokes equations (i.e. without the small gap approximation) is required.

In the following section, the series solution is analysed to see how the terms $\Psi^{(n)}$ capture the discontinuous behaviour of Ψ.

Analysis of the terms $\Psi^{(n)}$

When expanding Ψ in a formal power series (2.34), it is envisaged that each successive correction term is smaller than the former. By analysing the magnitude of each term in the series solution, see figure 2.39, it is observed that the size of first two terms is relatively unchanged over the range $0 < R_s < 200$. In contrast, for $R_s < 45$, there are many values of R_s at which some of the terms are of similar size i.e. disordered in magnitude. In particular, from figures 2.39 and 2.40 it appears that the ordering of the first few terms is perhaps most unfavourable within the interval $27 < R_s < 45$; for in this range, it is found that $\|\Psi^{(3)}\| > \|\Psi^{(2)}\| \sim \|\Psi^{(4)}\|$. Upon further inspection of figure 2.39, it is seen that the maximum angle of agreement of the series solution (see table 2.6), is closely related to the disordering of the magnitudes.

For clarity, the smallest value of R_s at which $\|\Psi^{(n)}\| \approx \|\Psi^{(n+1)}\|$, is recorded in table 2.7. As anticipated, the values in this table directly correspond to the values of R_s, at which the series solution must be truncated (at the term $\Psi^{(n)}$ inclusive) to give the best agreement with the numerical solution of Ψ, see table 2.6 on page 96. In view of this result, it is envisaged that the series representation of Ψ, at moderate Reynolds

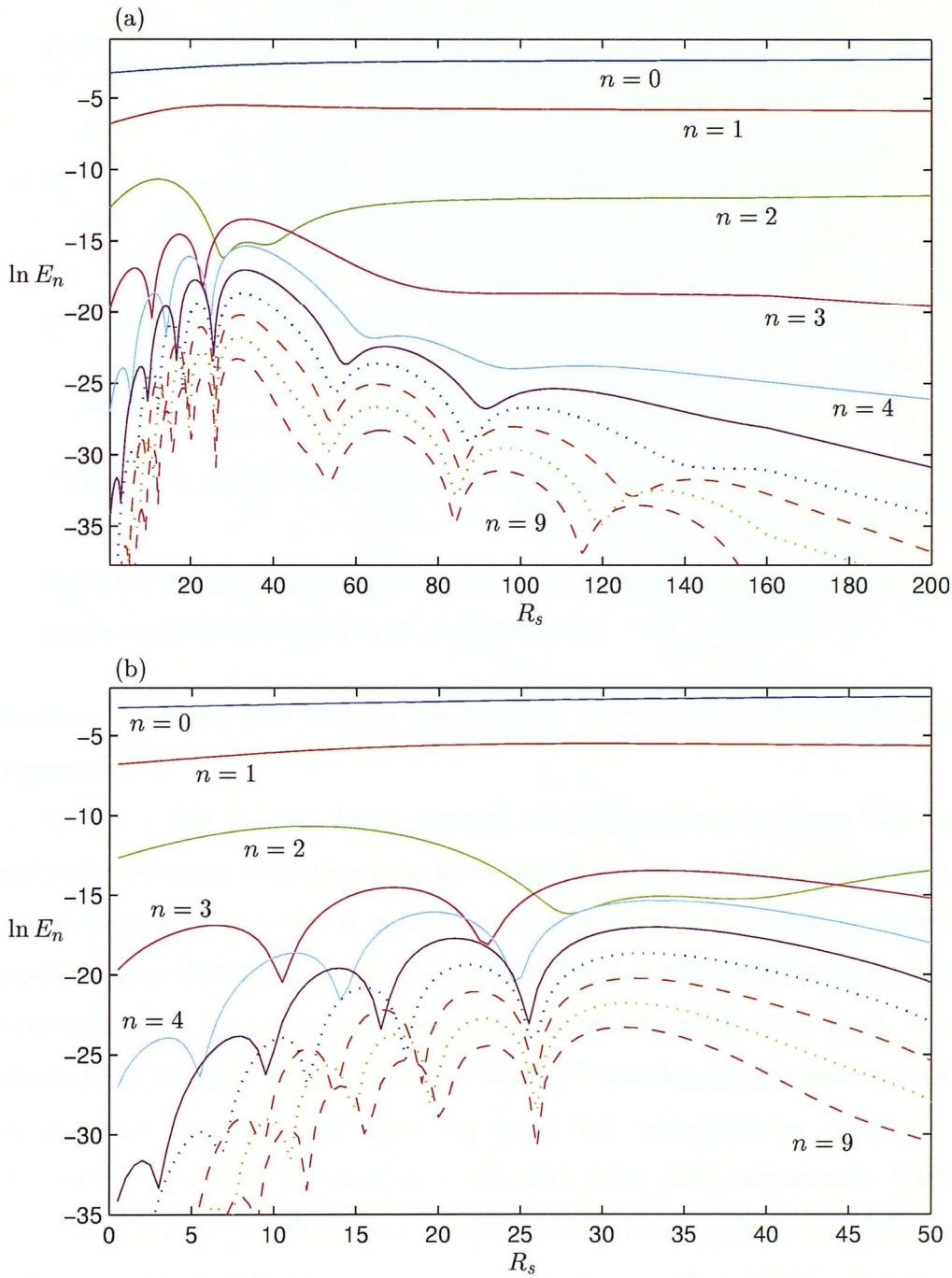


Fig. 2.39: The magnitude of each term $\Psi^{(n)}$ versus Reynolds number. Here the magnitude of each term is given by $E_n = \int \|\Psi^{(n)}\|^2 \, d\eta$.

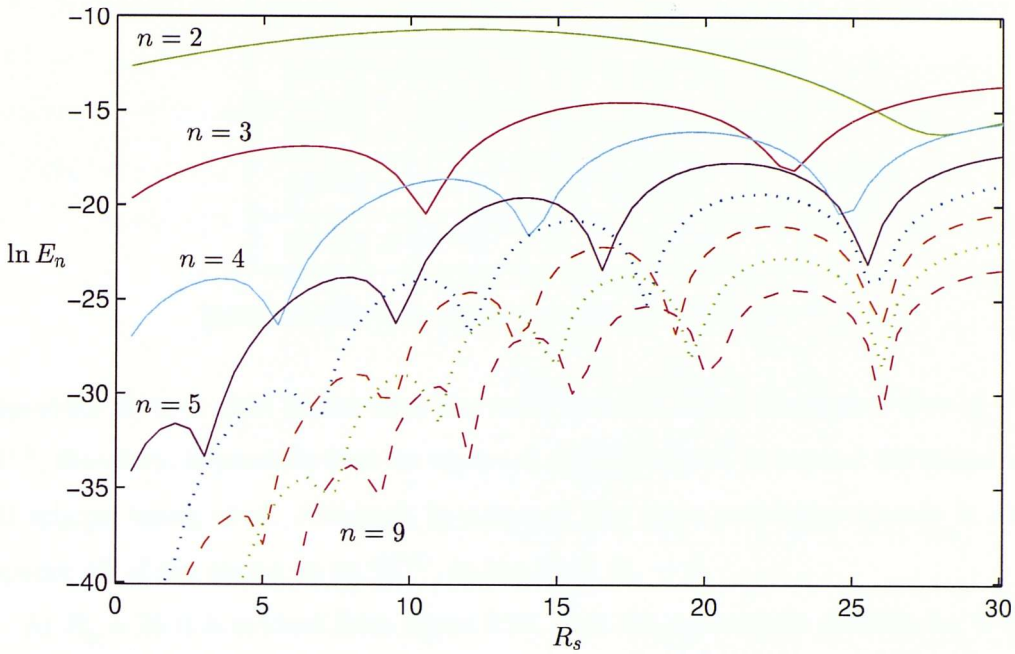


Fig. 2.40: The magnitude of each term $\Psi^{(n)}$ versus Reynolds number. Here the magnitude of each term is given by $E_n = \int \|\Psi^{(n)}\|^2 \, \mathrm{d}\eta$.

numbers, gradually fails because the terms in the expansion become disordered in magnitude.

For $R_s > 300$ (in the steady regime), all of the curves in figure 2.39 level off and each successive correction term is smaller in magnitude than the previous. Due to this restoration of order, it is anticipated that the series solution is a convergent representation of Ψ as $R_s \to \infty$. Since a DNS for Ψ is not available for $R_s > 55$, the series solution is compared with the steady asymptotic result for Ψ as $R_s \to \infty$, see equations (2.50) and (2.51). It is found that $\Psi^{(0)}$ matches its asymptotic form when R_s is greater than 200. The remaining terms that correspond to: $n = 1, 2, 3, 4$, match their asymptotic forms at $R_s \approx 400, 900, 1600, 2800$ respectively. With these five terms (and $R_s > 2800$), the truncated series solution extends well into the core region and the flow field is correctly represented up to $\theta = 160.1°$. Unfortunately, in this high Reynolds number limit, the terms $\Psi^{(n \geqslant 5)}$ cannot be determined to the desired accuracy (i.e. within a 1% maximum relative error along η). However, it is

$\|\Psi^{(n)}\| \approx \|\Psi^{(n+1)}\|$	R_s
$\|\Psi^{(5)}\| \approx \|\Psi^{(6)}\|$	3.2 & {9, 16, 26}
$\|\Psi^{(4)}\| \approx \|\Psi^{(5)}\|$	5.4 & {14.5, 24}
$\|\Psi^{(3)}\| \approx \|\Psi^{(4)}\|$	9.8 & {22}
$\|\Psi^{(2)}\| \approx \|\Psi^{(3)}\|$	25.8 & {44.4}

Table 2.7: The value of R_s at which $\|\Psi^{(n)}\| \approx \|\Psi^{(n+1)}\|$.

important to note that in the high Reynolds number limit, the typical size of $\Psi^{(5)}$ is 10^{-9}; therefore, it possible that an accuracy to this degree, is beyond the scope of the FD scheme being used. Although in contrast, the same numerical scheme *is* able to capture all of the terms up to $\Psi^{(11)}$, in the limit $R_s \to 0$.

At $R_s = 25$ it is evident from figure 2.27, that the asymptotic solution for Ψ (2.42) is no longer valid near $\theta = 0°$, see line A_1. In contrast, the series solution is always valid near $\theta = 0°$, see line S. This implies that the series solution leaves its small-R_s asymptotic representation at $R_s \gtrapprox 25$. Since the small-R_s asymptotic solution for Ψ (2.42) is still valid in the core, this solution is regarded as an outer solution for the flow field. Moreover, since the series solution is valid near $\theta = 0°$, this solution is regarded as the corresponding inner solution. To understand why the asymptotic form of Ψ is only valid in the core, and not near the $\theta = 0°$, let us now study the small-R_s result for Ψ (2.42).

The aim now is to approximate the range of R_s, over which the asymptotic solution is valid. For convenience, the notation t_i is used to denote the $(i+1)^{\text{th}}$ term in the asymptotic expansion (2.42). By examining the magnitudes of the terms t_0 and t_1, an upper bound is derived for R_s, below which, the magnitude of t_0 is larger than t_1. The upper bound obtained from the latter calculation will then provide an threshold, below which, the asymptotic solution is expected to converge. Next, it is necessary to specify a suitable measure of magnitude. The two measures considered here are, the M_1 measure: the maximum difference of $|t_0|$ and $|t_1|$ over η, and the M_2 measure: the difference of the $|t_0|^2$ and $|t_1|^2$ integrated over η (here the vertical bars denote the

absolute value). Although both measures appear to be equivalent, the former is more stringent and will therefore supply a smaller upper bound. On the other hand, the M_2 measure has the benefit that it is much easier to apply.

Since every term in the expansion is odd, it is sufficient to consider the terms t_i on the η-domain (0, 1). Starting with the M_1 measure, we note that t_0 and t_1 do not change sign on (0, 1). Therefore by equating t_0 equal to t_1, the following critical-value roots are obtained:

$$\eta = \begin{cases} \pm 2^{-\frac{1}{2}} \sqrt{-1 - \sqrt{560(\cos\theta R_s)^{-1} + 9}}\,, \\ \pm 2^{-\frac{1}{2}} \sqrt{-1 + \sqrt{560(\cos\theta R_s)^{-1} + 9}}\,. \end{cases} \tag{2.90a,b}$$

Since the first two roots (2.90a) are always complex, it is clear that they do not correspond to an intersection of t_0 with t_1. For $0 < \theta < \pi/2$, the second set of roots (2.90b) lie outside [-1, 1]. Therefore, to make sure that t_0 does not intersect with t_1 (for $\pi/2 < \theta < \pi$), it must be ensured that the roots (2.90b) are also non-real. By enforcing the latter condition, it is found that the Reynolds number must satisfy the inequality

$$R_s < 560/9 \approx 62.22. \tag{2.91}$$

A set of roots similar to (2.90) are obtained by equating t_0 equal to $-t_1$, except in this case $\cos\theta$ is replaced by $-\cos\theta$. From these similar equations, the criteria for 'no intersection' yields the same condition on R_s that has already been derived. Hence, it is concluded that the asymptotic solution for Ψ (2.42), is convergent somewhere below $R_s = 62$.

By generalising this analysis to the first two terms in asymptotic solution for $\Psi^{(n)}$ (2.43), the following roots are obtained by setting t_0^n equal to t_1^n:

$$\eta = \begin{cases} \pm 2^{-\frac{1}{2}} \sqrt{-1 - \sqrt{560(2^{2n}\cos\theta R_s)^{-1} + 9}}\,, \\ \pm 2^{-\frac{1}{2}} \sqrt{-1 + \sqrt{560(2^{2n}\cos\theta R_s)^{-1} + 9}}\,. \end{cases} \tag{2.92a,b}$$

By using a similar argument to the one above, an intersection of the terms t_0^n and t_1^n is avoided provided that

$$R_s < \frac{560}{2^{2n}9}. \tag{2.93}$$

This implies that the radius of convergence of each asymptotic expansion, for $\Psi^{(n)}$ (2.43), is expected to decrease as n increases.

The estimates obtained so far, have been constructed by considering the first two terms t_0 and t_1 only. An extension of this analysis to the terms t_1 and t_2, would require root seeking via numerical methods. Therefore in order to proceed analytically, the M_2 measure is now introduced, which as previously mentioned, is far easier to apply. To compare the result of the M_2 measure with the estimates obtained from the M_1 measure, the terms $|t_0|^2$ and $|t_1|^2$ are integrated over η. Therefore, in order for the first term to be larger than the second, it is necessary that

$$R_s < 7\sqrt{165} \approx 89.91. \tag{2.94}$$

As expected, the above estimate is larger than the equivalent approximation, $R_s < 62.2$, obtained by the M_1 method. However, continuing with the M_2 measure; it is found that the corresponding result for the terms t_0^n and t_1^n, in the asymptotic series for $\Psi^{(n)}$ (2.43) is

$$R_s < \frac{7\sqrt{165}}{2^{2n}}. \tag{2.95}$$

Note, in this case $R_s \sim (1/2)^{2n}$. Moreover, by applying the M_2 measure to the terms t_1^n and t_2^n, in the asymptotic series for $\Psi^{(n)}$; it is found that the second term is larger than the third, provided that

$$2^{4n+3} > \frac{R_s^2}{17325}\left(2292257 - 4978342\ 3^{2n+1} + 996491\ 3^{4n+3}\right), \tag{2.96}$$

and in this case $R_s \sim (2/3)^{2n}$. By continuing this analysis at the next order, the relation for the third and fourth terms is seen to vary as $R_s \sim (3/4)^{2n}$. This trend implies the condition on R_s becomes increasingly relaxed at progressively higher orders. Therefore, it is assumed that the analysis for the first two terms, i.e. $\int |t_0^n|^2 > \int |t_1^n|^2$, supplies the strictest condition for the convergence of the asymptotic solution for $\Psi^{(n)}$ (2.43).

In table 2.8, the agreement of the small-R_s asymptotic solution (2.43) with the numerical solution of $\Psi^{(n)}$, is compared to the predicted values obtained via the M_1 and

n	$\Psi^{(n)} = t_0^n + t_1^n$ approx.	$\Psi^{(n)} = t_0^n + t_1^n + t_2^n$ approx.	M_1 $t_0^n \sim t_1^n$ see (2.93)	M_2 $t_0^n \sim t_1^n$ see (2.95)	M_2 $t_1^n \sim t_2^n$ see (2.96)
0	27.0	12.0	62.22	89.91	181.2
1	2.70	5.00	15.55	22.48	60.51
2	1.00	2.60	3.88	5.620	26.16
3	0.22	0.90	0.9722	1.405	11.59
4	0.20	0.70	0.2430	0.3512	5.149
5	≈ 0.06	0.30	0.0608	0.0878	2.288
6	≈ 0.012	0.14	0.0152	0.0220	1.01704

Table 2.8: The first two columns of data record the maximum value of R_s, to which the small-R_s asymptotic solution of $\Psi^{(n)}$ (2.43), is in agreement with the numerical solution for $\Psi^{(n)}$ (maximum error of 1% along each η-profile). The remaining three columns contain the estimated values at which the terms in the asymptotic series (2.43) become disordered.

M_2 measures. By using three terms from the asymptotic solution i.e. the approximation $\Psi^{(n)} = t_0^n + t_1^n + t_2^n$, it is found that the agreement for each n (with the numerical solution of $\Psi^{(n)}$) always extends beyond the corresponding two term approximation ($\Psi^{(n)} = t_0^n + t_1^n$), except for the case $n = 0$. For $n = 0$, the inclusion of the third term actually reduces the range of agreement. For $n \geqslant 4$, the results in column one are predicted extremely well by the M_1 and M_2 measures for $t_0^n \sim t_1^n$. The M_2 measure for $t_1^n \sim t_2^n$ does not agree so well with the data in the second column, but the estimates supplied here are still upper bounds.

In conclusion, this analysis demonstrates that the series terms $\Psi^{(n)}$ leave their small-R_s asymptotic forms, at successively smaller Reynolds numbers as n is increased. Moreover, the analytical work in this section shows that all the critical values of $t_0^n \sim t_1^n$, see (2.93), are smaller than the corresponding value of $t_0 \sim t_1$ viz $R_s \approx 62.22$. Accordingly, from this analysis one can expect that the asymptotic solution (2.42) is a valid representation for Ψ in the core region (up to $R_s \approx 62.22$). On the other

hand, the same analysis indicates that the series solution is expected to deviate from this asymptotic representation, at a much lower value of R_s. The latter result is also confirmed by our numerical work, a summary of which, now follows. At $R_s = 27$, it is clear from figure (2.27) (lines A_1 and A_2) that the flow in the range $40° < \theta < 110°$, is still governed by the small-R_s asymptotic solution for Ψ (2.42). However, since all the terms $\Psi^{(n)}$ leave their small-R_s asymptotic forms at $R_s \geqslant 27$, see table 2.8, it is evident that the series solution cannot represent the flow in the core region ($40° < \theta < 110°$). Despite this fact, it is still envisaged that the first few terms in the series solution, still play an important role in determining the flow field close to the axis of oscillation.

In figure 2.27, it is seen that the agreement between the DNS and the series solution eventually decays to zero as R_s is increased. By analysing the DNS for Ψ, it is found that deterioration of the latter agreement, for $R \gtrapprox 40$, is brought about by the development of wavy/discontinuous θ-profiles, see figures 2.28 and 2.29. However, for large Reynolds numbers the series solution converges to its steady asymptotic form (2.50) and represents the flow field well into the core region $0° \leqslant \theta \leqslant 161°$. The recovery of the series representation for $R_s \gg 1$, supports the idea that the first few terms in the expansion are still important in determining the flow near $\theta = 0°$ when $R_s = O(1)$.

In the next section the unsteady regime is investigated by adopting a numerical approach that decomposes each term $\Psi^{(n)}$ into a Fourier series in time.

2.4.4 Fourier series decomposition

In §2.4.2 a linear stability analysis was used to show that the terms $\Psi^{(n)}$ cannot be computed by time marching. To avoid the instigation of growing perturbations, the search for periodic solutions is now continued by representing each term $\Psi^{(n)}$ as a Fourier series in time. Accordingly, each term in the series is expanded in the from

$$\Psi^{(n)}(\eta, \tau) = \sum_{k=-\infty}^{\infty} \Psi^{(n,\,k)} \exp(ik\Omega\tau), \tag{2.97}$$

where $i = \sqrt{-1}$ and Ω is an eigenvalue. By substituting the above expansion into (2.37), the governing equation for $\Psi^{(n,k)}$ is found to be

$$\Psi^{(n,k)}_{\eta\eta} ik\Omega = \frac{1}{R_s}\Psi^{(n,k)}_{\eta\eta\eta\eta} + \sum_{l=0}^{n}\sum_{j=-\infty}^{\infty}(2l+1)\left[\Psi^{(l,j)}\Psi^{(n-l,k-j)}_{\eta\eta\eta} - \Psi^{(n-l,j)}_{\eta}\Psi^{(l,k-j)}_{\eta\eta}\right], \quad (2.98a)$$

$$\left.\begin{aligned} \Psi^{(n,k)}(\mp 1) = 0, \quad \Psi^{(n,k)}_{\eta}(\mp 1) = 0 \quad \text{for} \quad k \neq 0, \\ \Psi^{(n,0)}_{\eta}(\mp 1) = \frac{(-1)^{n+1}}{(2n+1)!}. \end{aligned}\right\} \quad (2.98b)$$

Since $\Psi^{(0)}$ is computed by time marching, the eigenvalue Ω is obtained directly from its Fourier series representation. Moreover, it is still possible to compute each term $\Psi^{(n)}$ in a recursive manner i.e. there is no need for a simultaneous solver. To numerically evaluate each term $\Psi^{(n)}$, it is necessary to invert a large non-sparse matrix. Therefore, in order to minimise memory consumption, the result $\Psi^{(n,\,k)} = \Psi^{*(n,\,-k)}$ (for real solutions) is used to reduce the computational expense, here the asterisk denotes complex conjugate. In order to evaluate the terms $\Psi^{(n,k)}$ numerically, it is necessary to truncate the Fourier expansion (2.97). Accordingly, a finite summation is now assumed over the interval $-K \leqslant k \leqslant K$. The numerical results presented in this section, have been computed with: $K = 15,\ 24,\ 40$ (i.e. 31, 49 and 81 Fourier modes), and 100 steps in the η-interval [-1, 1]. The calculation with $K = 40$ and $\Delta\eta = 2/100$ is expensive and requires around 600MB of computer memory.

The aim now is to investigate the unsteady regimes of the series solution without time marching. The unsteady asymmetric regime of $\Psi^{(0)}$ arises in the interval $53 < R_s < 82$, see diagram 2.6. In this range of R_s, the leading order term $\Psi^{(0)}$ enters a period-doubling cascade and consequently becomes chaotic. In view of this behaviour, it is expected that the series solution will also turn chaotic at $R_s \approx 82$. In contrast, the unsteady symmetric regime of $\Psi^{(0)}$ arises at $R_s \approx 170$, see figure 2.10. In this case it is envisaged that the series solution will have a time period that increases linearly with R_s.

Numerical results

At $R_s = 55$ in the asymmetric regime, the energy spectrum of each term $\Psi^{(n)}$ indicates that each successive Fourier mode is larger than the previous. Upon increasing the number of Fourier modes from $K = 24$ to $K = 81$, this trend remains unchanged. In an effort to promote convergence, various Reynolds numbers were tested in the range $53 \leqslant R_s \leqslant 82$ and the size of $\Delta\eta$ was also decreased (with $K < 40$). Despite an exhaustive search, the series remained divergent in all the cases considered. However, it is interesting to note that each term $\Psi^{(n\neq 0,k)}$ is found to have an even η-profile. Moreover, this spatial feature is inline with the eigenfunctions, $\Phi^{(n)}$, found in the time marching procedure, see figure 2.23. Despite this characteristic similarity, it is unclear if the instability present in this numerical approach, is related to the one encountered in the time marching calculation.

In order to suppress the growing profiles of the terms $\Psi^{(n)}$ in asymmetric regime, the symmetric solution of $\Psi^{(0)}$ was forced and corresponding unsteady regime was studied with $R_s > 170$. At $R_s = 300$, the time period of the flow is 9.40, which is relatively small, and therefore 31 Fourier modes were used to sample the variation in this period. In figure 2.41(a), it is seen that the spectrum of the first three terms decay as k increases; this suggests that these terms may have converged. In order to see if these terms had converged, the energy spectrum of each term was monitored as the number of Fourier modes were increased from 31, see figures 2.41(b)–(c). From the latter diagrams it is seen that the terms $\Psi^{(0)}$, $\Psi^{(1)}$ and $\Psi^{(2)}$ remain unchanged as the number of Fourier modes are increased to 49 and 81. This result confirms that 31 modes are sufficient for the first three terms in the expansion. However, from figure 2.41(c) it is clear that the magnitudes of terms increase with n i.e. $\|\Psi^{(0)}\| < \|\Psi^{(1)}\| < \|\Psi^{(2)}\|$. This once again implies that the series is disordered and therefore invalid at $R_s = 300$. It is also worth noting, that with 49 modes, the spectrum of $\Psi^{(3)}$ does not decay all the way to zero, see figure 2.41(b). If the same spectrum is computed with 81 modes, figure 2.41(c), the decay to zero appears almost complete. Although a converged result for the term $\Psi^{(3)}$ is desirable, the numerical expense involved with this calculation is

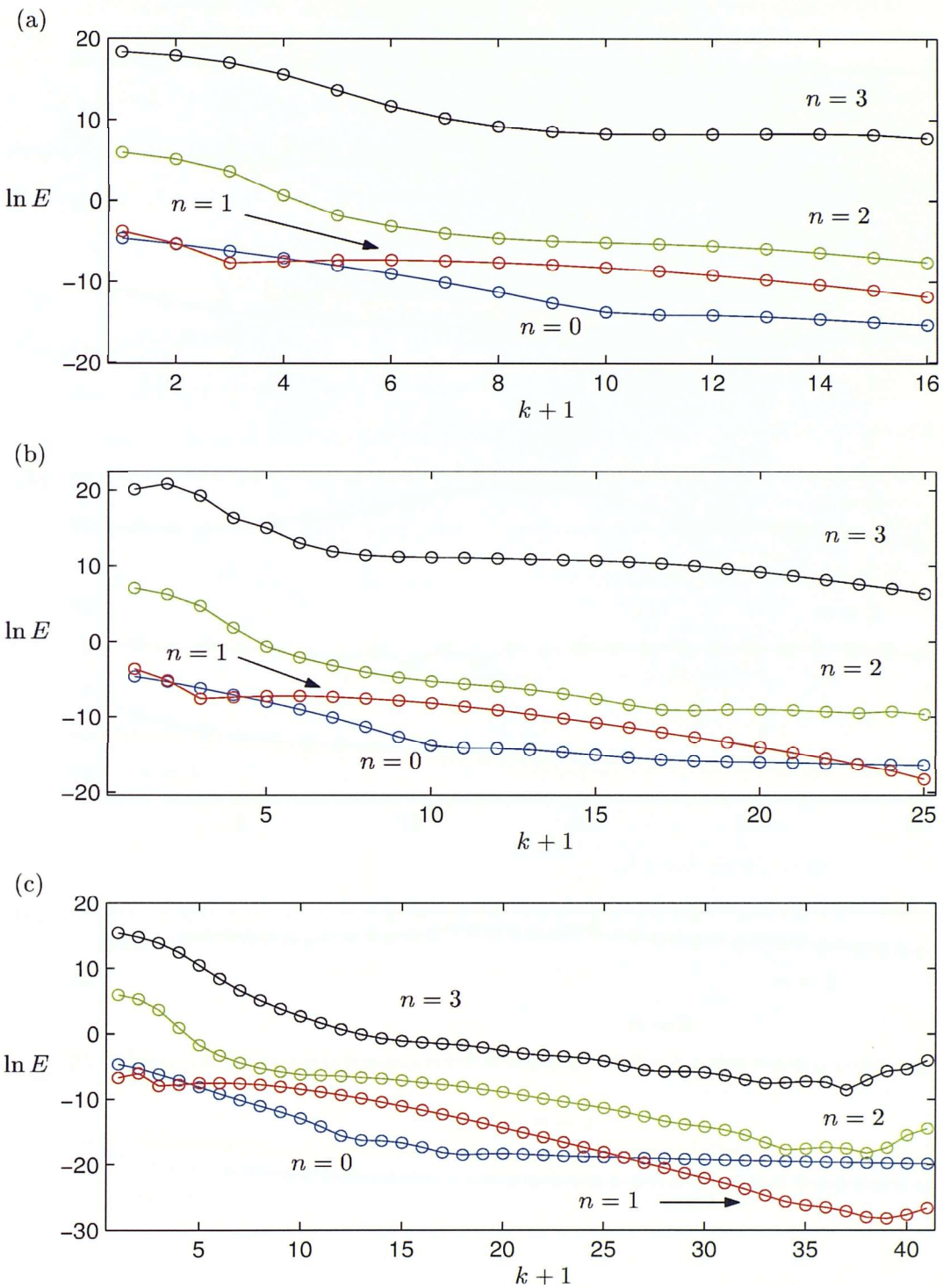


Fig. 2.41: Ψ_{sym}; the energy spectra of the Fourier modes at $R_s = 300$ using: (a) $K = 15$, (b) $K = 24$ and (c) $K = 40$. Here $E = \int \|\Psi^{(n,k)}\|^2 \mathrm{d}\eta$.

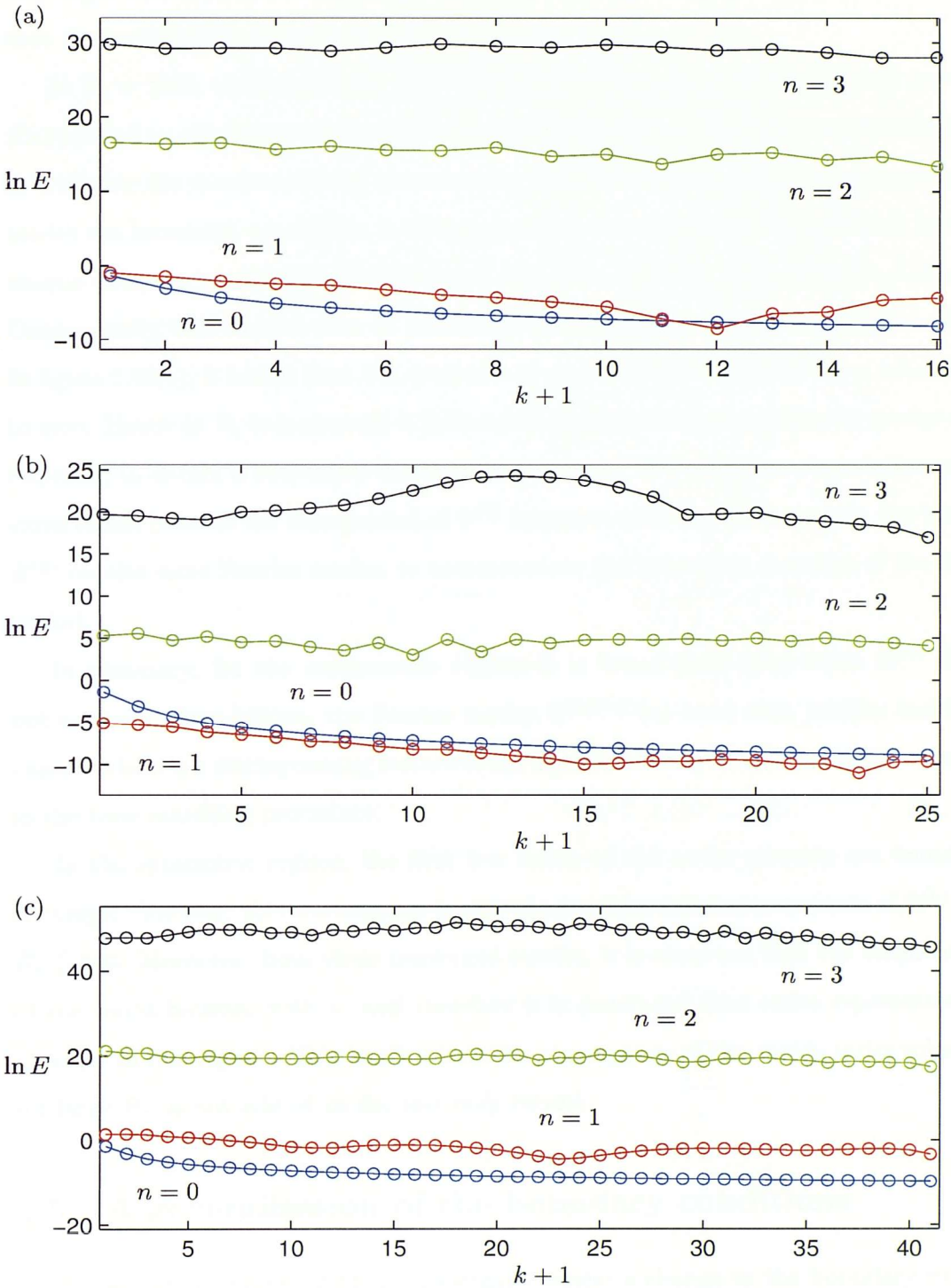


Fig. 2.42: Ψ_{sym}; the energy spectra of the Fourier modes at $R_s = 1600$ using: (a) $K = 15$, (b) $K = 24$ and (c) $K = 40$. Here $E = \int \|\Psi^{(n,k)}\|^2 \mathrm{d}\eta$.

very high. Moreover, the use of this term is rather limited because it is already clear that the series solution appears to be diverging.

At $R_s = 1600$, the time period of $\Psi^{(0)}$ is 112.57; moreover, it is found that 31 modes are required to obtain a converged representation for this term, see figures 2.42(a)–(b). In contrast, the spectrum of the second term, $\Psi^{(1)}$, continues to vary as the number of modes are increased, see figures 2.42(a)–(c). Since this spectrum does not lock into a unique decaying profile, it is deduced that this term does not converge with $K \leqslant 40$. Consequently, this implies that 81 modes are insufficient for the terms $\Psi^{(2)}$ and $\Psi^{(3)}$. In figure 2.42(c), it is seen that the spectrum of each term $\Psi^{(2)}$ and $\Psi^{(3)}$ does not decay to zero. Hence as R_s is increased, it is found that successively more Fourier modes are required, to obtain a converged solution for the terms $\Psi^{(n)}$. This result is inline with expectation because the time period of $\Psi^{(0)}$ increases with R_s; consequently, the terms $\Psi^{(n)}$ require more Fourier modes, to accommodate the increasing duration of the time period.

In summary, for the asymmetric regime it is found that every term $\Psi^{(n)}$ does not converge. In addition, the Fourier modes $\Psi^{(n\neq 0,k)}(\eta)$ have even profiles and this characteristic is a distinguishing feature of the eigenfunctions, $\Phi^{(n)}$, observed previously in the time marching procedure.

In the symmetric regime, the first few terms of the series solution are found to converge. However, this convergence is only observed for small time periods of $\Psi^{(0)}$ i.e. $R_s \lessapprox 500$. Moreover, from these converged results, it is observed that the magnitudes of the terms increase with n, and therefore it is concluded that series representation diverges in this regime. This implies that the convergence of the *steady* series solution for large R_s, is not echoed in the *unsteady* regime.

2.5 A generalisation of the boundary conditions

In this section, equation (2.33) is investigated under a change to the boundary conditions. Here the aim is to understand if a change to the boundary conditions qualitatively alters the nature of the solutions seen so far. The derivative conditions at the

walls are now changed to

$$\Psi_\eta = -\theta \exp(-\lambda\theta^2) \quad \text{at} \quad \eta = \mp 1,$$

where $\lambda(>0)$ is a constant. With this change to the boundary condition, the periodicity in the θ-direction is eliminated. The current generalisation of the cylinder problem will henceforth be referred to as the *modified problem.*

In this modified problem, Ψ is no longer periodic in θ, and therefore it is not possible to use a PS numerical method to solve the equation of motion (2.100). Instead, the VSF method proposed by E & Jian-Guo [98] is used. In this explicit scheme, the governing equations are represented by a FD approximation and the vorticity is updated at the boundaries. By letting D denote the three-point central difference formula for $\partial^2_{\eta\eta}$, the vorticity update (Thom's formula) at $\eta = -1$ is given by

$$\omega_{i,0} = \frac{2}{\Delta\eta^2}\Psi_{i,1} + \frac{2}{\Delta\eta} i\Delta\theta \exp(-\lambda i^2 \Delta\theta^2), \qquad D\Psi_{i,j} = \omega_{i,j}.$$

Here, i and j denote the grid points in the θ and η directions respectively, and $j = 0$ corresponds to the boundary at $\eta = -1$ (the update at $\eta = 1$ is similar). In this calculation, the small-R_s asymptotic solution for $\bar{\Psi}$, see (2.105), is used as an initial condition and the numerical solution is time marched under a fourth-order Runge-Kutta scheme. By letting the superscript k denote the iteration at the present timestep, the current values of the vorticity and stream function can be expressed as ω^k and Ψ^k respectively. Given the current values of $\{\omega^k, \Psi^k\}$, the values of $\{\omega^{k+1}, \Psi^{k+1}\}$ are computed via the following Runge-Kutta procedure: at $\left\{\begin{smallmatrix} 1\leqslant i\leqslant I-1, \\ 1\leqslant j\leqslant J-1 \end{smallmatrix}\right\}$ we compute ω_n by

$$\frac{\omega_1 - \omega^k}{\frac{1}{2}\Delta\tau} + (\boldsymbol{u}^k\cdot\boldsymbol{\nabla})\omega^k = \frac{1}{R_s} D\omega^k, \qquad \Psi_1 = D_0^{-1}\omega_1, \quad \text{and then } \omega_1|_{j=0,\,J} \text{ is updated,}$$

$$\frac{\omega_2 - \omega^k}{\frac{1}{2}\Delta\tau} + (\boldsymbol{u}_1\cdot\boldsymbol{\nabla})\omega_1 = \frac{1}{R_s} D\omega_1, \qquad \Psi_2 = D_0^{-1}\omega_2, \quad \text{and then } \omega_2|_{j=0,\,J} \text{ is updated,}$$

$$\frac{\omega_3 - \omega^k}{\Delta\tau} + (\boldsymbol{u}_2\cdot\boldsymbol{\nabla})\omega_2 = \frac{1}{R_s} D\omega_2, \qquad \Psi_3 = D_0^{-1}\omega_3, \quad \text{and then } \omega_3|_{j=0,\,J} \text{ is updated,}$$

$$k_4 = \Delta\tau(-(\boldsymbol{u}_3\cdot\boldsymbol{\nabla})\omega_3 + \frac{1}{R_s} D^{-1}\omega_3), \quad \omega^{k+1} = \tfrac{1}{3}(-\omega^k + \omega_1 + 2\omega_2 + \omega_3) + \tfrac{1}{6}k_4,$$

$\Psi^{k+1} = D_0^{-1}\omega^{k+1}$, and finally $\omega^{k+1}|_{j=0,\,J}$ is updated after the last inversion.

Here

$$\boldsymbol{u} = (\Psi_\eta, -\Psi_\theta), \quad \boldsymbol{\nabla} = (\partial_\theta,\ \partial_\eta) \quad \text{and} \quad \omega|_{i=0,I} = \omega_n|_{i=0,I} = 0. \tag{2.99}$$

The zero subscript in D_0^{-1}, is used to highlight the important fact that the boundary value of the vorticity, $\omega_n|_{j=0,J}$, must be updated in accordance with Thom's formula after each inversion ($\Psi_n = D_0^{-1}\omega_n$). The exact details regarding the derivation of the VSF formulation, and the alternative primitive variable formulation (the classical MAC scheme), are summarised in the original paper by E & Jian-Guo [98].

Continuing with our analysis, it is clear that the choice of λ, will inevitably affect the size of the θ-domain used in the numerical scheme i.e. Ψ will decay to zero over a smaller domain, if λ is made more positive. Accordingly, the choice of λ will also affect the number of terms required to give an adequate representation of the flow in the θ-direction. It is now shown that the involvement of λ can be scaled out of the governing equations, to give a canonical problem. The governing equations for Ψ, with the altered boundary conditions, are

$$\Psi_{\eta\eta\tau} = \frac{1}{R_s}\Psi_{\eta\eta\eta\eta} + \Psi_\theta\Psi_{\eta\eta\eta} - \Psi_\eta\Psi_{\eta\eta\theta}, \tag{2.100a}$$

$$\Psi(\theta = 0) = 0, \quad \Psi(\eta = \mp 1) = 0, \quad \Psi_\eta(\eta = \mp 1) = -\theta\exp\left(-\lambda\theta^2\right). \tag{2.100b}$$

With the following change of variables:

$$\xi = \theta\lambda^{1/2}, \qquad \bar{\Psi} = \Psi\lambda^{1/2}, \tag{2.101}$$

the canonical form of (2.100) is then given by

$$\bar{\Psi}_{\eta\eta\tau} = \frac{1}{R_s}\bar{\Psi}_{\eta\eta\eta\eta} + \bar{\Psi}_\xi\bar{\Psi}_{\eta\eta\eta} - \bar{\Psi}_\eta\bar{\Psi}_{\eta\eta\xi}, \tag{2.102a}$$

$$\bar{\Psi}(\xi = 0) = 0, \quad \bar{\Psi}(\eta = \mp 1) = 0, \quad \bar{\Psi}_\eta(\eta = \mp 1) = -\xi\exp\left(-\xi^2\right). \tag{2.102b}$$

Accordingly, $\bar{\Psi}$ is expanded in the form

$$\bar{\Psi} = \sum_{n=0}^{\infty} \bar{\Psi}^{(n)}(\eta, \tau)\,\xi^{2n+1}. \tag{2.103}$$

By substituting the above expansion into (2.102), it is found that the terms in the series are governed by the equations

$$\bar{\Psi}^{(n)}_{\eta\eta\tau} = \frac{1}{R_s}\bar{\Psi}^{(n)}_{\eta\eta\eta\eta} + \sum_{i=0}^{n}(2i+1)\left[\bar{\Psi}^{(i)}\bar{\Psi}^{(n-i)}_{\eta\eta\eta} - \bar{\Psi}^{(n-i)}_{\eta}\bar{\Psi}^{(i)}_{\eta\eta}\right], \tag{2.104a}$$

$$\bar{\Psi}^{(n)}(\eta = \mp 1) = 0, \quad \bar{\Psi}^{(n)}_{\eta}(\eta = \mp 1) = \frac{(-1)^{n+1}}{n!}. \tag{2.104b}$$

Since λ has been scaled out of the governing system of equations, it is sufficient to compute a single numerical solution for each term $\bar{\Psi}^{(n)}$ at a fixed value of R_s. In this way, the effect of λ is implicitly incorporated in the series expansion (2.103). Moreover, it is now clear that λ plays a passive role in the physical interpretation of the flow. However, the added flexibility of the parameter λ, can in practice, be used to increase/decrease the size of computational domain associated with equation (2.102).

Before any numerical results are discussed, it is convenient to present the steady state asymptotic solutions for $\bar{\Psi}$ and $\bar{\Psi}^{(n)}$. Moreover, since it is found that the DNS of (2.102) is always η-symmetric, only the η-symmetric asymptotic solutions of $\bar{\Psi}$ and $\bar{\Psi}^{(n)}$ are presented.

2.5.1 Steady asymptotic solutions

In this section, the symmetric asymptotic solutions of (2.102) and (2.104) are presented. As before, these solutions will setup the necessary framework for analysing the numerical results that follow.

For small values of R_s, $\bar{\Psi}$ is expanded in a regular R_s-power series and then substituted into (2.102) (as in §2.3.1). By solving the appropriate equation at each order, the unique small-R_s solution for $\bar{\Psi}$ is calculated to be

$$\begin{aligned}\bar{\Psi}(\eta,\xi) = &-\frac{1}{2}\xi\exp(-\xi^2)(\eta^3-\eta) - \frac{R_s}{280}\xi(2\xi^2-1)\exp(-2\xi^2)\eta(\eta^2-1)^2(2+\eta^2)\\
&- \frac{R_s^2}{7761600}\xi\exp(-3\xi^2)\eta(\eta^2-1)^2\Big\{(-402+3003\xi^2-2538\xi^4)\\
&+\eta^2(100+1694\xi^2-996\xi^4)+7\eta^4(86-539\xi^2+474\xi^4)\\
&+84\eta^6(-1-11\xi^2+6\xi^4)\Big\}+\ldots\end{aligned} \tag{2.105}$$

Similarly, by expanding each term $\bar{\Psi}^{(n)}$ in an analogous manner, the corresponding series terms are given by

$$\bar{\Psi}^{(n)} = \frac{(-1)^{n+1}}{n!}\eta(\eta^2-1) + R_s\frac{(-2)^n}{280n!}(n+1)\eta(\eta^2-1)^2(2+\eta^2) + O(R_s^2). \quad (2.106)$$

Although the small-R_s solution (2.105) is formerly valid for $R_s \ll 1$; in view of our previous analysis (of equation (2.33)), it is inferred that (2.105) will also be valid for $R_s > 1$. Moreover, for $R_s > 1$, it is expected that (2.105) will represent an outer solution for $\bar{\Psi}$ in the ξ-direction. In view of the results obtained for the cylinder problem, it is anticipated that the terms $\bar{\Psi}^{(n)}$, will quickly depart from their small-R_s asymptotic forms as R_s is increased. After this dissociation is complete, it is expected that only the first few terms in the series will constitute part of a valid expansion i.e. a truncation of the higher order terms will be required. Accordingly, it is predicted that the series solution will only represent the flow for small values of ξ. For large values of R_s, it is expected that the terms $\bar{\Psi}^{(n)}$ will converge to their asymptotic forms; hence leading to a recovery of the series representation.

For large Reynolds numbers, $\bar{\Psi}$ is expanded in powers of R_s^{-1}, see (2.44). By solving the governing equations at each order, it is found that the asymptotic forms of $\bar{\Psi}$ and $\bar{\Psi}^{(n)}$ are given by:

$$\bar{\Psi}(\eta,\xi) = \pi^{-1}\xi\exp(-\xi^2)\sin\pi\eta + O(R_s^{-1}), \quad (2.107)$$

$$\bar{\Psi}^{(n)} = \frac{(-1)^n}{n!\pi}\sin\pi\eta + O(R_s^{-1}). \quad (2.108)$$

By calculating the error parameter Δ_e (see (2.88)), it is estimated that 32 terms are required to obtain a converged representation of $\bar{\Psi}$ from $\xi = 0$ to $\xi = \pi$ c.f 6-7 terms for the cylinder problem. The decision to estimate the required number of terms over the ξ-range $[0,\ \pi]$, was made purely to keep inline with the same range used for the cylinder problem (note, the 'infinity' location used in the numerics is $\xi = \xi_\infty = 2\pi$ and certainly $\bar{\Psi}_\eta \not\to 0$ at $\xi = \pi$). Due to the fact that 32 terms are required for this new system, it may appear that the rate of convergence, of this new series, is now considerably slower than the corresponding series for the oscillating cylinder. This is

not entirely true, since the requirement of more terms is partly due to the scaling out of λ. Once the series has converged to a fixed angle in ξ-space, the corresponding angle in θ-space is found by using relation (2.101). Hence if the series solution converges to $\xi = \pi$ with $\lambda < 1$, then the corresponding angle in θ-space is greater than $\theta = \pi$.

2.5.2 Numerical Results

In the VSF scheme, the ξ-domain $[0, 2\pi]$ is divided into 256 equal partitions and the typical size of the timestep is $\Delta\tau = 7.5 \times 10^{-3}$. Moreover, the step size in the η-direction is taken as $\Delta\eta = 2/100$. As before, it is convenient to define the integer variable $n_\xi = 256\ \xi/2\pi$, which denotes the partition number in the ξ-domain. Since the current numerical method is based on a FD scheme (in both spatial directions), the results produced by the explicit VSF method, are not guaranteed to be as accurate as those obtained by the PS method. For this reason, the series solution is now said to agree with the DNS if the maximum error is within 2% (as opposed to the previous value of 1% see page 93).

In accordance with our previous work, it is found that the DNS of equation (2.102) is steady and η-symmetric at all (computable) values of R_s, for example see figure 2.43. As the Reynolds number is decreased from $R_s = 25$, it is necessary to reduce the size of timestep from 7.5×10^{-3}, and in the most severe case, $R_s = 0.5$, a value of $\Delta\tau = 1 \times 10^{-4}$ is required. Further time marching below $R_s = 0.5$ is desirable, but this requires an exceptionally small timestep. Fortunately, there is no need to time march below $R_s = 0.5$ and it is now explained why this is the case. From figure 2.45, it is observed that the agreement of the asymptotic solution (2.105) and the DNS, always extends from the line A_{256} to the line $\xi = \xi_\infty$. In particular, for $R_s \leqslant 12$ it is found that the line A_{256} merges with $\xi = 0$ and in this case, the asymptotic solution (2.105) matches the DNS exactly. Since the asymptotic solution is unique in the limit $R_s \to 0$, further time marching below $R_s = 0.5$ is unnecessary, and therefore the asymptotic solution can be used as a valid representation (over the ξ-range $[0, \xi_\infty]$) for $R_s \leqslant 12$.

In figure 2.45, the line S_{256} indicates that for $R_s < 5$, the series solution rapidly

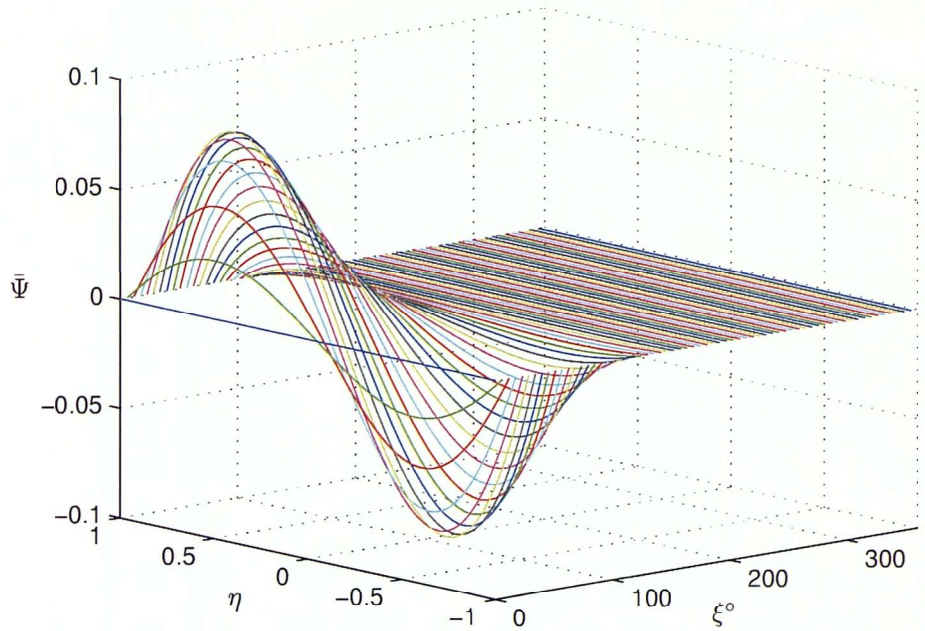


Fig. 2.43: The DNS for $\bar{\Psi}$ at $R_s = 40$. This solution is calculated under the VSF formulation with $\Delta\xi = 2\pi/256$, $\Delta\eta = 2/100$ and $\Delta\tau = 7.5 \times 10^{-3}$.

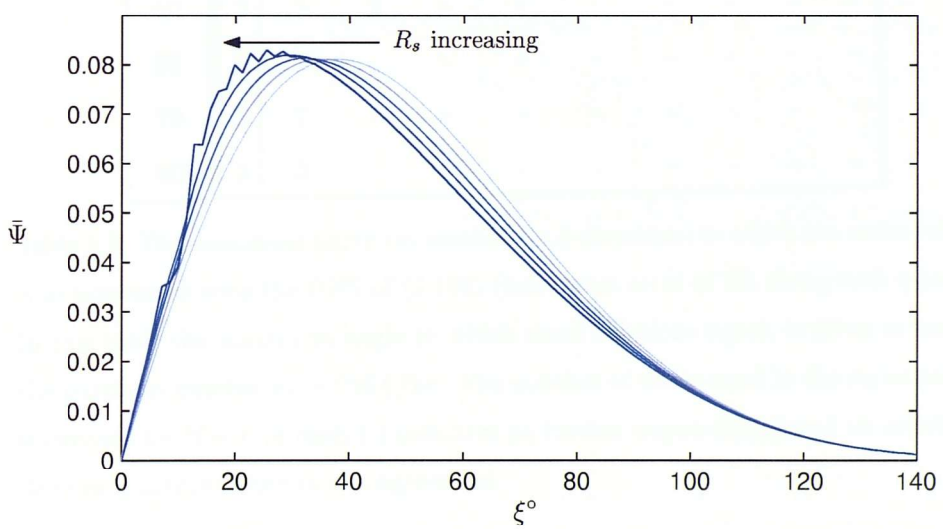


Fig. 2.44: The DNS for $\bar{\Psi}$ at $R_s = 10,\ 20,\ 30,\ 40,\ 50$ with $\Delta\xi = 2\pi/256$. Here η is fixed at 0.6 and the timestep is $\Delta\tau = 7.5 \times 10^{-3}$. Moreover, note that ξ is evaluated in degrees, so that a direct comparison with cylinder problem is possible.

$N=$	0	1	2	3	4	5	6	7	8	9
R_s										
0.5	1	19	19	35	33*	44	46	48	49	-
5	2	16	21	24	25	-	-	-	-	-
10	3	15	22	20*	20	-	-	-	-	-
15	3	14	21	19*	19	-	-	-	-	-
20	3	15	21	21	-	-	-	-	-	-
25	3	17	14*	15	15	-	-	-	-	-
30	3	19	12*	12	-	-	-	-	-	-
35	3	13	12*	12	-	-	-	-	-	-
40	4	6	6	-	-	-	-	-	-	-
45	5	4*	4	-	-	-	-	-	-	-
50	2	3	3	-	-	-	-	-	-	-
60	2	2	-	-	-	-	-	-	-	-
70	2	2	-	-	-	-	-	-	-	-
80	3	3	-	-	-	-	-	-	-	-

Table 2.9: The maximum partition number (in ξ-direction) to which the series solution is in agreement with the DNS of (2.102) (maximum error of 2% along each η-profile). In this table the maximum angle to which these solutions agree, is given in terms of the partition number $n_\xi = 256\ \xi/2\pi$. The number of terms used in the series solution is denoted by $N+1$. A dash (-) indicates no further improvement and an asterisk (*) denotes a deterioration in the agreement.

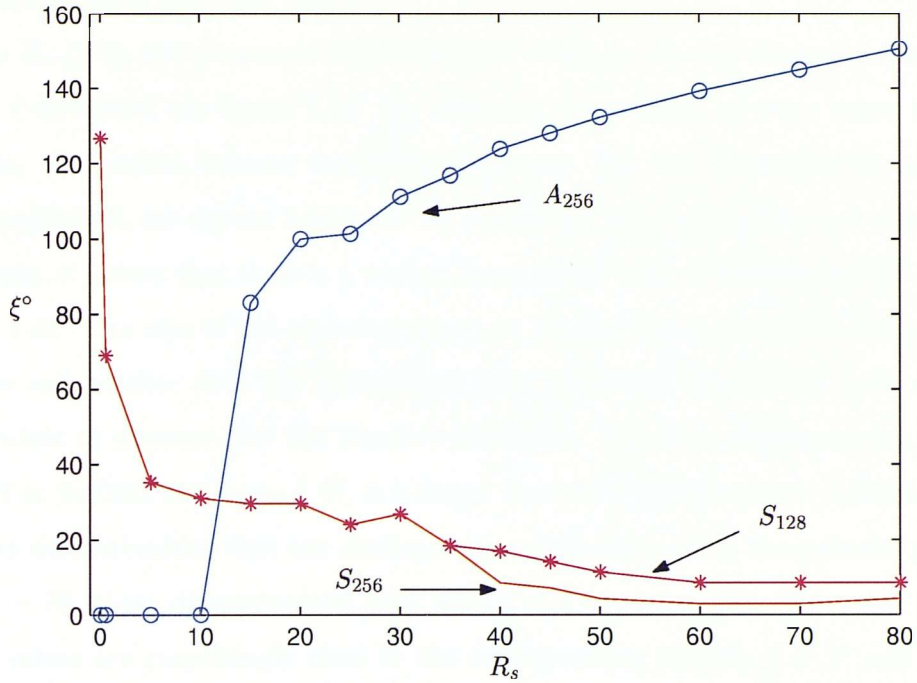


Fig. 2.45: The agreement of the DNS with: 1) the series solution, and 2) the asymptotic solution for small R_s (2.105). The lines S_{256} and S_{128} represent the extent to which the series solution matches with $\bar{\Psi}$; the subscripts denote the number of steps used (in ξ-direction) in the numerical calculation for $\bar{\Psi}$. The line A_{256} shows where the asymptotic solution (2.105) first begins to match with $\bar{\Psi}$; this agreement is always found to extend from line A_{256}, up to $\xi_\infty = 360°$. The corresponding line A_{128} is identical to A_{256}.

converges to its asymptotic form. However at $R_s = 0.5$, it is evident that the series solution does not represent a complete solution for $\bar{\Psi}$ over the full ξ domain, see table 2.9. Despite this fact, if the series solution is compared to the small-R_s asymptotic solution of $\bar{\Psi}$ (2.105), an agreement to $\xi = 126.6°$ is obtained with $R_s = 0.01$. This indicates that the series representation improves as R_s is decreased below $R_s = 0.5$. For $R_s > 30$, it is seen in figure 2.45 (lines S_{128} and S_{256}), that the series solution is only valid near $\xi = 0°$, as predicted. Moreover, from table 2.9 it is observed that the first two terms, $\bar{\Psi}^{(0)}$ and $\bar{\Psi}^{(1)}$, still form part of valid expansion at $R_s = 35$. In this case, the higher order terms are invalid because the agreement with the DNS

deteriorates upon including them.

For $R_s \gtrapprox 45$, the numerical solutions for $\bar{\Psi}$ begin to develop discontinuous profiles in the ξ-direction, see figure 2.44. By reducing the number of steps taken in the ξ-domain, the profiles become increasingly smooth, but the discontinuities are never fully eradicated, see figures 2.46-2.48. By increasing the number of steps taken in the ξ-domain, it is seen that there is a weaker decay of the high modes in the FFT of $\bar{\Psi}$, see figure 2.49. The size of the timestep does not change the shape of the discontinuous profiles and neither does the duration of time marching. Hence the error does not accumulate or disperse over the iterative procedure. Moreover, by decreasing $\Delta\xi$ from $2\pi/128$ to $2\pi/256$, see figure 2.47, it is found that the ξ-profiles at $\eta = 0.6$ develop two distinct discontinuities that are similar to the ones observed in the cylinder problem. At $R_s = 70$, these discontinuities arise near $\xi = 8°$ and $\xi = 18°$. Note also, that the latter values are surprisingly close to the corresponding results: $\theta = 9°$ and $\theta = 20°$ associated with the cylinder problem. If $\Delta\xi$ is decreased from $2\pi/256$ to $2\pi/512$; at $R_s = 60$, two distinct slanted regions are formed near $\xi = 7°$ and $\xi = 15°$. These slanted regions are akin to the plateaus observed at $R_s = 55$ for the cylinder problem, see figure 2.37 on page 108. Since there is an increase in the Gibbs'-like oscillations when $\Delta\xi$ is decreased, it is inferred that these effects are brought about by at least one underlying jump discontinuity. The distinct features of the VSF solutions i.e. the plateau regions and the two steep slopes near $\xi = 8°$ and $\xi = 18°$, certainly echo the findings of our previous analysis for the cylinder problem (with the original boundary conditions). For this reason, it is envisaged that the process that brings about the discontinuities in this modified problem, is identical to the one that underpins the original cylinder problem.

Since we are discussing the numerical solutions of the cylinder problem (PS) and the modified problem (FD), a few words on the expected behaviour of each numerical method, near a discontinuity, is desirable. It is useful to note, that in addition to faster convergence rates, PS methods (in practice) are known to handle discontinuities far better than FD methods. A simple illustration of the latter statement can be found

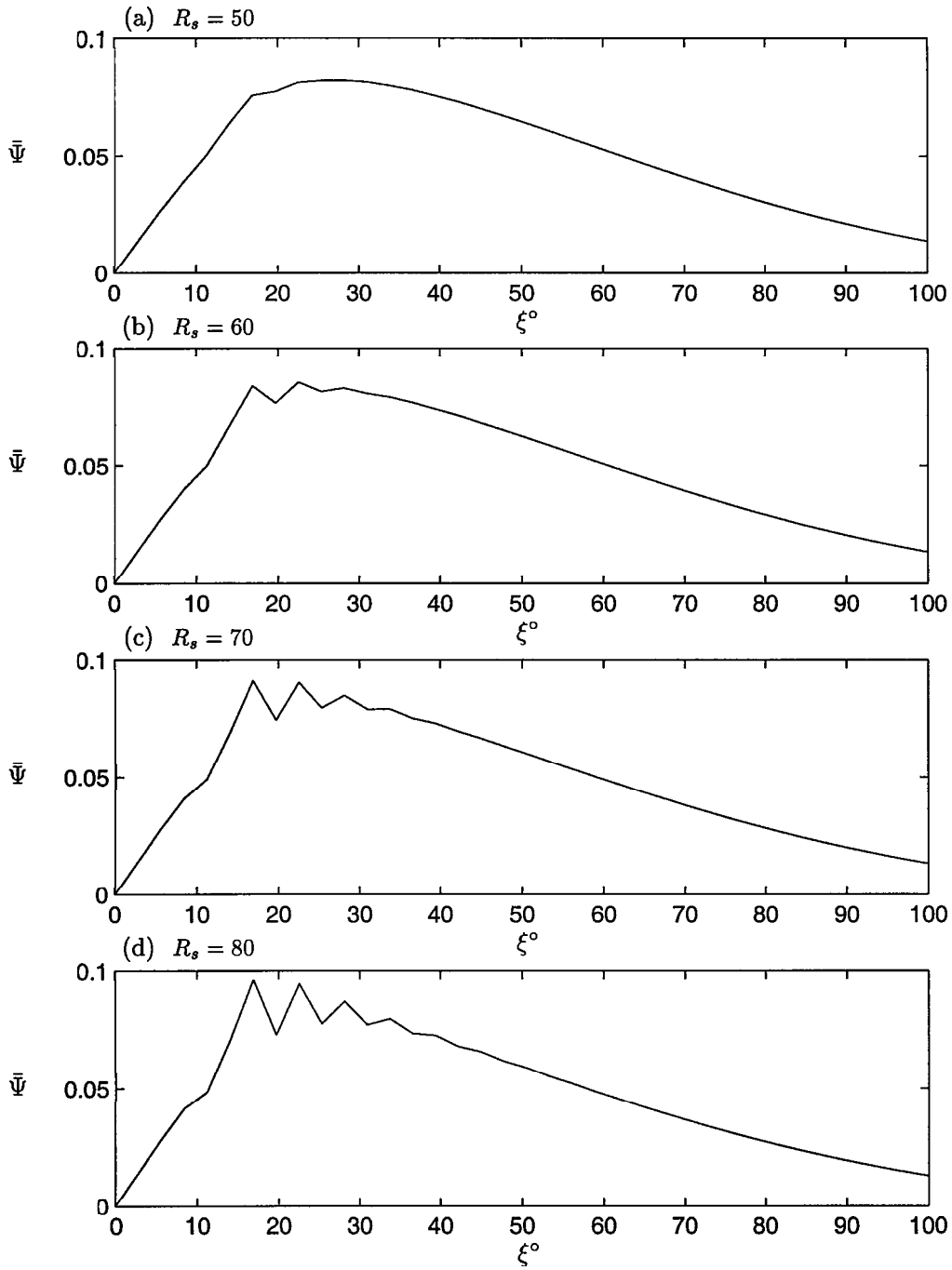


Fig. 2.46: The DNS for $\bar{\Psi}$ at $R_s = 50,\ 60,\ 70,\ 80$ with $\Delta\xi = 2\pi/128$. Here η is fixed at 0.6 and the timestep is $\Delta\tau = 7.5 \times 10^{-3}$.

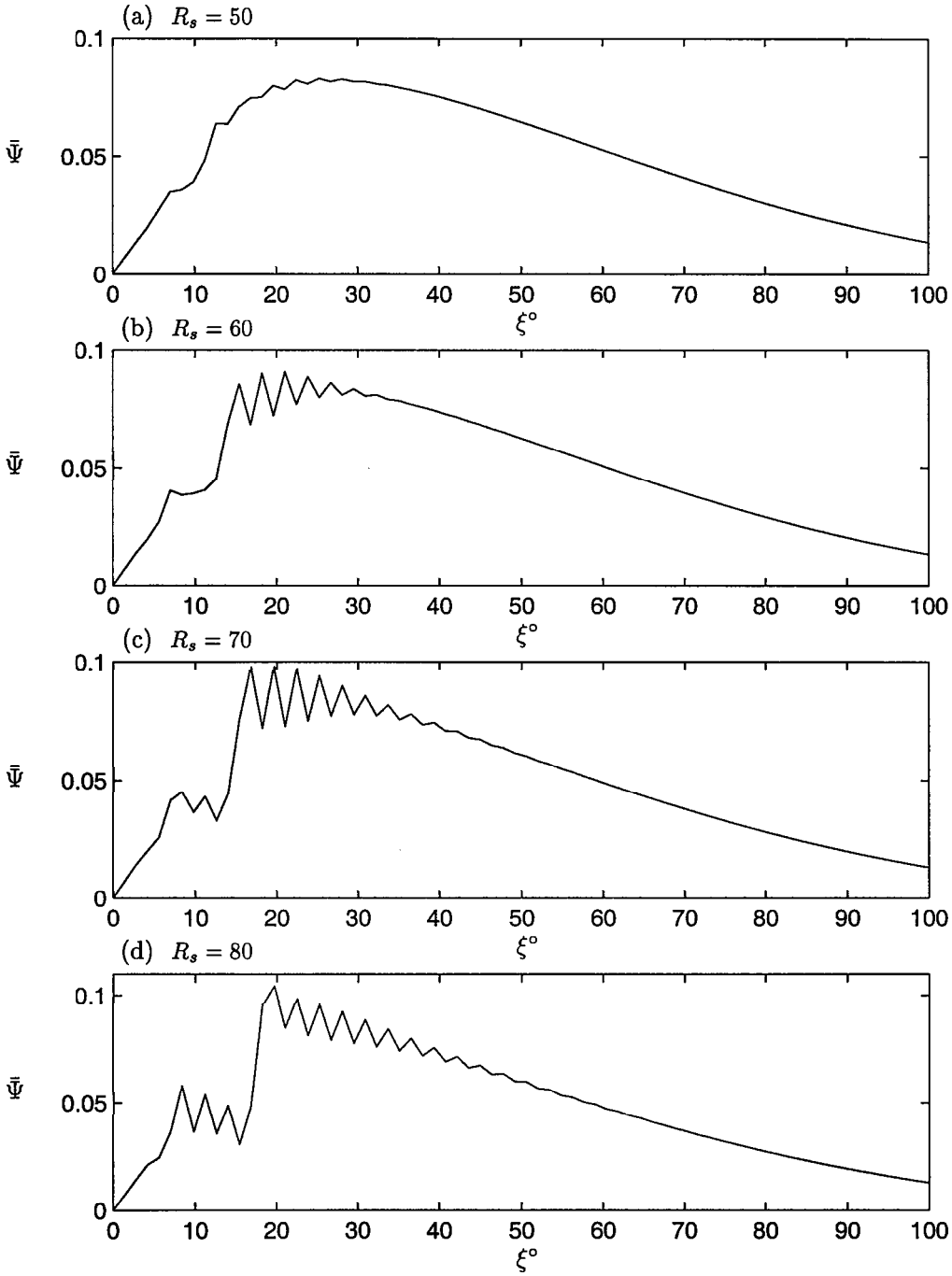


Fig. 2.47: The DNS for $\bar{\Psi}$ at $R_s = 50,\ 60,\ 70,\ 80$ with $\Delta\xi = 2\pi/256$. Here η is fixed at 0.6 and the timestep is $\Delta\tau = 7.5 \times 10^{-3}$.

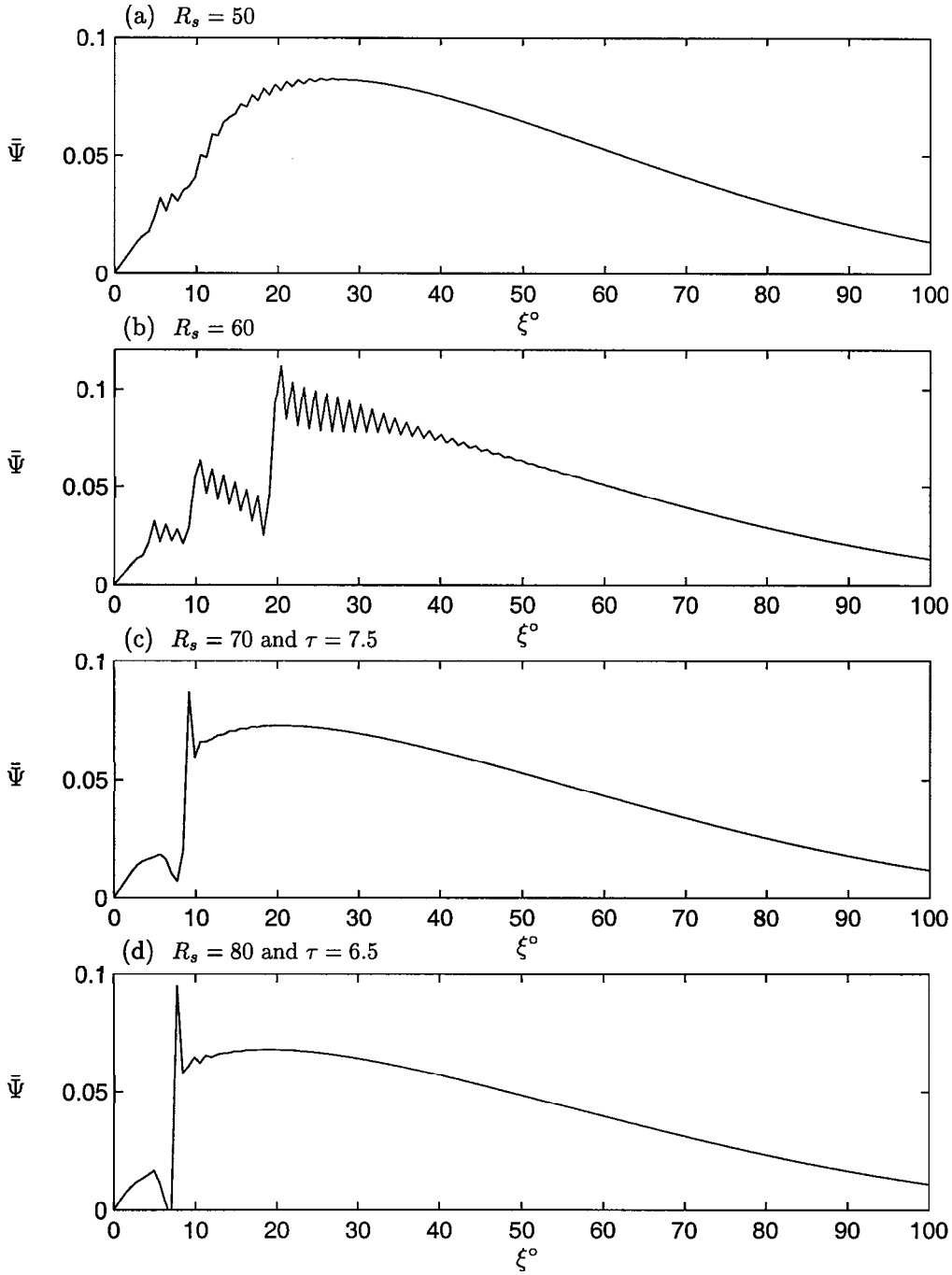


Fig. 2.48: The DNS for $\bar{\Psi}$ at $R_s = 50,\ 60,\ 70,\ 80$ with $\Delta\xi = 2\pi/512$. Here η is fixed at 0.6 and $\Delta\tau = 7.5 \times 10^{-3}$. The ξ-profiles in diagrams (c) and (d) are taken at $\tau = 7.5$ and $\tau = 6.5$ respectively. Note, it is impossible to obtain a converged result for $R_s \gtrsim 70$ because the numerical solution becomes unbounded for $\tau > 8$.

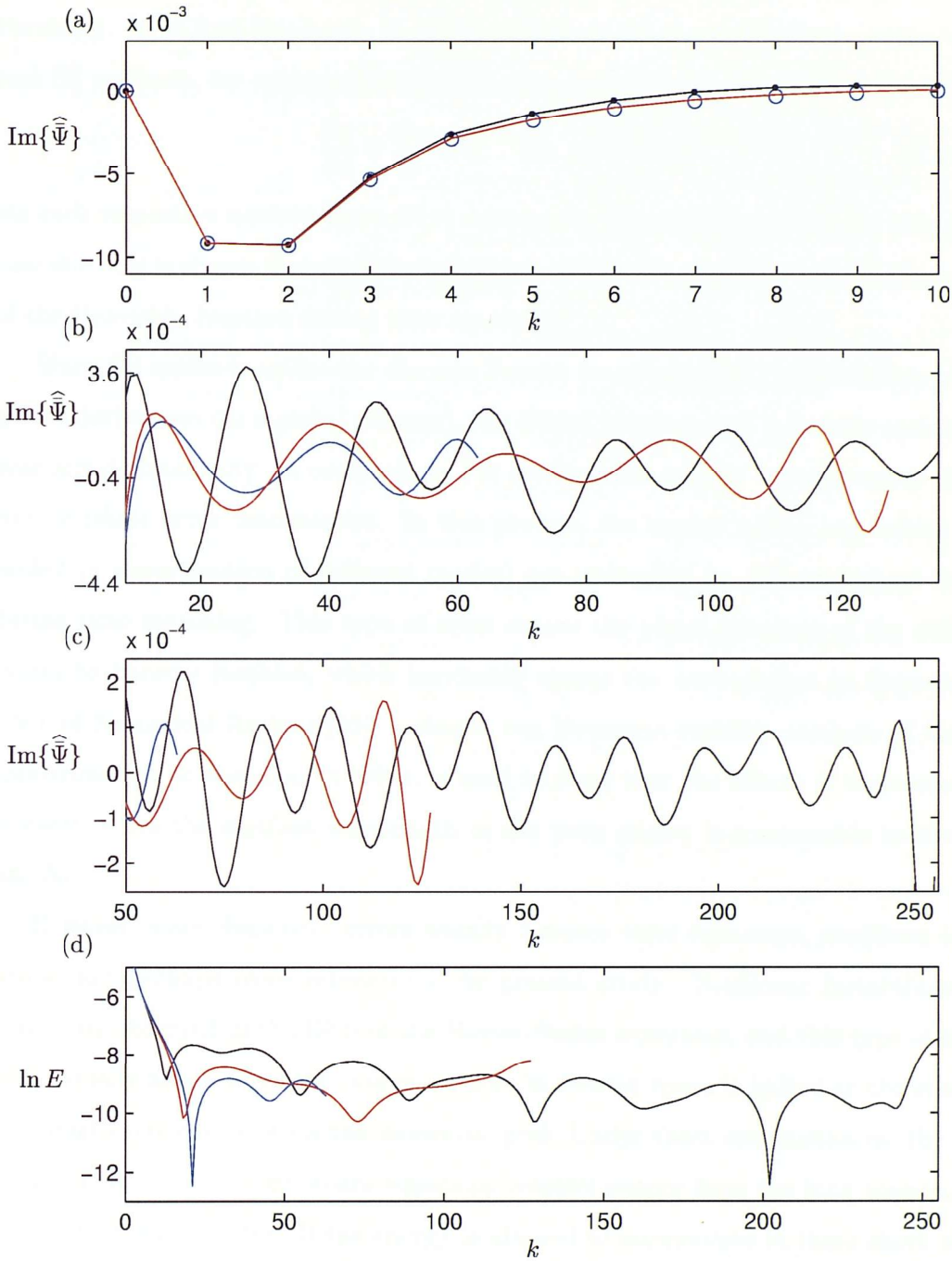


Fig. 2.49: For $R_s = 60$, the above diagrams show the FFT of the ξ-profile at $\eta = 0.6$ with: $\Delta\xi = 2\pi/128$ (blue curve), $\Delta\xi = 2\pi/256$ (red curve) and $\Delta\xi = 2\pi/512$ (black curve). In diagram (d), E denotes the magnitude of each Fourier mode i.e. $E = \|\hat{\bar{\Psi}}^{(n,k)}\|$.

in the book entitled "A practical guide to pseudospectral methods" [23] written by Fornberg. In §4.2 of this book, Fornberg compares the convergence properties of FD and PS methods, for nonsmooth functions, by computing the DNS of

$$\frac{\partial u}{\partial x} + \frac{\partial u}{\partial t} = 0, \quad u(x,0) = H(x) \tag{2.109a,b}$$

via each respective method (here $H(x)$ denotes the Heaviside function). In this simple case study, it is shown that the PS method is much better at preserving the steep slope of the Heaviside function during time marching.

Since PS methods utilise the discrete Fourier transform (DFT) to calculate the required derivatives (in a global manner), the Gibbs' phenomenon is usually anticipated near any discontinuity. In comparison, FD methods are usually more prone to *dispersive* or *phase* error inaccuracies. In this process, the modes within any initial *wave packet* (a superposition of different modes) get multiplied by different phase factors during time marching. This type of error causes the phase relations of the different modes to become jumbled, which inevitably causes the wave packet to disperse. In §19.1 of Numerical Recipes [60], a simple von Neumann stability analysis of the FD approximation to equation (2.109a), is used to show that the effects of dispersion are greatest, when the smallest wavelength in the wave packet is comparable to the grid size Δx.

However, since dispersive errors usually concern wave equations, nonlinear instabilities are perhaps more relevant to the present study. Nonlinear instabilities are commonly observed in the DNS of the Navier-Stokes equations, and this type of instability usually arises when the energy cascade in Fourier space is halted at the shortest wavelength representable on the numerical grid. Under these circumstances, the nonlinear terms in the Navier-Stokes equations transfer energy from the long wavelengths to the short wavelengths. If the energy is allowed to accumulate in these short wavelengths, the long wavelengths become obscured by the error accumulated in the modes with large wavenumbers.

In fluid dynamics, shock formation and nonlinear instabilities usually indicate an underlying physical condition/behaviour of the fluid (as opposed to a inappropriate

numerical formulation). However, in the cases where the integrity of the numerical formulation is doubted, one may consider the introduction of numerical viscosity (dissipation). The art of adding artificial numerical viscosity is a very complicated and diverse subject in itself. In addition to artificial viscosity, the various *smoothing* procedures for nonlinear instabilities include filtering methods (during time marching) and post processing techniques. Further discussions on this and other spectral viscosity techniques can be found in Tadmor [89][90].

From our results it is found that the size of $\Delta\xi$ (alone), dictates the extent to which these discontinuities are present in the computational domain. In figure 2.45 it is seen that if $\bar{\Psi}$ is computed with $\Delta\xi = 2\pi/128$ instead of $\Delta\xi = 2\pi/256$, then a better agreement is obtained with the series solution. However, by increasing the size of $\Delta\xi$, the discontinuities are suppressed at the cost of compromising the accuracy of the results. With these two factors in opposition, it is difficult to distinguish if the step size $\Delta\xi = 2\pi/128$ is sufficient for $R_s > 80$. Although further comparisons of the DNS with the series solution are impossible beyond $R_s = 80$ (due to the increasing development of discontinuities), from figure 2.45 it appears that the first term in the series expansion is still valid up to $R_s = 80$, see line S_{128}.

From figure 2.50 it is observed that the magnitude of the terms $\bar{\Psi}^{(n)}$ are all ordered desirably for a convergent series expansion, except for $\bar{\Psi}^{(0)}$ which is always smaller than $\bar{\Psi}^{(1)}$. Once again, it is thought that the maximum extent of agreement in table 2.9 is related to the disordering of the magnitudes of the terms $\bar{\Psi}^{(n)}$. However, for $n \geqslant 1$, the magnitude of each successive term is found to be smaller than the former. In view of this result, it appears that the decrease in the number of valid terms in the series expansion (see table 2.9), is caused by the magnitude of $\bar{\Psi}^{(0)}$ becoming comparable to other terms of higher order. This situation is unlike the scenario in the cylinder problem, where the decrease in the number of valid terms is related to the value of R_s at which $\|\Psi^{(n)}\| \sim \|\Psi^{(n+1)}\|$. At $R_s \approx 20$, the number of valid terms in the series expansion decreases from $N = 3$ to $N = 2$, see table 2.9, and this process coincides with disordering of the terms $\bar{\Psi}^{(0)}$ and $\bar{\Psi}^{(2)}$ which occurs over the R_s-range [15, 25].

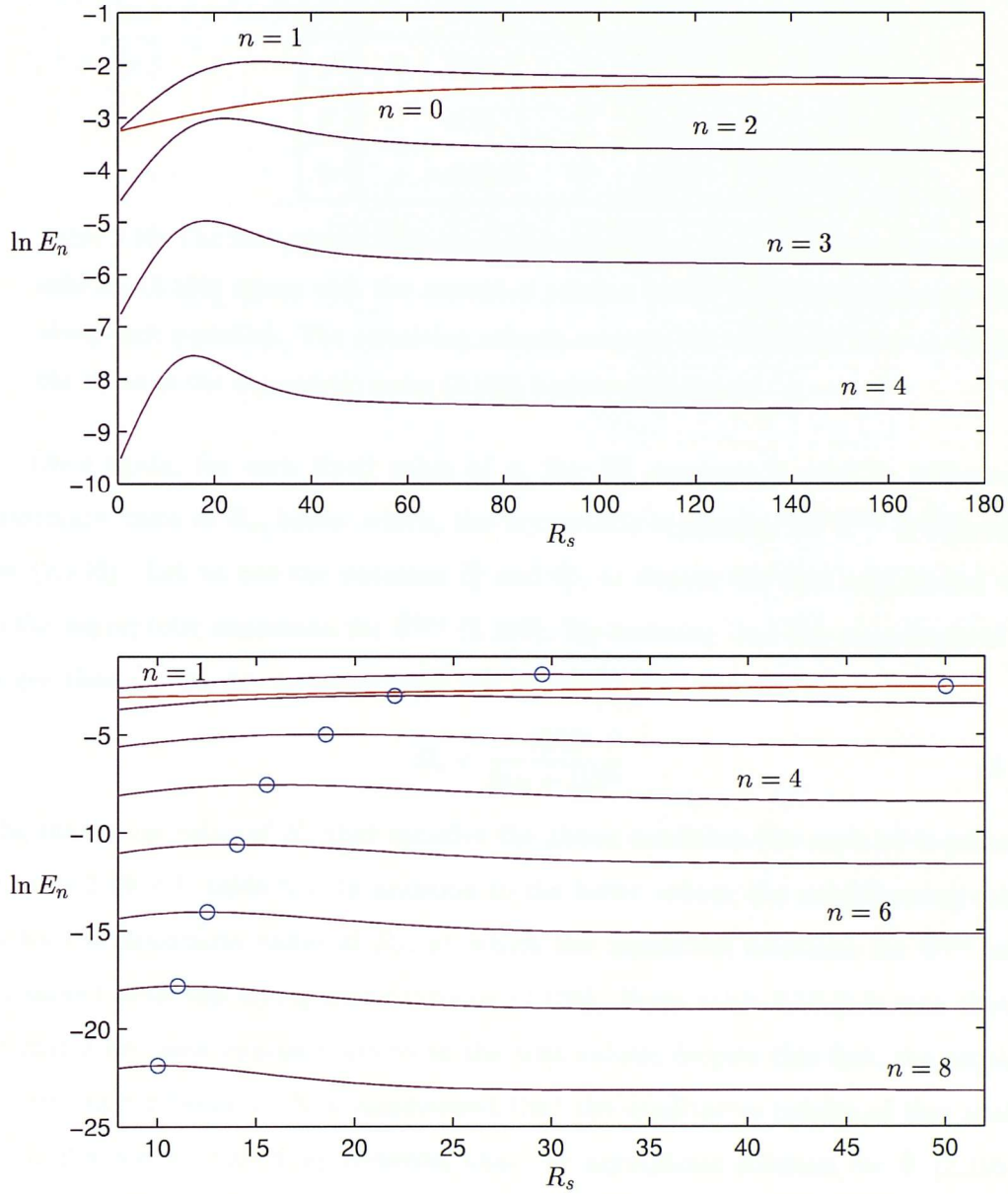


Fig. 2.50: The magnitude of each term $\bar{\Psi}^{(n)}$ versus Reynolds number (for the exponential BC). Here the magnitude of each term is given by $E_n = \ln \int \|\bar{\Psi}^{(n)}\|^2 \, d\eta$. An open circle marks the maximum on each curve.

n	$\bar{\Psi}^{(n)} = \bar{t}_0^n + \bar{t}_1^n$ approx.	M_1 $\bar{t}_0^n \sim \bar{t}_1^n$ see (2.110)
0	14.0	124.4
1	2.60	31.11
2	0.15	10.37
3	$\approx$0.015	3.889

Table 2.10: The first column contains maximum value of R_s to which the asymptotic solution (2.106) agrees with the numerical solution for $\bar{\Psi}^{(n)}$ (maximum error of 2% along each η-profile). The remaining column contains the estimated value at which the terms in the asymptotic series (2.106) become disordered.

Once again, for each fixed value of n, the M_1 measure is used to estimate the maximum value of R_s, below which, the asymptotic expansion for $\bar{\Psi}^{(n)}$ is convergent, see (2.106). Let us use the notation $\bar{t}_0^n$ and $\bar{t}_1^n$, to denote the first and second terms in the asymptotic expansion for $\bar{\Psi}^{(n)}$ (2.106). By insisting that the magnitude of $\bar{t}_0^n$ is larger than $\bar{t}_1^n$, the M_1 measure gives the following condition on R_s:

$$R_s < \frac{1120}{9(n+1)2^n}. \tag{2.110}$$

The maximum value of R_s that satisfies the above condition (for each n) is presented in table 2.10, c.f. table 2.8. In addition to the latter values, the neighbouring column shows the maximum value of R_s, at which the numerical solutions for $\bar{\Psi}^{(n)}$ are in agreement with the asymptotic solutions (2.106). From table 2.10 it is seen that the estimates are poor approximations to the true values; despite this fact, the estimates are still upper bounds. It is emphasised that the qualitative results of this analysis are important because they indicate, that the asymptotic solution for $\bar{\Psi}$ (2.105), is valid over a larger R_s-range than the corresponding asymptotic solutions (2.106) for the terms $\bar{\Psi}^{(n)}$. In figure 2.50, it is clear that the hierarchy of magnitude begins to reorder favourably as the Reynolds number increased. Accordingly, it is found that each steady term $\bar{\Psi}^{(n)}$ converges to its large R_s asymptotic form, see table 2.11. From these results it is seen that there is a slight discrepancy at $R_s = 10000$. At $R_s = 10000$,

$N=$	0	1	2	3	4	5	6	7	8	9	10	11
R_s												
500	5	17	25	34	36	46	40*	41	-	-	-	-
1000	5	17	26	34	39	46	46	55	49*	-	-	-
2000	5	17	26	34	40	46	49	55	55	63	57*	-
3000	5	17	26	34	40	46	50	55	57	63	62*	-
10000	5	17	27	34	40	46	50	55	58	50*	-	-

Table 2.11: The agreement (in ξ-direction) of the series solution with the steady asymptotic solution for large R_s (2.107). Once again the ξ-domain is split into 256 intervals, and maximum partition number, $n_\xi = 256\ \xi/2\pi$, of agreement is recorded in the above table.

the inclusion of the tenth term produces a solution for $\bar{\Psi}$, which is worse than the ten term approximation at $R_s = 3000$. Hence the tenth term in the series expansion, $\bar{\Psi}^{(9)} \sim 10^{-7}$, is beyond the accuracy of the scheme at $R_s = 10000$, c.f. the numerical difficulty of computing the term $\Psi^{(5)} \sim 10^{-9}$ in the cylinder problem, see page 112.

An investigation into the unsteady regime is found to echo the findings of the original cylinder problem. For the unsteady asymmetric regime ($R_s \approx 53$), the energy spectrum of each term $\bar{\Psi}^{(n\geqslant 1)}$, indicates that each Fourier mode is larger than the previous. Moreover, this is also found to be the case in the symmetric regime ($R_s > 170$); therefore, the Fourier series representation is divergent in both regimes (with 81 modes). It is also worth mentioning that a DNS of (2.100) was also attempted with different values of λ. Despite the added flexibility of λ, the terms in the series remained disordered in magnitude. Once again, this implies that within the unsteady regime, it is inappropriate to expand $\bar{\Psi}$ using a regular ξ-power series.

Despite the fact that a smooth DNS cannot be computed for $R_s \gtrapprox 55$, it is maintained that the term $\theta\Psi^{(0)}$, still constitutes part of a valid series expansion for the steady regime of the cylinder problem (and the corresponding steady regime of the modified problem). In the steady regime, the asymptotic forms of Ψ at large and

small-R_s, are readily decomposable into a θ-series. By comparing these asymptotic expansions with the numerical solutions of Ψ and $\Psi^{(n)}$, it is clear that the term $\theta\Psi^{(0)}$ represents the flow close to $\theta = 0$ for $R_s \leqslant 40$ and $R_s \gg 1$.

To this point, the bounded numerical solutions for Ψ have been restricted to $R_s < 60$ (and $R_s < 80$ for the modified problem), and in this regime the solutions are found to be steady. Hence the involvement of $\Psi^{(0)}$, in the unsteady regime of Ψ, has not yet been characterised. From our Fourier analysis (in time) it is known that the unsteady symmetric and asymmetric regimes of $\Psi^{(0)}$, do not give rise to a series solution that is monotonically decreasing. Hence, assuming that $\Psi^{(0)}$ still constitutes the leading order approximation to Ψ at large Reynolds numbers, it is doubtful that the DNS for Ψ ever settles into a time periodic solution as $\tau \to \infty$.

In the next section, the effects of transportation errors in the numerical calculations for Ψ and $\bar{\Psi}$, are minimised by using upwind differencing (UWD). If the discontinuities observed to this point are indeed genuine, it is envisaged that UWD will suppress the formation of the Gibbs' oscillations and thus improve the resolution of the underlying discontinuities.

2.6 Upwind differencing

2.6.1 The cylinder problem (original boundary condition)

In this section, the numerical scheme that was previously used to calculate the DNS of Ψ, is now adapted to minimise the effects of transportation errors. The original PS method is now replaced by a FD scheme that incorporates UWD. In the UWD scheme, the errors incurred in the advective terms are only allowed to propagate in the direction of the flow (unlike a central difference scheme, which distributes the error in both the positive and negative θ-directions). By using this new formulation, it is hoped that the UWD scheme will "improve" the representation of the physical flow (especially near the discontinuities), and thus reduce the intensity of the Gibbs' oscillations.

Since the discontinuities in the DNSs only occur in the θ-direction, UWD is only

applied to the term ω_θ; here $\omega = \Psi_{\eta\eta}$, and the governing equation for ω is (see equation (2.99) also)

$$\omega_\tau = \frac{1}{R_s}\omega_{\eta\eta} - \boxed{u\omega_\theta} - v\omega_\eta.$$

The overall numerical formulation for the UWD scheme is essentially the same as the original PS method i.e. the nonlinear terms are treated explicitly and the Crank-Nicholson method is employed for the term $\omega_{\eta\eta}$. However, in the present formulation, the manner in which the term ω_θ is calculated, is dependent on the sign of u. If u is positive, then ω_θ is calculated by using a first-order backward FD formula, otherwise a forward difference formula is used (note, the term $v(= \Psi_\theta)$ is still calculated via a second-order central difference formula). Since the current FD scheme does not require the use of FFTs, it is sufficient to consider Ψ on the θ-range $[0, \pi]$. With $\Delta\eta$ set equal to $2/100$, a mesh size of $\pi/128$ was found to be a sufficiently small value for $\Delta\theta$ in all of the calculations. Moreover, since the iteration at each time level (in the present FD scheme) is much faster than the corresponding iteration in PS scheme, a smaller timestep of size $\Delta\tau = 2 \times 10^{-4}$ was used to increase the accuracy of the results.

Numerical Results

By using the UWD scheme to calculate the DNS of (2.33), it is found that the calculations can be extended up to $R_s = 1000$ (the largest Reynolds number tested), which is well above the limit of the original PS code ($R_s \approx 65$). With $\Delta\theta$ set equal to $\pi/128$, the numerical solutions for Ψ are found to be steady and η-symmetric up to $R_s = 138$ i.e. $\Psi \equiv \Psi_{\text{sym}}$ for $R_s \leqslant 138$. By increasing R_s from 50 to 130, see figure 2.51, the development of at least two discontinuities are observed in the θ-direction. From figure 2.51, it is also observed that UWD has the desired effect of suppressing the Gibbs' oscillations near each discontinuity; subsequently, the present method captures the profile of each shock far better than the original PS formulation.

By comparing the series solution to the DNS for Ψ, it is found that the term $\theta\Psi^{(0)}$ correctly represents the flow (near $\theta = 0$) up to $R_s = 110$, see table 2.12. This result demonstrates the important fact that only the η-symmetric regime of $\Psi^{(0)}$ is

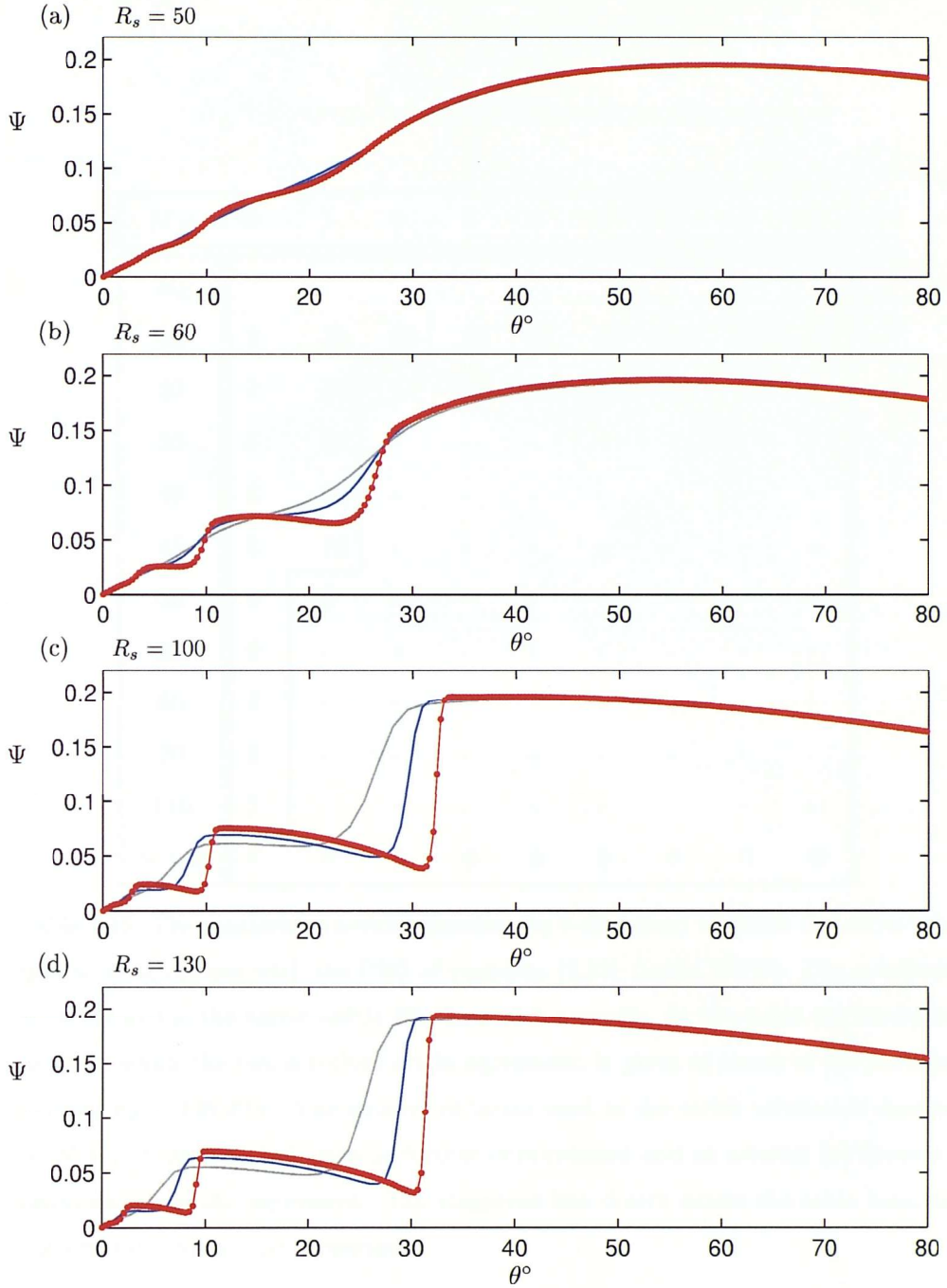


Fig. 2.51: The numerical solution for Ψ_{sym} at $R_s = 50, 60, 100, 130$ with $\Delta\theta = \pi/128$ (grey curve), $\Delta\theta = \pi/256$ (blue curve) and $\Delta\theta = \pi/512$ (dotted red curve). Here $\eta = 0.6$ and $\Delta\tau$ is set equal to 2×10^{-4} in the computations. Note that the η-symmetric solution for Ψ is forced in these cases and that the resulting solutions are steady.

$N =$	0	1	2	3	4	5	6	7	8
R_s									
10	8	33	56	58	67	65*	68	64*	78
20	7	37	44	47	60	53*	51*	50*	*
30	8	31	-	-	-	-	-	-	-
40	8	20	-	-	-	-	-	-	-
45	8	12	-	-	-	-	-	-	-
50	8	6*	-	-	-	-	-	-	-
55	6	-	-	-	-	-	-	-	-
60	3	-	-	-	-	-	-	-	-
70	2	-	-	-	-	-	-	-	-
110	2	-	-	-	-	-	-	-	-
> 110	0	0	0	0	0	0	0	0	0

Table 2.12: The maximum partition number (in θ-direction) to which the series solution is in agreement with the DNS of equation (2.33) (using UWD). The maximum error allowed in the agreement is 1% along each η-profile. In this table the maximum angle to which the two solutions are in agreement, is given in terms of the partition number $n_\theta = 128\ \theta/\pi$. The number of terms used in the series solution is denoted by $N+1$. A dash (-) indicates no further improvement and an asterisk ($*$) denotes a deterioration in the agreement. The staggered line drawn across the table indicates the general trend of the agreement.

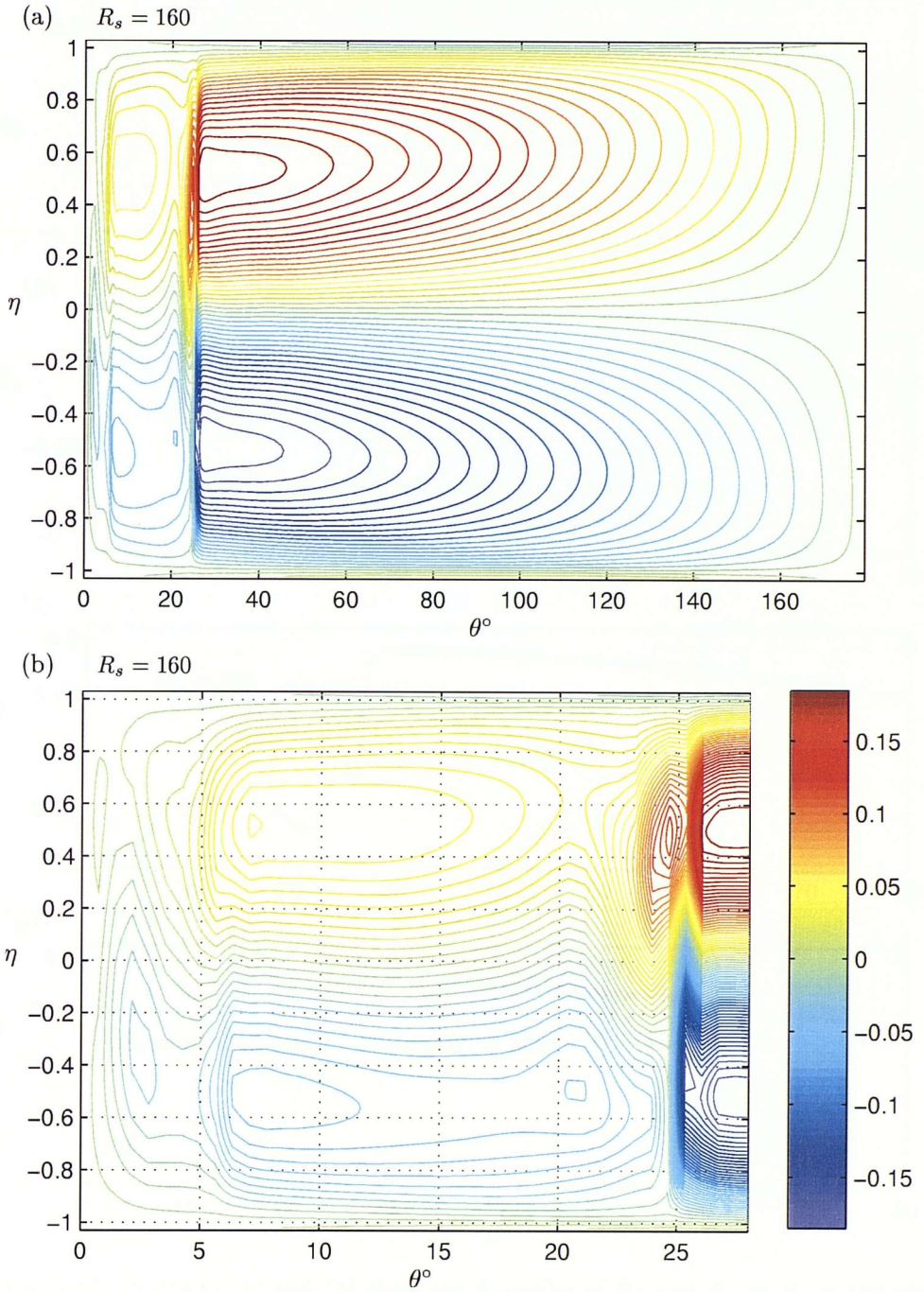


Fig. 2.52: A snapshot of Ψ at $R_s = 160$ (unsteady regime) with $\Delta\theta = \pi/256$.

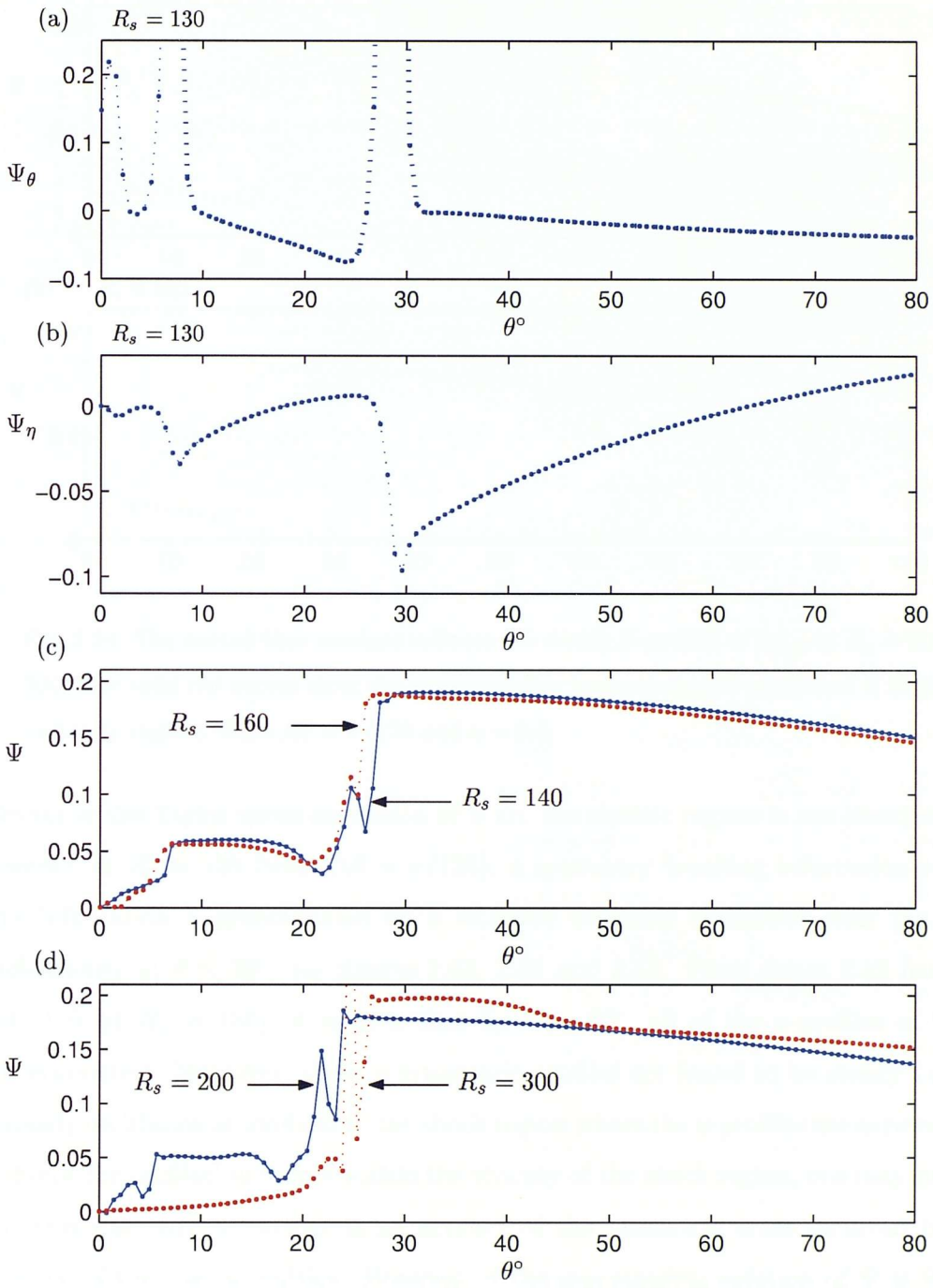


Fig. 2.53: Diagrams (a) and (b) show the θ-profiles of Ψ_θ and Ψ_η at $R_s = 130$ with $\eta = 0.6$. Diagrams (c) and (d) show the θ-profiles of Ψ at $R_s = 140$, 160, 200, 300 with $\eta = 0.6$ and $\Delta\theta = \pi/256$.

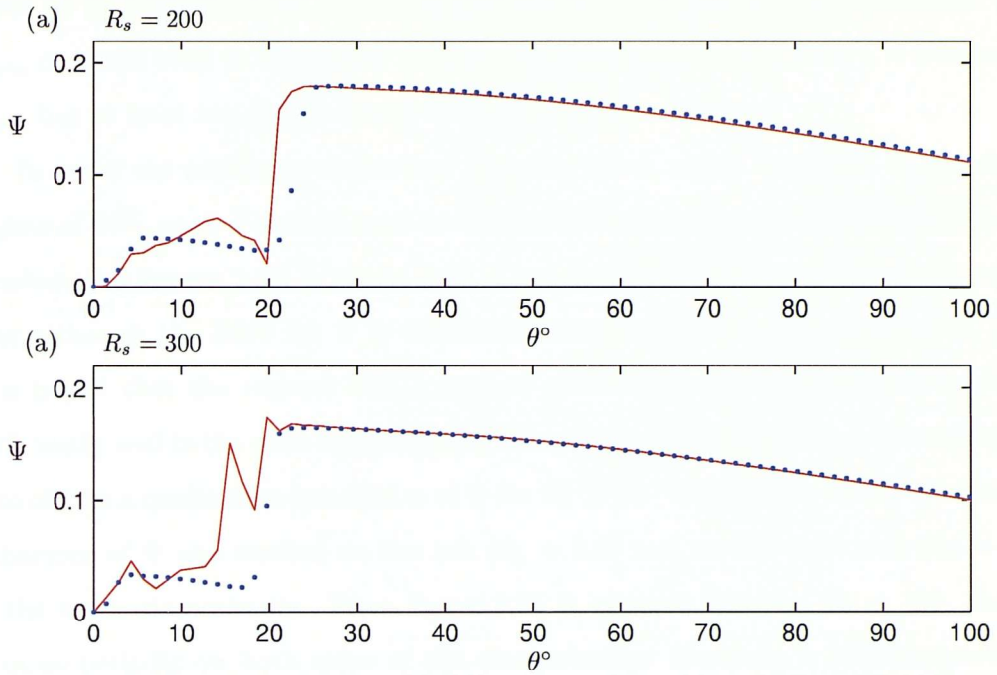


Fig. 2.54: The dotted blue markers indicate the steady θ-profiles of Ψ_{sym} at $R_s = 200$, 300. The solid red curves show the corresponding instantaneous θ-profiles of Ψ in the unsteady regime. Here $\Delta\theta = \pi/128$ and $\eta = 0.6$.

relevant in the Taylor series expansion of Ψ i.e. the chaotic regime is not incorporated. However, at $R_s \approx 138$ (with $\Delta\theta = \pi/128$), a symmetry breaking bifurcation occurs. This bifurcation is accompanied by a localised unsteady oscillation near the main discontinuity at $\theta \approx 30°$, see figures 2.52, 2.53 and 2.54. From figure 2.52 (contour plot of Ψ at $R_s = 160$), it is seen that for $\theta > 60°$, all of the η-profiles of Ψ are still symmetric. Moreover, these η-symmetric profiles are found to be steady i.e. the unsteady oscillation is confined to the shock region where the η-profiles are asymmetric.

Since the oscillation occurs within the vicinity of the shock region, one may suspect that this unsteady behaviour is an artifact of the numerical error incurred by the presence of the discontinuities. However, if the η-symmetric solution of Ψ is forced, the numerical solution for Ψ_{sym} is found to be steady, and for this reason, the unsteady oscillation of Ψ does appear to be a genuine feature of the flow. It is important to note that at large Reynolds numbers, the numerical solutions for Ψ and Ψ_{sym} are always

found to be discontinuous; moreover, the solutions for Ψ_{sym} are always steady. Since Ψ_{sym} does not tend to the steady asymptotic form predicted by (2.51), it follows that Ψ_{sym} has at least two steady states at large Reynolds numbers.

To see if the oscillatory behaviour near the shock region is related to the chaotic regime of $\Psi^{(0)}$, some Poincaré cross sections of Ψ were constructed at various Reynolds numbers, see figures 2.55, 2.56 and 2.57. On a formal note, it is important to mention that although the DNS for Ψ is discontinuous over a small θ-interval for $R_s \gtrapprox 60$, it is hoped that the current UWD method succeeds in capturing the shock profiles sufficiently well in the post-shock regime. Hence, the intention of the following analysis is to obtain a qualitative description of Ψ for $R_s > 60$. With this in mind, the unsteady behaviour of Ψ was studied on the left ($\theta_L = 9.8$) and on the right side ($\theta_R = 49.2$) of the main discontinuity. From figure 2.55 it appears that for $R_s = 140$, the flow is quasi-periodic on both sides of the discontinuity. However, a close inspection of the node at $\mathcal{A}$, reveals that the node is actually a line shaped trajectory. Moreover, this distinctive line trajectory has already been observed in the asymmetric regime of $\Psi^{(0)}$ at $R_s = 86$, see figure 2.18. Since the size of the line appears upon a scale that is smaller than the accuracy of the numerical scheme, the regime at $R_s = 140$ is classified as quasi-periodic. Moreover, in all of the cases that were studied, every quasi-periodic regime was found to possess the same line shaped distribution near each node. For a fixed Reynolds number, the order of the quasi-periodicity at θ_L i.e. the number of points appearing in the Poincaré cross section, was found to be different from the order observed at θ_R; however, the time periods calculated at these two different locations were always found to be the same.

For $R_s \geqslant 188$, the flow near the shock region is no longer quasi-periodic and a turbulent behaviour is observed in the Poincaré cross sections, see figures 2.56 and 2.57. Although a period-doubling cascade does not ensue before the turbulent behaviour is observed, the time period of the flow is found to double at some values of R_s, see table 2.13. Since the steepness of the slope near the main discontinuity is affected by the size of $\Delta\theta$, see figure 2.51, the Poincaré cross sections were also calculated with refined

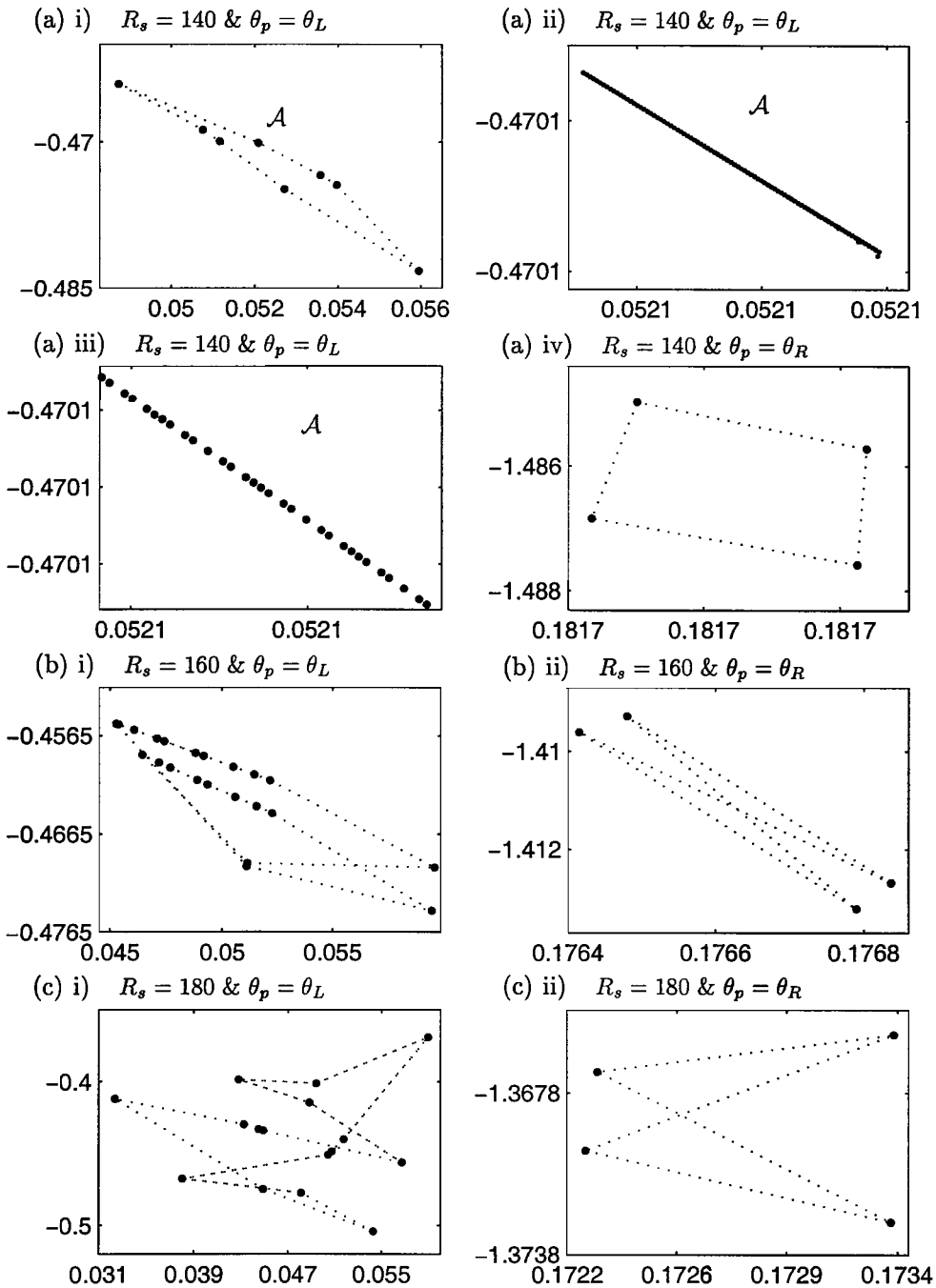


Fig. 2.55: The Poincaré cross section of Ψ at various values of R_s. The coordinate variables $x_1(\tau)$, $x_2(\tau)$ and $x_3(\tau)$ are given by: $\Psi(\theta_p, \eta = 0.5)$, $\Psi_{\eta\eta}(\theta_p + 2\Delta\theta, \eta = 0.6)$ and $\int |\Psi(\theta_p)|\, d\eta$ (the two values of θ_p considered here are $\theta_L = 9.8°$ and $\theta_R = 49.2°$). The Poincaré sections are taken in the plane $\dot{x}_3 = 0$. Note $\Delta\theta = \pi/128$ in the DNSs.

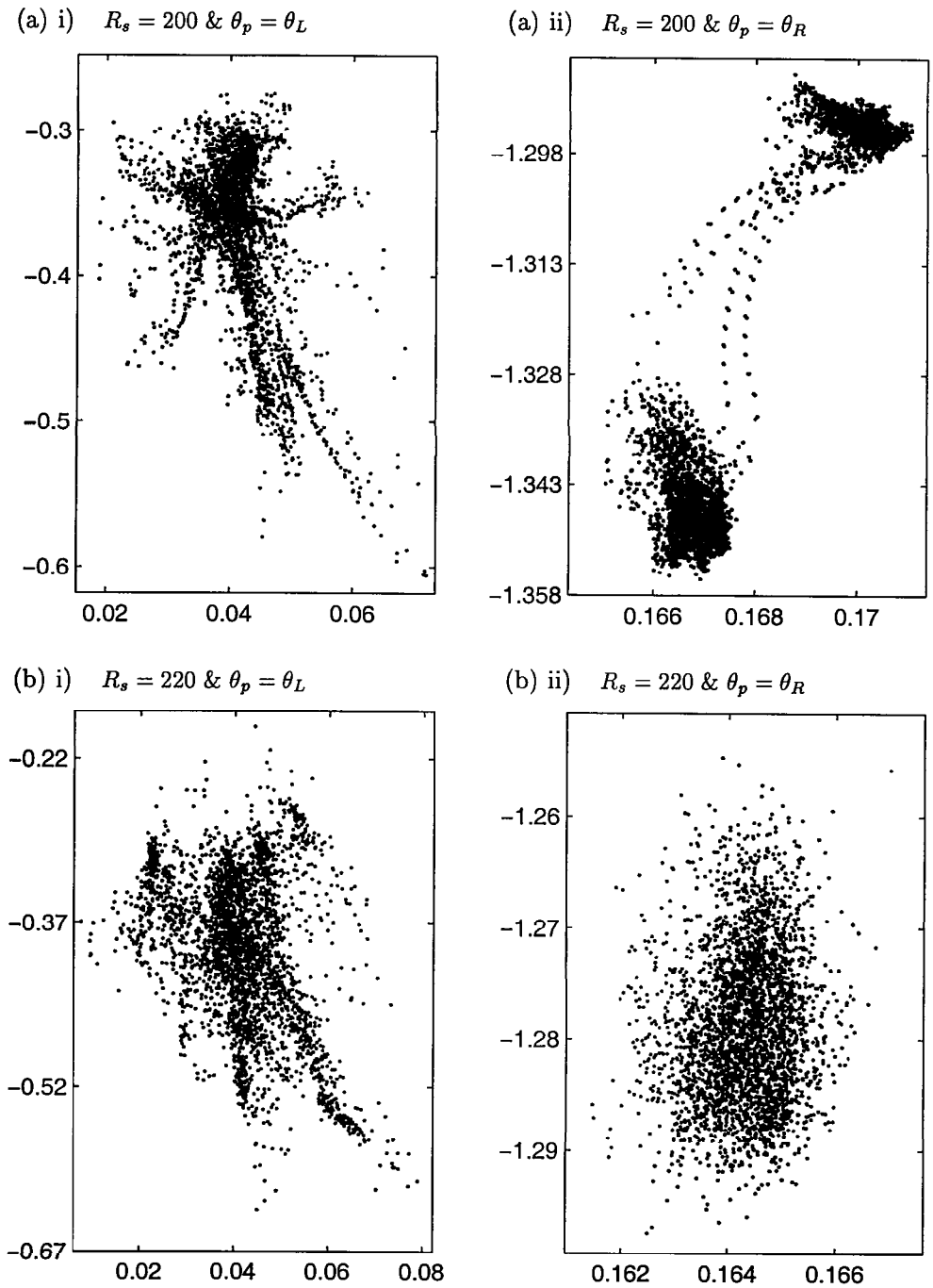


Fig. 2.56: The Poincaré cross section of Ψ at $R_s = 200, 220$. Here $\Delta\theta = \pi/128$ in the numerical calculations.

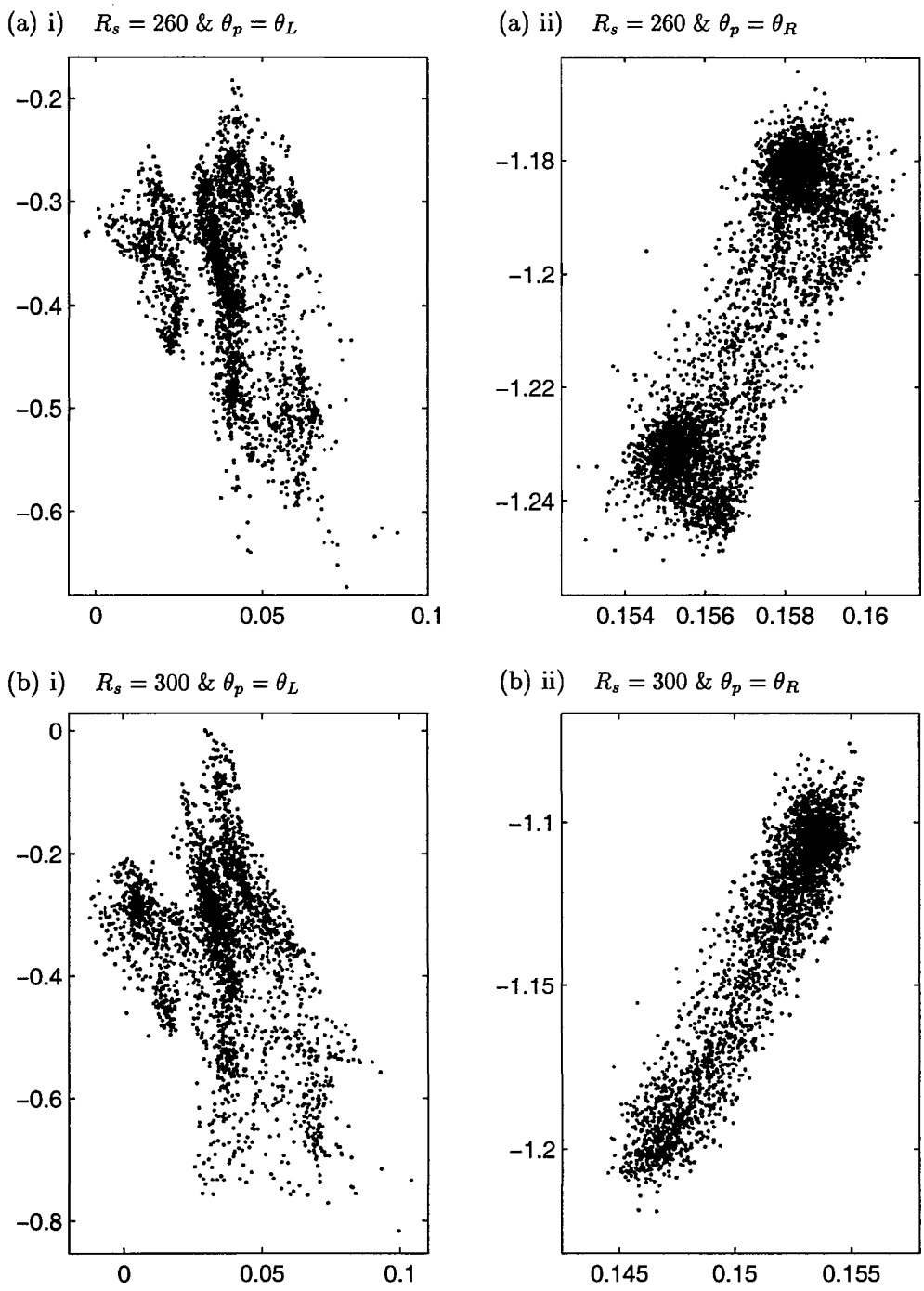


Fig. 2.57: The Poincaré cross section of Ψ at $R_s = 260, 300$. Here $\Delta\theta = \pi/128$ in the numerical calculations.

R_s	Period of $\Psi^{(0)}$
100	29.1045
110	38.334
120	Chaotic
125	Chaotic
130	65.804
135	Chaotic
140	74.528
160	53.076
180	Chaotic
200	93.182
300	61.400
400	Chaotic

R_s	Period of Ψ with $\Delta\theta = \pi/128$
140	1.888
159	P_1=1.883
160	$\approx 2P_1$ (3.772)
161–163	$\approx 4P_1$ (7.576)
164	P_2=9.471
164.4	$\approx 2P_2$ (18.916)
168	Turbulent
172	14.291
176	5.037
180	4.647
186	4.211
188–196	Turbulent

Table 2.13: The time period of $\Psi^{(0)}$ and Ψ at various Reynolds numbers.

settings ($\Delta\theta = \pi/256$) and the results were found to be remarkably different.

With $\Delta\theta$ set equal to $\pi/256$, the symmetry breaking bifurcation, accompanied by the unsteady oscillation, is now found to occur at $R_s \approx 100$ (the corresponding value with $\Delta\theta = \pi/128$ is $R_s \approx 138$). For $100 < R_s \leqslant 118$ the flow is quasi-periodic with a time period approximately equal to 0.91, and for $R_s > 118$, the Poincaré cross sections at θ_L all indicate that the flow is turbulent. In contrast, for $R_s > 118$, the diagrams for θ_R all indicate that the flow on the RHS of shock is quasi-periodic (with a time period that is approximately 0.91), see figures 2.58 and 2.59. However, a close inspection of the nodes in the θ_R diagrams, reveals that all the points are distributed along loci that are rotationally symmetric. Once again it is important to note that these loci develop on a very small scale i.e. with a variation of size 1×10^{-5} to 1×10^{-7}. Strictly speaking, a variation on the latter scales is largely influenced by the errors associated with the approximations in the numerical scheme; therefore, despite the characteristic

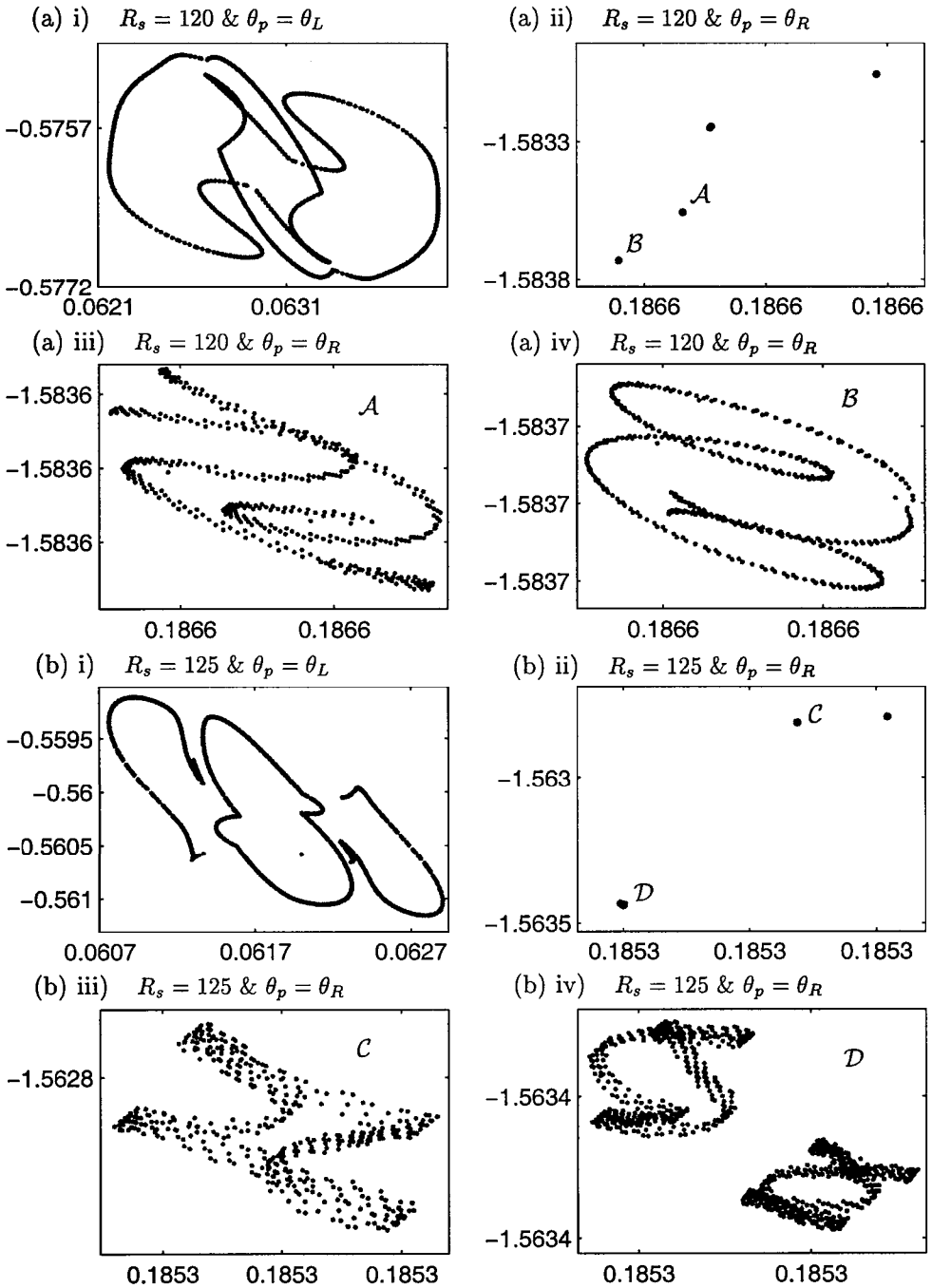


Fig. 2.58: The Poincaré cross section of Ψ at $R_s = 120$, 125 with $\Delta\theta = \pi/256$.

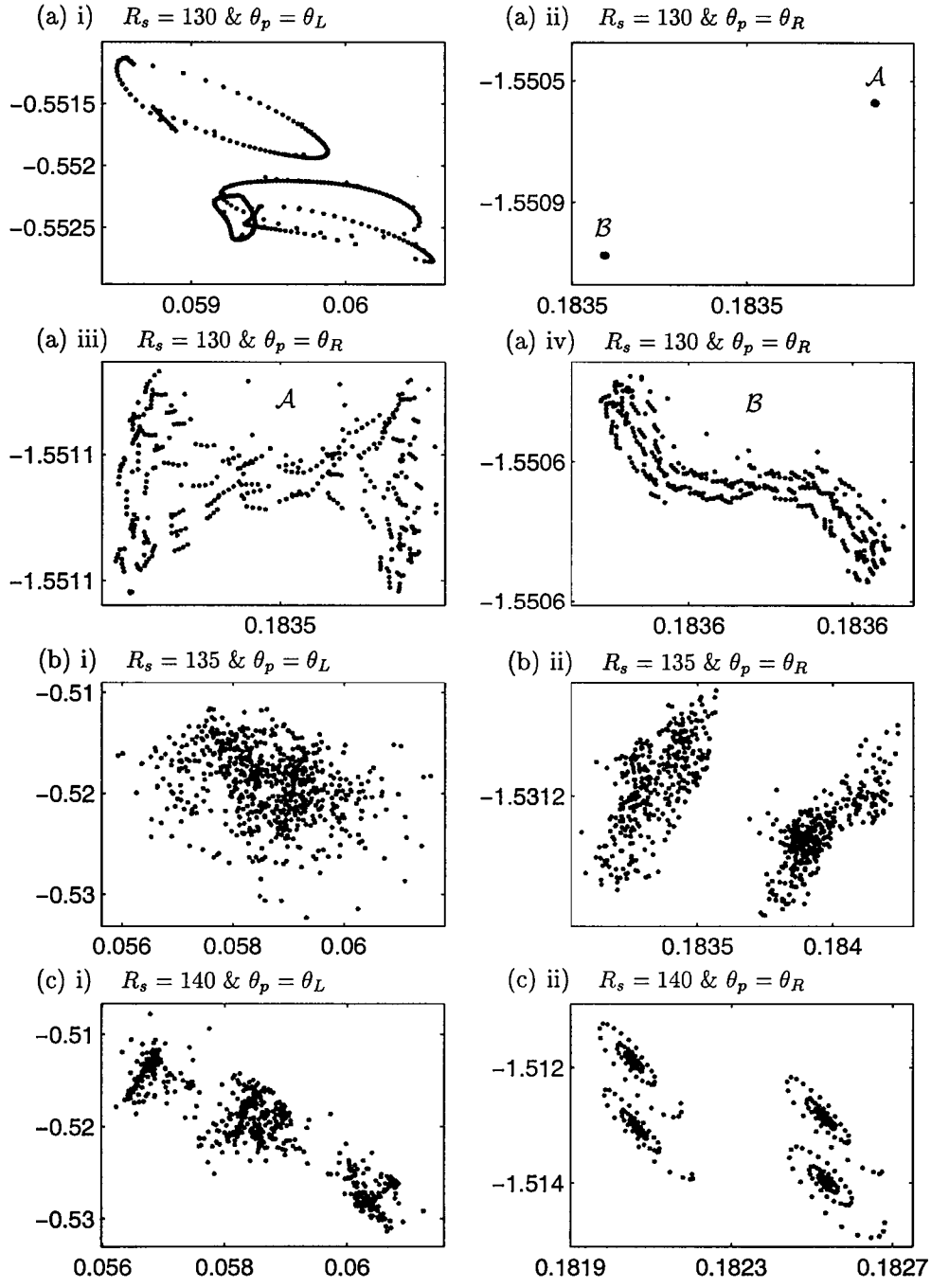


Fig. 2.59: The Poincaré cross section of Ψ at $R_s = 130, 135, 140$ with $\Delta\theta = \pi/256$.

structure in the θ_R diagrams, it is impossible to ascertain whether the oscillation is genuinely chaotic for $R_s > 118$.

To compare the numerical solutions for Ψ to the unsteady asymmetric regime of $\Psi^{(0)}$, some Poincaré cross sections of $\Psi^{(0)}$ were also constructed, see figure 2.60. As previously mentioned, some quasi-periodic regimes of $\Psi^{(0)}$ do exist for $R_s \geqslant 82$; however, it is important to note that these periodic regimes are frequently interrupted, at unpredictable Reynolds numbers, by chaotic states. Based on the assumption that $\Psi^{(0)}$ is a valid term in the power series expansion of Ψ, it is expected the time period of Ψ should always be an integer multiple of the corresponding period of $\Psi^{(0)}$. However, contrary to intuition, the time period of $\Psi^{(0)}$ (in the quasi-periodic regimes), is always found to be larger than the time period of Ψ with $\Delta\theta = \pi/128$. The latter result is also found to be the case when $\Delta\theta$ is refined to $\pi/256$, except the range of comparison in this case is limited to interval $100 \leqslant R_s \leqslant 118$ (the quasi-periodic regime).

To understand the dynamics of the physical flow near a shock, it is often helpful to determine whether the shock is *tangential* or not. A *tangential* or *contact* discontinuity is said to exist if the normal velocity component is zero through the plane of a shock. Under such circumstances, it is usually found that the flow is susceptible to an instability of the Kelvin-Helmholtz type. However, in the present study, the unsteady oscillation near the discontinuity is unlikely to be the result of a Kelvin-Helmholtz instability because Ψ_η does not pass through zero continuously at each shock, see figure 2.53. Hence, assuming that the numerical scheme has captured the shock profile sufficiently well at $R_s = 130$, it is likely that the oscillation near $\theta = 30°$ is brought about via some other mechanism.

The results in this section seem to suggest that the unsteady forcing of $\Psi^{(0)}$, may not be responsible for the unsteady oscillation observed in DNS for Ψ. However, from our numerical calculations, it is discovered that the time period of Ψ is dependent on the size of $\Delta\theta$. Therefore, it could be the case that the present numerical scheme does not capture the unsteady behaviour near the discontinuity sufficiently well. On the other hand, when $\Delta\theta$ is refined to $\pi/256$, the solution for Ψ does remain unchanged in

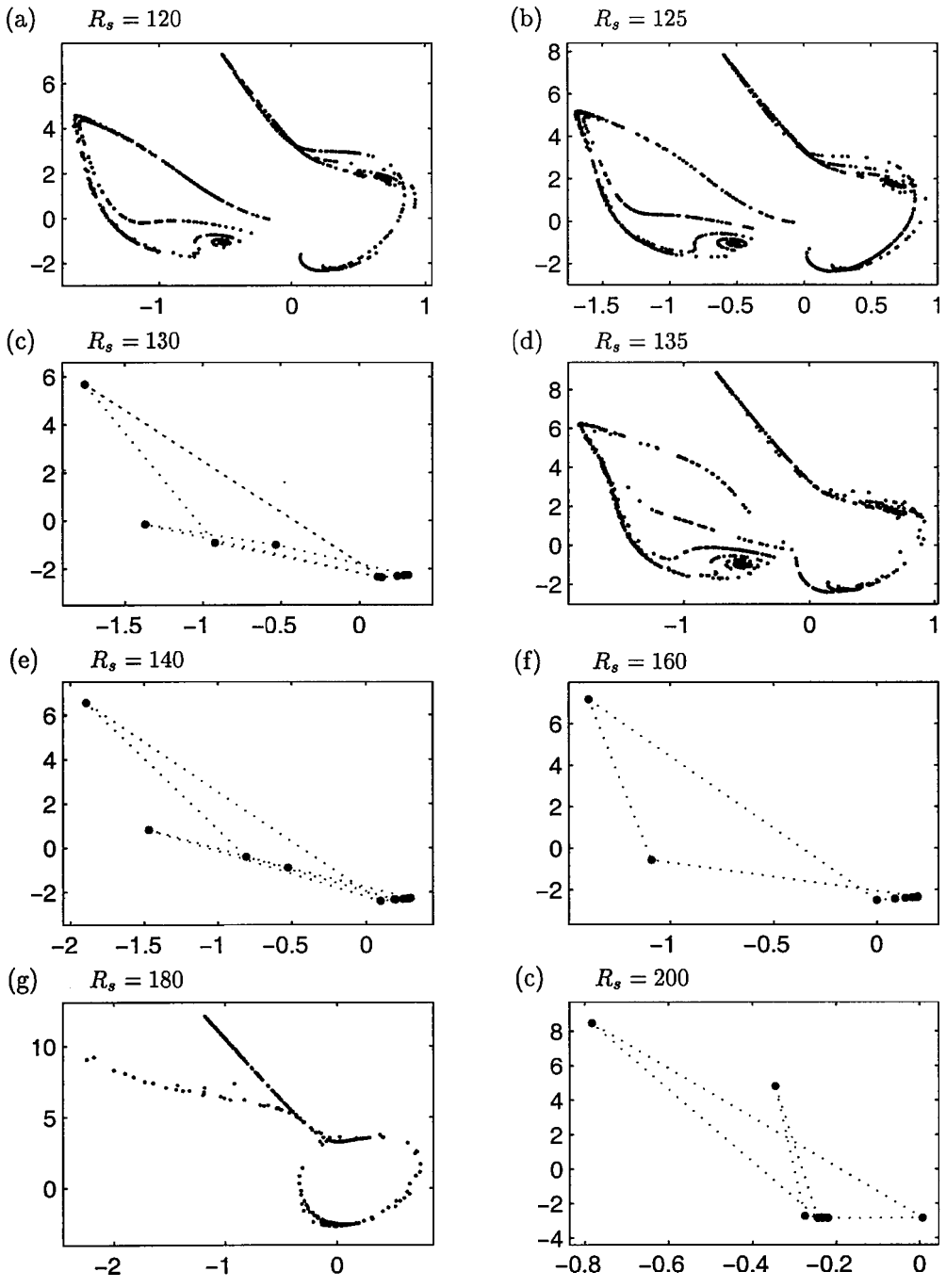


Fig. 2.60: The Poincaré cross section of $\Psi^{(0)}$ at various values of R_s. The coordinate variables used in the construction of these diagrams are identical to the ones used in figure 2.16.

the regions that are far from the discontinuity i.e $\theta > 60°$. Accordingly, it envisaged that the solution in this outer region is being correctly determined by the current numerical scheme.

In summary, the results obtained via the UWD method, do suggest that the flow near the main discontinuity ($\theta = 30°$) is unstable to a symmetry breaking perturbation. Although a direct connection between the oscillatory behaviour of Ψ and unsteady regime of $\Psi^{(0)}$ has not been uncovered in this study; it is likely that the symmetry breaking bifurcation of Ψ, at $R_s \approx 100$, may indicate the onset of a genuine secondary state. Moreover, the oscillatory behaviour near the main discontinuity leads us to believe that flow is locally chaotic/unstable in the vicinity of $\theta = 30°$. However, this hypothesis can only be tested by capturing the shock profile via a more robust/appropriate numerical method than is considered in this thesis.

2.6.2 The modified problem

Since the use of UWD has been successful for the original cylinder problem, the modified problem is now revisited to see if UWD can improve the resolution of the suspected discontinuity near $\xi = 0$.

Numerical Results

As anticipated the adapted VSF scheme has the desired effect of suppressing the Gibbs' oscillations that had previously masked the discontinuity. As R_s is increased from 50 to 160, the development of a single discontinuity is clearly observed at $\xi = 11°$, see figure 2.61 c.f. figure 2.51. Once again, it is found that the numerical results for this modified problem, are characteristically similar to the solutions for the original cylinder problem. For $R_s \leqslant 169$, the solutions for $\bar{\Psi}$ are steady and η-symmetric. If the series solution is compared to the numerical solution of $\bar{\Psi}$, it is found that $\bar{\Psi}^{(0)}$ remains a valid approximation, near $\xi = 0$, up to $R_s = 80$, see table 2.14. This result is consistent with the finding in the cylinder problem, and once again this reasserts the fact that for $R_s > 54$, the asymmetric regime of $\bar{\Psi}^{(0)}$ is not incorporated in the series

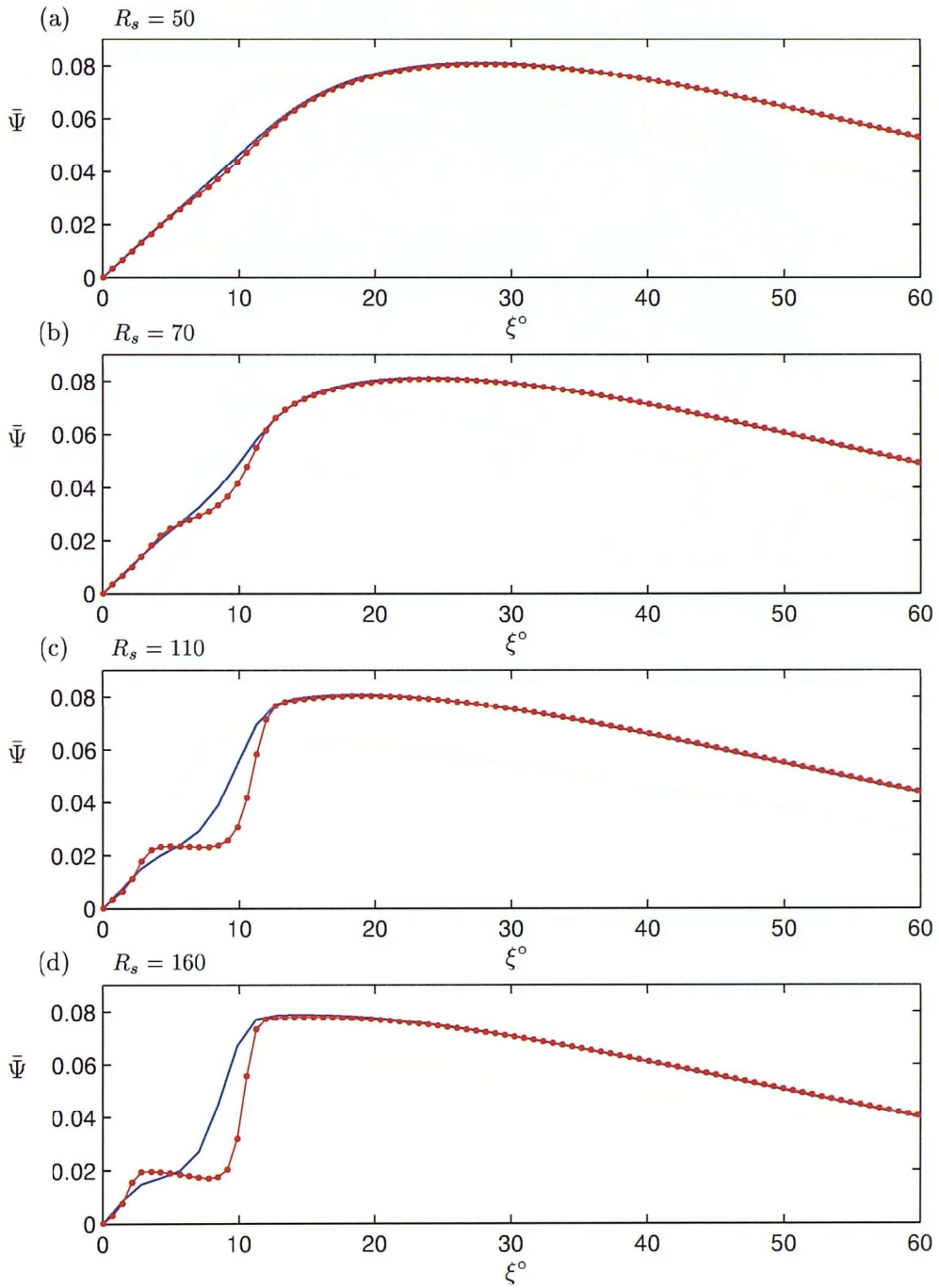


Fig. 2.61: The numerical solution for $\bar{\Psi}$ at $R_s = 50$, 70, 110, 160 with $\Delta\xi = 2\pi/256$ (blue curve) and $\Delta\xi = 2\pi/512$ (dotted red curve). Here $\eta = 0.6$ and $\Delta\tau$ is set equal to $2{\times}10^{-4}$ in the computations.

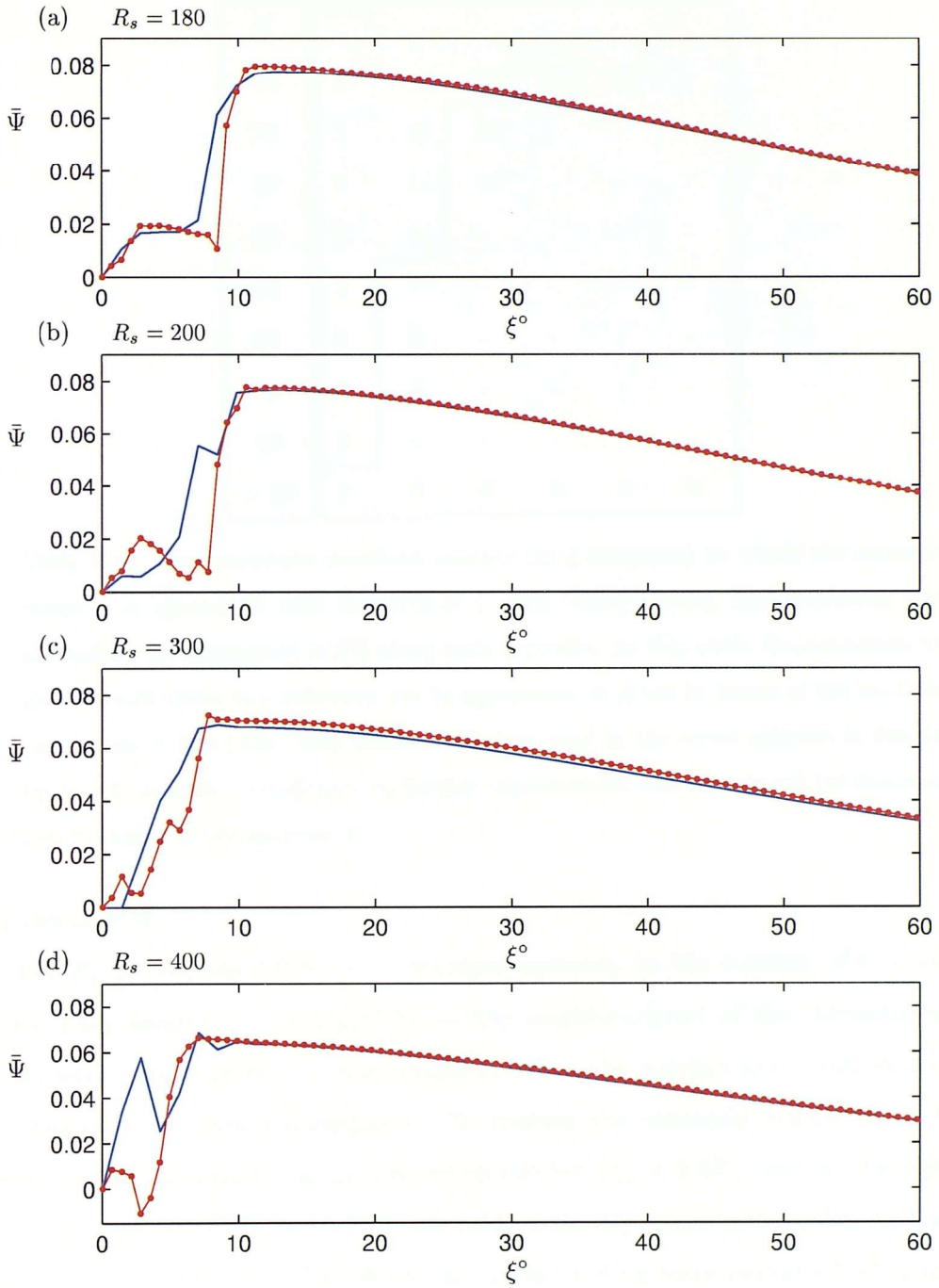


Fig. 2.62: The instantaneous ξ-profiles of $\bar{\Psi}$ at $R_s = 180, 200, 300, 400$ with $\Delta\xi = 2\pi/256$ (blue curve) and $\Delta\xi = 2\pi/512$ (dotted red curve). Here $\eta = 0.6$ and $\Delta\tau$ is set equal to 2×10^{-4} in the computations.

$N=$	0	1	2	3	4	5
R_s						
10	2	16	32	32	23*	-
20	2	17	12*	-	-	-
30	3	11	10*	-	-	-
40	3	11	-	-	-	-
50	3	7	-	-	-	-
60	3	3	-	-	-	-
70	2	3	-	-	-	-
80	2	-	-	-	-	-
> 80	0	0	0	0	0	0

Table 2.14: The maximum partition number (in ξ-direction) to which the series solution is in agreement with the DNS of (2.102) (using UWD). The maximum error allowed in the agreement is 2% along each η-profile. In this table the maximum angle to which these two solutions are in agreement, is given in terms of the partition number $n_\xi = 256\ \xi/2\pi$. The number of terms used in the series solution is denoted by $N+1$. A dash (-) indicates no further improvement and an asterisk (*) denotes a deterioration in the agreement.

expansion of $\bar{\Psi}$.

For $R_s > 169$, the DNS for $\bar{\Psi}$ becomes unsteady in the vicinity of $\xi = 11°$, see figure 2.62; moreover, the η-profiles in the neighbourhood of the discontinuity are asymmetric. As with the cylinder problem, when the η-symmetric solution is forced, the unsteady oscillation disappears. To analyse the unsteady behaviour of $\bar{\Psi}$, the period of the oscillation was monitored on the left ($\xi_L = 5.63°$) and on the right side of the discontinuity ($\xi_R = 19.69°$), see table 2.15. By fixing a Reynolds number and comparing the time period of $\bar{\Psi}$ to the corresponding time period of $\bar{\Psi}^{(0)}$, the two regimes are found to be distinct. Moreover, as with the original cylinder problem, the time period of the DNS is found to be dependent on the size of $\Delta\xi$. With $\Delta\xi$ set equal to $2\pi/256$, the time period of $\bar{\Psi}$ is found to double at $R_s = 205$. Although the

R_s	Period of $\bar{\Psi}$ with $\Delta\xi = 2\pi/256$
170	5.284
180	5.236
190	4.956
200	4.554
204	$P_1 \approx 4.435$
205–214	$\approx 2P_1$ (8.83)
215	$\approx P_1$ (4.37)
222	4.52
223	Turbulent
225	60.716
226	51.614
227	Turbulent
231	42.876
232–260	Turbulent

R_s	Period of $\bar{\Psi}$ with $\Delta\xi = 2\pi/512$
170	6.575
179	$P_1 \approx 6.302$
180	$\approx 2P_1$ (12.625)
181–182	Turbulent
183	4.724
184	5.924
185–190	Turbulent
195	4.724
200	6.784
205	5.924
210–215	Turbulent
220	2.02
225–240	Turbulent
260	2.01

Table 2.15: The time period of $\bar{\Psi}$ at various Reynolds numbers c.f. table 2.13.

period of the flow does not continue to double when R_s increased, the DNS for $\bar{\Psi}$ does continue to follow the emerging $2P_1$-state, i.e the period-doubled state, from $R_s = 205$ to $R_s = 214$. In addition, it is interesting to note that the first turbulent state of $\bar{\Psi}$ is observed at $R_s = 223$, which is quite close to the R_s-range of the $2P_1$-state. However, when $\Delta\xi$ is refined to $2\pi/512$, the $2P_1$-state occurs at $R_s = 180$. In this case, the turbulent state follows immediately at $R_s \approx 181$.

From figures 2.63 – 2.66 it is seen that when $\Delta\xi$ is refined, the change in the time period is often accompanied by a change in the order of the quasi-periodicity. Moreover, in figure 2.66 it can be seen that the quasi-periodic regime at $R_s = 260$ arises after a long transient phase. This transient phase was often observed at other Reynolds numbers too. However, the duration of the transient, does not appear to be

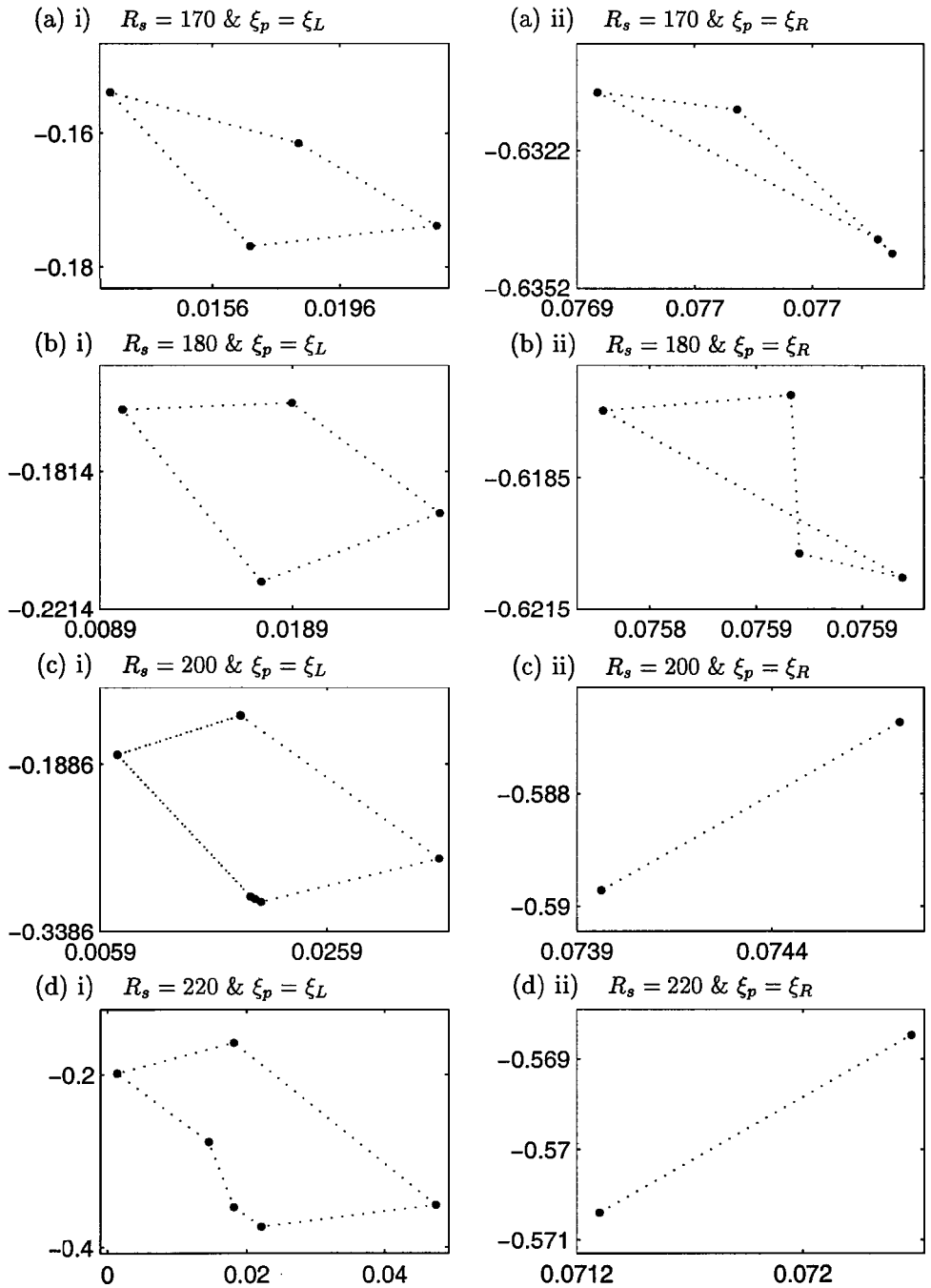


Fig. 2.63: The Poincaré cross section of $\bar{\Psi}$ at $R_s = 170, 180, 200, 220$ with $\Delta\theta = 2\pi/256$. Here $\xi_L = 5.63°$ and $\xi_R = 19.69°$.

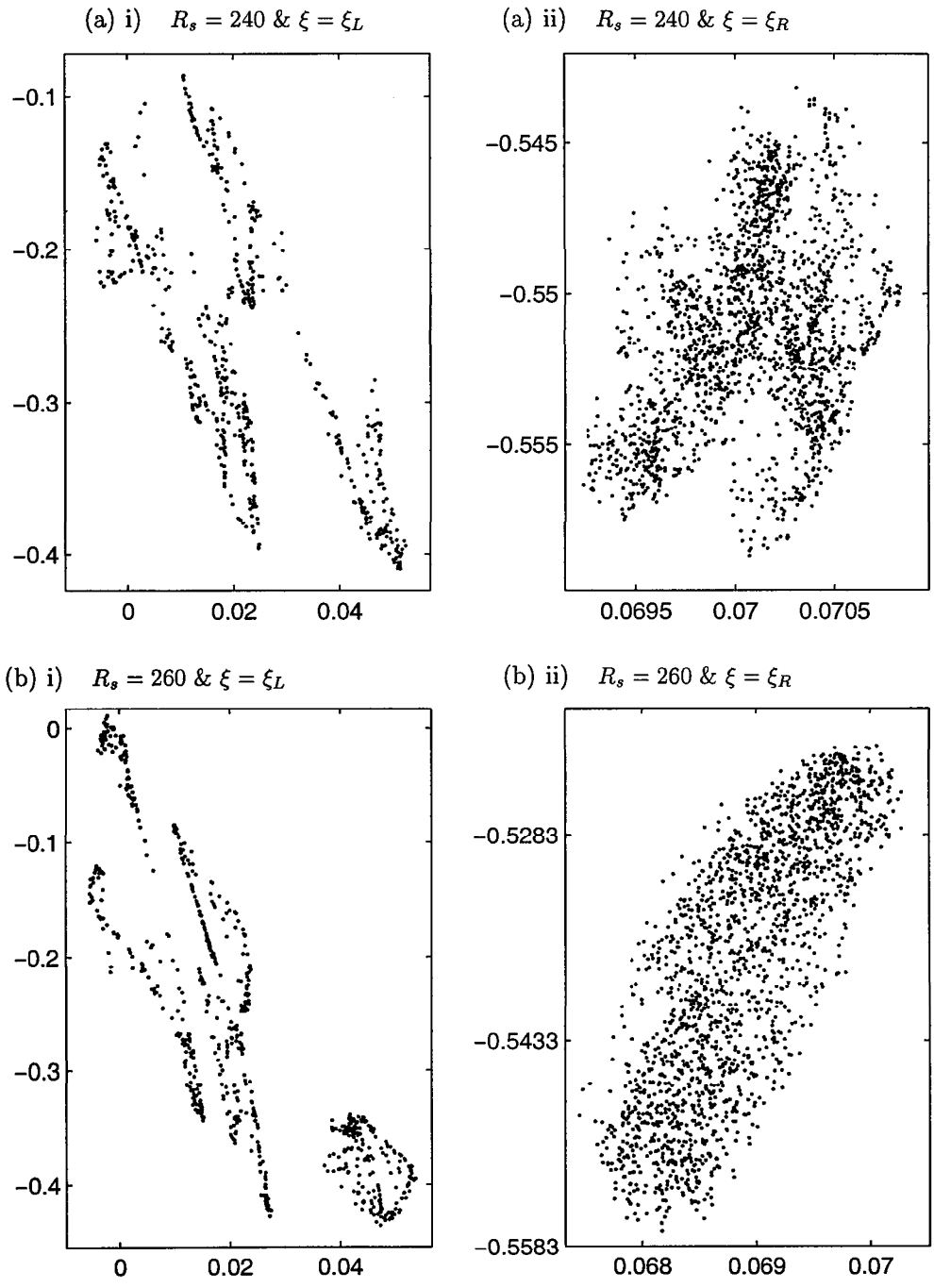


Fig. 2.64: The Poincaré cross section of $\bar{\Psi}$ at $R_s = 240$, 260 with $\Delta\theta = 2\pi/256$.

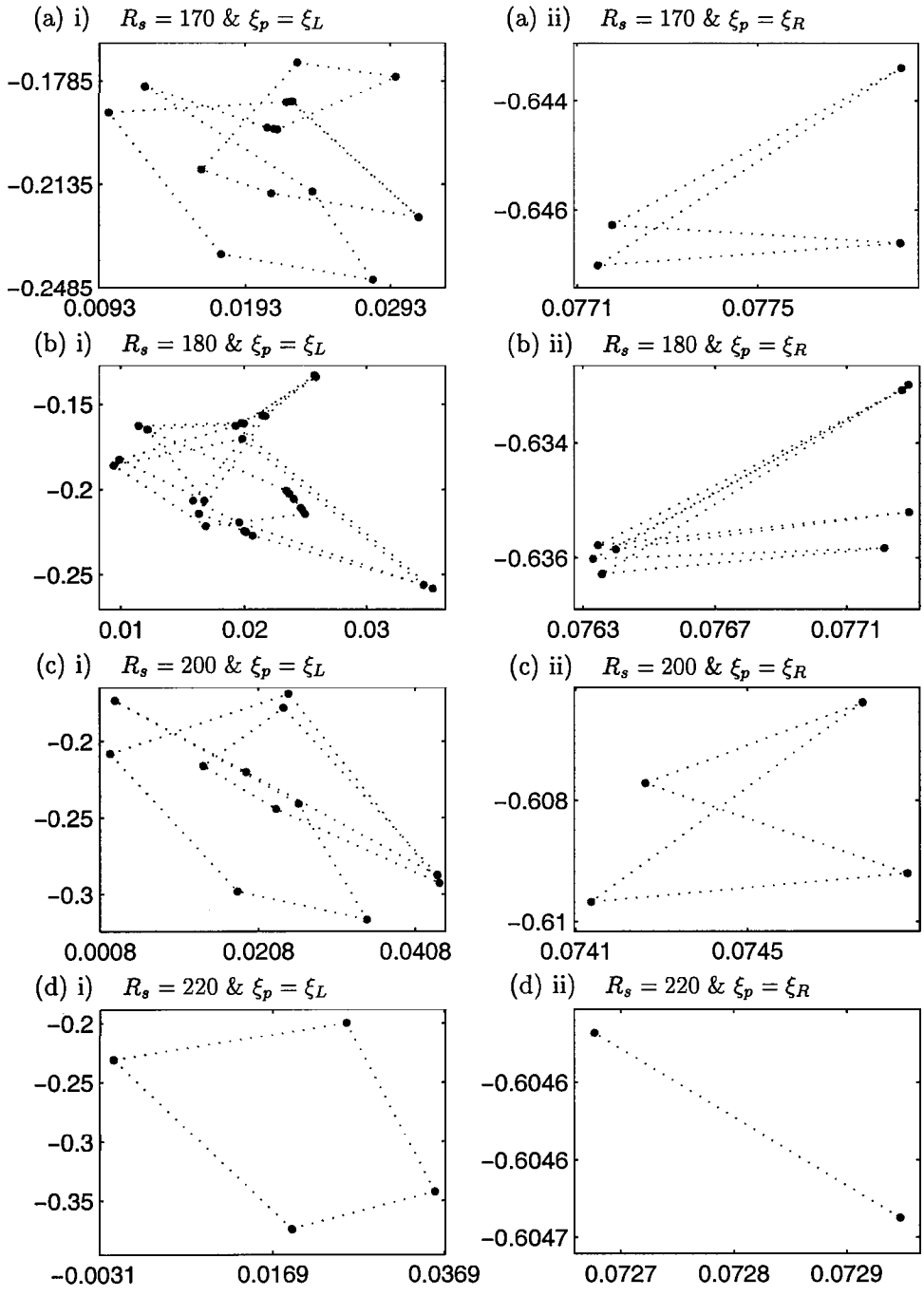


Fig. 2.65: The Poincaré cross section of $\bar{\Psi}$ at $R_s = 170, 180, 200, 220$ with $\Delta\theta = 2\pi/512$. Here $\xi_L = 5.63°$ and $\xi_R = 19.69°$.

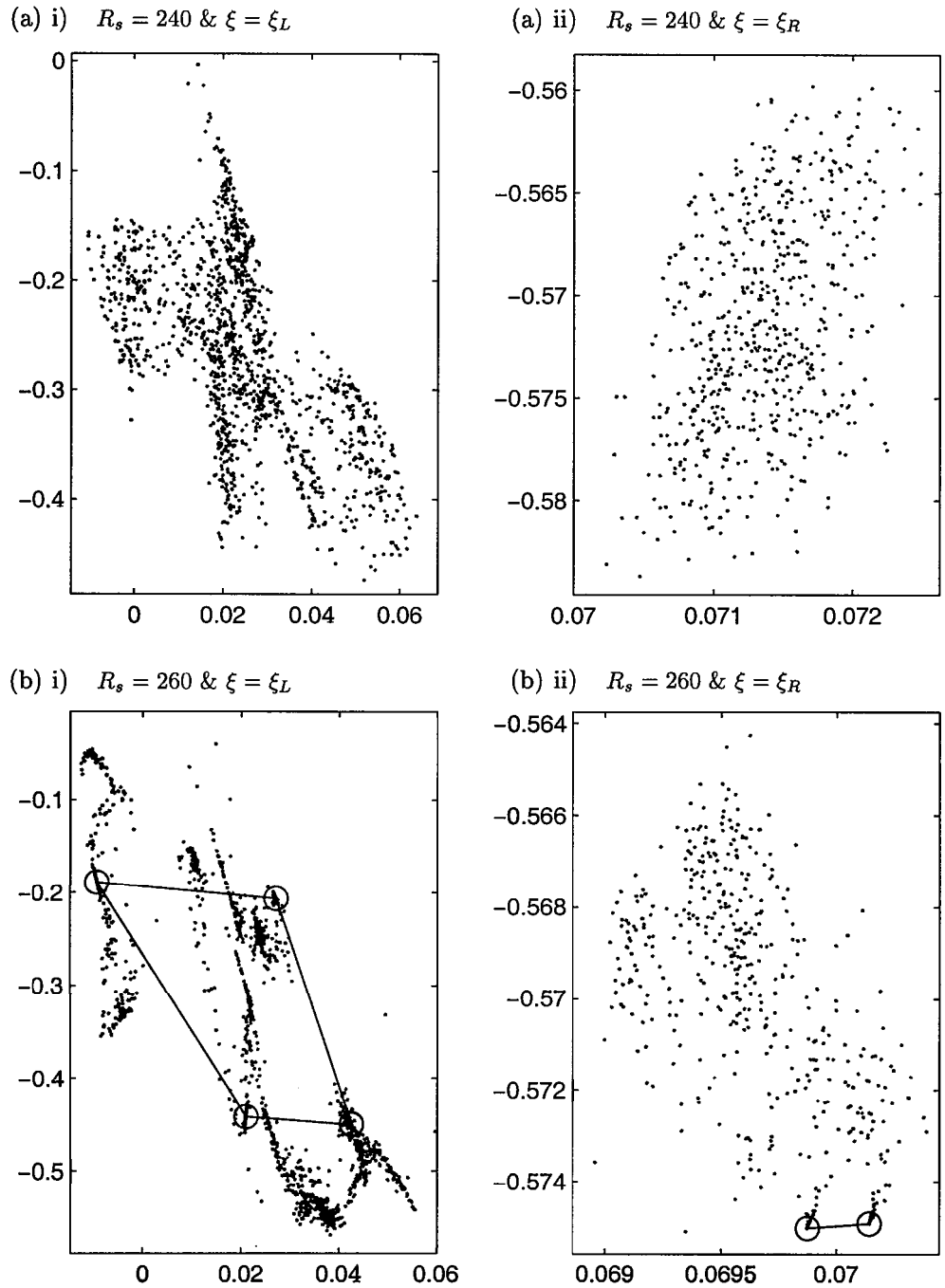


Fig. 2.66: The Poincaré cross section of $\bar{\Psi}$ at $R_s = 240, 260$ with $\Delta\theta = 2\pi/512$.

a simple function of R_s.

As expected, the results obtained for this modified problem are characteristically similar to the solutions of the original cylinder problem. Although a direct connection between the unsteady oscillation of $\bar{\Psi}$ and the asymmetric regime of $\bar{\Psi}^{(0)}$ cannot be verified at this stage, the results obtained in this study do suggest that the symmetry breaking bifurcation, which appears after the onset of the discontinuity, is a genuine feature of the flow. Since the numerical results obtained by UWD are discontinuous over a small ξ-interval for $R_s \gtrapprox 60$, the results obtained in this section are only considered to be qualitative descriptions of the flow (once the discontinuity has set in). Guided by these results, it is thought that once the Taylor series for Ψ has broken down for $R_s \gtrapprox 60$, a new expansion is required to account for the singularity. In this case, it is expected that the leading term in the new inner-expansion, is responsible for the chaotic behaviour observed near the discontinuity.

2.7 Conclusion

In this study, the induced steady streaming flow between two cylinders has been investigated in the small gap limit. Since the flow is of stagnation type, the governing stream function is expanded in a θ-power series and in this manner, the structure of the local problem at $\theta = 0$ is incorporated into the full description of the flow. From the earlier studies by H & P [37] and WBZD [97], the leading order equation is known to support chaotic solutions, in addition to stable solutions that are η-symmetric. By directly solving the governing equation for Ψ, it is found that there is no symmetry breaking bifurcation at the predicted value of $R_s = 17.3$, (see the $\Psi^{(0)}$ regime in figure 2.6).

By using a time marching procedure to calculate the terms $\Psi^{(n)}$, it is found that each successive term becomes unstable at $R_s = R_n$, where $R_1 = 6.6 > R_2 > R_3 > \ldots > R_n$. The onset of these instabilities is predicted extremely well by a linear stability analysis. Moreover, in the latter stability analysis, it is shown that $R_n = 21.76/(2n+1)$ as $n \to \infty$ and that the corresponding eigenfunctions $\Phi^{(n)}$ are even. By computing the

growth rates γ_n at different Reynolds numbers, it is found that the eigenfunctions $\Phi^{(n)}$ remain even for $R_s > R_n$. An asymptotic analysis of the particular case $R_s \gg 1$ with $\gamma_n \approx 2n + 1$, confirms that the solutions for $\Phi^{(n)}$ are even. Since the series solution cannot be computed via time marching, the steady solutions for the terms $\Psi^{(n)}$ are sought directly.

It is our view that the solution to the physical problem is given by the DNS and that the series solution is a formal approximation to the realised flow. With this in mind, it is interesting to discuss the relevance of the time marching instabilities (of the series solution) to the DNS. Since the numerical results for the DNS are bounded and continuous for $R_s \lessapprox 50$ (UWD method), it is clear that the solution to the physical problem is unaffected by any temporal instabilities (at least for $R_s < 50$). Let us now propose an explanation as to why the latter result is at variance with the instabilities present in the series solution. The results from our stability analysis for the series solution, suggest that the DNS should be unstable at all finite values of R_s. However, since our linear stability equations are independent of θ, it follows that in order for the stability analysis of the series solution to be relevant to the DNS, Ψ must be analytic in the entire complex θ-plane. In contrast, the results from our study of the *steady* series solution, suggest that Ψ does possess a singularity in the complex θ-plane (the nature of this singularity is discussed in detail later on). Hence, it is our belief that since Ψ is not analytic in the entire complex θ-plane, the stability analysis for the series solution cannot be extended to the physical solution represented by the DNS.

By using a PS numerical method to calculate Ψ, the DNS begins to develop wavy θ-profiles at $R_s = 45$, see figure 2.28. If the Reynolds number is further increased, these wavy profiles become discontinuous. For $R_s > 53$, the solutions for Ψ grow without bound, during the time marching procedure, because of two unstable η-profiles near $\theta \approx 28°$, $152°$. To minimise the effects of transportation errors, the original PS method was exchanged for a FD scheme that incorporates UWD. The application of the UWD is found to suppress the jagged θ-profiles that had previously been observed at $R_s \approx 50$. Moreover, by using UWD to calculate Ψ, it is possible to extend the calculations up

to $R_s = 1000$ (the largest Reynolds number tested). In this extended range of R_s, the numerical solutions for Ψ are bounded and the location of the two discontinuities remain confined to the θ-interval $0° \leqslant \theta \leqslant 40°$.

For $R_s < 138$, the solutions for Ψ (with $\Delta\theta = \pi/128$) are found to be steady and η-symmetric. However, by increasing the Reynolds number from $R_s = 60$ to $R_s = 130$, it is seen that the wavy θ-profiles at $R_s = 60$, eventually become discontinuous near $\theta \approx 9°$ and $\theta \approx 30°$, see figure 2.51. Despite the presence of the two discontinuities, the series solution remains a valid approximation (near $\theta = 0$) up to $R_s = 110$, see table 2.12. Since the DNS for Ψ is steady and η-symmetric up to $R_s = 138$, it is clear that the asymmetric regime of $\Psi^{(0)}$ plays no role in the series expansion of Ψ. Accordingly, it is expected that the realised flow is not chaotic for $R_s < 138$.

At $R_s = 138$, the DNS for Ψ (with $\Delta\theta = \pi/128$) loses symmetry in the vicinity of the discontinuity and the resulting asymmetric η-profiles are unsteady. At this point, it is important to mention that in this regime, the validity of the numerical results is entirely dependent on the robustness of the UWD scheme. With this in mind, the results obtained within the discontinuous regime are only considered to be qualitative descriptions of Ψ.

Since the governing equations for Ψ are parabolic in θ, one should consider the validity of the numerical solutions beyond the location of the first discontinuity. For every fixed value of R_s, our results suggest that once the second discontinuity is passed, the numerical solution for Ψ always converges to the same result, regardless of the grid size chosen for $\Delta\theta$, see figure 2.51. This result is encouraging because it suggests that the numerical solution has converged to the correct result for the θ-interval beyond the last discontinuity.

Since the DNS for Ψ is discontinuous over a small θ-interval for $R_s > 60$, the unsteady oscillation near the shock, may be regarded as an artifact of the numerical error associated with the scheme. However, contrary to the latter view, when the η-symmetric solution is forced, the resulting solution for Ψ is steady. This result suggests that the symmetry breaking bifurcation at $R_s = 138$ is a genuine feature of the flow.

With $\Delta\theta$ set equal to $\pi/128$ in the calculations, the oscillation near the discontinuity is found to be quasi-periodic over the range $138 < R_s < 168$. At $R_s = 168$, the first turbulent state is observed; moreover, if R_s is increased further, the flow near the discontinuity returns to a quasi-periodic state.

When $\Delta\theta$ is decreased to $\pi/256$, the symmetry breaking bifurcation occurs at $R_s = 100$ and the time periods of the quasi-periodic states are found to change. Since these quantitative aspects of the DNS do not remain consistent when $\Delta\theta$ is refined, a direct link between the DNS and the asymmetric regime of $\Psi^{(0)}$, cannot be readily established. Despite the fact that a quantitative agreement is elusive, a characteristic similarity does exist between the DNS and the chaotic regime of $\Psi^{(0)}$. For instance, there is a doubling of the time period just before the first turbulent state of Ψ is observed, this is reminiscent of the period doubling cascade of $\Psi^{(0)}$. Moreover, since the turbulent states of Ψ occur at sporadic Reynolds numbers, the asymmetric regime of Ψ is characteristically similar to the asymmetric regime of $\Psi^{(0)}$. The latter result is particularly encouraging because it fortifies our belief, that the numerical scheme has not collapsed once the oscillation has set in. Had the scheme collapsed, one might expect that there would be a threshold value of R_s, above which, all the unsteady oscillations are turbulent; in this case, the DNS would be different from the asymmetric regime of $\Psi^{(0)}$.

Having summarised the direct numerical solutions for Ψ, we now compare the DNS to the results obtained via the θ-series expansion. For $R_s < 1.1$, the series solution is found to agree with the DNS and a complete representation from $\theta = 0°$ to $\theta = 180°$ is obtained. However, as R_s is increased, the agreement of the series solution is reduced to successively smaller angles. At $R_s = 110$, the agreement is confined to $\theta \leqslant 2.8°$ and $\Psi^{(0)}_{\text{sym}}$ is the only valid term in the series expansion, see tables 2.6 and 2.12. By comparing the DNS for Ψ, to the small-R_s asymptotic solution (2.42), it is found that the two solutions are identical for $R_s \leqslant 15$, see figure 2.27. For $R_s > 15$, the agreement near $\theta = 0°$ is lost, but the asymptotic solution continues to represent the flow field in the core region i.e. $0° < \theta < 180°$. In contrast, for $R_s > 15$, the series solution

continues to agree with the DNS near $\theta = 0°$. Accordingly, this indicates that the series solution is no longer in agreement with its asymptotic form (2.43). By analysing the small-R_s asymptotic solution for Ψ, it is found that this solution is convergent for a larger range of R_s, than the corresponding asymptotic solution for $\Psi^{(n)}$, see (2.91) and (2.93). These conflicting results, are reconciled by the fact that the asymptotic solution for Ψ (2.42) varies like $\sin\theta$; therefore, the associated convergence criteria, derived by the M_1 measure, may breakdown in the vicinity of $\theta = 0$. Consequently, the correct behaviour near $\theta = 0$ is governed by the asymptotic analysis of the terms $\Psi^{(n)}$. For $n \geqslant 4$, the M_1 measure accurately predicts the dissociation of the terms $\Psi^{(n)}$, from their asymptotic forms, see table 2.8.

To avoid the growing eigenfunctions in the time marching procedure, the unsteady regime is studied by expanding each term $\Psi^{(n)}$ in a Fourier series. In the asymmetric regime of $\Psi^{(0)}$ ($R_s > 53$), it is found that the numerical solutions for $\Psi^{(n)}$ do not converge. Moreover, in this asymmetric regime, each Fourier mode $\Psi^{(n\geqslant 1,k)}(\eta)$ is found to have an even profile. It is thought that the divergence of each $\Psi^{(n)}$ term, is related to the growing even perturbations in the time marching procedure. However, in the symmetric regime of $\Psi^{(0)}$ ($R_s > 170$), the Fourier spectrum for each of the first few terms does decay to zero. Despite this convergence, the terms are disordered in terms of magnitude i.e. $\|\Psi^{(0)}\| < \|\Psi^{(1)}\| < \|\Psi^{(2)}\|$ etc. By investigating this symmetric regime at large values of R_s i.e. $R_s \approx 1600$, it is found that progressively more Fourier modes are required to represent each term $\Psi^{(n\geqslant 1)}$. However, the need for more Fourier modes is anticipated, because the period of the driving term, $\Psi^{(0)}$, increases with R_s.

From our numerical investigation of equation (2.33), it is found that the DNS for Ψ is discontinuous for $R_s > 60$. However, our asymptotic analysis suggests that a continuous solution for Ψ is also supported at large values of R_s, see equation (2.51). This implies that there are at least two η-symmetric steady states of Ψ: one which is continuous (asymptotic result) and the other which is discontinuous (DNS). Based on this assumption, we now propose a possible mechanism that describes how the series solution relates to the two different steady states of Ψ.

For asymptotically small values of R_s, the solution for Ψ is: unique, steady and η-symmetric. In this case, the DNS and the series solution agree over the full θ-range $0° \leqslant \theta \leqslant 180°$. However, as R_s is increased the series representation of Ψ begins to deteriorate. The latter claim is easily justified by considering the DNS and the small-R_s asymptotic solution for Ψ, see equation (2.42). At $R_s = 15$, the DNS and the asymptotic solution for Ψ are in complete agreement, see figure 2.27. This shows that the DNS is not affected by any discontinuity at this stage. In contrast, at $R_s = 15$, the series representation of Ψ is only valid for $\theta \leqslant 80°$. This implies that the convergence of the series solution is being affected as R_s is increased. The results in table 2.6 suggest that the inclusion of more terms, do not benefit the series representation of Ψ. Accordingly, it is envisaged that the breakdown of the Taylor series is due to a singularity of Ψ. Since this singularity does not occur on the real θ-axis, it must occur in the complex plane. In this manner, the location of the singularity (in the complex plane) dictates the radius of convergence of the series solution. Since the series representation of Ψ deteriorates as R_s is increased above $R_s = 15$, it is deduced that the singularity moves closer to the point $\theta = 0°$. At $R_s = 130$, the singularity of Ψ is clearly observed on the real θ-axis (in fact, our results indicate that at least two discontinuities are present), see figure 2.51. In this case it is clear that the series solution will not converge beyond the location of the discontinuity. However, if R_s is increased to $R_s = 1600$, the series solution does converge and the large-R_s asymptotic solution for Ψ is obtained. This suggests that the two different steady states of Ψ, must emerge from the same η-symmetric state after the discontinuity has set in on the real θ-axis. For $R_s > 130$, it is proposed that the series solution converges to the asymptotic state because the associated singularity moves away from $\theta = 0°$. However, since the DNS for Ψ remains discontinuous at large Reynolds numbers, it is envisaged that a second steady regime exists where the singularity does not move away from $\theta = 0°$. Accordingly, this explains why the series solution does not converge to the DNS at large values of R_s.

Let us now turn our attention to the results for the series solution in the unsteady

regime. By using the unsteady asymmetric solution of $\Psi^{(0)}$ to drive the higher order terms, it is found that a converged result cannot be obtained for each $\Psi^{(n\geqslant 1)}$. Moreover, a similar divergence of the series is observed when the unsteady solution of $\Psi^{(0)}_{\text{sym}}$ is considered. Accordingly, this suggests that no (continuous) time periodic states exist for Ψ. However, this idea is at variance with the intuitive expectation, that the solutions for Ψ are similar to regimes of $\Psi^{(0)}$. By using the solutions for $\Psi^{(0)}$ as a guide to predict the behaviour of Ψ, one might have expected that the steady η-symmetric regime of Ψ would be the least "preferred" mode i.e. the most unstable mode (the hierarchy of the $\Psi^{(0)}$ regimes are shown in figure 2.6). From our numerical investigation of the governing PDE, we have only found one continuous solution for Ψ, and this solution is steady and η-symmetric. Since the steady symmetric regime appears to be the preferred mode for Ψ, it is our view that the governing PDE does not support any (continuous) unsteady periodic solutions for Ψ. As previously mentioned, this view is also supported by our Fourier analysis of the series solution in the unsteady regime.

Despite the absence of continuous unsteady solutions in the DNS; our numerical results for the discontinuous regime of Ψ, show that an unsteady oscillation develops near the shock. Since the qualitative behaviour of this oscillation closely resembles the asymmetric regime of $\Psi^{(0)}$, it is thought that the term $\theta\Psi^{(0)}$ might constitute part of a valid inner-expansion near $\theta = 0°$. To investigate this idea it is necessary to obtain an accurate numerical description of the oscillation. Since our results only describe the qualitative behaviour of Ψ, a direct connection between the DNS and the series solution was not established.

Although the findings above are particular to the cylinder problem, it is thought that many of the key features are also observed in similar flows i.e. flows that are approximated locally by the leading order equation for $\Psi^{(0)}$. In this study, the latter issue has been explored by changing the derivative conditions at the walls from $-\sin\theta$ to $-\theta\exp(-\lambda\theta^2)$, see (2.33e,f). The results obtained for this new problem, are qualitatively similar to findings in the original cylinder problem. For example, the numerical

solutions for $\bar{\Psi}$ are steady and η-symmetric for $R_s \leqslant 169$. Once again this shows that the asymmetric regime of $\bar{\Psi}^{(0)}$, plays no role in the required series expansion for $\bar{\Psi}$. Moreover, for $R_s \ll 1$, it is found that the series solution is in complete agreement with the DNS. As expected, when R_s is increased above unity, the series representation of Ψ is confined to a progressively smaller angle.

By analysing the magnitude of each term in the series expansion, it is found that terms become disordered at $O(1)$ values of R_s; in particular, for $10 < R_s < 30$ it is found that $\|\bar{\Psi}^{(0)}\| \sim \|\bar{\Psi}^{(2)}\|$. In order for the series solution to converge at every value of ξ, $\bar{\Psi}$ must be analytic in the complex plane. However, our results show that the series solution begins to diverge and accordingly, this suggests the presence of a singularity (whose location is dependent on R_s). At $R_s = 110$, the singularity is clearly seen on the real axis at $\xi = 11°$, see figure 2.61. At $R_s = 170$, an unsteady oscillation develops near the discontinuity; this is completely analogous to scenario in original cylinder problem. By forcing the η-symmetric solution of $\bar{\Psi}$, this oscillation disappears. Since this result corroborates the findings in the cylinder problem, it is thought that the sequence of events in the modified problem, are also explained by the original proposition regarding the singularity in the complex plane.

In conclusion, our results demonstrate that the series solution for Ψ, is only convergent in the limits $R_s \to 0$ and $R_s \to \infty$. Moreover, in these limits, the convergent series solution is driven at leading order by the steady η-symmetric solution of $\Psi^{(0)}$. Since the latter regime of $\Psi^{(0)}$ is the least stable of all the possible configurations, see figure 2.6, it is expected that the same, steady η-symmetric, configuration is the least stable regime of Ψ. If this happens to be the case, this explains why the DNS for Ψ converges to a discontinuous configuration (at high Reynolds numbers), even when a continuous solution coexists. At $R_s \approx 138$, the DNS for Ψ develops an unsteady oscillation in the vicinity of the discontinuity. Moreover, the onset of this unsteadiness is synchronous with a symmetry breaking bifurcation. By analysing the time period of the oscillation, it is found that many quasi-periodic states exist in addition to many turbulent ones. Moreover, the latter solutions are found to resemble the results obtained for $\Psi^{(0)}$ in

the chaotic regime. However, in order to establish a direct link between the DNS and $\Psi^{(0)}$, it is necessary to obtain an accurate description of the flow near the discontinuity. Since the current UWD method does not give the required resolution, this aspect of the regime remains open to further investigation. To explore the unsteady oscillation, it is expected that a robust shock capturing numerical method is required. When devising such a method (or when testing an alternative approach), one must ensure that the values of the: mass flux, momentum flux, and energy flux are conserved at the shock i.e. the pre- and post-shock values of each entity are the same. Moreover, our results for the cylinder problem indicate that two discontinuities exist within close proximity of each other, see figure 2.51. One can imagine that this added difficulty, further complicates the task of capturing the unsteady oscillation near the shock.

Chapter 3

The flow in a torsionally oscillating circular pipe

The present study concerns the instability of a viscous incompressible flow within a horizontal circular pipe, that oscillates torsionally about its vertical axis of symmetry. Our stability analysis has been motivated by the experimental work of Bolton & Maurer [10] and their discovery of a new roll-type instability. In their experiment, the circular pipe is replaced by a Hele-Shaw cell, which is made of two vertical rectangular plates that are separated by a gap of small width. In this configuration, Bolton & Maurer have observed the development of longitudinal rolls at large oscillation frequencies.

In this study, the equivalent roll-type instability is sought in the circular pipe, for small-amplitude and high-frequency oscillations. A dispersion relation for the frequency parameter, Φ, is derived and subsequently it is shown that the instability is initiated within a boundary layer, of thickness $O(\Phi^{-1/2})$, close to the pipe wall. Moreover, at $\theta = 0$ i.e. along the horizontal diameter of the pipe, the latter dispersion relation reduces to the one that is derived for the Hele-Shaw cell. In view of this result, one might expect that the leading order approximation for the critical value of Φ, is given by the result for the local problem i.e. the value corresponding to the Hele-Shaw cell. However, by using the method of Soward & Jones [82], it is shown that the correct minimisation of Φ is achieved not on the real latitude, but in its extension to the complex plane i.e. $\mathrm{Im}\{\theta\} \neq 0$. An initial attempt to compute the neutral surface via time marching is found to be inappropriate. This is because the

numerical procedure initially locks into one neutral surface, but then jumps to another. To resolve this difficulty the velocity components are expanded in a Fourier series in time, and subsequently the correct turning point is identified by numerically solving the resulting eigensystem.

3.1 Introduction

The present study concerns the onset of a new roll-type instability within a horizontal circular pipe, that oscillates torsionally about its vertical axis of symmetry. This instability was first reported experimentally by Bolton & Maurer [10] (henceforth referred to as BM), who categorise the development of these rolls into four main phases: 1) The onset of weak rolls, 2) strong roll development, 3) wavy modes (a wavy instability superimposed on a strong roll state) and 4) turbulent rolls (a turbulent state superimposed upon a well defined roll structure). The above sequence of transitions, closely resembles the course of events observed in other Taylor-Couette flows. Since the vortices in Taylor-Couette flow align themselves in a direction that is parallel to the base flow, see Coles [13], Fenstermacher *et al.* [21] and Koschmieder [48], the instability identified by BM can be thought of as a configuration that is characteristically similar. For consistency, we shall make use of the notation adopted by BM, and refer to Φ and α as the frequency parameter and the maximum amplitude of oscillation respectively. For the Hele-Shaw cell, at $O(1)$ values of Φ and α, the transitions occur in a uniform fashion as described above. However, for small amplitude forcing ($\alpha < \pi/2$), there is hysteresis i.e. the frequency marking the onset of strong rolls, is found to be larger than frequency associated with the disappearance of rolls (found by decreasing Φ). In this case, BM believe that the onset of the strong rolls is possibly subcritical and therefore not amenable to a linear stability analysis. In the particular regime where α is small ($\alpha \lessapprox 0.75$ and $\Phi \gtrapprox 700$), BM also predict, from their experimental data, that the onset of turbulence could possibly be synchronous with the onset of strong rolls.

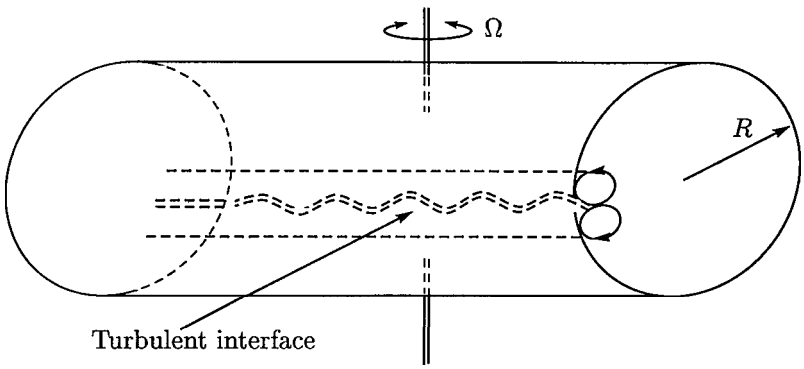


Fig. 3.1: The unstable interface between two rolls in the circular pipe problem.

In addition to the original Hele-Shaw cell experiment, BM have also observed a similar roll-type instability in a torsionally oscillating circular pipe. Although BM have not characterised the flow in this regime, some interesting observations are made. If the radius of the cylinder is R, the configuration approximately corresponds to a Hele-Shaw cell of square cross section i.e. with the separation gap and vertical height both equal to R. At sufficiently large frequencies, a single strong roll develops in the pipe. Moreover, this roll structure is sensitive to the initial state of the fluid. For certain initial states, two counter rotating rolls are formed in the pipe, see figure 3.1. The interface between these two neighbouring rolls is typically turbulent. Since this configuration has not been thoroughly examined, it is unclear if the turbulent behaviour continues into regime considered in this study i.e. for small amplitude oscillations.

The experimental problem investigated by BM was also studied theoretically by Hall [36]. Hall finds that a linear stability analysis, for $O(1)$ values of Φ and α, is able to capture the onset of strong rolls extremely well. However, nothing emerges from this analysis to suggest that the weak roll state, is a genuine instability. Hall attributes these states to the end effects of the Hele-Shaw cell, whereas BM associate them with the introduction of higher harmonics from the mechanical linkage in their apparatus. Despite the limited amount of data available from the experimental work (data was collected in the range $0.7 < \alpha < 3.3$), Hall also carried out an asymptotic analysis for two special cases: 1) $\alpha \gg 1$ with $\Phi \ll 1$, and 2) $\alpha \ll 1$ with $\Phi \gg 1$. The predictions

from the former case, when extended to the experimental range, are found to be in poor agreement with the experimental results; in contrast, the analysis for the latter case produces better results. However, it should be emphasised that the range of α investigated by BM, is certainly not within the scope of the definitively validating the results of such asymptotic limits.

It was also deduced in [36], that shear flow instabilities (periodic in the base flow direction) are not responsible for driving the wavy modes observed by BM. In the large frequency limit, the governing stability equation is found to be that of a Stokes layer, see Kerczek & Davis [46] and Hall [26]. Subsequently, it is shown that a shear flow instability can only be the dominant instability, for amplitudes of exceptionally small ($\alpha < 0.05$) or extremely large size ($\alpha > 3965\Phi^{-2}$ as $\Phi \to 0$). However, it is interesting to note that the wavy modes are only observed within the intermediate range $1.04 < \alpha < 1.92$. Since the large amplitude condition, $\alpha > 3965\Phi^{-2}$, is only valid for small Φ, it was rationalised by Hall that the shear wave instabilities could be more unstable (than the roll-mode instabilities) at finite values of Φ. However this analysis was not pursued. Bolton has also put forward the idea, that the wavy mode could in fact be a secondary instability of the rolls. Finally, by considering the destabilising terms in the governing stability equations, Hall concluded that Coriolis effects were responsible for triggering the strong roll instabilities.

The aim of the present study, is to extend the high-frequency and small-amplitude analysis of the Hele-Shaw cell, to the circular pipe. After deriving the base flow, it is found that the velocity of the basic state is largest near the edge of the pipe. Moreover, by considering the geometrical symmetry, it is anticipated that the instability must first manifest along the horizontal diameter of the pipe i.e. at $\theta = 0$ with $r \sim \frac{1}{2}$ see figure 3.3 on page 186. Thereafter, a perturbation is introduced to the base flow. The $O(\Phi^{-1/2})$ length scale in the θ direction is incorporated into the stability equations by expanding the perturbation using the WKBJ method. This procedure leads to an eigenvalue problem of the form

$$\mathcal{F}(k, B, \mu) = 0, \tag{3.1}$$

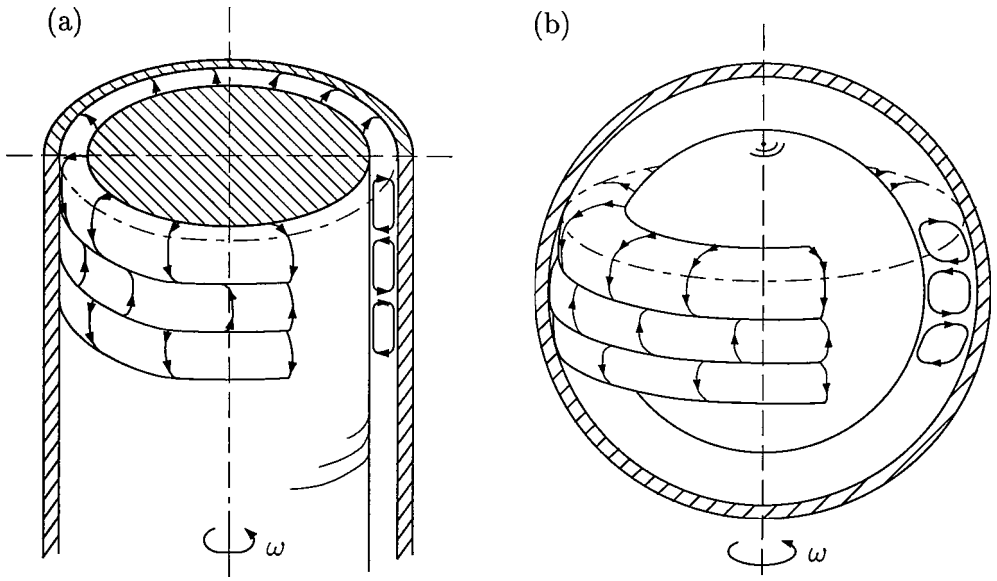


Fig. 3.2: Vortices in : (a) cylindrical, and (b) spherical Taylor-Couette flow (with inner body rotating only).

where k is the wave number, μ is the growth rate in time and B is the eigenvalue that requires minimising. At $\theta = 0$, the eigen relation reduces to the one obtained for the Hele-Shaw cell, see Hall [36] (3.27). However, it is readily anticipated that the leading order approximation for B does *not* correspond to the result obtained for Hele-Shaw cell. This fact has now become a well known result, owing to the studies undertaken by Walton [96], Hocking & Skiepko [42], Hocking [43] and the subsequent followup work by Soward & Jones [82].

In 1978 Walton [96] investigated the flow between two concentric spheres in the narrow gap limit. In this configuration the inner sphere rotates with constant angular velocity, while the outer one remains at rest. Walton's study had been motivated by the experimental investigations of Wimmer [99] (see [100] also), Munson & Menguturk [53][54][55] and Sawatzki & Zierep [71]. From the experimental studies, it is known that if the two spheres are separated by a small gap, then the instabilities first develop near the equator. Moreover, these instabilities are similar to the vortices observed in Taylor-Couette flow, see figure 3.2. For larger gaps, there is no such secondary flow and the transition to chaos ensues directly. In addition, for small gaps, the torque

required to rotate the inner sphere, is found to be dependent on the gap size. For larger gap sizes, the required torque is predicted well by the theory for the unbounded one-sphere problem.

Walton envisaged that it would be possible to expand the critical Taylor number, T, (for the two-spheres problem) in a series by using the non-dimensional gap width, $\epsilon(\ll 1)$, as a perturbation parameter. Accordingly, Walton found that the leading order governing equation, near the equator $\theta = 0$, is identical to the one derived for the associated cylinder problem. Since this result is inline with intuition, Walton sought to incorporate the results for cylindrical Taylor-Couette flow, into his stability analysis for the two-spheres problem. Consequently, this formulation leads to the expansion

$$T(k, \theta = 0, \mu = 0) = T_{cyl} + \epsilon T_1 + \epsilon^2 T_2 + \ldots \tag{3.2}$$

with

$$T_{cyl} = 1694.95 \quad \text{and} \quad k = k_{cyl} = 3.1266. \tag{3.3}$$

Here k, μ and θ are as previously defined (see page 178), and the subscripts *cyl* denote the corresponding results for the cylinder problem. By proceeding to the next order to obtain T_1, Walton's analysis encounters a fatal error. Within a small layer near the equator, where $\theta \sim \epsilon^{\frac{2}{3}}$, Walton derives an amplitude equation of the form (see [96] (5.14))

$$\frac{\mathrm{d}^2 A}{\mathrm{d}\phi^2} + i\phi A = 0, \qquad \text{with} \quad A \to 0 \quad \text{as} \quad \phi \to \pm\infty. \tag{3.4}$$

Here $\phi = \epsilon^{-\frac{2}{3}}\theta$. In order to proceed with the analysis, it is necessary that $A(\phi)$ decays exponentially fast towards each pole. However, it is well known that the above complex Airy equation does not permit such solutions. This shortcoming in Walton's analysis is the result of assuming $T_0 = T_{cyl}$.

Hocking & Skiepko [42] (henceforth referred to as H. & S.), were the first to appreciate the subtle but important effects of curvature. In their study, H. & S. consider the flow between two-spheroids and subsequently introduce the parameter δ, where the complete range of shapes from cylinder to sphere is covered by letting δ increase

from 0 to 1. By using a slightly different formulation to Walton, H.& S. were able to produce the following expansion for the critical Taylor number:

$$T = T_{cyl} + 1969.24\,\epsilon + 876.07\,\epsilon^2 + 916.08\,\epsilon\delta + \underline{73.17\,\delta^2} + \ldots, \tag{3.5a}$$

$$k = k_{cyl} - 0.01485\,\epsilon + \underline{0.54324\,\delta}, \quad \text{with} \quad \epsilon = O(\delta). \tag{3.5b}$$

From the above expansion, it is clear that for a particular spheroid (fixed δ), the critical Taylor number in the small gap limit ($\epsilon \to 0$) does not approach the corresponding result for the two-cylinders. In part two of this study, Hocking [43] attempted to generalise the latter discussion, by analysing the flow between two-spheroids with a separating gap of arbitrary size. In this subsequent formulation the first approximation to the wave number, k_c, is left arbitrary i.e not equal to k_0; here (k_0, T_0) corresponds to the minimum on the (k, T) curve, which in this case is (k_{cyl}, T_{cyl}). Hocking's assumption that $k_c \neq k_0$, was based on his prior knowledge of the so called *singular* limit of $\epsilon \to 0$ in (3.5). The solvability condition for this problem, gives rise to two amplitude equations which must be solved simultaneously. Hocking then demonstrates that under the incorrect assumption $k_c = k_0$, a new scaling would be necessary. However under this new scaling, the coupled amplitude equations do not support solutions of the required form c.f Walton [96]. In addition, Hocking shows that this difficulty is not overcome even when a previously neglected nonlinear term, is incorporated into the equations. Accordingly the assumption that $k_c = k_0$, was shown to be incorrect.

To resolve this issue, Hocking proceeded by finding a class of particular solutions to the governing amplitude equations. From this class of particular solutions, Hocking accepts the solutions that give the lowest value of T_0. By minimising T in this way with $\delta = 1$ i.e. for a spheroid that is a sphere, the approximation for the critical Taylor number, $T = 1786$, is found to be slightly in excess of the experimental value $T = 1731$. However, in order to physically observe the instability, over the meridional circulation, it is necessary to increase the Taylor number slightly above the 'true' value of the onset. This implies that the experimental value recorded by Wimmer, is slightly in excess of the actual value associated with the onset. In view of the latter fact,

Hocking's value, $T = 1786$, is unsatisfactory because it is larger than the Wimmer's experimental value.

In a final attempt to reduce the value of his critical Taylor number, Hocking also considered non-axisymmetric disturbances. This was inspired by Wimmer's experimental observation, that not all of the vortices near the equator were toroidal (some were spirals of small pitch). Unfortunately these disturbances were found to be more stable than the axisymmetric ones.

Soward & Jones [82] then undertook the two-spheres problem, and subsequently they put forward a mathematical idea that is applicable to other generalised studies that include curvature. To understand the reasoning behind their proposal, let us examine the differential of T with respect to variations in k, θ and the growth rate μ:

$$\mathrm{d}T = T_k \,\mathrm{d}k + T_\theta \,\mathrm{d}\theta - iT_\mu \,\mathrm{d}\omega. \tag{3.6}$$

Here the subscripts denote partial derivatives and ω $(= i\mu)$ is the frequency of the oscillation. Hence for any given real values of $\mathrm{d}k$ and $\mathrm{d}\theta$, at the minimum of T, there must exist a real value of $\mathrm{d}\omega$ which satisfies the differential (3.6) with $\mathrm{d}T = 0$. This is only possible if T satisfies

$$\mathrm{Re}(T_k/T_\mu) = 0, \qquad \mathrm{Re}(T_\theta/T_\mu) = 0. \tag{3.7}$$

In many cases it suffices to satisfy (3.7) with the conditions

$$T_k = 0, \qquad T_\theta = 0. \tag{3.8}$$

Now, returning to Walton's analysis it is found that $T_k = 0$ with $T_\theta \neq 0$ at $(k, T) = (k_{cyl}, T_{cyl})$ i.e. T is not minimised appropriately. As previously discussed, the acceptance of these values leads to an Airy equation (3.4) with unacceptable solutions. Hence, it is proposed by Soward & Jones that the correct values of (k_0, T_0) are found where $T_k = T_\theta = 0$, and in order to obey these conditions, it maybe necessary to accept complex values of k and θ (of course T must still be real). For geometries with equatorial symmetry, the search for such a critical point can be simplified by imposing

the conditions

$$\mathrm{Re}\{\theta\} = 0, \qquad \mathrm{Im}\{k\} = 0. \tag{3.9}$$

When this method is applied to the two-spheres problem, the resulting value of T_0 is found to be slightly higher than the value obtained by Hocking. In view of this result, Soward & Jones examined the experimental methods used by Wimmer in his study. By investigating the setup used by Wimmer, Soward & Jones conclude that the experiments conducted by Wimmer were not accurate enough to clearly distinguish between: T_{cyl}, $T_{Hocking}$ and the critical value obtained in their own analysis. Later on, we shall see that the critical point defined by $T_k = T_\theta = 0$, is coincidental with the double turning point associated with our WKBJ solutions.

Since the nature of the Taylor-Couette instability closely resembles the roll-type instability currently under consideration, it is interesting to mention the results of some numerical studies regarding the spherical annulus flow problem. In 1982 Bartels [3] investigated the number of possible stable *modes* (configurations) that existed after the critical Taylor number is exceeded. For the specific non-dimensional gap width $s = 0.15$, his code successfully simulated the development of the 0-, 1- and 2-vortex modes near the equator of the spheres, as observed experimentally by Sawatzki & Zierep [71] [106]. In addition, he also confirmed that spherical Couette flow is non-unique i.e. in order to observe a particular mode, the spin-up acceleration of the inner sphere (to the final constant velocity), must be chosen specifically (as reported by Wimmer [99] and Sawatzki & Zierep [106]).

In some special cases, a transition from one mode to another is possible. Although these transitions had already been seen in the experiments, from the numerical results it is found that each mode bifurcates from the same subcritical-flow regime (opposed to each mode bifurcating successively). In his investigation, Bartels specifically wrote his numerical code to generate axisymmetric solutions with equatorial symmetry. However, in order to bring about the different vortex modes, it was necessary to offset the symmetry of the computational domain by artificially extending it from $0 \leqslant \theta \leqslant \pi/2$ to $0 \leqslant \theta \leqslant (\pi/2 + 0.0122)$. Bartels' study was successful in that it clarified the struc-

ture of the modes, but intriguingly his code did not produce the $0 \rightarrow 1$ or the $2 \rightarrow 1$ vortex transitions. Although these transitions had not been observed in experiments (up until then), Bartels was unable to understand why.

By using an axisymmetric pseudospectral code over the full range $0 \leqslant \theta \leqslant \pi$, Marcus & Tuckerman [51] [52] were the first to produce the $0 \rightarrow 1$ transition. Moreover the $2 \rightarrow 1$ transition for Reynolds number $R_e < 1300$ was also simulated. Prior to the study of Marcus & Tuckerman, the $2 \rightarrow 1$ transition had only been seen experimentally by K. Bühler (1983 private communication) and is not to be confused with Wimmer's observation of the same transition at $R_e = 3950$.

It is also found that pinches form in flow field before the onset of Taylor vortices. These pinches are identified at locations where streamlines cross (i.e. stagnation points) and first form near the equator, but are difficult to observe experimentally. In contrast to intuition, the closure of each pinch does not give the associated vortex, this is because the circulation would be in the opposite sense. This in turn implies that the introduction of every additional vortex alters the direction of the radial flow at the equator. It is also interesting to note, that the formation of pinches has not been seen in the simulations of Taylor-vortex flow in infinitely long cylinders, but have been observed in finite cylinders by Keller & Bolstead (1983 private communication).

Based on their numerical simulations, Marcus & Tuckerman [52] have devised a set of empirical laws which govern the generation (or destruction/merging) of vortices from (or to) the associated pinches. As of yet there has been no successful theoretical derivation of these laws. Although the physics describing these rules are in accord with intuition. A detailed explanation is also given for the $0 \rightarrow 1$ and $2 \rightarrow 1$ transition processes. The generation of the 0- and 2-vortex states is an equatorially symmetric process, whereas the transition to the 1-vortex state is an asymmetric one; moreover, a transition to the 1-vortex state takes place on long timescale. A linear stability analysis indicates, that the 0- and 2-vortex states are only susceptible to a transition to the 1-vortex over a small range of Reynolds number. In light of this analysis, Marcus & Tuckerman are able to explain the absence of the 1-vortex mode, from previous

experimental and numerical investigations.

In the next section, the problem investigated in this study is stated formally and the basic flow is derived for small amplitude oscillations $\alpha \ll 1$. For large frequencies, $\Phi \gg 1$, it is shown that the flow develops a boundary layer near the inner edge of the pipe. Subsequently, the stability of the flow is considered in the annular layer of thickness $O(\Phi^{-\frac{1}{2}})$ close to the cylinder surface. It is then possible to expand the imposed perturbation as a WKBJ solution (based on the large frequency parameter Φ), to incorporate the slow variation on the θ length scale. In the resulting equations, the scaling

$$\alpha \Phi^{\frac{1}{4}} = O(1) = B + \ldots \qquad \text{where } B = \text{ constant} \tag{3.10}$$

is required for acceptable solutions. Consequently, this gives rise to an eigenvalue problem for B. Moreover, at $\theta = 0$ the set of stability equations reduce to the ones derived by Hall [36] for the corresponding Hele-Shaw cell. The minimisation of B is then conducted using the method of Soward & Jones [82], and in section 3.3 the numerical results of this procedure are discussed.

3.2 Formulation

Consider a viscous incompressible fluid, inside a horizontal circular pipe of infinite length and radius $d/2$. The pipe is then set to oscillate about its vertical axis of symmetry with angular velocity $\Omega = \alpha\omega \sin \omega t^*$, where t^* denotes time and 2α denotes the maximum angle of oscillation. The fluid which is otherwise at rest, is then set in motion purely by the action of the angular oscillations of the pipe.

By fixing a cylindrical coordinate system (r^*, θ, z^*) in the frame of the pipe, we can write down the Navier-Stokes equations for the flow as follows (see Yih [101] p. 52 for a discussion of the Navier-Stokes in rotating systems):

$$\frac{\partial \boldsymbol{u}^*}{\partial t^*} + \boldsymbol{u}^* \cdot \boldsymbol{\nabla} \boldsymbol{u}^* + 2\boldsymbol{\Omega} \times \boldsymbol{u}^* + \frac{\boldsymbol{\nabla} p^*}{\rho} - \nu \boldsymbol{\nabla}^2 \boldsymbol{u}^* + \boldsymbol{\Omega} \times (\boldsymbol{\Omega} \times \boldsymbol{r}^*) + \frac{\partial \boldsymbol{\Omega}}{\partial t^*} \times \boldsymbol{r}^* = \boldsymbol{0}, \tag{3.11a}$$

$$\boldsymbol{\nabla} \cdot \boldsymbol{u}^* = 0, \qquad \text{with} \quad \boldsymbol{u}^* = \boldsymbol{0} \quad \text{on} \quad r = d/2. \tag{3.11b}$$

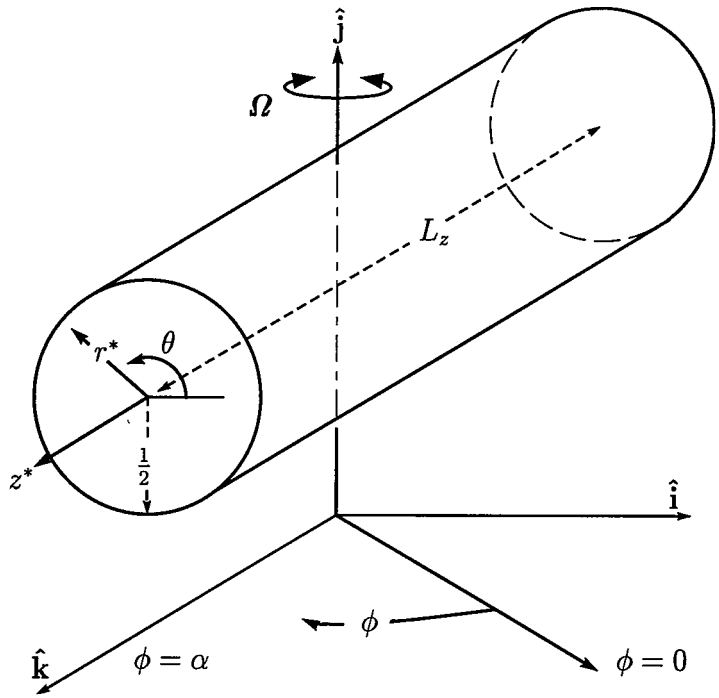


Fig. 3.3: The rotating circular pipe with body coordinates (r^*, θ, z^*). Here $\Omega = \alpha\omega \sin \omega t^*$.

Here,

$$\nabla^2 = (1,1,1)\nabla^2, \qquad \nabla^2 = \partial^2_{r^*} + \frac{1}{r^*}\partial_{r^*} + \frac{1}{r^{*\,2}}\partial^2_\theta + \partial^2_{z^*},$$

$$\text{and} \quad \nabla = (\partial_{r^*},\ \frac{1}{r^*}\partial_\theta,\ \partial_{z^*}).$$

In this configuration, the z^*-axis is parallel to the length of the pipe and θ is measured from the x^*-axis which passes through the horizontal diameter of the pipe, see figure 3.3. Accordingly $\boldsymbol{r}^*$ is the position vector from the origin. The velocity vector is denoted by $\boldsymbol{u}^* = (u^*, v^*, w^*)$ which is resolved into radial, angular and z^* components respectively. The familiar notation of ρ, p^* and ν in equation (3.11) has been used to denote the fluid density, pressure and kinematic viscosity respectively.

3.2.1 Basic flow

In the present section, the basic flow for small amplitude oscillations, $\alpha \ll 1$, is derived. Following Bolton & Maurer we define a dimensionless frequency parameter Φ by

$$\Phi = \omega d^2/\nu. \tag{3.12}$$

In addition, a Reynolds number can be defined by writing $R_e = \alpha\Phi$. Thus for fixed values of α, the viscous effects of the flow are characterised by Φ; for $\Phi \gg 1$, the viscous effects are passive and with $\Phi \ll 1$, the flow is dominated by viscosity.

The pressure, distance, velocity and time are made non-dimensional as follows:

$$\begin{gathered} p = (\alpha\rho\omega^2 d^2)^{-1} p^*, \qquad r = d^{-1} r^*, \qquad z = d^{-1} z^*, \\ \boldsymbol{u} = (\alpha\omega d)^{-1} \boldsymbol{u}^*, \qquad t = \omega t^*. \end{gathered} \tag{3.13}$$

Accordingly the Navier-Stokes equations (3.11) are

$$\left.\begin{aligned} \frac{\partial u}{\partial t} + \alpha\Big((\boldsymbol{u}\cdot\boldsymbol{\nabla})\, u - \frac{v^2}{r}\Big) &= -\frac{\partial p}{\partial r} - 2\alpha w \sin t \cos\theta + \frac{1}{\Phi}\Big(\nabla^2 u - \frac{u}{r^2} - \frac{2}{r^2}\frac{\partial v}{\partial\theta}\Big), \\ \frac{\partial v}{\partial t} + \alpha\Big((\boldsymbol{u}\cdot\boldsymbol{\nabla})\, v + \frac{uv}{r}\Big) &= -\frac{\partial p}{\partial\theta}\frac{1}{r} + 2\alpha w \sin t \sin\theta + \frac{1}{\Phi}\Big(\nabla^2 v - \frac{v}{r^2} + \frac{2}{r^2}\frac{\partial v}{\partial\theta}\Big), \\ \frac{\partial w}{\partial t} + \alpha\,(\boldsymbol{u}\cdot\boldsymbol{\nabla})\, w &= -\frac{\partial p}{\partial z} + 2\alpha \sin t\,(u\cos\theta - v\sin\theta) + 2r\cos t\cos\theta + \frac{1}{\Phi}\nabla^2 w, \end{aligned}\right\} \tag{3.14a-c}$$

$$\frac{u}{r} + \frac{\partial u}{\partial r} + \frac{1}{r}\frac{\partial v}{\partial\theta} + \frac{\partial w}{\partial z} = 0, \tag{3.14d}$$

with

$$u = v = w = 0 \quad \text{on} \quad r = \tfrac{1}{2}. \tag{3.14e}$$

Thus for small amplitude oscillations it is possible to seek a perturbation solution in powers of α ($\ll 1$). Moreover, since the pipe is infinitely long, the governing equations are not subject to any boundary conditions in the z-direction. Hence a solution independent of z is sought in the following form (note with $\partial_z = 0$, w does not enter the

continuity equation):

$$u = u_b(r,\theta,t) = u^{(0)} + \alpha u^{(1)} + \alpha^2 u^{(2)} + \ldots, \tag{3.15a}$$

$$v = v_b(r,\theta,t) = v^{(0)} + \alpha v^{(1)} + \alpha^2 v^{(2)} + \ldots, \tag{3.15b}$$

$$w = w_b(r,\theta,t) = w^{(0)} + \alpha w^{(1)} + \alpha^2 w^{(2)} + \ldots \tag{3.15c}$$

Here the base flow is denoted by u_b. By collecting the terms at $O(\alpha^0)$ in equation (3.14a,b), it can be seen that $u^{(0)} = v^{(0)} = 0$. Therefore, starting with equation (3.14c) we have

$$w_t^{(0)} = \frac{1}{\Phi}\left(w_{rr}^{(0)} + r^{-1}w_r^{(0)} + r^{-2}w_{\theta\theta}^{(0)}\right) + 2r\cos\theta\cos t. \tag{3.16}$$

A particular solution, $w_p^{(0)}$, of the above equation can be obtained by separating variables. One possible solution is

$$w_p^{(0)} = 2r\cos\theta\sin t. \tag{3.17}$$

Next, we seek the corresponding homogeneous solution $w_h^{(0)}$. It is expected that $w_h^{(0)}$ coincides with the angular forcing of the pipe which varies like $\sin t$. Since equation (3.16) is linear with real coefficients we write

$$w_h^{(0)} = e^{it}\cos\theta A(r) + \text{c.c}, \tag{3.18}$$

where c.c denotes complex conjugate. The homogeneous problem then reduces to

$$\begin{aligned} &A'' + \frac{1}{r}A' + (-i\Phi - \frac{1}{r^2})A = 0, \\ \Longrightarrow\ &A(r) \sim J_1(r\lambda) \qquad \text{with} \quad \lambda = (-i\Phi)^{\frac{1}{2}}. \end{aligned} \tag{3.19}$$

Note, solutions of the form $Y_n(r\lambda)$ (Bessel functions of the second kind) are unacceptable because they are unbounded as $r \to 0$. Therefore, the required solution, satisfying the zero boundary conditions, is

$$w^{(0)} = e^{it}\cos\theta\big[-ir + k_1\, J_1(r\lambda)\big] + \text{c.c} \qquad \text{with} \quad k_1 = \frac{i}{2J_1(\lambda/2)}. \tag{3.20}$$

Next we proceed to equations (3.14a,b). For convenience a two-dimensional stream function ψ is introduced for $u^{(1)}$ and $v^{(1)}$ (note that $u^{(0)} = v^{(0)} = 0$). Accordingly we

write

$$u^{(1)} = \frac{1}{r}\,\psi_\theta, \qquad v^{(1)} = -\psi_r. \tag{3.21}$$

The introduction of ψ ensures that the continuity equation is automatically satisfied. By eliminating the pressure term from equations (3.14a,b), the governing equation for ψ is given by

$$\begin{aligned}\frac{1}{r}\psi_{\theta\theta t} + \psi_{rt} + r\psi_{rrt} = -2\sin t(w_\theta^{(0)}\cos\theta + rw_r^{(0)}\sin\theta) + \frac{1}{\Phi}\big(r\psi_{rrrr} + 2\psi_{rrr} \\ - \frac{1}{r}\psi_{rr} + \frac{2}{r}\psi_{\theta\theta rr} + \frac{1}{r^2}\psi_r - \frac{2}{r^2}\psi_{\theta\theta r} + \frac{1}{r^3}\psi_{\theta\theta\theta\theta} + \frac{4}{r^3}\psi_{\theta\theta}\big).\end{aligned} \tag{3.22}$$

Upon simplifying the inhomogeneous terms involving w we have

$$2\sin t(w_\theta\cos\theta + rw_r\sin\theta) = -\tfrac{1}{2}ik_1\sin 2\theta r\lambda J_2(r\lambda)\{e^{2it}-1\} + \text{ c.c } + O(\alpha) + \ldots \tag{3.23}$$

Thus indicating solutions of the form

$$\psi(r,\theta,t) = \left\{\psi^{(u)}(r,\theta)\; e^{2it} + \psi^{(s)}(r,\theta)\right\} + \text{ c.c.} \tag{3.24}$$

Here the superscripts (s) and (u) denote the steady and unsteady contributions respectively. Starting with the unsteady terms we substitute

$$\psi^{(u)} = \sin 2\theta A(R), \qquad \text{with} \quad R = \lambda r. \tag{3.25}$$

Collecting the terms proportional to e^{2it} in (3.22) gives

$$\begin{aligned}
-2\left\{A'' + \frac{1}{R}A' - \frac{4}{R^2}A\right\} &= \frac{1}{2\lambda}k_1J_2(R) + \left\{A'''' + \frac{2}{R}A''' - \frac{9}{R^2}A'' + \frac{9}{R^3}A'\right\}, \\
\Longrightarrow \qquad -2\left\{\mathcal{B}_2(A) - A\right\} &= \frac{1}{2\lambda}k_1J_2(R) + \left\{\mathcal{B}_2(\mathcal{B}_2(A)) - 2\mathcal{B}_2(A) + A\right\}, \\
\Longrightarrow \qquad \mathcal{B}_2(\mathcal{B}_2(A)) - A &= -\frac{1}{2\lambda}k_1J_2(R), \\
\Longrightarrow \qquad (\mathcal{B}_2 - 1)(\mathcal{B}_2 + 1)A &= -\frac{1}{2\lambda}k_1J_2(R).
\end{aligned} \tag{3.26}$$

Here $\mathcal{B}_2$ is the second order Bessel operator, defined in general by

$$\mathcal{B}_n = \frac{\partial^2}{\partial R^2} + \frac{1}{R}\frac{\partial}{\partial R} + \left\{1 - \frac{n^2}{R^2}\right\}. \tag{3.27}$$

From the factorisation in (3.26), it is clear that a particular solution to the equation is

$$A_p(R) = \frac{1}{2\lambda} k_1 J_2(R). \tag{3.28}$$

To obey the boundary conditions at $r = \frac{1}{2}$, it is necessary to find two complementary solutions to accompany the particular solution above. If we consider the equation

$$\mathcal{B}_2(A) - A = 0, \quad \Longrightarrow \quad A(R) \sim R^2, R^{-2}, \tag{3.29}$$

it follows that R^2 is an acceptable homogeneous solution to (3.26). Whereas R^{-2} must be rejected because it is singular. Similarly, by considering the equation

$$\mathcal{B}_2(A) + A = 0,$$

$$\Longrightarrow \qquad A_{RR} + \frac{1}{R} A_R + \left\{ 2 - \frac{4}{R^2} \right\} A = 0, \qquad \text{putting } h = \sqrt{2}R \text{ gives} \tag{3.30}$$

$$A_{hh} + \frac{1}{h} A_h + \left\{ 1 - \frac{4}{h^2} \right\} A = 0, \qquad \Longrightarrow A(R) = J_2(\sqrt{2}R). \tag{3.31}$$

Hence, the unsteady component of the stream function, satisfying zero velocity at $r = \frac{1}{2}$, is

$$\psi^{(u)} = \sin 2\theta \left\{ c_1 R^2 + c_2 J_2(\sqrt{2}R) + \frac{k_1}{2\lambda} J_2(R) \right\} + \text{c.c}, \tag{3.32}$$

where the constants c_1 and c_2 are given by

$$c_1 = \frac{2k_1}{\lambda^3} \left[\frac{J_2(\lambda/\sqrt{2}) J_3(\lambda/2)}{\sqrt{2} J_3(\lambda/\sqrt{2})} - J_2(\lambda/2) \right], \tag{3.33}$$

$$c_2 = -\frac{k_1 J_3(\lambda/2)}{2\sqrt{2}\lambda J_3(\lambda/\sqrt{2})}. \tag{3.34}$$

Similarly, by writing

$$\psi^{(s)} = \sin 2\theta A(R), \tag{3.35}$$

and collecting the steady terms in (3.22), the equation satisfied by $A(R)$ is found to be

$$A'''' + \frac{2}{R} A''' - \frac{9}{R^2} A'' + \frac{9}{R^3} A' = \frac{1}{2\lambda} k_1 J_2(R), \tag{3.36a}$$

$$\Longrightarrow \qquad (\mathcal{B}_2 - 1)^2 \; A = \frac{1}{2\lambda} k_1 J_2(R). \tag{3.36b}$$

As before it easy to identify a particular solution, $A_p(R)$, from the above factorisation. In this case the solution is identical to (3.28).

On the other hand, the expanded form (3.36a) is favourable when dealing with the homogeneous problem. When calculated, the polynomial solutions suggested by (3.36a) are found to be R^n for $n = \pm 2,\ 0,\ 4$. As before R^{-2} is rejected, moreover we must also reject the constant R^0 so that $u^{(1)}$ is finite at $r = 0$. Hence the steady stream function component can be written as

$$\psi^{(s)} = \left\{ c_3 R^2 + c_4 R^4 + \frac{k_1}{2\lambda} J_2(R) \right\} + \text{c.c}, \tag{3.37}$$

with

$$c_3 = \frac{k_1}{2\lambda^3} \left[\lambda J_1(\lambda/2) - 12 J_2(\lambda/2) \right], \tag{3.38}$$

$$c_4 = \frac{2k_1}{\lambda^4} J_3(\lambda/2). \tag{3.39}$$

Hence, the complete solution for ψ is given by

$$\psi = \sin 2\theta \Big[\left\{ c_1 R^2 + c_2 J_2(\sqrt{2}R) + \frac{k_1}{2\lambda} J_2(R) \right\} e^{2it} + \left\{ c_3 R^2 + c_4 R^4 + \frac{k_1}{2\lambda} J_2(R) \right\} \Big] + \text{c.c.} \tag{3.40}$$

Having obtained the base flow to leading order, we proceed by considering the particular case where the amplitude of oscillations is small, $\alpha \ll 1$, and the frequency is large, $\Phi \gg 1$.

3.2.2 Asymptotic expansions for $\Phi \gg 1$

Here we compute the asymptotic form of the base flow for large Φ. By applying the *principal* asymptotic expansions for Bessel functions of large arguments (see [1] p.364), the velocity component $w^{(0)}$ (3.20) and the stream function ψ (3.40) are approximated

for large λ. Thus, to leading order the velocity approximations are calculated to be

$$w^{(0)} = \cos\theta\Big[\sin t - Q(\eta,t)\Big] + O(\Phi^{-1/2}), \tag{3.41a}$$

$$u^{(1)} = \frac{2}{\Phi^{1/2}}\cos 2\theta\Big[(2^{-1/2}-1)\cos(2t+\tfrac{1}{4}\pi) - 2^{-1/2}e^{-\eta}\cos(2t+\tfrac{1}{4}\pi-\eta) + 2e^{-\eta/\sqrt{2}}\cos(t+\tfrac{1}{4}\pi-\tfrac{1}{\sqrt{2}}\eta)\cos t + 2^{-1/2}\Big] + O(\Phi^{-1}), \tag{3.41b}$$

$$v^{(1)} = \sin 2\theta\Big[-\tfrac{1}{2}e^{-\eta}\sin(2t-\eta) + e^{-\eta/\sqrt{2}}\sin(t-\tfrac{1}{\sqrt{2}}\eta)\cos t\Big] + O(\Phi^{-1/2}) \tag{3.41c}$$

and

$$\eta = \Phi^{1/2}(\tfrac{1}{2}-r), \qquad Q(\eta,t) = e^{-\eta/\sqrt{2}}\sin(t-\tfrac{1}{\sqrt{2}}\eta). \tag{3.42}$$

In addition, the result

$$\frac{\sin(r\lambda m - a)}{\cos(\lambda n - b)} \approx \pm i\exp\Big(\sqrt{\frac{\Phi}{2}}\{rm-n\}(i+1) + i\{b-a\}\Big) \quad \text{as} \quad \Phi\to\infty, \tag{3.43}$$

$$\text{with} \quad \lambda = (-i\Phi)^{1/2} = \frac{1\pm i}{\sqrt{2}}\,\Phi^{1/2} \tag{3.44}$$

has also been used to determine the velocity components. For consistency, the asymptotic results (3.41) have also been derived by solving the limiting form of the base flow equations (3.16)-(3.22) with $\Phi \gg 1$. This method also reproduces the solutions (3.41) and therefore verifies our working.

At $\theta = 0$, the expression for $w^{(0)}$ is exactly the same as the equation derived by Hall [36] for the Hele-Shaw cell (note, the Q defined in this study is analogous to the Q obtained in [36]). As expected, the function Q in equation (3.41a) gives a significant contribution to $w^{(0)}$ within a boundary layer of thickness $O(\Phi^{-1/2})$ near $r = \frac{1}{2}$. Outside this layer, Q is exponentially small. Moreover, we note that the oscillatory term in $w^{(0)}$ can be eliminated by shifting to coordinate system that is relative to the oscillatory motion of the fluid in the z-direction. Thus in the absence of Q, the resulting configuration in the new frame of reference will correspond to zero flow, which of course is stable. Hence if any instability is initiated, it must be associated with the term Q and must therefore be confined to a $O(\Phi^{-1/2})$ boundary layer near the surface of the pipe.

In the next section, the stability of the basic flow is investigated. In the subsequent analysis, the relative sizes of the viscous and inertial terms are compared and consequently a relationship between α and Φ^{-1} is obtained.

3.2.3 Stability Analysis

By examining the analytic solution of the base flow, it is readily anticipated that the roll-type instability arises within a $O(\Phi^{-1/2})$ boundary layer close to the pipe wall for $\Phi \gg 1$. Therefore, it is within this proximity that we centre our stability analysis.

Next, a perturbation of the WKBJ type is imposed on the base flow. In this manner, the slow variation in the angular direction is accommodated and the θ-derivatives are brought back into the stability equations at leading order. Accordingly we write

$$\boldsymbol{u} = \boldsymbol{u}_b + \epsilon A(\theta)\tilde{\boldsymbol{u}}(\eta, t)\exp\{\tfrac{1}{2}i\Phi^q \int_{\theta_M}^{\theta} k(\vartheta)\,\mathrm{d}\vartheta\} + c.c \quad \text{with} \quad \epsilon \ll 1 \tag{3.45}$$

$$\text{and} \qquad \tilde{\boldsymbol{u}}(\eta, t) = (\alpha\tilde{u},\ \alpha\tilde{v},\ \tilde{w}).$$

Here ϵ is a vanishingly small parameter and $A(\theta)$ is the amplitude. In the above expression, θ_M can be chosen freely because variations in its value only change the resulting solutions by a multiplicative factor. However, the constant q is determined by the leading order $\tilde{w}$-stability equation which is given by

$$\tilde{w}_t + \alpha^2\left[ik\Phi^q v^{(1)}\tilde{w} + 2\tilde{v}w_\theta^{(0)} - \Phi^{1/2}u^{(1)}\tilde{w}_\eta - \Phi^{1/2}\tilde{u}w_\eta^{(0)}\right]$$
$$= \tilde{w}_{\eta\eta} - \Phi^{2q-1}k^2\tilde{w} + 2\alpha^2 \sin t(\cos\theta\tilde{u} - \sin\theta\tilde{v}). \tag{3.46}$$

From the above equation, it is clear that the viscous and inertial terms balance if $q = \frac{1}{2}$ and $\alpha \sim \Phi^{-1/4}$ (note these results are analogous to the ones obtained by Hall [36] (3.27)). Hence the appropriate scaling for α is

$$\alpha = \frac{B}{\Phi^{1/4}} + \ldots, \tag{3.47}$$

where B is a constant. Now, since the continuity equation reduces to

$$\tilde{v} = -\frac{i}{k}\tilde{u}_\eta, \tag{3.48}$$

the stability equations can be expressed in terms of $\tilde{u}$ and $\tilde{w}$. Accordingly, equations (3.14a-c) are rewritten as:

$$\left.\begin{aligned}
&(\partial_\eta^2 - k^2 - \partial_t)\tilde{w} = B^2(ikv^{(1)}\tilde{w} - \tilde{u}w_\eta^{(0)}),\\
&(\partial_\eta^2 - k^2 - \partial_t - ikB^2v^{(1)})(\partial_\eta^2 - k^2)\tilde{u} = -2\sin t(ik\sin\theta\tilde{w}_\eta + k^2\cos\theta\tilde{w})\\
&\qquad\qquad - ikB^2v_{\eta\eta}^{(1)}\tilde{u},\\
&\tilde{w} = \tilde{u} = \tilde{u}_\eta = 0 \quad \text{at} \quad \eta = 0 \quad \text{and} \quad \tilde{u},\ \tilde{u}_\eta,\ \tilde{w} \to 0 \quad \text{as} \quad \eta \to \infty.
\end{aligned}\right\} \tag{3.49}$$

Note, at leading order $u^{(1)}$ does not enter the stability equations. This is because $u^{(1)} \sim v^{(1)}\Phi^{-1/2}$, and therefore $u^{(1)}$ is of lower order than $v^{(1)}$ and $w^{(0)}$. As one might have intuitively expected, when the stability equations are evaluated at $\theta = 0$ they reduce to the corresponding equations for the Hele-Shaw cell, see equation (3.27) of Hall [36]. Note, in (3.27) of [36] a factor of $B/2$ is missing on the RHS of the first equation.

Having obtained the stability equations, our aim now is to seek the onset of the roll-type instability. Moreover, since we are concerned with disturbances that are symmetric with respect to θ, it is insisted that the instability arises at $\theta = 0$ i.e. along the horizontal diameter of the pipe. In the next section, we present the details regarding the numerical procedure that is used to seek the critical value of B.

3.2.4 Discussion of theory

For the current eigenvalue problem one might be tempted to presume, as did Walton [96], that for symmetric disturbances the critical value of B can be extracted from the neutral stability curve at $\theta = 0$. This however implies that the eigenvalue problem for the pipe reduces to that of the Hele-Shaw cell. However, this idea is too simplistic and is flawed by the fact that it is impossible to satisfy $B_\theta = 0$ at $\theta = 0$ (where the subscript denotes partial derivative), see (3.6). In Walton's [96] discussion of the two-spheres problem, where the latter condition was not enforced, it was envisaged that an $O(\epsilon)$ correction to the critical Taylor number could be calculated under the presumption that the first approximation was T_{cyl}, see expansion (3.3). Unfortunately

by proceeding under this assumption, Walton's work develops a serious inconsistency. The collapse in his analysis arises from obtaining an oversimplified amplitude equation near the equator. Because of this oversimplification, an Airy-type equation is obtained to which there is no solution that decays exponentially towards both poles.

Moreover, the investigation by H. & S. into the same problem, reveals that even as the gap width tends to zero, the critical Taylor number for the two-spheres problem does not converge to the corresponding result for the two concentric cylinders. Consequently, it is concluded by H. & S. that the minimum associated with $T_\theta \neq 0$, does not lead to suitable solutions that are neutrally stable.

From these studies it is evident that when extending a problem of rectangular geometry, to one that includes curvature, the accompanying eigenvalue minimisation process requires greater attention. Although both problems have identical governing equations at the axis of symmetry, one must not be deceived by this similarity, as the stability calculations in each case are quite different. Let us now clarify this minimisation process for equations (3.49). The variation of B with respect to its dependent variables k, θ and growth rate μ can be expressed as

$$\mathrm{d}B = B_k\,\mathrm{d}k + B_\theta\,\mathrm{d}\theta - iB_\mu\,\mathrm{d}\gamma, \tag{3.50}$$

where the (real) frequency $\gamma = i\mu$. Following the earlier discussion of (3.6), it is sufficient to identify an extremal of B ($\mathrm{d}B = 0$) on the neutral stability surface with

$$B_k = 0, \quad B_\theta = 0, \quad \text{at} \quad (B,\ \theta,\ k,\ \gamma) = (B_0,\ \theta_0,\ k_0,\ \gamma_0). \tag{3.51}$$

It is proposed by Soward & Jones [82], that the physically relevant solution satisfies the stability equations (3.49) in the vicinity of $\theta = \theta_0$, even if θ_0 is not real. Since $B_\theta \neq 0$ on the real θ latitude, we must find the critical point at which $B_\theta = 0$, even if this means accepting complex values of θ_0 and k_0. Hence, the aim now is to minimise B by seeking the critical point $\{\theta_0, k_0\}$ at which, the physically acceptable, neutral solutions of (3.49) exist. In §3.3 the numerical procedure used to find $\{\theta_0, k_0\}$ is discussed in detail.

The search for the appropriate critical point, in $\{\theta, k\}$-space, can in general be a rather tedious process. Fortunately, the equatorial symmetries of the problem, greatly reduce the domains in which θ_0 and k_0 *may* be situated. There is an element of caution associated with the last statement, in that the equatorial symmetries are only indicative guides for locating θ_0 and k_0. We shall see later that although the symmetries strongly suggest the whereabouts of θ_0, one cannot presume in advance that the required root is necessarily confined to the suggested domain, nor be assured of its uniqueness, see Soward & Jones [82].

From Hall's analysis of the Hele-Shaw cell, it is expected that the disturbances are synchronous with the basic flow i.e $\mathrm{Im}\{\mu\} = 0$ for $\mathrm{Re}\{\mu\} > 0$. Therefore it is anticipated that the instability does not take the form of a travelling wave, and so γ_0 of (3.51) is zero. From (3.49) it is clear that for any given value of B there are six possible roots of k, and associated with each of these roots is a WKBJ solution $\mathbf{Y}^{(n)}$, where

$$\mathbf{Y}^{(n)} = (\tilde{u},\ \tilde{w}) \exp\{\tfrac{1}{2} i \Phi^{\frac{1}{2}} \int_{\theta_M}^{\theta} k^{(n)}(\vartheta)\, \mathrm{d}\vartheta\}. \tag{3.52}$$

Here, $(\tilde{u},\ \tilde{w})$ is the perturbation velocity and the above expression should be compared with (3.45). From equation (3.49), it is found that only three of these WKBJ solutions are independent owing to the relation

$$k = k^{(n)}(\theta) = -k^{(n)}(-\theta) \quad \text{for} \quad n = 1,\ 2,\ 3. \tag{3.53}$$

Note, the condition $B_k = 0$ implies that (3.49) has a repeated root at θ_0 i.e.

$$k^{(1)}(\theta_0) = k^{(2)}(\theta_0) = k_0. \tag{3.54}$$

Therefore, the point $P(\theta = \theta_0)$ in the complex θ-plane defines a transition point in the vicinity of which, there are two indistinguishable solutions $\mathbf{Y}^{(1)}$ and $\mathbf{Y}^{(2)}$. The degeneracy of the roots at $\theta = \theta_0$ coupled with the remaining condition, $B_\theta = 0$, implies that the two neighbouring transition points are coincident at $P(\theta = \theta_0)$ in the limit $\Phi \to \infty$, see [82] (1.16)-(1.22). The Stokes and anti-Stokes lines passing through

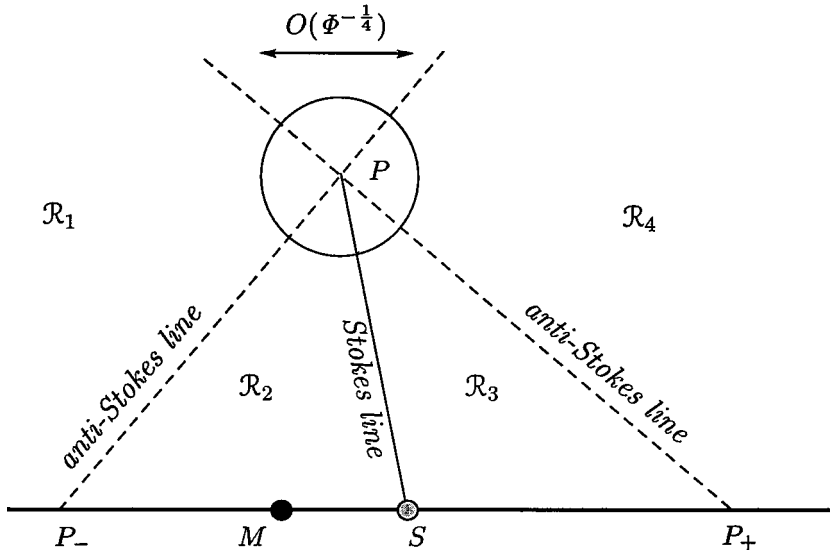


Fig. 3.4: The point $P = P(\theta = \theta_0)$ indicates the double transition point, the surrounding $O(\Phi^{-1/4})$ circular region is the domain of validity for the inner solution see (3.60). The outer regions $\mathcal{R}_n$ are the domains in which the WKBJ solutions are valid. Note further that the dominent/subdominent character of a particular WKBJ solution is dependent on the regions $\mathcal{R}_n$.

the double transition point P are defined by

$$\text{Re}\left\{\int_{\theta_0}^{\theta}(k^{(2)}-k^{(1)})\,\mathrm{d}\theta\right\}=0 \quad \text{and} \quad \text{Im}\left\{\int_{\theta_0}^{\theta}(k^{(2)}-k^{(1)})\,\mathrm{d}\theta\right\}=0 \qquad (3.55\text{a,b})$$

respectively. The anti-Stokes lines (3.55b) divide the complex θ-plane into four regions denoted by $\mathcal{R}_n$ in figure 3.4 (these lines are curved in general). At distances greater than $O(\Phi^{-1/4})$ from P (within this radius the WKBJ solutions are invalid), it is expected that one of the WKBJ solutions, say $\mathbf{Y}^{(1)}$, is dominant in region $\mathcal{R}_2+\mathcal{R}_3$ and subdominant in $\mathcal{R}_1+\mathcal{R}_4$. Accordingly, the counterpart solution, $\mathbf{Y}^{(2)}$, is dominant in $\mathcal{R}_1+\mathcal{R}_4$ and subdominant in $\mathcal{R}_2+\mathcal{R}_3$. Hence a Stokes line is drawn from P and its intersection with the real θ-axis is denoted by $S(\theta=\theta_S)$. The point M represents the location of maximum dominance i.e the maximum ratio of $\mathbf{Y}^{(1)}$ to $\mathbf{Y}^{(2)}$. Hence the realised instability corresponding to the WKBJ solutions $\mathbf{Y}^{(1)}$ and $\mathbf{Y}^{(2)}$ is initiated on the real θ-axis at $M(\theta=\theta_M)$ (note, the other four WKBJ solutions are not required as they are not linked to the turning point P). Within the vicinity of $M(\theta=\theta_M)$ it is

possible to approximate the solution locally by

$$\mathbf{Y} = (\hat{U}(\theta_M),\ \hat{W}(\theta_M)) \exp\left\{\tfrac{1}{2} i \Phi^{-1/2} (k_M \Delta\theta + \tfrac{1}{2} k_{\theta M} \Delta\theta^2)\right\}, \qquad (3.56)$$

$$\text{with} \qquad \Delta\theta = (\theta - \theta_M) = O(\Phi^{-1/4}).$$

Note $(\hat{U},\ \hat{W}) \neq (\tilde{u},\ \tilde{w})$ because $(\hat{U},\ \hat{W})$ varies on the scale $\Phi^{-1/4}$. Moreover, the location of M is determined by the conditions:

$$\text{Im}\,\{k_M\} = 0 \quad \text{with} \quad \text{Im}\,\{k_{\theta M}\} > 0, \qquad (3.57a,b)$$

$$\text{where} \quad k_M = k(\theta = \theta_M) \quad \text{and} \quad k_{\theta M} = \left.\frac{\partial k}{\partial \theta}\right|_{\theta=\theta_M}.$$

The conditions above ensure that $\mathbf{Y}$ is neutrally stable at $\theta = \theta_M$ and locally decaying in both directions of the real θ-axis.

To obtain a valid representation of the realised disturbance along the real θ-axis, the Stokes phenomenon must be taken into consideration. This is because, by crossing the Stokes line at S, the original approximation $\mathbf{Y}^{(1)}$, which is dominant in $\mathcal{R}_2 + \mathcal{R}_3$, inherits a contribution from the subdominant solution $\mathbf{Y}^{(2)}$. Therefore, in general $\mathbf{Y}$ (3.58) is a discontinuous function on the real θ-axis e.g see Heading [40] for a discussion of the Stokes phenomenon.

$$\mathbf{Y} = \begin{cases} \mathbf{Y}^{(1)} & , \quad \theta \leqslant \theta_S \\ \mathbf{Y}^{(1)} + \tau \mathbf{Y}^{(2)} & , \quad \theta > \theta_S. \end{cases} \qquad (3.58)$$

The Stokes constant τ is a function of $\Phi^{1/4}\alpha$, and the asymptotic expansion of $\Phi^{1/4}\alpha$ is

$$\Phi^{1/4}\alpha = B^{(0)} + \frac{1}{\Phi^{1/2}} B^{(1)} + \frac{1}{\Phi} B^{(2)} + \ldots \qquad (3.59)$$

Here the leading order term $B^{(0)}$ is the B in the previous notation (see (3.47)) and is determined by the identification of the saddle point P. Hence it is possible to construct a particular solution which is uniformly valid on the real line, by insisting that the Stokes constant τ vanishes. This is achieved by considering the appropriate instability equations that are valid at the transition point P, and matching the inner

solution (3.60) which is valid there, to the outer solution with τ set equal to zero.

$$\mathbf{Y} = \hat{\boldsymbol{U}}_0(\Theta)E + \frac{1}{\Phi^{1/4}}\hat{\boldsymbol{U}}_1(\Theta)E + \frac{1}{\Phi^{1/2}}\hat{\boldsymbol{U}}_2(\Theta)E + \ldots, \tag{3.60a}$$

$$\text{where} \quad E = \exp\left\{\tfrac{1}{2}ik_0\Theta\Phi^{1/4}\right\}, \quad (\theta - \theta_0) = \Theta\Phi^{-1/4}, \quad \hat{\boldsymbol{U}}_n = (\hat{U}_n, \hat{W}_n). \tag{3.60b}$$

The inner solution corresponding to the smallest eigenvalue of $B^{(1)}$ is accepted. This ensures that α is minimised and that $\mathbf{Y}^{(1)}$ is a valid approximation along the real θ-axis. This process of continually minimising $B^{(n)}$ and matching the inner solution to the outer one, can be repeated at higher orders and consequently yields an asymptotic approximation to the realised disturbance.

In general, it is impossible to determine *a priori* whether further transition points of $\mathbf{Y}^{(n)}$ (for $n = 1, 2$) exist in the complex θ-plane. If multiple transition points exist, one can expect that the solution described above, will encounter further complications when the associated Stokes lines are crossed (see Heading [40]).

3.2.5 Simplifications of symmetry

From the symmetry relation (3.53), it is clear that for every instability initiated at $\theta = +\theta_M$, there is a corresponding one at $\theta = -\theta_M$ which is governed by the WKBJ solution $\mathbf{Y}^{(1)}(-\theta, \eta)$. Since the present study concerns disturbances that are θ-symmetric, it follows that the instability must be initiated at $\theta_M = 0$. With symmetry in mind, one may search for the transition point P along the imaginary θ-axis, see (3.55). In this case, the coefficients in the stability equations (3.49) are real if $\mathrm{Im}\{k\} = 0$. This has the desired implication that B is a real function of the real variables ζ and k, where

$$\theta = i\zeta. \tag{3.61}$$

Under these assumptions, $k^{(1)}$ and $k^{(2)}$ are both real along the real ζ-axis, which is then identified as a Stokes line for $\mathbf{Y}^{(1)}$ and $\mathbf{Y}^{(2)}$ see (3.55a). Accordingly this implies that $\theta_S = 0$. Moreover, the condition for the maximum disturbance (3.57a) is also satisfied at $\theta = 0$. The remaining condition (3.57b) cannot be verified in advance, but the unlikely case:

$$\mathrm{Im}\,\{k_{\theta M}\} < 0, \tag{3.62}$$

corresponds to a solution that grows locally, and this in turn implies that the disturbance is not initiated at $\theta = 0$. In practice, one merely has to verify that the solution obtained via this method decays locally at $\theta = 0$ (which is most often the case see §3 of Soward & Jones [82] and Papageorgiou [57]). Therefore, assuming that (3.57b) satisfied, θ_M is also zero. Hence under the assumption that k is real, the required saddle point is sought along the imaginary θ-axis.

3.3 Numerical Results

Since the basic flow is periodic in time, solutions of the stability equations (3.49) are sought in from

$$(\tilde{u}, \tilde{w}) = \mathrm{e}^{\mu t}(\hat{u}(\eta, t), \hat{w}(\eta, t)), \tag{3.63}$$

and $\mu = \mu(\theta, B, k)$. Hence, the neutrally stable solutions are acquired when $\mathrm{Re}\{\mu\} = 0$. From Hall's study of the allied problem, it is anticipated that $\mathrm{Im}\{\mu\} = 0$ for unstable solutions. This implies that the disturbed flow is synchronous with the basic state and hence $\gamma_0 = 0$ in (3.51). Our aim now is to seek the saddle point (θ_0, k_0) at which, the physically acceptable, neutral solutions of (3.49) exist. This saddle point (non-unique) is characterised by $B_\zeta = B_k = 0$ and is sought for real values of ζ and k (where $\theta = i\zeta$).

The search for the required saddle point is conducted in the following manner. For each fixed value of ζ, a neutral stability curve is constructed in the k-B plane. Moreover, the minimum on this curve (k_{min}, B_{min}) is stored (note that $B_k = 0$ at $k = k_{min}$). The idea is then to follow $B_{min}(\zeta)$ in ζ-space until a local maximum is attained. Consequently, at this local maximum, the remaining condition $B_\zeta = 0$ is satisfied. Hence resulting in the identification of the required values (k_0, B_0, θ_0).

In our numerical study of (3.49), the governing equations are discretized and solved by using a second order finite difference scheme. Within this scheme, the Crank-Nicholson method is incorporated to give an $O(\Delta\eta^2 + \Delta t^2)$ accuracy (here, $\Delta\eta$ and Δt are the steps sizes in η and time respectively). For fixed values of (k, B, ζ), the resulting system is time marched. In this way, the secant method is used to update B for each

run and the growth rate, $\mathrm{Re}\{\mu\}$, is eventually driven to zero. Once a minimum in k-B plane is detected, a parabola fitting procedure is used to home in on (k_{min}, B_{min}). By setting $\Delta\eta = 0.01$ and $\Delta t = 8 \times 10^{-3}$ in the numerical runs, the computed values of B_{min} are found to converge to 3 d.p. Moreover, the conditions at 'infinity' are enforced at $\eta_\infty = 30$, which is found to be sufficiently large in all our calculations.

Results

In figure 3.5, it is seen that the neutral stability surface decays quickly for $|\zeta| > 0.2$, and therefore it appears that the saddle point P must be located somewhere within the range $0 < \zeta < 0.2$. However, a closeup of this region in figure 3.6 reveals the presence of a discontinuity in the surface. The contour diagram shows that the discontinuity is the result of an abrupt shift in the value of B_{min} at $\zeta \approx 0.1225$. Moreover, this discontinuity is not the result of any numerical inaccuracies because the contour remains unchanged when refinements are made to: $\Delta\eta$, Δt and the size of the η-domain. From figures 3.7 and 3.8, it is clearly visible that the velocity profiles are smooth and that the decay of each profile is well accommodated by the size of the chosen domain. As expected it is found that all the computed disturbances have Im $\{\mu\} = 0$, and therefore these perturbations are synchronous with the basic state. In contrast, at $\zeta = 0$ the computed value of $B_{min} = 4.54$, see figure 3.9, is at variance with the result, $B_{min} = 2.9$, obtained by Hall for the Hele-Shaw cell problem. Ideally, to identify the correct value of B_{min}, it is desirable to compare each result with the experimental results of Bolton & Maurer. However, more experimental data is needed in the range $0 < \alpha < 0.79$ so that a better agreement is obtained with either result; for as it stands, neither result is clearly corroborated by the limited experimental data.

It is interesting to point out, that Aoidef *et al.* [2] have investigated the Hele-Shaw cell problem for finite values of (α, Φ), and in their study a value of $B_{min} = 3.73$ has been obtained with $\alpha = 1.06$ and $\Phi = 150$. Moreover, this was the largest value of Φ investigated by the latter authors. In figure 4 of [2], the results indicate that the value of B_{min} increases with Φ, and therefore the results in this independent investigation,

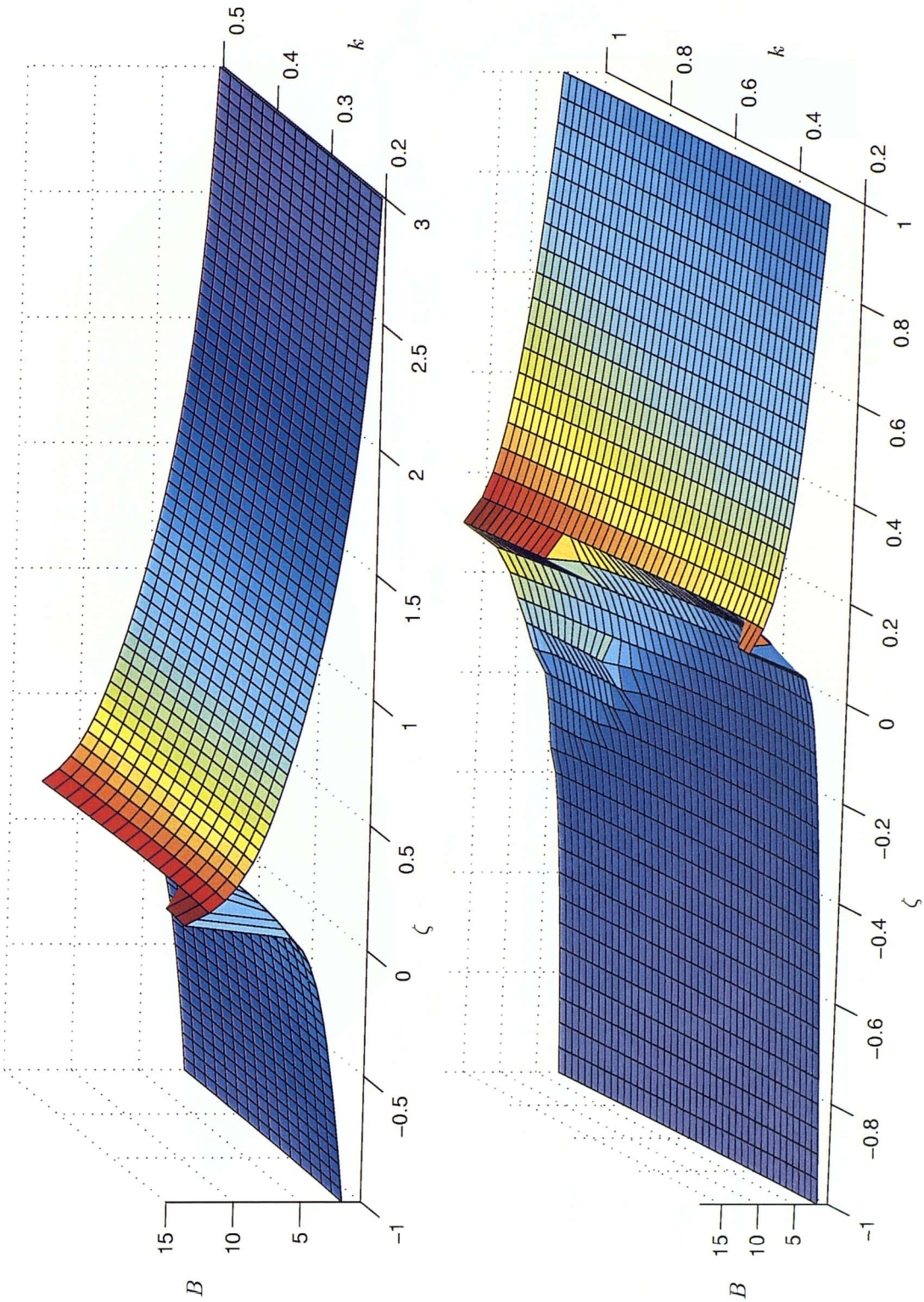


Fig. 3.5: The evolution of the stability surface in (k, B, ζ)-space.

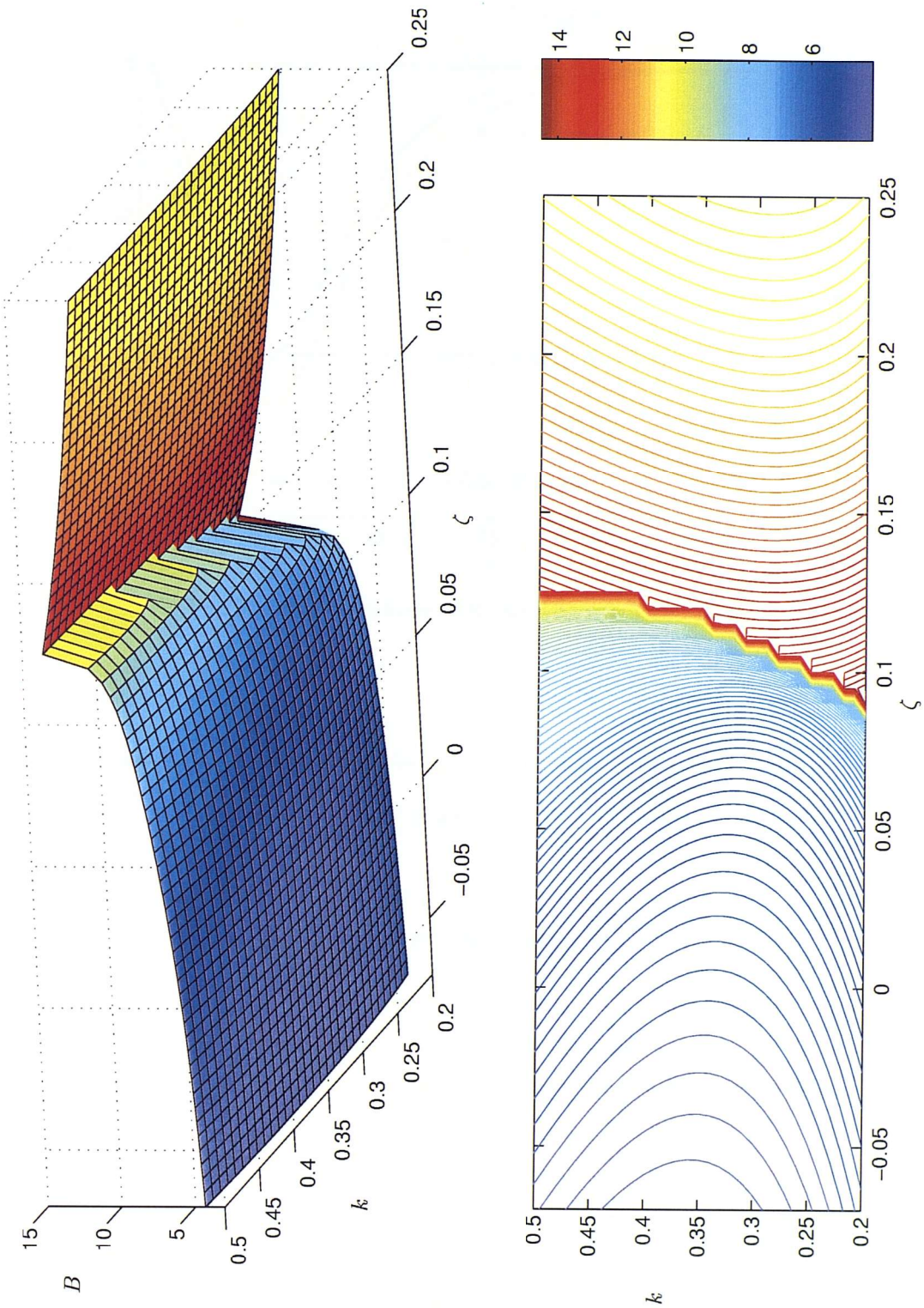


Fig. 3.6: The neutral stability surface and contour lines near the discontinuity.

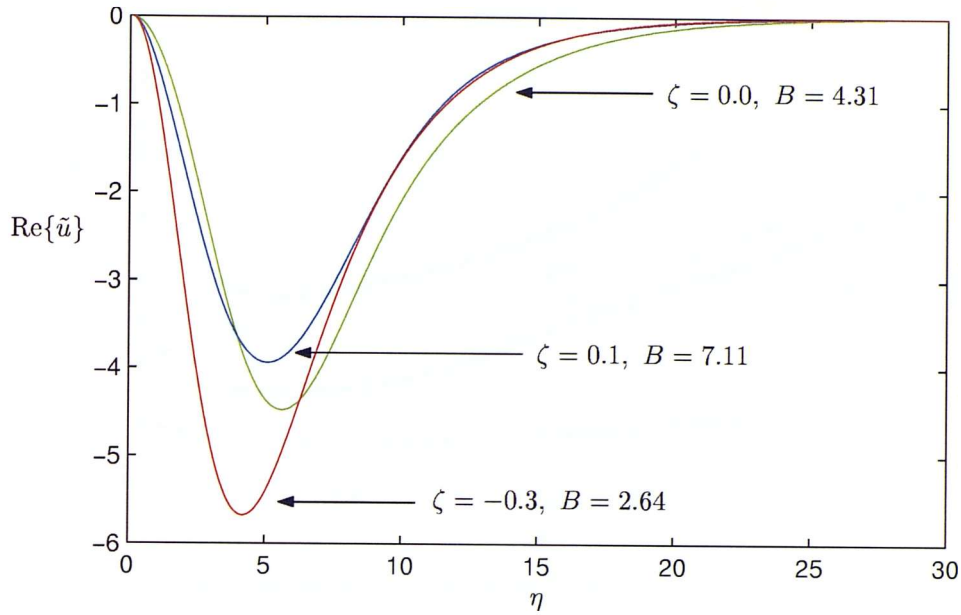


Fig. 3.7: The magnitude of $\mathrm{Re}\{\tilde{u}\}$ with $k = 1$ and $\mu = 0$.

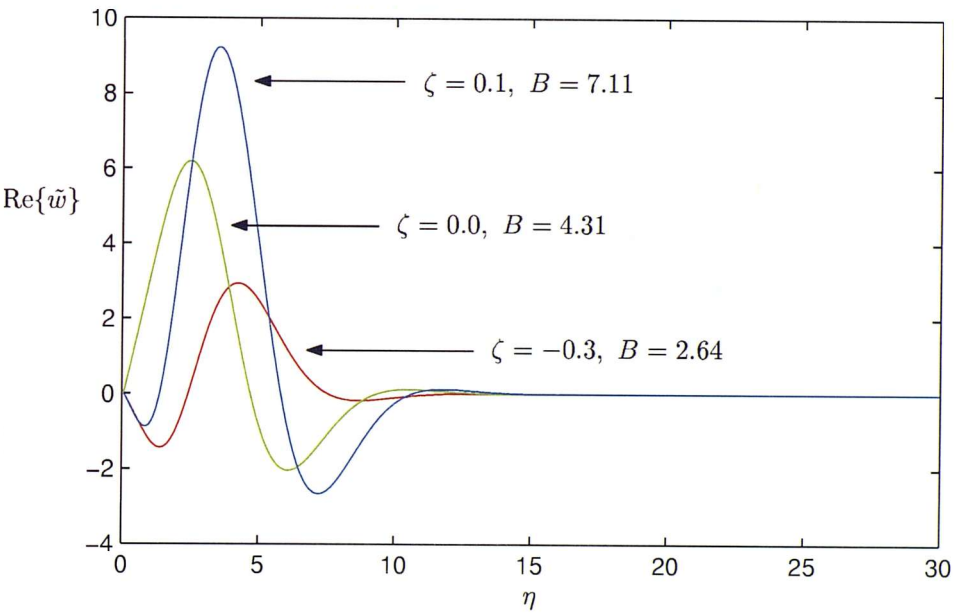


Fig. 3.8: The magnitude of $\mathrm{Re}\{\tilde{w}\}$ with $k = 1$ and $\mu = 0$.

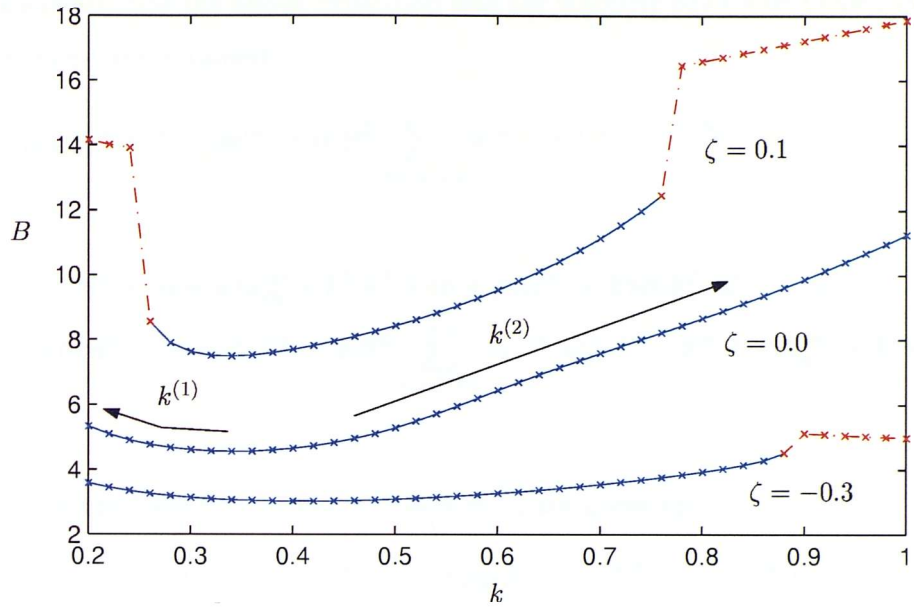


Fig. 3.9: The neutral stability curves in the k-B plane produced by time marching. The curves in red show the jump from the original smooth contour associated with the blue curve. The local minimum on each curve marks the merging of the two curves $k^{(1)}$ and $k^{(2)}$ for the WKBJ solutions $\mathbf{Y}^{(1)}$ and $\mathbf{Y}^{(2)}$.

support the value of $B_{min} = 4.54$ obtained in this study.

3.3.1 Fourier series analysis

The jump from one neutral stability surface to another cannot be fully understood by using the time marching scheme. This is because it is impossible to exercise a controlling influence over the solution being followed by the time marching procedure. In order to monitor the evolution of the first few dominant (i.e. least stable) eigen solutions $(\tilde{u}, \tilde{w})$, we switch to a Fourier series representation and expand $(\tilde{u}, \tilde{w})$ in the form

$$(\tilde{u}, \tilde{w}) = \mathrm{e}^{\mu t} \sum_{n=-\infty}^{\infty} (\tilde{u}^{(n)}, \tilde{w}^{(n)}) \mathrm{e}^{int}. \tag{3.64}$$

By the substituting the above expansion into the stability equations (3.49), the following equations are obtained:

$$\tilde{w}^{(n)}_{\eta\eta} - (in+k^2)\tilde{w}^{(n)} - \mu\tilde{w}^{(n)} = ikB^2 \sum_{m=0,\pm 2} \tilde{w}^{(n-m)} v^{(1,m)} - B^2 \sum_{m=\pm 1} \tilde{u}^{(n-m)} w^{(1,m)}_{\eta}, \quad (3.65a)$$

$$\begin{aligned} &\tilde{u}^{(n)}_{\eta\eta\eta\eta} - (2k^2 + in + \mu)\tilde{u}^{(n)}_{\eta\eta} + k^2(k^2 + in + \mu)\tilde{u}^{(n)} = k\sin\theta\{\tilde{w}^{(n+1)}_{\eta} - \tilde{w}^{(n-1)}_{\eta}\} \\ &- ik^2\cos\theta\{\tilde{w}^{(n+1)} - \tilde{w}^{(n-1)}\} + ikB^2 \sum_{m=0,\pm 2} (v^{(1,m)}\tilde{u}^{(n-m)}_{\eta\eta} - \tilde{u}^{(n-m)}\{v^{(1,m)}_{\eta\eta} + k^2 v^{(1,m)}\}). \end{aligned} \quad (3.65b)$$

In addition the base flow terms, $v^{(1)}$ and $w^{(1)}$, are given by:

$$\begin{aligned} v^{(1)} &= \{v^{(1,0)} + e^{2it}v^{(1,2)} + e^{-2it}v^{(1,-2)}\}\sin\theta, \qquad v^{(1,0)} = -\tfrac{1}{2}e^{-\eta/\sqrt{2}}\sin\tfrac{1}{\sqrt{2}}\eta, \\ v^{(1,2)} &= \frac{1}{4}i(e^{-\eta(1+i)} - e^{-\eta(1+i)/\sqrt{2}}), \qquad v^{(1,-2)} = v^{*(1,2)} \end{aligned} \quad (3.66)$$

and

$$\begin{aligned} w^{(1)} &= \{e^{it}w^{(1,1)} + e^{-it}w^{(1,-1)}\}\cos\theta, \\ w^{(1,1)} &= \tfrac{1}{2}i(e^{-\eta(1+i)/\sqrt{2}} - 1), \qquad w^{(1,1)} = w^{*(1,-1)}. \end{aligned} \quad (3.67)$$

Here the asterisk denotes complex conjugate. Moreover, the growth rate μ is interchangeably referred to as the eigenvalue of equations (3.65). In order to numerically calculate the Fourier coefficients, it is necessary to truncate (3.64) so that $2N+1$ modes are used in the scheme. Accordingly, the summation in (3.64) is now assumed over the finite range $-N \leqslant n \leqslant N$. Thereafter, a generalised eigenvalue solver (NAG subroutine F02GCF for complex valued matrices) is used to calculate selected eigenvalues for any given values of (k, B, ζ). The procedures used to update k and B are similar to the ones used in time marching scheme.

Our first task is to reproduce the surface in figure 3.6. This is achieved by following the solution associated with the least stable eigenvalue, and we shall refer to this dominant instability as the primary instability. Accordingly, the associated eigenvalue is referred to as the primary eigenvalue. Due to the requirements of large computer memory, a slightly smaller value of $\eta_\infty = 25$ is used. The numerical results obtained

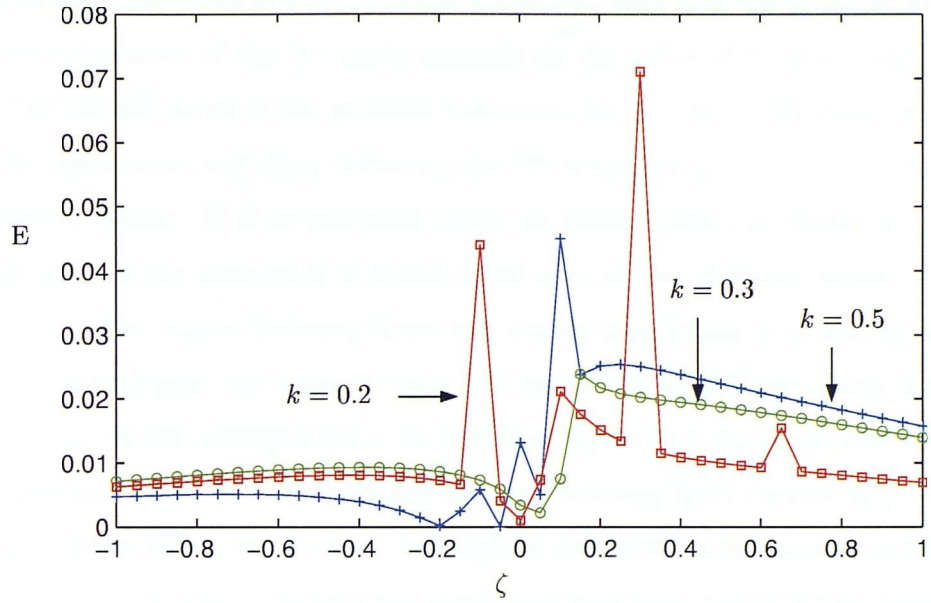


Fig. 3.10: For fixed values of k, E represents the difference between the results computed by time marching and the eigen mode analysis ($N = 4$ and $I = \eta_\infty/\Delta\eta = 80$). The trajectories above have been computed for k =0.2, 0.3, 0.5. Note, the time marching procedure is deemed the most accurate of the two numerical methods because a greater refinement is possible in the computations.

with $N = 4$, and $I = 80$ steps in the η-domain, agree extremely well with the data obtained from time marching. In figure 3.10, it is seen that the difference between the two approaches is predominantly confined to an absolute error of 0.03. This agreement also serves as a check on our numerical work and informs us that the time marching scheme has always attracted to the least stable solution. However, by using the Fourier analysis it is found that as $\zeta \to 0.12^-$ (i.e. as ζ tends to 0.12 from the left side) the primary and secondary eigenvalues exchange positions, and what *was* the secondary instability for $\zeta < 0.12$ is now the dominant instability and now has the most positive growth rate in time. Hence, the discontinuity in the neutral stability surface (see figure 3.6) is caused by the original instability becoming subdominant.

Before analysing the switching of the eigenvalues at $\zeta \approx 0.12$, it helps our case to study what happens prior to the discontinuity. For $\zeta < 0.12$, the primary eigenvalue is a continuation of the one associated with the Hele-Shaw cell instability, and shall

henceforth be referred to as the HS mode. Moreover, note that the primary/secondary instability character of the HS mode depends on the value of ζ, and it will soon be clear that the HS mode is the primary instability for $\zeta < 0.12$. By fixing a value of k in the eigen code, and then following the HS mode for $\zeta < 0.12$, something very unsuspected occurs. If B is increased above its neural value i.e. where $\mathrm{Re}\{\mu\} = 0$, the real part of the eigenvalue is found to be zero at two different values of B, see figure 3.11. The region between these two curves has $\mathrm{Re}\{\mu\} > 0$ and is therefore unstable; accordingly, the regions below the lowest curve (L) and above the upper curve (U) are stable configurations. In addition, figure 3.11 clearly depicts the decay of the unstable region (i.e. the vertical distance between both curves) as $\zeta \to 0.12^{-}$. For $\zeta \gtrapprox 0.13$ the HS mode is stable, but slightly before this transition to stability, i.e. with $\mathrm{Re}\{\mu_{HS}\} > 0$, the HS mode loses dominance and gives way to a new mode which then becomes the primary instability. For convenience we shall refer to this new mode as the 'S' mode, where the S abbreviates 'saddle'.

In figure 3.12, the HS eigenvalue is plotted at $\zeta = 0.12$ for various values of k. For clarity, the curves are plotted for $0.38 < k < 0.41$ because within this interval, the peaks on each curve rise with an increase in k. If k is increased beyond 0.41, the peaks descend back into the stable region and consequently overlap the curves plotted for $0.38 < k < 0.41$. A more complete view of the neutral curves for the HS mode is seen in figure 3.13, which depicts the joining of the upper and lower neutral stability curves. Here it is seen that the finite region of instability diminishes as ζ increases and subsequently vanishes for $\zeta > 0.13$. Thereafter the S mode dominates as the primary instability.

Having observed the recessive behaviour of the HS mode, we can now interpret the surfaces computed by time marching with a better understanding. It is now recognised that the surface computed for $\zeta > 0.13$, see figure 3.6, corresponds to the S mode, whereas the HS mode is associated with the remaining smooth section of the surface originating from $\zeta = 0$. From figure 3.10 we observe that for $\zeta < 0.12$ (where the HS mode is dominant), the Fourier representation and time marching scheme produce

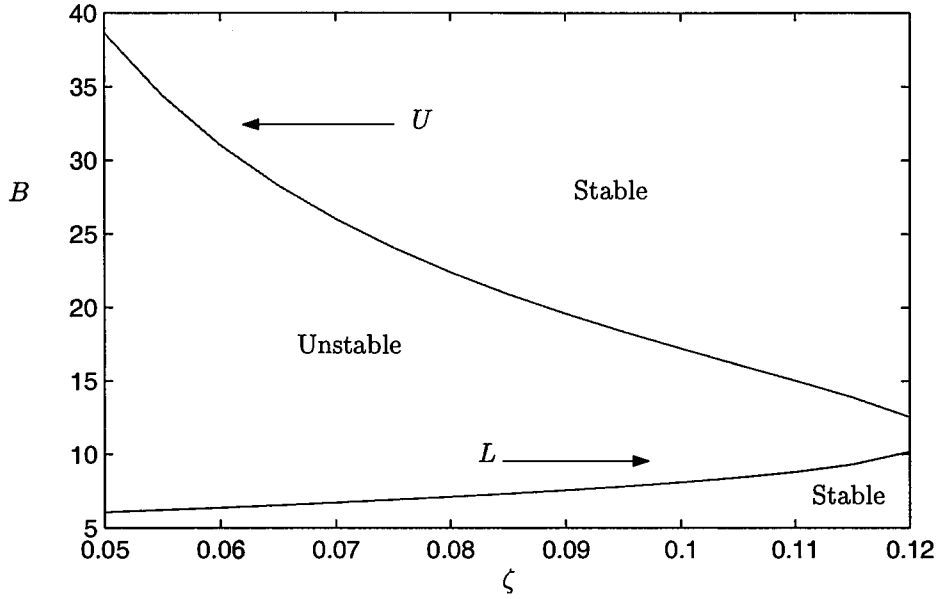


Fig. 3.11: The upper and lower neutral stability curves of the Hele-Shaw cell instability at $k = 0.46$ i.e. $\mathrm{Re}\{\mu\} = 0$ on both curves and $\mathrm{Re}\{\mu\} > 0$ in the vertical range between these curves.

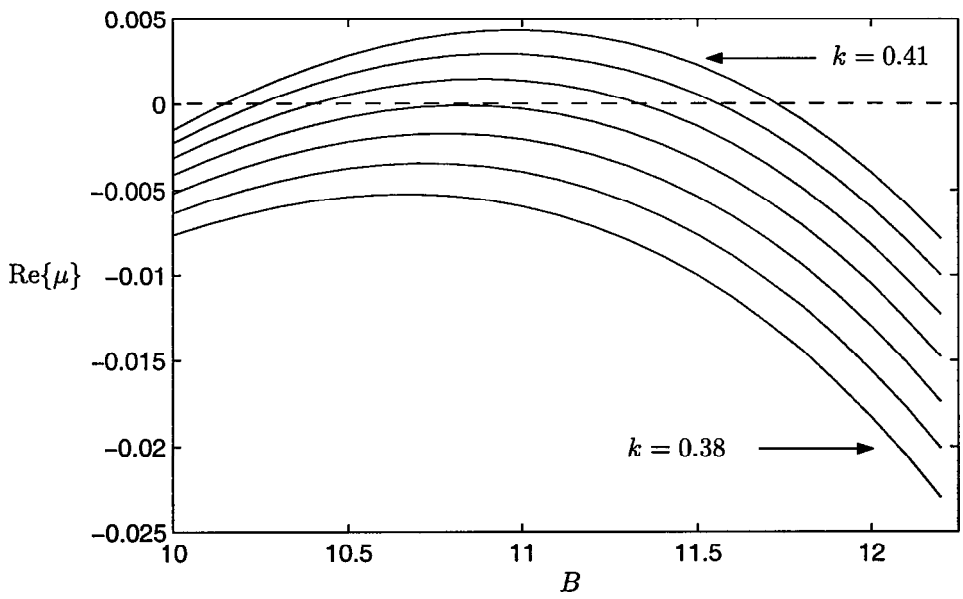


Fig. 3.12: The growth rate μ of the HS mode at $\zeta = 0.12$ and $0.38 \leqslant k \leqslant 0.41$, with $\Delta k = 0.005$.

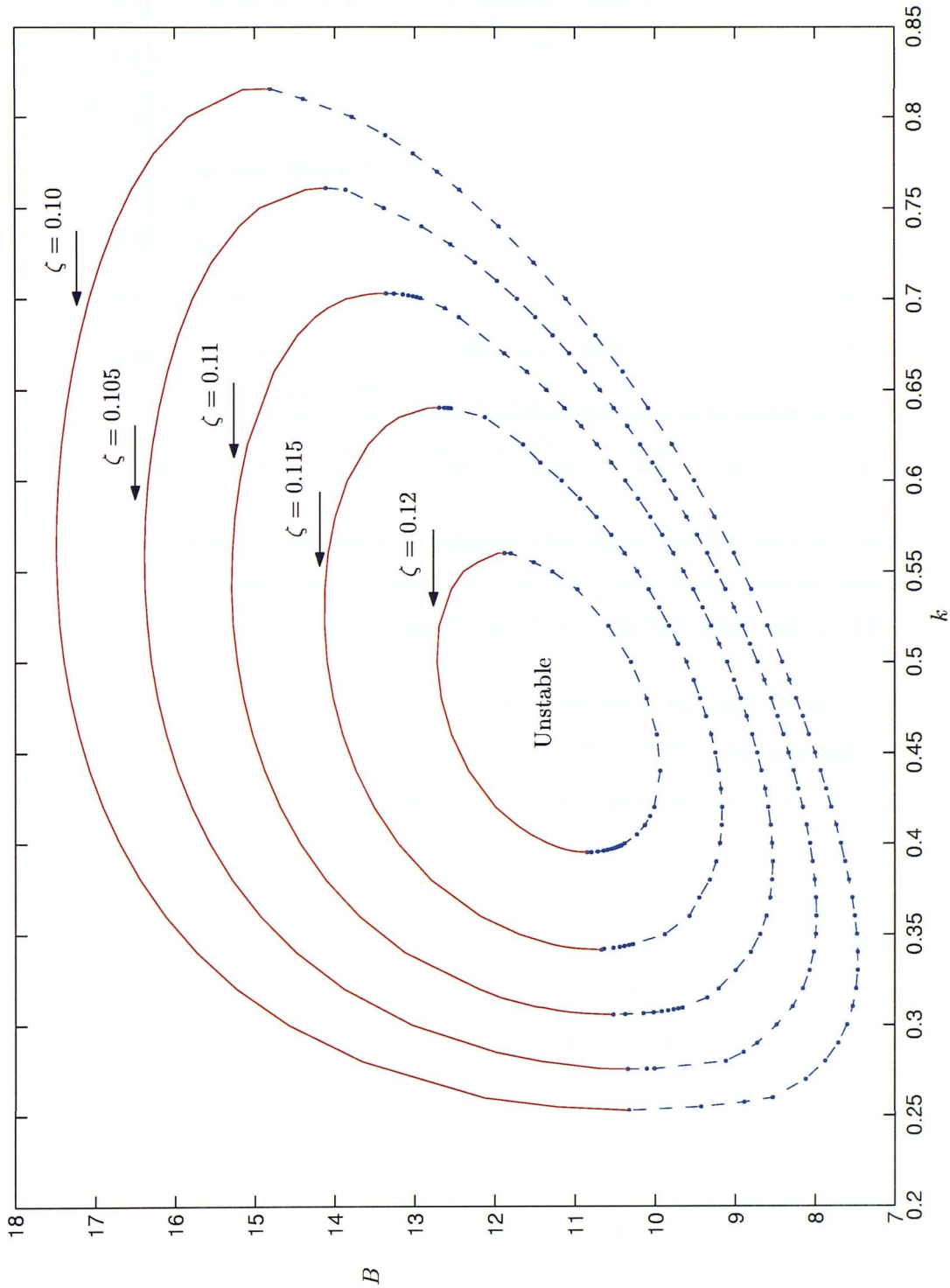


Fig. 3.13: The upper and lower neutral stability curves for the HS mode with $0.10 \leqslant \zeta \leqslant 0.12$. Here, $\mathrm{Re}\{\mu\} > 0$ within each circular loop and $\mathrm{Re}\{\mu\} = 0$ on the boundary.

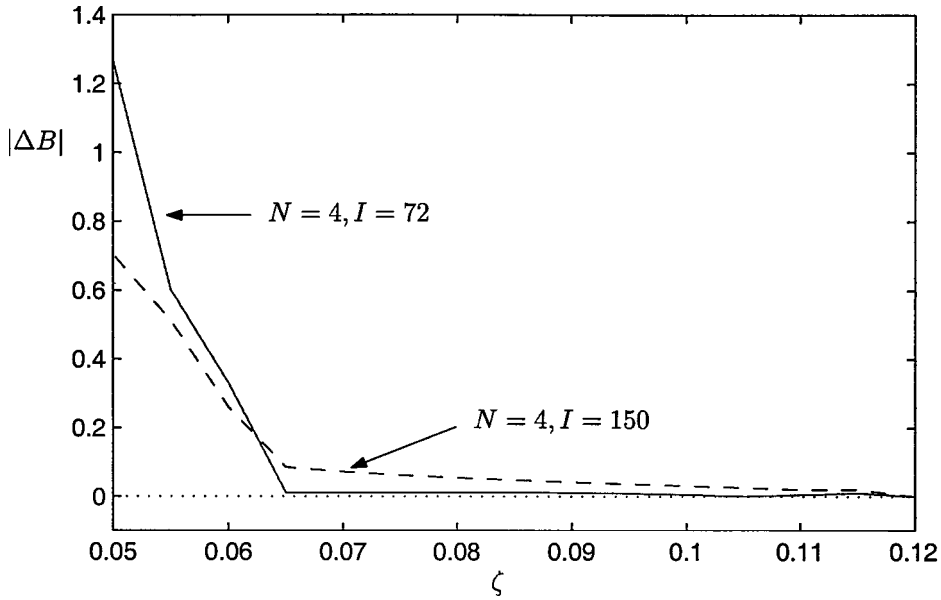


Fig. 3.14: The error associated with computing the upper stability curve at $k = 0.4$. The upper curves are computed with $(N, I) = (4, 72)$ and $(4, 150)$ and the absolute difference with the value of B obtained with $(N, I) = (6, 100)$ is denoted by $|\Delta B|$.

results that are in good agreement ($E < 0.01$). Whereas the data computed for the S mode is slightly more discrepant with $0.005 < E < 0.03$. This suggests that the Fourier representation is in need of more terms as B increases. This idea is supported by the fact that E decreases (see figure 3.10) on both sides of the discontinuity i.e. in the same directions where B_{min} is decreasing.

The requirement of more modes and smaller mesh sizes is also evident in figure 3.14. Here the upper curve is followed using various values for N and I $(= \eta_\infty/\Delta\eta)$. For $0.065 < \zeta \leqslant 0.12$, all the trajectories are in good agreement, see figure 3.14. However at $\zeta \approx 0.065$ (where $B \approx 28$), the various solutions begin to disagree. For $\zeta > 0.065$, it is found that the agreement between the results obtained with $(N, I) = (6, 100)$ and $(4, 72)$, is better than corresponding agreement between $(N, I) = (6, 100)$ and $(4, 150)$, see figure 3.14. This implies that the accuracy is profoundly improved by increasing I, whereas a modest improvement is gained with an increase in N. Hence in this case, the trajectory computed with $(N, I) = (4, 150)$ gives the best approximation. In light

of this result, one may expect to encounter some numerical difficulties with the Fourier code, when $B \gtrapprox 28$ on the neutral stability curves.

3.3.2 Search for the saddle point

From figures 3.6 and 3.13, it is clear that the neutral stability surface corresponding to the HS mode does not have a saddle point on the ζ-axis. However, there is a strong possibility that a saddle point exists for the S mode. From figure 3.6 it is seen that the neutral surface for the S mode decays for $\zeta > 0.13$. This implies that if a saddle point exists for this mode, it is likely to be located in k-space with $\zeta < 0.13$.

Since the HS mode is the primary instability for $\zeta < 0.13$, the numerical code is set to follow the eigenvalue that corresponds to the second least stable mode. Consequently, we obtain the required continuation of the S mode neutral surface. Since B_{min} is likely to increase very rapidly, producing a full neutral surface (with refined settings) would be very inefficient. Instead, a few trajectories (corresponding to neutral stability) are computed for some fixed values of k with $(N, I) = (6, 90)$, see figure 3.15. From this diagram it appears that the saddle point is located within the vicinity of $\zeta = -0.02$. Accordingly, the search is concentrated within this area and the neutral surface is computed with a finer grid, see figures 3.16 and 3.17 (the large dark arrow in these figures indicates the presence of the saddle point). Moreover, close to the location of the saddle point, it is found that parts of the neutral stability surface are crumpled. However, in this case we do not relate these discontinuous regions to the involvement of another mode dominating over the S mode, and we shall return to discuss this issue later.

Although the saddle point is located close to the discontinuous region of the surface (separated by a gap of $\Delta k \approx 0.04$), see figure 3.18, it is found that the saddle point is perfectly preserved. In view of this result, a parabola minimising technique is used to home in on the critical values (k_0, B_0, ζ_0). Moreover, the location of the saddle point is calculated with $(N, I) = (6, 100)$ and $(8, 100)$. Accordingly, the values of k_0, B_0 and

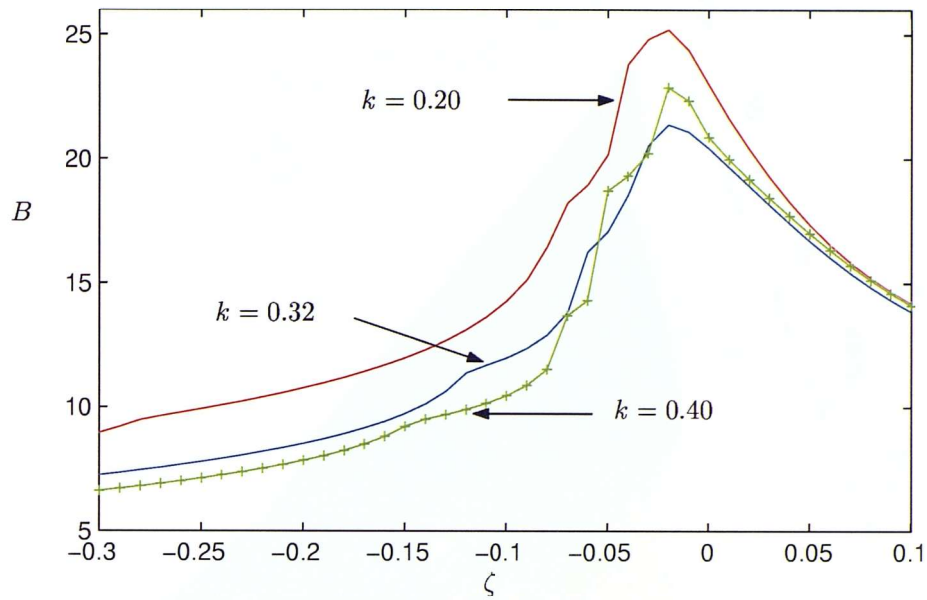


Fig. 3.15: The lower neutral stability curves of the S mode instability. These trajectories are computed for $k = 0.20,\ 0.32$ and 0.40 with $(N, I) = (6, 90)$.

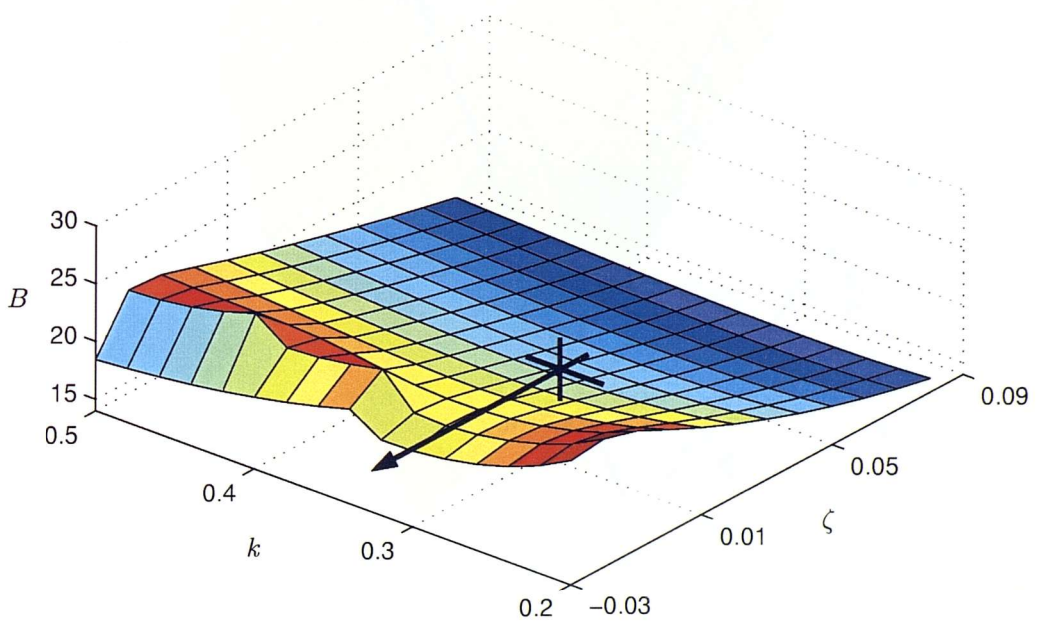


Fig. 3.16: The lower neutral stability surface of the S mode. This surface is computed with $(N, I) = (6, 90)$.

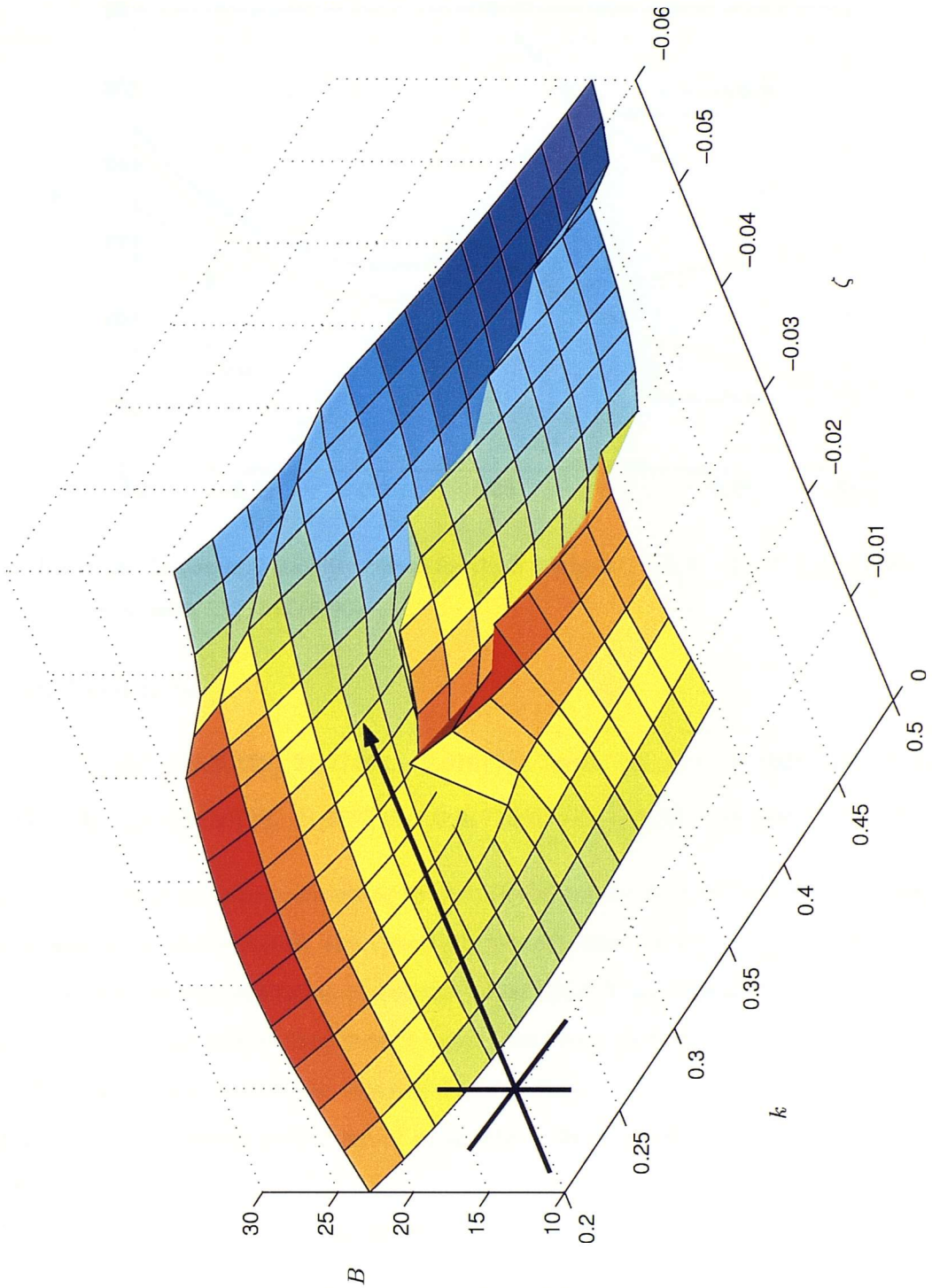


Fig. 3.17: The lower neutral stability surface of the S mode. This surface is computed with $(N, I) = (6, 90)$.

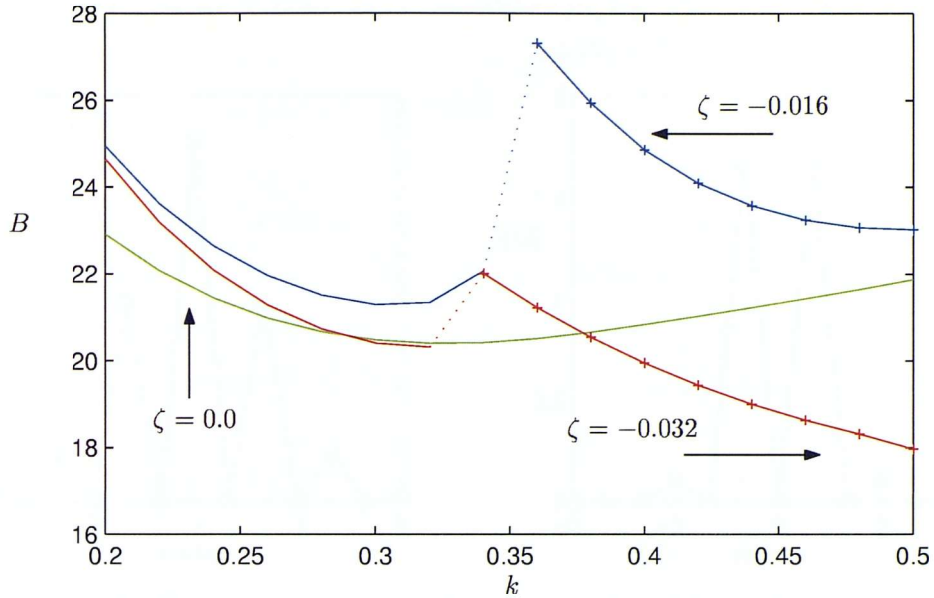


Fig. 3.18: The neutral stability curves for the S mode at $\zeta = 0.0,\ -0.016$ and -0.032, calculated with $(N, I) = (6, 90)$.

ζ_0 are found to be

$$(k_0,\ B_0,\ \zeta_0) = (0.30829,\ 21.27468, -0.016775) \quad \text{with} \quad (N, I) = (6, 100) \quad \text{and} \tag{3.68a}$$

$$(k_0,\ B_0,\ \zeta_0) = (0.30178,\ 21.402745, -0.017150) \quad \text{with} \quad (N, I) = (8, 100). \tag{3.68b}$$

The energy spectrum corresponding to each of the results in (3.68) are shown in figures 3.19 and 3.20. As required, the spectrum in each case decays rapidly to zero. This implies that the representation of the eigen functions, is appropriately captured by the number of Fourier modes used in each case. The two results for B_0 in (3.68) are within 0.6% of each other, and so the value of B_0 in (3.68b) is accepted as a converged result. Accordingly, the asymptotic form of α, at which the S mode instability is initiated, is given by

$$\alpha = 21.40/\Phi^{1/4} + \ldots \quad \text{as} \quad \Phi \to \infty \tag{3.69}$$

It is interesting to note that this result for B_0 is approximately 4.8 times the size of the corresponding value for the Hele-Shaw cell configuration. Consequently, this implies that the flow within a circular pipe is more stable.

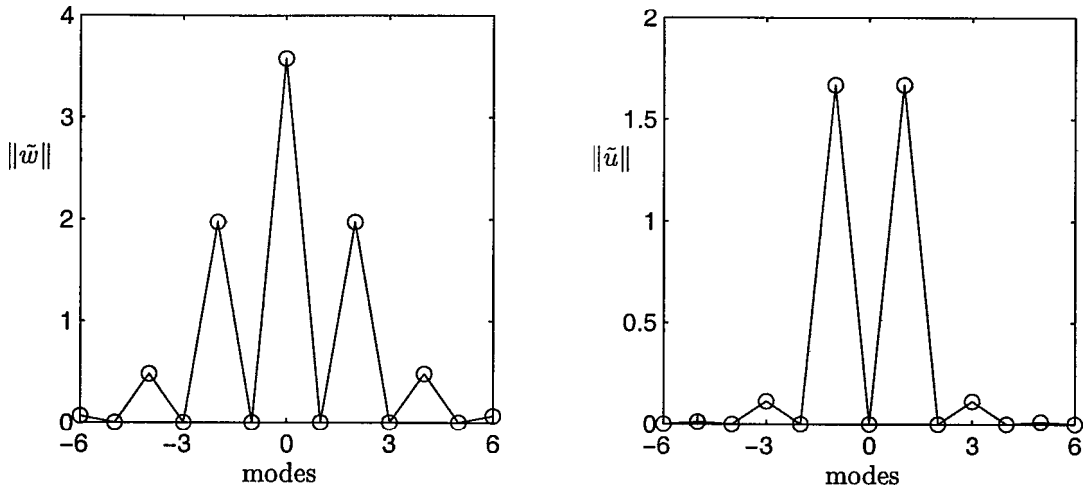


Fig. 3.19: The energy spectrum of the S mode near the saddle point, calculated with $(N, I) = (6, 100)$. Here, $\|\tilde{w}\|^2 = \tilde{w}\tilde{w}^*$, where the asterisk denotes complex conjugate.

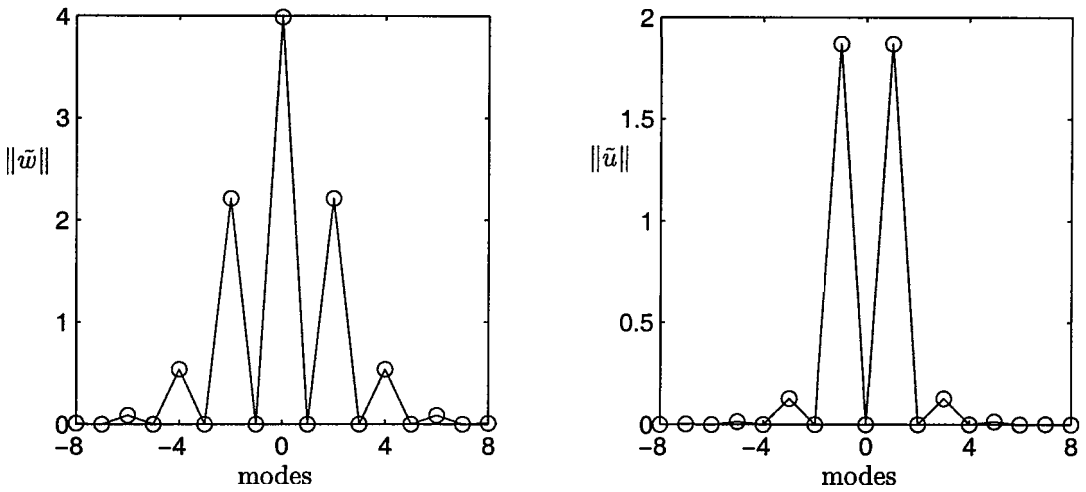


Fig. 3.20: The energy spectrum of the S mode near the saddle point, calculated with $(N, I) = (8, 100)$. Here, $\|\tilde{w}\|^2 = \tilde{w}\tilde{w}^*$, where the asterisk denotes complex conjugate.

Let us now return to the issue concerning the crumpled region in the vicinity of the saddle point. In this particular case, the discontinuity is caused by a dominating mode that appears sporadically and has $\mathrm{Im}\{\mu\} \neq 0$. The appearance of this mode is brought about by the numerical inaccuracies in the scheme. These inaccuracies are probably incurred by using a step size that is too large or perhaps by using an insufficient number of Fourier modes. Although the step size and the number of Fourier modes, being used in these calculations are sufficient for S mode, they are insufficient for calculating the other eigenvalues of (3.65) i.e. the eigenvalues that correspond to the tertiary and quaternary instabilities. Under these circumstances, the Fourier code sorts the eigenvalues incorrectly by listing an unconverged sporadic eigenvalue in place of the S mode eigenvalue. This results in the eigenvalue for the S mode being placed lower down in the hierarchy of the dominating instabilities. Hence the discontinuities near the saddle point are the result of an unconverged eigenvalue in the numerics. Moreover, since the real and imaginary parts of the sporadic eigenvalue vary erratically with small changes to (k, B, ζ), it is clear that this mode is not an authentic solution to (3.65). Fortunately, since the saddle point is preserved, there is no need to adopt another strategy to follow the neutral surface of the S mode instability.

3.4 Conclusion

In this study, the onset of a new roll-type instability (as observed by BM [10]) is investigated for the flow in a torsionally oscillating pipe. This problem is considered in the small-amplitude and high-frequency limit. Moreover, the theory of Soward & Jones [82] is used to find physically acceptable solutions of the governing stability equations.

In order to accommodate the slow variation of θ (in the stability equations), the velocity perturbation is represented in the WKBJ form. Consequently, this leads to an eigenvalue problem for B, where $\alpha = B/\bar{\Phi}^{1/4}$. The task thereafter is to minimise B with respect to θ and the wave number k. However, in order to minimise B appropriately, it is necessary to extend the search for the required saddle point into the complex θ-plane.

By time marching the stability equations, it is found that the neutral stability surface is discontinuous at $\zeta \approx 0.12$ (see figure 3.6 on page 203, note $\theta = i\zeta$). Since there are no saddle points on either side of this discontinuity, it is necessary to pursue the search by using a Fourier series representation for the velocity perturbation ($\tilde{u}$, $\tilde{w}$). By using the Fourier representation, it is found that the stability surface for the HS mode does not give the required saddle point. Moreover, for fixed values of ζ, it is found that the growth rate for the HS mode is zero upon circular trajectory (as opposed to curve shaped like a catenary), see figure 3.13. This circular region becomes smaller as ζ is increased and eventually vanishes at $\zeta \approx 0.12$. Consequently, the HS mode is stable for $\zeta > 0.12$. In view of this result, the eigenvalue corresponding to the second least stable mode (the S mode) is investigated and a saddle point is found at $\zeta \approx -0.017$, see (3.68). In this case, the value of B_0 is roughly 4.7 times larger than the value corresponding to the Hele-Shaw cell. In addition, the instability at this value of B_0 is synchronous with the basic state because $\mathrm{Im}\{\mu\} = 0$. Despite an exhaustive search in the ζ-plane, no subharmonic instabilities were found to exist. Moreover, the latter result echoes the findings in the investigation by Aoidef *et al.* [2], who study the oscillating Hele-Shaw cell for $O(1)$ values of α and Φ. In the study by Aoidef *et al.*, all the perturbations were found to be synchronous with the basic state, and this was also found to be the case in a separate investigation by Hall [36].

In our Fourier analysis, it is found that when $B \approx 28$, the settings in the numerical code need to be refined i.e. N needs to be larger than 6 and I needs to be larger than 100 (here, the number of Fourier modes is $2N+1$ and $\Delta\eta = \eta_\infty / I$, and $\eta_\infty = 25$). For this reason, the upper surface corresponding to the S mode has not been computed, and the existence of a saddle point on the upper surface remains open to investigation. If a saddle point does exist on the upper surface, it would be interesting to investigate its physical relevance to the experimental observations of BM [10]. In the experimental investigation of circular pipe, BM report that the final configuration of the instability is sensitive to the initial state of the fiuid in the pipe, see figure 3.1. Under some circumstances, two rolls are seen in the pipe and the interface between these rolls is

typically turbulent. To this date, the flow in a circular pipe has not been characterised in detail, and the exact circumstances that give rise to the latter turbulent state are still unknown.

It is also worth mentioning that in the investigation by Aoidef *et al.* [2], it is found that the stability curve bifurcates at $\Phi \approx 51.6$ and $\alpha \approx 5.8$. As Φ is further decreased, two additional bifurcations take place and the interval, $\Delta\Phi$, between each of these bifurcations decreases successively, see figure 4 of [2]. It is envisaged that a similar $O(1)$ analysis for the circular pipe, may shed some light on the turbulent roll state observed by BM. However, due to the complicated nature of such a numerical pursuit, it is likely that further theoretical developments will not be made, unless an experimental analysis of the pipe configuration is conducted first.

It is hoped that the present study offers an interesting insight into the roll-type instability observed in a torsionally oscillating pipe. Moreover, the findings in this study, are unlike those reported for the flow between two spheres, see Soward & Jones [82]. In the latter study, the required saddle point is located on a continuation of the neutral curve that corresponds to the flow between two cylinders. In this respect, the present study is interesting because the primary instability of the HS mode, is not responsible for initiating the same instability that develops in the pipe configuration.

Bibliography

[1] ABRAMOWITZ, M. AND STEGUN, I. A. (1965) Handbook of mathematical functions. *Dover publications.*

[2] AOIDEF, A., NORMAND C. AND WESFREID, J. E. (1995) Coriolis instablity of pulsed flow. *Phys. Fluids* **7 No.9**, 2230-2242.

[3] BARTELS, FRITZ (1982) Taylor vortices between two concentric rotating spheres. *J. Fluid Mech.* **119**, 1-25.

[4] BÉNARD, H. (1900) Les tourbillons cellulaires dans une nappe liquide. *Revue Gén. Sci. Pur. Appl.* **11**, 1261-1271 and 1309-1328.

[5] BERGÉ, P., POMEAU, Y., AND VIDAL, C. (1984) Order within chaos - Towards a deterministic approach to turbulence. *John Wiley and Sons Ltd.*

[6] BERMAN, A. S. (1953) Laminar flow in channels with porous walls. *J. Appl. Phys.* **24**, 1232-1235.

[7] BERTELSEN, ARNOLD F. (1973) An experimental investigation of high Reynolds number steady streaming generated by oscillating cylinders. *J. Fluid Mech.* **64**, 589-597.

[8] BICKLEY, W. G. (1937) The plane jet. *Phil. Mag.* **23**, 727-731.

[9] BLOCK, M. J. (1956) Surface tension as the cause of Bénard cells and surface deformation in a liquid film. *Nature* **178**, 650-651.

[10] BOLTON, E. AND MAURER, J. (1994) A new roll-type instability in an oscillating fluid plane. *J. Fluid Mech.* **268**, 293-313.

[11] BOYD, JOHN P. (2000) Chebyshev and Fourier spectral methods. *Dover publications*
http://www-personal.engin.umich.edu/~jpboyd

[12] BRADY, J. F. AND ACRIVOS, A. A. (1981) Steady flow in a channel or tube with an accelerating surface velociy. An exact solution to the Navier-Stokes equations with reverse flow. *J. Fluid Mech.* **112**, 127-150.

[13] COLES, D. (1965) Transition in circular Couette flow. *J. Fluid Mech.* **21**, 385-425.

[14] COUETTE, M. (1890) Études sur le frottement des liquides. *Ann. Chim. Phys.* (6) **21**, 433-510.

[15] DAVIDSON, B. J. AND RILEY, N. (1972) Jets induced by oscillatory motion. *J. Fluid Mech.* **53**, 589-597.

[16] DAVIS, STEPHEN. H. (1976) The stability of time-periodic flows. *Ann. Rev. Fluid Mech.* **8**, 287-303.

[17] DIPRIMA, R. C. (1961) Stability of nonrotationally symmetric disturbances for viscous flow between rotating cylinders. *Phys. Fluids* **4**, 751-755.

[18] DIPRIMA, R. C. AND SJBRAND, J. (1982) Instability in the mechanics of continuae. *Springer* 383.

[19] DRAZIN, P. G. AND REID, W. H. (1981) Hydrodynamic stability. *Cambridge University Press.*

[20] DUCK, P. W. AND SMITH, F. T. (1979) Steady streaming between oscillating cylinders. *J. Fluid Mech.* **91**, 93-110.

[21] FENSTERMACHER, P. R., SWINNEY, H. L. AND GOLLUB, J. P. (1979) Dynamical instabilities and the transition to chaotic Taylor vortex flow. *J. Fluid Mech.* **94**, 103-129.

[22] FETTIS, H. E. (1956) On the integration of a class of differential equations occuring in boundary-layer and other hydrodynamical problems. *Proc. 4th Mid West Conf. Fluid Mech.* Purdue Univ., 93-114.

[23] FORNBERG, BENGT (1996) A practical guide to pseudospectral methods. *Cambridge University Press.*

[24] GÖRTLER, H. (1940) Über eine dreidimensionale instabilität laminarer grenzschichten an konkaven wäden. *Nachr. Ges. Wiss. Göttingen* N.F. **2**.

[25] HADDON, E. W. AND RILEY, N. (1979) The steady streaming induced between oscillating circular cylinders. *Q. Jl Mech. appl. Math* **32 No.4**, 265-282.

[26] HALL, P. (1978) The linear stability of flat Stokes layers. *Proc. R. Soc. Lond.* A **359**, 151-166.

[27] HALL, P. (1981) Centrifugal instability of a Stokes layer: subharmonic destabilization of the Taylor vortex mode. *J. Fluid Mech.* **105**, 523-530.

[28] HALL, P. (1982a) Taylor-Görtler vortices in fully developed or boundary layer flows: linear theory. *J. Fluid Mech.* **124**, 475-494.

[29] HALL, P. (1982b) On the non-linear evolution of Görtler vortices in non-parallel boundary layers. *J. Inst. Math.* **29**, 173-196.

[30] HALL, P. (1983) The linear development of Görtler vortices in growing boundary layers. *J. Fluid Mech.* **130**, 41-58.

[31] HALL, P. (1984) On the stability of the unsteady boundary layer on a cylinder oscillating transversly in a viscous fluid. *J. Fluid Mech.* **146**, 347-367.

[32] HALL, P. (1988a) The nonlinear development of Görtler vortices in growing boundary layers. *J. Fluid Mech.* **193**, 243-266.

[33] HALL, P. AND LAKIN, W. D. (1988b) The fully nonlinear development of Görtler vortices in growing boundary layers. *J. Fluid Mech.* **193**, 243-266.

[34] HALL, P. (1990) Görtler vortices in growing boundary layers: the leading edge receptivity problem, linear growth and the noninear breakdown stage. *Mathematika* **37**, 151-189.

[35] HALL, P. AND HORSEMAN, N. J. (1991) The inviscid instability of longitudinal vortex structures in boundary layers. *J. Fluid Mech.* **232**, 357-375.

[36] HALL, P. (1994) On the instability of the flow in an oscillating tank of fluid. *J. Fluid Mech.* **268**, 315-331.

[37] HALL, P. AND PAPAGEORGIOU, D. T. (1999) The onset of chaos in a class of the Navier-Stokes solutions. *J. Fluid Mech.* **393**, 59-87.

[38] HÄMMERLIN, G. (1955) Über das eigenwert problem der dreidimensionalen instabilität laminarer grenzschichten an konkaven wänden. *J. Rat. Mech. Anal.* **4**, 279-321.

[39] HÄMMERLIN, G. (1956) Zur theorie der dreidimensionalen instabilität laminarer grenzschichten. *Z. Angew. Math. Phys* **7**, 156-164.

[40] HEADING, J. (1962) An introduction to phase-integral methods. *Methuen & Co.*

[41] HERBERT, G. (1976) On the stability of a boundary layer on a curved wall. *Arch. Mech.* **28**, 1039.

[42] HOCKING, L. M. AND SKIEPKO (1981) The instability of flow in the narrow gap between two prolate spheriods. Part 1. Small axis ratio. *Q. Jl Mech. appl. Math* **34 No.1**, 57-68.

[43] HOCKING, L. M. (1981) The instability of flow in the narrow gap between two prolate spheriods. Part 2. Arbitrary axis ratio. *Q. Jl Mech. appl. Math* **34 No.4**, 475-488.

[44] HONJI H. (1981) Streaked flow around an oscillating circular cylinder. *J. Fluid Mech.* **107**, 509-520.

[45] LIEPMANN, H. W. (1945) Investigation of boundary layer transition on concave walls. NACA *Wartime Rep.* **W-87**
http://naca.larc.nasa.gov.

[46] KERCZEC, C. VON AND DAVIS, S. H. (1974) Linear stability theory of oscillatory Stokes layers. *J. Fluid Mech.* **62**, 753-773.

[47] KHLEBUTIN, G. N. (1968) Stability of fluid motion between a rotating and stationary sphere. *Fluid Dyn.* **3**, 31.

[48] KOSHMIEDER, E. L. (1979) Turbulent Taylor vortex flow. *J. Fluid Mech.* **93**, 515-527.

[49] KRUGER, E. R., GROSS, A. G., AND DIPRIMA, R. C. (1966) On the relative importance of Taylor-vortex and non-axisymmetric modes in flows between rotating cylinders. *J. Fluid Mech.* **24**, 521-538.

[50] MALLOCK, A. (1896) Experiments on fluid viscosity. *Phil. Trans. Roy. Soc. London* Ser. A **183**, 41-56.

[51] MARCUS, PHILIP S. AND TUCKERMAN, LAURETTE S. (1987) Simulation of flow between concentric rotating spheres. Part 1. Steady states. *J. Fluid Mech.* **185**, 1-30.

[52] MARCUS, PHILIP S. AND TUCKERMAN, LAURETTE S. (1987) Simulation of flow between concentric rotating spheres. Part 2. Transitions. *J. Fluid Mech.* **185**, 31-65.

[53] MUNSON, B. R. AND JOSEPH, D. D. (1971) Viscous incompressible flow between concentric rotating spheres. Part 1. Basic flow. *J. Fluid Mech.* **49**, 289.

[54] MUNSON, B. R. AND JOSEPH, D. D. (1971) Viscous incompressible flow between concentric rotating spheres. Part 2. Hydrodynamic stability. *J. Fluid Mech.* **49**, 305.

[55] MUNSON, B. R. AND MENGUTURK (1975) Viscous incompressible flow between concentric rotating spheres. Part 3. Linear stability and experiments. *J. Fluid Mech.* **69**, 705-719.

[56] PANAGOPOULOS, A. A. , PSILLAKIS, Z. M. AND KARAHALIOS, G. T. (1991) Steady streaming induced by a cylinder performing transverse and torsional oscillations. *Phys. Fluids* **3 No.5**, 782-792.

[57] PAPAGEORGIOU, D. T. (1987) Stability of the unsteady viscous flow in a curved pipe. *J. Fluid Mech.* **182**, 209-233.

[58] PARK, K., BARENGHI, C. AND DONNELLY, R. J. (1980) Subharmonic destabilization of Taylor vortices near an oscillating cylinder. *Phys. Lett.* A **78**, 152-154.

[59] PEARSON, J. R. A. (1958) On convection cells induced by surface tension. *J. Fluid Mech.* **4**, 489-500.

[60] PRESS, W., TEUKOLSKY, S., VETTING, W., AND FLANNERY, B. (1988) Numerical recipies in C. *Cambridge University Press.*
http://www.nr.com.

[61] PROUDMAN, I. (1960) An example of steady laminar flow at large Reynolds number. *J. Fluid Mech.* **9**, 593-602.

[62] RAYLEIGH, LORD (1916) On convection currents in a horizontal layer of fluid, when the higher temperature is on the underside. *Phil. Mag.* (6) **32**, 529-546.

[63] RAYLEIGH, LORD (1916) On the dynamics of revolving fluids. Sci. Papers C.U.P., (6), 447-453.

[64] REYNOLDS, O. (1883) An experimental investigation of the circumstances which determine whether the motion of water shall be direct or sinuious, and of the law of resistance in parallel channels. *Phil. Trans. Roy. Soc.* **174**, 935-982.

[65] RILEY, N. (1965) Oscillating viscous flows. *Mathematika* **12**, 161.

[66] RILEY, N. (1967) Oscillatory viscous flows. Review and exension. *J. Inst Math. Appl.* **3**, 419-434.

[67] RILEY, N. (1975) The steady streaming induced by a vibrating cylinder. *J. Inst Math. Appl.* **68**, 801-812.

[68] RING, MICHAEL (2001) Mikes Arbitrary Precision Math Library, University of Minnesota (Written in C with a C++ handling class)
http://www.tc.umn.edu/~ringx004/mamp-main.html.

[69] ROBINSON, W. A. (1987) The existence of multiple solutions for the laminar flow in a uniformly porous channel with suction at both walls. *J. Appl. Math.* **10**, 526-533.

[70] SARIC, W. S. (1994) Görtler vortices. *Ann. Rev. Fluid. Mech.* **26**, 379-409.

[71] SAWATZKI, O. AND ZIEREP, J (1970) Das Stromfeld im Splat zwischen zwei konzentrischen Kügelfächen von denen die innere rotiert. *Acta Mechanica* **9**, 13-35.

[72] SCHLICHTING, H. (1932) Berechnung ebner periodischer Grenzchichtströmungen. *Phys. Z.* **33**, 327.

[73] SCHULZE, TIM H. (1999) A note on subharmonic instabilities. *Phys. Fluids* **11**, 3573-3576.
http://www.math.utk.edu/ ~schulze/publications.htm.

[74] SEGEL, LEE A. (1961) Application of conformal mapping to viscous flow between moving circular cylinders. *Quart. Appl. Math.* **18 No.4**, 335-353.

[75] SELLARS, J. R. (1955) Laminar flow in a channel with porous walls at high suction Reynolds number. *J. Appl. Phys.* **26**, 489-490.

[76] SEMINARA, G. AND HALL, P. (1976) Centrifugal instability of a Stokes layer: linear theory. *Proc. R. Soc. Lond.* A **350**, 299-316.

[77] SEMINARA, G. AND HALL, P. (1977) Centrifugal instability of a Stokes layer: Nonlinear theory. *Proc. R. Soc. Lond.* A **354**, 119-126.

[78] SHORTIS, A. AND HALL, P. (1999) On the nonlinear stability of the oscillatory viscous flow of an incompressible fluid in a curved pipe. *J. Fluid Mech.* **379**, 145-163.

[79] SMITH, A. M. O. (1955) On the growth of Taylor-Görtler vortices along highly concave walls. *Quart. Appl. Math.* **13**, 233-262.

[80] SNYDER, H. A. (1968) Stability of rotating Couette flows. Part 1: Asymmetric waveforms. *Phys. Fluids* **11**, 728-734.

[81] SORENSEN, D. C., LEHOUCQ, R. B. AND YANG, C. (Weblink) Implicitly restarted Arnoldi package for eigenvalue problems (Fortran 77 and C++ versions). http://www.caam.rice.edu/software/ARPACK.

[82] SOWARD, A. M. AND JONES, C. A. (1983) The linear stability of the flow in the narrow gap between two concentric rotating spheres. *J. Mech. Appl. Math* **36**, 19-42.

[83] STUART, J. T. (1963) Laminar Boundary Layers (chapters 7 and 9) edited by ROSENHEAD, L. *Oxford University Press.*

[84] STUART, J. T. (1966) Double boubdary layers in oscillatory viscous flow. *J. Inst Math. Appl.* **24**, 673-687.

[85] STUART, J. T. (1971) Nonlinear stability theory. *Ann. Review* **3**, 347-370.

[86] STUART, J. T. (1986) Taylor-vortex flow: A dynamical system. *SIAM Review* **28**, 315-342.

[87] SWEARINGEN, J. D. AND BLACKWELDER, R. F. (1987) The growth and breakdown of streamwise vortices in the presence of a wall. *J. Fluid Mech.* **182**, 255-290.

[88] SYNGE, J. L. (1938) On the stability of a viscous liquid between two rotating coaxial cylinders. *Proc. Roy. Soc. London* Ser. A **167**, 250-256.

[89] TADMOR, EITAN (1989) Convergence of spectral methods for nonlinear conservation laws. *SIAM J. Numer. Anal.* Issue. 1 **26**, 30-44.

[90] TADMOR, EITAN (1989) Shock capturing by the spectral viscosity method. *Computer methods in applied mechanics and engineering.* **78**, 197-208.
http://cscamm.umd.edu/~tadmor

[91] TAYLOR, G. I. (1921) Experiments with rotating fluids. *Proc. Camb. Phil. Soc.* **20**, 326-329.

[92] TAYLOR, G. I. (1923) Stability of a viscous contained between two rotating cylinders. *Phil. Trans. Roy. Soc.* Ser. A **223**, 289-343.

[93] TERRILL, R. M. (1964) Laminar flow in a uniformly porous channel. *Aeronaut. Q.* **15**, 299-310.

[94] TERRILL, R. M. (1965) Laminar flow in a uniformly porous channel with large injection. *Aeronaut. Q.* **16**, 323-332.

[95] THOMSON, J. (1881) On a changing tessellated structure in certain liquids. *Proc. Phil. Soc. Glasgow* **13**, 464-468.

[96] WALTON, I. C. (1978) The linear stability of the flow in a narrow spherical annulus. *J. Inst Math. Appl.* **86**, 673-693.

[97] WATSON, E., BANKS, W., ZATURSKA, M. AND DRAZIN, P. (1988) On transition to chaos in two-dimensional channel flow symmetrically driven by accelerating

walls.

J. Fluid Mech. **212**, 451-485.

[98] WEINAN, E. AND LIU, JIAN-GUO (1995) Vorticity boundary condition and related issues for finite difference schemes. *J.Computational Physics* **124**, 368-382. http://www.math.umd.edu/~jliu/research/list.html

[99] WIMMER, M. (1976) Experiments on a viscous fluid flow between concentric rotating spheres. *J. Fluid Mech.* **78**, 317.

[100] WIMMER, M. (1981) Experiments on the stability of viscous flow between two concentric rotating spheres. *J. Fluid Mech.* **103**, 117-131.

[101] YIH, CHIA-SHUN (1969) Fluid Mechanics. *West River Press, Ann Arbor.*

[102] YIH, C.-S. AND LI, C.-H. (1972) *J. Fluid Mech.* **54**, 143-152.

[103] YOUNG, A. D. (1989) Boundary Layers. *Blackwell Scientific Publications.*

[104] YUAN, S. W. (1956) Further investigation of laminar flow in a channel with porous walls. *J. Appl. Phys.* **27**, 267-269.

[105] ZATURSKA, M. B., DRAZIN, P. G., AND BANKS, W. H. H. (1988) On the flow of a viscous fluid driven along a channel by suction at porous walls. *Fluid Dyn. Res.* **4**, 151-178.

[106] ZIEREP, J. AND SAWATZKI, O. (1970) Three dimensional instabilities and vortices between two rotating spheres. In *8th Symp. Naval Hydrodyn.* 275-288.